DISS. ETH NO. 28702

SEISMIC BEHAVIOR OF ROCKING BRIDGES EXHIBITING NEGATIVE STIFFNESS

A thesis submitted to attain the degree of

DOCTOR OF SCIENCES of ETH ZURICH

(Dr. sc. ETH Zurich)

presented by

NATALIA REGGIANI MANZO

Mestra em Engenharia Civil, Universidade Estadual de Campinas

born on *01.10.1994*

citizen of Italy and Brazil

submitted for the recommendation of

Prof. Dr. Michalis F. Vassiliou

Prof. Dr. Bozidar Stojadinovic

Prof. Dr. Matthew DeJong

2022

Abstract

Rocking structures with negative lateral stiffness are a promising solution for enabling the use of precast elements in the substructure of bridges constructed in seismically active regions. Such structural systems are resilient, presenting minimal or no residual displacements and damages after an earthquake; and they potentially reduce the forces transmitted to the foundation, and consequently reduce its size. Nevertheless, despite its advantages, such design concept has not found widespread implementation, mainly because of the limited number of experimental studies on their seismic performance, and because of the absence of established simplified design methods. This dissertation is an effort to bring such systems closer to practice. It provides both a simplified design method for systems with negative lateral stiffness, as well as experimental evidence of their seismic resilience.

The simplified design method presented herein was developed based on the observation that, when the rocking motion is described in terms of horizontal displacements (not rotations), the response of the system depends mainly on its uplift force and not on its displacement capacity. Thus, by disregarding the displacement capacity term, a unique spectrum for systems with same uplift force, but different displacement capacity can be constructed. Two approaches were explored for estimating the displacement demand of a given system using the proposed spectrum: the equal displacement rule and the equal energy rule. Case studies comparing the results given by the proposed method and time history analyses reveal that equal energy rule is more conservative than the equal displacement rule. In all studied cases, the proposed design method returned displacement demands with a maximum of 40% deviation from the displacement demand predicted by the time history analysis, which suggests its adequacy for preliminary design calculations.

A uniform risk spectrum (URS), which introduces the uncertainties of seismic actions into the previously proposed spectrum, was also presented in this dissertation. After discussing the methodology for its construction, site-specific uniform risk spectra constructed using the geomean of the peak ground acceleration (PGA) and peak ground velocity (PGV) as intensity measures are presented for six different locations in Europe. Bootstrapping analysis were employed to indirectly investigate the efficiency of each intensity measure. It was concluded that PGV is the optimal intensity measure for predicting the peak rocking response, while PGA is optimal for predicting rocking initiation. Finally, analytical approximations of the PGV-based spectra, which facilitate their implementation in practice, were also offered.

In addition, an experimental campaign comprising quasi-static cyclic tests and shaking table tests on restrained rocking systems with negative lateral stiffness was performed. The specimens consisted of rocking columns simply standing on the ground and only connected to a cap-beam or slab through unbonded tendons in series with springs. At the quasi-static tests, the rocking piers were subjected to drift ratios of up to 16%, presenting almost no damage and no residual displacements, an indication of the resilience of the system. Furthermore, the system response agreed reasonably well with the response of a rigid body model.

The seismic resilience of the system was also confirmed by shaking table tests. The specimen was subjected to 181 excitations, scaled to two different levels of the peak ground velocity, and the only observed damage was the abrasion of the edges of the column ends. The slab experienced torsion, which was caused by small imperfections in the system. The system collapsed during the last excitation due to premature failure of the tendons. This highlights that the tendons should be designed with a large safety factor.

The dissertation concludes with the statistical validation of a 3D rigid body model against the experimental data from the shaking table tests. Despite the simplicity of the model, which disregards a number of physical mechanisms observed in the tests, the numerical empirical cumulative distribution functions (CDF) were within the 95% confidence interval of the experimental empirical CDF, giving a first indication that the numerical model can be considered a good descriptor for the tested system.

Zusammenfassung

Schaukelnde Strukturen mit negativer lateraler Steifigkeit sind eine vielversprechende Lösung für die Verwendung vorfabrizierter Elemente im Unterbau von Brücken in seismisch aktiven Regionen. Solche Tragwerkssysteme sind elastisch und weisen nach einem Erdbeben nur minimale oder gar keine bleibenden Verformungen und Schäden auf; außerdem können sie die auf das Fundament übertragenen Kräfte und damit dessen Abmessungen verringern. Trotz dieser Vorteile konnte sich dieses Entwurfskonzept bisher nicht durchsetzen, vor allem weil es nur wenige experimentelle Studien über das seismische Verhalten und keine etablierten vereinfachten Bemessungsmethoden gibt. Diese Dissertation versucht solche Systeme der Praxis näher zu bringen. Sie liefert sowohl eine vereinfachte Bemessungsmethode für Systeme mit negativer lateraler Steifigkeit als auch experimentelle Nachweise für ihre seismische Widerstandsfähigkeit.

Die vereinfachte Bemessungsmethode basiert auf der Beobachtung, dass wenn die Schaukelbewegung mittels horizontaler Verschiebung beschrieben wird, das Verhalten des Systems hauptsächlich von seiner anhebenden Kraft und nicht von seiner Verschiebungskapazität abhängt. Durch Vernachlässigung der Verschiebungskapazität kann daher ein eindeutiges Spektrum für Systeme mit gleicher anhebender Kraft aber unterschiedlicher Verschiebungskapazität erstellt werden. Dabei wurden zwei Ansätze zur Abschätzung des Verschiebungsbedarfs eines bestimmten Systems unter Verwendung des vorgeschlagenen Spektrums untersucht: die Regel der gleichen Verschiebung und die Regel der gleichen Energie. Fallstudien, welche die vorgeschlagenen Bemessungsmethode mit Zeitverlaufsanalysen vergleichen, zeigen, dass die Regel der gleichen Energie konservativer ist als die Regel der gleichen Verschiebung. In allen untersuchten Fällen ergab die vorgeschlagene Bemessungsmethode Verschiebungsanforderungen mit einer maximalen Abweichung von 40% von der durch die Zeitverlaufsanalyse vorhergesagten Verschiebungsanforderung, was auf ihre Eignung für vorläufige Bemessungsberechnungen schließen lässt.

Ein einheitliches Risikospektrum (URS), dass die Unsicherheiten seismischer Einwirkungen in das zuvor vorgeschlagene Spektrum einbezieht, wurden ebenfalls in dieser Dissertation vorgestellt. Nach der Erörterung der Methodik für die Erstellung dieses Spektrums werden für sechs verschiedene Standorte in Europa standortspezifische einheitliche Risikospektren vorgestellt, die unter Verwendung des geometrischen Mittels der maximalen horizontalen

Bodenbeschleunigung (PGA) und der maximalen horizontalen Bodengeschwindigkeit (PGV) als Intensitätsmasse erstellt wurden. Bootstrapping-Analysen wurden eingesetzt, um die Effizienz der einzelnen Intensitätsmasse indirekt zu untersuchen. Es wurde festgestellt, dass PGV das optimale Intensitätsmass für die Vorhersage der maximalen Schaukelverschiebung und PGA optimal für die Vorhersage der Initiierung der Schaukelbewegung ist. Schließlich wurden auch analytische Näherungen für die PGV-basierten Spektren angeboten, die ihre Umsetzung in der Praxis erleichtern.

Darüber hinaus wurde eine Versuchskampagne mit quasistatischen zyklischen Versuchen und Rütteltischversuchen an eingespannten schaukelnden Systemen mit negativer lateraler Steifigkeit durchgeführt. Die Probekörper bestanden aus schaukelnden Stützen, die einfach auf dem Boden standen und nur über unverankerte Spannglieder in Reihe mit Federn mit einem Kopfbalken oder einer Platte verbunden waren. Bei den quasistatischen Tests wurden die Schaukelstützen Driftverhältnissen von bis zu 16 % ausgesetzt, wobei sie fast keine Schäden und keine Restverschiebungen aufwiesen, was auf die Widerstandsfähigkeit des Systems hinweist. Außerdem stimmte die Reaktion des Systems recht gut mit der Reaktion eines Starrkörpermodells überein.

Die seismische Widerstandsfähigkeit des Systems wurde auch durch Rütteltischversuche bestätigt. Der Probekörper wurde 181 Rütteltischversuchen ausgesetzt, die auf zwei verschiedene Niveaus der maximalen Bodengeschwindigkeit skaliert waren, und die einzige beobachtete Beschädigung war der Abrasion der Kanten an den Stützenenden. Die Platte erfuhr eine Torsion, die durch kleine Imperfektionen im System verursacht wurde. Beim letzten Versuch kollabierte das System aufgrund eines vorzeitigen Versagens der Spannglieder. Dies zeigt, dass die Spannglieder mit einem großen Sicherheitsfaktor entworfen werden sollten.

Die Dissertation endet mit der statistischen Validierung eines 3D-Starrkörpermodells anhand der experimentellen Daten aus den Rütteltischversuchen. Trotz der Einfachheit des Modells, das eine Reihe von beobachteten physikalischen Mechanismen vernachlässigt, lagen die numerischen empirischen kumulativen Verteilungsfunktionen (CDF) innerhalb des 95%-Konfidenzintervalls der experimentellen empirischen CDF, was als ersten Hinweis angesehen werden kann, dass das numerische Modell ein guter Deskriptor des getesteten Systems ist.

Table of Contents

1. Introduction

Abstract

This chapter offers a brief introduction to the work presented in this dissertation, which is related to the seismic behavior of rocking bridges exhibiting negative lateral stiffness. Firstly, the motivation of the work is presented, followed by a literature review with the most relevant past studies. At the end of the literature review, the research gaps and objectives of this work are identified. The chapter ends with an outline of the structure of the dissertation and its key contributions.

1.1. Motivation and problem statement

Capacity-design is currently one of the main concepts used for designing seismic-resistant structures. It emerged during the 70-80's (Fardis, 2018), revolutionizing the design philosophy in seismically active regions, and dramatically improving the seismic performance of structures. According to this design philosophy, plastic deformation and damage is concentrated at predefined points of the structure, which are designed to be ductile enough.

The concept was perceived as a great advance in earthquake engineering because it guarantees that structures fulfill both "life safety" and "collapse prevention" performance levels, as defined in (FEMA 356, 2000). Although effective in achieving the above goals, recent earthquakes have brought up the main drawback of the capacity-design concept: after a strong seismic event, the structures are designed to exhibit significant damage, which requires large repairs, if not demolition of the structure.

For the society, such by-products of the earthquake are translated in economic and environmental losses. For instance, the total economic losses due to the 2010-2011 Canterbury earthquakes are estimated at $NZ 40 billion (Insurance Council of New Zealand, 2019). A preliminary study has also presented the environmental impact of the demolition of buildings in Christchurch due to the 2010-2011 Canterbury earthquakes (Gonzalez et al., 2021). The total embodied CO_2 was estimated at 3.08×10^8 kg, which corresponds to approximately the annual CO_2 emissions generated by the electricity consumption of 400,000 average homes in New Zealand. In Switzerland, a country with moderate seismicity, the expected economic losses due to an earthquake of magnitude 6.6 with epicenter in Basel are estimated between CHF 50 and 100 billion (Swiss Seismological Service, 2012). According to the same agency (Swiss Seismological Service, 2022), the return period of an earthquake with magnitude 6.0 or 7.0 occurring in Switzerland is 100 and 1000 years, respectively.

A class of structures of utmost importance during and after earthquakes are bridges. The closure of bridges, apart from hindering the access to rescue, also significantly impacts the region in the following months, causing several traffic disruptions and economic losses for the businesses in the surroundings. One example is the overpass bridge on Moorhouse Avenue, Christchurch, New Zealand. One of its piers failed during the 2011 Christchurch earthquake, causing its closure and traffic disruptions in the region for more than a month (Mashal, 2015; Palermo et al., 2012). The 2010 Chilean earthquake is another example of such disruptions in the aftermath of earthquakes. It has been reported that 30 bridges had to be closed, while another 70 bridges had their traffic restricted (Schanack et al., 2012). Similarly, in 2008, an

earthquake stronger than the design-level earthquake hit Wenchuan, China. The damage to several bridges isolated the area, preventing the access to emergency services (Han et al., 2009).

Besides being resilient, bridges also have to be quickly built in order to minimize the disturbances during construction. In non-seismic areas, bridge construction has been efficiently expedited by the use of precast elements both in the substructure and superstructure (Culmo, 2011). In high-seismicity areas, however, some challenges still exist for using prefabricated elements in the substructure.

Therefore, the work summarized in this dissertation is motivated by the societal need for quickly built, resilient, and sustainable structures, with a focus on bridge structures. The call for a resilient structure has been clearly presented through estimated economic losses and disruptions caused by previous earthquakes. Meanwhile, the need for more sustainable structures has been only preliminarily shown herein by the estimated greenhouse gases emitted due to the demolition of buildings. However, its importance can be clearly demonstrated by the United Nations 9th Sustainable Development Goal, which has as a mission statement "build resilient infrastructure, promote inclusive and sustainable industrialization, and foster innovation" (United Nations, 2015).

1.2. Background and state-of-art

As mentioned in the previous section, bridges need to be resilient and quickly constructed. With the goal of accelerating construction, precast elements have been widely adopted for the superstructure of the bridge. The use of precast elements in the substructure of the bridge, however, is less widespread.

In order to enable the use of precast elements in the substructure of seismic-resistant bridges, "emulative" and "non-emulative" connection solutions have been proposed. Emulative connections, as the name discloses, intend to mimic the seismic behavior of the connections of cast in-situ concrete structures. They can be categorized based on the force transfer mechanism (Marsh et al., 2011):

(a) Bar Coupler Connection (Figure 1.1a): the longitudinal reinforcement of the column is mechanically coupled to the foundation or cap-beam reinforcement. The load is transferred from the rebar of one element to the co-aligned rebar of the other element.

(b) Pocket Connection (Figure 1.1b): the foundation or cap-beam is precast with a void

("pocket"), in which the extended longitudinal reinforcement of the column is fitted into. After assembling the elements, the void is cast in-situ, connecting both elements.

(c) Grouted Duct Connection (Figure 1.1c): the longitudinal reinforcement of the column is connected to the foundation or cap-beam through individual ducts, which are later filled with grout. The force in the connecting rebars is transferred to the surrounding concrete.

(d) Socket Connection (Figure 1.1d): the column is precast with an extra length to embed it in the foundation or cap-beam. If the other element is also precast, the connecting element (i.e. the foundation and/or cap-beam) is cast with a void, and, after assemblage, the gap between them is filled with grout. The column is anchored by the bond between the interface surfaces and the grout.
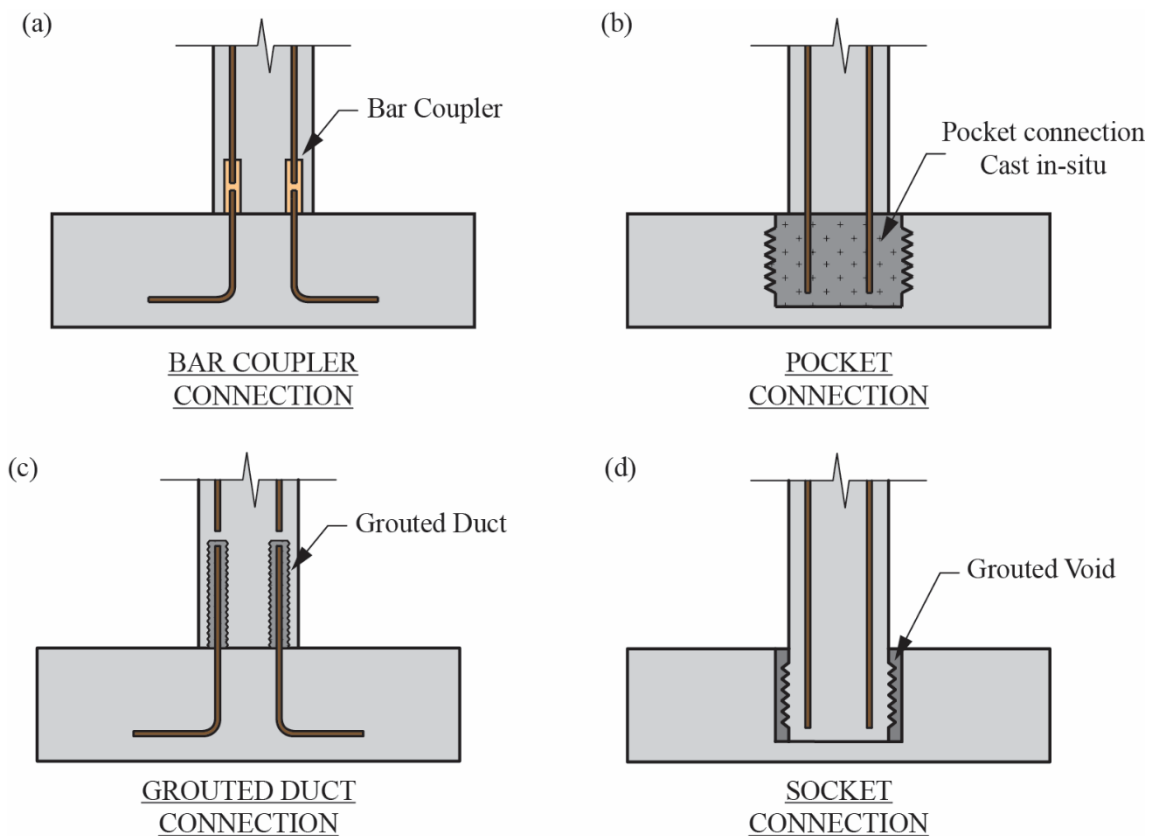
Figure 1.1. Emulative connections.

Although emulative connections reduce the construction time, they still lead to the same level of damage observed in capacity-designed structures. Non-emulative connections, on the other hand, reduce the system's residual displacements and damages, and, hence, are also resilient. The non-emulative connection consists of a dry connection, in which the precast column is only connected to the foundation and/or cap-beam through unbonded tendons. As the columns are allowed to rock, the joints can sustain large displacement demands with

reduced or no damage. The unbonded tendons provide a recentering mechanism, which reduces the system's residual displacements. In some cases, energy dissipating devices are employed for controlling displacement demands.

The concept was early explored as connections for precast frame elements (Nakaki et al., 1999; Priestley et al., 1999; Priestley & Tao, 1993; Stone et al., 1995), where the rocking section was located at the end of the beams, allowing the precast posttensioned beams to rock. Mild-steel reinforcing bars were also provided for energy dissipation. Their test results have shown that, in terms of residual displacement and accumulated damage, the proposed system presents similar or better seismic performance than cast in-situ structures.

Mander & Cheng (1997) introduced the concept of non-emulative connections to bridge structures. They performed cyclic tests on a precast rocking bridge system, in which posttensioning was provided to the piers, and the pier ends were protected by a steel disc. The system presented good recentering capabilities and almost no damage, but low energy dissipation. In an attempt to increase energy dissipation and control the displacement demands, it has been proposed to introduce bonded mild-steel reinforcing bars (Davis et al., 2012; Finnsson, 2013; Thonstad et al., 2016, 2017) or external energy dissipating devices (Guerrini et al., 2015; Marriott et al., 2009; Mashal & Palermo, 2019; White & Palermo, 2016) to the connection. Both solutions are effective, but the external energy dissipaters are more practical for repair after an earthquake event.

Apart from the energy dissipation mechanism, the design and detailing of the column ends have also been a subject of study. Due to the column rotation, there is stress concentration on the rocking toe and, therefore, it needs to be appropriately designed to avoid damage. The simplest proposed solution, which does not require the use of unconventional construction material or complex construction methods, is the confinement of the concrete in these regions with a steel jacket (Mashal & Palermo, 2019; Thonstad et al., 2016, 2017; White & Palermo, 2016). The use of ductile and high-strength materials has also been suggested. Finnsson (2013) tested a rocking column cast with a fiber-reinforced concrete shell, while Guerrini et al. (2015) assessed the seismic behavior of a composite steel-concrete hollow-core column. The column was constructed with an inner and outer steel shell cast with high-performance concrete. Others (Nguyen et al., 2017; Panagiotou et al., 2015; Trono et al., 2015) adopted hybrid fiber-reinforced concrete (HyFRC) on the column ends, improving the concrete's ductility in the rocking toes, and consequently, reducing the observed damage.

Within the effort of applying precast elements in seismic active regions, precast segmental columns have also been explored. It follows a similar philosophy as the non-segmental columns; the segments are connected through unbonded tendons and extra energy dissipating devices can be adopted. Some researchers (Chou & Chen, 2006; Ou et al., 2010; Wang et al., 2008, 2018; Yamashita & Sanders, 2009) have explored the concept aiming to provide enough prestress and/or shear keys so that the segments do not slide. Sideris et al. (2014a, 2014b) tested hybrid sliding-rocking (HSR) segmental columns, which have a rocking-dominant bottom joint and sliding-dominant intermediate joints. The sliding joints provide a source of energy dissipation, avoiding the need for extra energy-dissipating devices. Although the joints behaved as expected in the cyclic tests (Sideris et al., 2014b) (i.e. sliding or rocking in the predefined joints), only the first intermediate joint slid during the shaking table tests (Sideris et al., 2014a). Salehi et al. (2021) improved the design of the HSR columns by reducing the number of sliding joints and refining of the design of the sliding interface. The specimens were tested under several loading protocols, including bilateral and torsional loading. The specimens performed satisfactorily with limited damage.

Most of the studies on the seismic behavior of bridges designed with non-emulative connections (including the ones discussed above) focused on systems with positive lateral stiffness. Meanwhile, the seismic behavior of systems exhibiting negative lateral stiffness has received less attention, at least in terms of experimental work. Cheng (2008) conducted shaking table tests on precast columns with and without the restraining tendon. The specimen without a tendon ("R30PNK250") presented negative lateral stiffness, and all specimens (restrained or not) experienced similar drift ratios and no damage or residual displacements. Zhou et al. (2019) also conducted shaking table tests on a system with negative lateral stiffness. The system was composed of four posttensioned rocking columns, a foundation and a slab. No damages were observed and negligible residual displacements were reported.

Tests on small-scale specimens representing systems with negative lateral stiffness have also been performed. Interested in comparing the experimental response with the analytical equations presented by Housner (1963), some researchers (Lipscombe & Pellegrino, 1993; Peña et al., 2008; Priestley et al., 1978; Wittich & Hutchinson, 2015) have performed shaking table or free-vibration tests on free-standing blocks (without any tendon). ElGawady et al. (2011) evaluated the effects of the interface material on the dynamic response of free-standing blocks. Three different interface materials were explored: concrete, timber and rubber. When a rigid interface material (i.e. timber or concrete) was adopted, the measured coefficient of

restitution of the free-standing block agreed well with the analytical restitution coefficient adopted by Housner (1963), which is calculated assuming conservation of angular momentum. When a soft interface material was adopted, however, the analytical coefficient of restitution overestimated the measured values. Moreover, in order to validate an analytical model for a deformable rocking column, Truniger et al. (2015) conducted shaking table tests on a small-scale cantilever column allowed to rock. The comparison of the experimental and analytical responses showed that the response of the analytical model is satisfactory for predicting the maximum rotation of the system.

In contrast to the limited amount of experimental work, the response of systems exhibiting negative lateral stiffness has been, analytically and numerically, extensively studied. Housner (1963) was one of the pioneer authors to discuss the seismic stability of free-standing rigid blocks. He has shown that the seismic stability of blocks is dependent on their size and the frequency of the excitation; the larger the block or the excitation frequency, the more stable is the system. Makris (2014) has shown that the enhanced seismic stability of the blocks with larger size sources from the increased rotational inertia of the larger blocks. Meanwhile, Makris & Kampas (2016) investigated the influence of two competing parameters to the rocking response: the block's size and slenderness, which are proportionally and inversely related to the seismic stability of the system, respectively. They concluded that, depending on the characteristics of the ground motion and if it has a dominant frequency, one of the parameters has larger influence on the seismic response of the system than the other.

Using dimensional and orientational analysis, Dimitrakopoulos & DeJong (2012b) have explored self-similarities in the response of rigid rocking blocks. Recently, Charalampakis et al. (2022) revisited the dynamics of the rigid rocking block. Using energy conservation, the authors claim to have derived "exact" criteria for the overturning of the block in the free-vibration regime.

Makris & Vassiliou (2013, 2014) have studied the seismic response of rigid cap-beam freely supported by rigid rocking columns. They show that the seismic response of the rocking frame is equivalent to the seismic response of a larger rigid rocking block. Therefore, similarly to the single block, the heavier the frame's cap-beam, the more stable is the system. Dimitrakopoulos & Giouvanidis (2015) studied the response of rocking frames with asymmetric columns. The authors compared the response of asymmetric and symmetric frames, and concluded that the asymmetry has a marginal influence on the response of rocking frames. DeJong & Dimitrakopoulos (2014) proposed a methodology to obtain equivalence

between different rocking systems and the solitary rigid rocking block. Using the proposed methodology, the response of different systems can be predicted using only the formulations for the solitary rocking block. Dar et al. (2018) investigated the influence of top eccentricities on the stability of rocking frames and concluded that the closer the contact point between the beam and pier, to the pier center, the less seismically stable is the rocking frame.

Taking into consideration the deformations of the analysed system, Acikgoz & DeJong (2012) presented the distinct characteristics of the response of a deformable rocking structure. Their work concluded that flexible rocking structures are more stable than rigid rocking structures. Vassiliou et al. (2017b) developed a finite-element model for flexible rocking frames. Similarly to Acikgoz & DeJong (2012), they concluded that the system's flexibility is not detrimental for the system's stability. Bachmann et al. (2017) assessed the seismic response of an elastic structure placed on top of a rocking frame, which can be interpreted as a building designed with a "soft-story". They explored the stability of the system when subjected to ground-motion excitations.

Using a nonsmooth dynamic analysis approach, Giouvanidis & Dimitrakopoulos (2017a) studied the impact and uplifting phenomena of both flexible and rigid rocking blocks. Their analyses show that the proposed formulations capture well the post-impact behavior of both types of structures, without requiring any assumptions on the post-impact state of the system (i.e. rocking, bouncing, detachment, or full contact). Vlachakis et al. (2021) proposed a novel viscous damping model for rocking systems, which, based on the conducted analyses, capture well the energy dissipation of the system at impact.

Vassiliou & Makris (2015) and Makris & Vassiliou (2015) derived the equations of motion for rigid rocking blocks and frames, respectively, restrained by elastic restrainers. The authors showed that the lateral post-uplift stiffness of the system depends on the axial stiffness of the elastic restrainers and, thus, the system can present negative or positive lateral stiffness. They also conclude that the restrainer contribution to the system's stability becomes insignificant for systems with larger columns. In such cases, the system's seismic resistance comes mainly from the rotational inertia.

Alternatively to elastic restrainers, it has also been proposed to use energy dissipating devices to control the displacements of a rocking system. Dimitrakopoulos & DeJong (2012a) explored the response of rocking columns equipped with viscous dampers. Their analyses included unilateral and bilateral linear and nonlinear viscous dampers. They concluded that

linear dampers are more effective in reducing the displacement demand of the system. Thiers-Moggia & Málaga-Chuquitaype (2019) studied the response of rocking blocks equipped with inerters, which is a mechanical device that develops resisting forces proportional to the acceleration of its terminals. Makris & Aghagholizadeh (2019) also investigated the seismic response of the rocking blocks equipped with energy dissipating devices. The authors observed that, in most cases, the viscous or hysteretic dampers reduce the displacement demand of the block. Nevertheless, the opposite was also observed. Aghagholizadeh (2020) compared the response of a solitary rocking block equipped with viscous or hysteretic dampers and proposed a finite element model for such systems. He concluded that viscous dampers should be preferred to hysteretic dampers. Giouvanidis & Dimitrakopoulos (2017b) investigated the seismic behavior of a rocking frame equipped with both elastic restrainers and energy dissipators. They concluded that the system can outperform or underperform free-standing blocks.

The three-dimensional (3D) behavior of rocking systems has also been explored. Koh & Mustafa (1990) derived the equations of motion for a rigid cylindrical block on top of a rigid foundation. The block was allowed to rock, roll, but not to slide. Later on, this work was extended by Koh & Hsiung (1991), modeling the deformability of the underlying foundation through springs and dashpots (Winkler foundation). Vassiliou et al. (2017a) also proposed equations of motion for a rigid cylindrical block. However, differently from Koh & Mustafa (1990), in their derivations, the block is not allowed to roll, but only to wobble. Using the same constraints, Vassiliou (2018) extended the derivations for a 3D rocking frame. Similarly to the two-dimensional (2D) formulations, it was concluded that the introduction of the slab increases the seismic stability of the system. The equations of motion for the 3D response of blocks with rectangular cross-section has also been derived (Chatzis & Smyth, 2012; Zulli et al., 2012). Whenever the 3D response was compared to the 2D response, the authors (Vassiliou, 2018; Vassiliou et al., 2017a; Zulli et al., 2012) concluded that the 2D response is unconservative, predicting smaller displacement demands than the ones observed in the 3D model.

As presented above, there is a large number of analytical and numerical models for predicting the response of systems with negative lateral stiffness. However, such models have not been trusted by the engineering community because they fail to reproduce the system's seismic response observed in experiments to a particular ground motion (Lipscombe & Pellegrino, 1993; Peña et al., 2008; Priestley et al., 1978; Yim et al., 1980; Wittich & Hutchinson, 2015). Recently, Bachmann et al. (2018) proposed that analytical and numerical

models do not need to accurately predict the response of a system to a single ground motion, as the conventional validation test in seismic engineering is, but that it is sufficient that the model predicts the statistics of the system response. They showed that the model proposed by Housner (1963) can be used to predict the probability distribution of the maximum tilt angle of a rigid rocking oscillator. Using the same approach, Vassiliou et al. (2021) conducted shaking table tests on a rocking podium, and compared the statistics of the maximum observed displacement of the system to the statistics of the maximum displacement predicted by several numerical models. The statistics of the observed and predicted maximum displacement were in reasonably good agreement.

1.3. Research gap and objectives

Despite the push for resilient and rapidly constructed bridges, as well as the vast number of analytical and numerical studies showing that systems exhibiting negative lateral stiffness are seismically stable and can outperform capacity-designed structures (Agalianos et al., 2017), negative stiffness systems have drawn less attention. This "lack of interest" is because the response of systems with negative lateral stiffness has been thought to be less predictable (Peña et al., 2008; Yim et al., 1980) (at least in a deterministic approach) and it cannot be related to the response of systems with positive lateral stiffness (Makris & Konstantinidis, 2003), which hinders the use of code-provided spectra for their design.

However, systems with negative lateral stiffness have a potential advantage. When the rocking column is simply supported on a foundation (i.e. no sort of connection between the foundation and the column exists), the rocking uplift acts as a fuse, limiting the forces transmitted to the foundation and consequently, the foundation's design forces and moments. Hence, such a system can be perceived as an alternative seismic isolation technology for precast structures. It has the potential to reduce the size of pile foundations compared to conventional bridges, and consequently, the amount of material used for their construction. This is an appealing advantage, which can make bridges not only resilient and quickly built, but also more sustainable than their counterparts with positive lateral stiffness.

In order for bridges designed with negative lateral stiffness to find their way to practice, it is imperative that the following research gaps are filled: (1) a simple analysis and design method for such structures is established, and (2) shake table tests are performed so that their performance is evaluated and data for the validation of numerical models is generated.

This dissertation presents analytical and experimental studies addressing both the above research gaps. The analytical part addresses the need for a simple design method for systems with negative lateral stiffness. It explores how to construct spectra for such systems and culminates in the development of a uniform risk spectra for systems with negative lateral stiffness. Meanwhile, the experimental campaign offers further experimental data on large-scale testing of bridge systems with negative lateral stiffness, providing further evidence on their satisfactory seismic behavior. The experimental campaign consisted of quasi-static cyclic tests and shaking table tests on reinforced-concrete rocking columns. The results of the tests were used to validate rigid body analytical models.

1.4. Structure of the dissertation

This dissertation comprises seven chapters. Chapter 1 presents a short introduction to the seismic behavior of rocking structures exhibiting negative stiffness, which is the central topic of the dissertation. Chapter 2 presents an analytical study on the dynamic response of rigid rocking blocks. The chapter proposes an alternative formulation for the equations of motion that govern the rocking motion, which reveals that, provided the block is not close to overturn, its displacement demand only depends on the block's slenderness, and not on its size. The independence of the displacement demand is proved for both analytical pulses and recorded ground motions. Such property of the system allows for the construction of rocking spectra that can be applied to blocks of different sizes. The chapter concludes with a design method that adopts the proposed rocking spectra.

Chapter 3 extends the work described in the previous chapter for other systems that present negative lateral stiffness (e.g. restrained rocking blocks, or rocking block with an extended curved base). Studying the dynamic response of such systems, the chapter shows that, similarly to the rigid rocking block explored in Chapter 2, their displacement demand can also be estimated through a simplified system. This simplified system, called therein Zero Stiffness Bilinear Elastic (ZSBE) system, is a system with a lateral bilinear elastic response, which consists of an initial positive stiffness branch, and a second zero stiffness branch. The zero stiffness branch is a simpler system that needs one less parameter to be defined. Using the ZSBE system, the displacement demand of systems with negative lateral stiffness is estimated through two approaches: the equal displacement rule (previously discussed in Chapter 2 for the rigid rocking block), and the equal energy rule. The displacement demands predicted by both approaches are explored using recorded ground motions. The analyses reveal that, although

both approaches lead to good predictions of the displacement demand, the equal energy rule is usually more conservative than the equal displacement rule.

After generalizing the spectra for different rocking structures, Chapter 4 casts the rocking response within the framework of performance-based engineering. Using the ZSBE system proposed in the previous chapter, this chapter presents a methodology for constructing uniform risk spectra for rocking structures. It offers the spectra for six different locations in Europe constructed with two different intensity measures: the peak ground velocity (PGV) and the peak ground acceleration (PGA). The chapter follows with a discussion on the efficiency of the intensity measures in different ranges of displacement demand. It shows that the PGA is more efficient for predicting rocking initiation, while the PGV is a better intensity measure for predicting the maximum displacements. Finally, an analytical approximation of the PGV-based spectra is proposed.

Chapters 5 and 6 address the need for more experimental tests on large-scale precast rocking systems. Chapter 5 presents quasi-static cyclic experimental tests conducted on two variations of a 1:5 scale restrained rocking column and a cap-beam, in which the only difference between the two specimens was the protection of their ends. One of the columns had its ends protected by steel jackets, while the other one was protected only by steel discs. The columns were subjected to drift ratios of up to 16%, showing only minor damage. The chapter shows that the observed lateral behavior compared reasonably well with the rigid body model presented in Chapter 3, performing poorly only in terms of predicting the pre-uplift stiffness.

Chapter 6 follows with the results of the shaking table tests of a rocking system. The specimen comprised a slab on top of four rocking columns, designed and constructed similarly to the columns tested in Chapter 5. The specimen was subjected to 181 ground motions. Although the last ground motion caused the unexpected collapse of the specimen due to premature failure of the unbonded tendons, negligible damage was observed in the previous 180 tests. The main observed damage was the abrasion at the perimeter of the columns ends. Additionally to the experimental observations, the chapter also discusses the statistical validation of a 3D rigid body model for rocking frames.

The dissertation closes with Chapter 7, which summarizes the key findings and important contributions, as well as suggestions for future research.

References

Acikgoz, S., & DeJong, M. J. (2012). The interaction of elasticity and rocking in flexible structures allowed to uplift. *Earthquake Engineering & Structural Dynamics*, *41*(15), 2177–2194.

Agalianos, A., Psychari, A., Vassiliou, M. F., Stojadinovic, B., & Anastasopoulos, I. (2017). Comparative Assessment of Two Rocking Isolation Techniques for a Motorway Overpass Bridge. *Frontiers in Built Environment*, *3*.

Aghagholizadeh, M. (2020). A finite element model for seismic response analysis of vertically-damped rocking-columns. *Engineering Structures, 219*, 110894.

Bachmann, J. A., Vassiliou, M. F., & Stojadinović, B. (2017). Dynamics of rocking podium structures. *Earthquake Engineering & Structural Dynamics*, *46*(14), 2499–2517.

Bachmann, J. A., Strand, M., Vassiliou, M. F., Broccardo, M., & Stojadinović, B. (2018). Is rocking motion predictable? *Earthquake Engineering & Structural Dynamics*, *47*(2), 535–552.

Charalampakis, A. E., Tsiatas, G. C., & Tsopelas, P. (2022). New insights on rocking of rigid blocks: Analytical solutions and exact energy-based overturning criteria. *Earthquake Engineering & Structural Dynamics*.

Chatzis, M. N., & Smyth, A. W. (2012). Modeling of the 3D rocking problem. *International Journal of Non-Linear Mechanics*, *47*(4), 85–98.

Cheng, C.-T. (2008). Shaking table tests of a self-centering designed bridge substructure. *Engineering Structures*, *30*(12), 3426–3433.

Chou, C.-C., & Chen, Y.-C. (2006). Cyclic tests of post-tensioned precast CFT segmental bridge columns with unbonded strands. *Earthquake Engineering & Structural Dynamics*, *35*(2), 159–175.

Culmo, M. P. ; L., Byron; Huie, Mary; Beerman, Benjamin. (2011). *Accelerated Bridge Construction: Experience in Design, Fabrication and Erection of Prefabricated Bridge Elements and Systems: Final Manual* (FHWA-HIF-12-013).

Dar, A., Konstantinidis, D., & El-Dakhakhni, W. (2018). Seismic response of rocking frames with top support eccentricity. *Earthquake Engineering & Structural Dynamics*, *47*(12), 2496–2518.

Davis, P. M., Janes, T. M., Eberhard, M. O., & Stanton, J. F. (2012). *Unbonded Pre-Tensioned Columns for Bridges in Seismic Regions* (PEER Report 2012/04). Pacific Earthquake Engineering Research Center.

DeJong, M. J., & Dimitrakopoulos, E. G. (2014). Dynamically equivalent rocking structures. *Earthquake Engineering & Structural Dynamics*, *43*(10), 1543–1563.

Dimitrakopoulos, E. G., & DeJong, M. J. (2012a). Overturning of Retrofitted Rocking Structures under Pulse-Type Excitations. *Journal of Engineering Mechanics*, *138*(8), 963–972.

Dimitrakopoulos, E. G., & DeJong, M. J. (2012b). Revisiting the rocking block: Closed-form solutions and similarity laws. *Proceedings of the Royal Society A: Mathematical, Physical and Engineering Sciences*, *468*(2144), 2294–2318.

Dimitrakopoulos, E. G., & Giouvanidis, A. I. (2015). Seismic Response Analysis of the Planar Rocking Frame. *Journal of Engineering Mechanics*, *141*(7), 04015003.

ElGawady, M. A., Ma, Q., Butterworth, J. W., & Ingham, J. (2011). Effects of interface material on the performance of free rocking blocks. *Earthquake Engineering & Structural Dynamics*, *40*(4), 375–392.

Fardis, M. N. (2018). Capacity design: Early history. *Earthquake Engineering & Structural Dynamics*, *47*(14), 2887–2896.

FEMA 356. (2000). *Prestandard and Commentary for the Seismic Rehabilitation of Buildings*

((FEMA Publication No. 356)). Federal Emergency Management Agency.

Finnsson, G. (2013). *Unbonded Pre-tensioned Bridge Columns with Hybrid Fiber-Reinforced Concrete Shells*. University of Washington.

Giouvanidis, A. I., & Dimitrakopoulos, E. G. (2017a). Nonsmooth dynamic analysis of sticking impacts in rocking structures. *Bulletin of Earthquake Engineering, 15*, 2273-2304.

Giouvanidis, A. I., & Dimitrakopoulos, E. G. (2017b). Seismic Performance of Rocking Frames with Flag-Shaped Hysteretic Behavior. *Journal of Engineering Mechanics*, *143*(5), 04017008.

Gonzalez, R. E., Stephens, M. T., Toma, C., Elwood, K. J., & Dowdell, D. (2021). Post-earthquake Demolition in Christchurch, New Zealand: A Case-Study Towards Incorporating Environmental Impacts in Demolition Decisions. In S. Akkar, A. Ilki, C. Goksu, & M. Erdik (Eds.), *Advances in Assessment and Modeling of Earthquake Loss* (pp. 47–64). Springer International Publishing.

Guerrini, G., Restrepo, J. I., Massari, M., & Vervelidis, A. (2015). Seismic Behavior of Posttensioned Self-Centering Precast Concrete Dual-Shell Steel Columns. *Journal of Structural Engineering*, *141*(4), 04014115.

Han, Q., Du, X., Liu, J., Li, Z., Li, L., & Zhao, J. (2009). Seismic damage of highway bridges during the 2008 Wenchuan earthquake. *Earthquake Engineering and Engineering Vibration*, *8*(2), 263–273.

Housner, G. W. (1963). The behavior of inverted pendulum structures during earthquakes. *Bulletin of the Seismological Society of America*, *53*(2), 403–417.

Insurance Council of New Zealand. *Canterbury earthquakes—ICNZ*. Retrieved 19 April 2022, from https://www.icnz.org.nz/natural-disasters/canterbury-earthquakes

Koh, A.-S., & Hsiung, C.-M. (1991). Base Isolation Benefits of 3-D Rocking and Uplift. I: Theory. *Journal of Engineering Mechanics*, *117*(1), 1–18.

Koh, A.-S., & Mustafa, G. (1990). Free Rocking of Cylindrical Structures. *Journal of Engineering Mechanics*, *116*(1), 35–54.

Lipscombe, P. R., & Pellegrino, S. (1993). Free Rocking of Prismatic Blocks. *Journal of Engineering Mechanics*, *119*(7), 1387–1410.

Makris, N. (2014). The Role of the Rotational Inertia on the Seismic Resistance of Free-Standing Rocking Columns and Articulated Frames. *Bulletin of the Seismological Society of America*, *104*(5), 2226–2239.

Makris, N., & Aghagholizadeh, M. (2019). Effect of Supplemental Hysteretic and Viscous Damping on Rocking Response of Free-Standing Columns. *Journal of Engineering Mechanics*, *145*(5), 04019028.

Makris, N., & Kampas, G. (2016). Size Versus Slenderness: Two Competing Parameters in the Seismic Stability of Free-Standing Rocking Columns. *Bulletin of the Seismological Society of America*, *106*(1), 104–122.

Makris, N., & Konstantinidis, D. (2003). The rocking spectrum and the limitations of practical design methodologies. *Earthquake Engineering & Structural Dynamics*, *32*(2), 265–289.

Makris, N., & Vassiliou, M. F. (2013). Planar rocking response and stability analysis of an array of free-standing columns capped with a freely supported rigid beam. *Earthquake Engineering & Structural Dynamics*, *42*(3), 431–449.

Makris, N., & Vassiliou, M. F. (2014). Are Some Top-Heavy Structures More Stable? *Journal of Structural Engineering*, *140*(5), 06014001.

Makris, N., & Vassiliou, M. F. (2015). Dynamics of the Rocking Frame with Vertical Restrainers. *Journal of Structural Engineering*, *141*(10), 04014245.

Mander, J. B., & Cheng, C. T. (1997). *Seismic Resistance of Bridge Piers Based on Damage Avoidance Design* (Techncial Report NCEER-97-0014; pp. 1–144). National Center for Earthquake Engineering Research.

Marriott, D., Pampanin, S., & Palermo, A. (2009). Quasi-static and pseudo-dynamic testing of unbonded post-tensioned rocking bridge piers with external replaceable dissipaters. *Earthquake Engineering & Structural Dynamics*, *38*(3), 331–354.

Marsh, M. L., Wernli, M., Garrett, B. E., Stanton, J. F., Eberhard, M. O., & Weinert, M. D. (2011). *Application of Accelerated Bridge Construction Connections in Moderate-to-High Seismic Regions* (NCHRP Report 698).

Mashal, M. (2015). *Post-Tensioned Earthquake Damage Resistant Technologies for Accelerated Bridge Construction*.

Mashal, M., & Palermo, A. (2019). Low-Damage Seismic Design for Accelerated Bridge Construction. *Journal of Bridge Engineering*, *24*(7), 04019066.

Nakaki, S. D., Stanton, J. F., & Sritharan, S. (1999). An Overview of the PRESSS Five-Story Precats Test Building. *PCI Journal*, *44*(2), 26–39.

Nguyen, W., Trono, W., Panagiotou, M., & Ostertag, C. P. (2017). Seismic response of a rocking bridge column using a precast hybrid fiber-reinforced concrete (HyFRC) tube. *Composite Structures*, *174*, 252–262.

Ou, Y.-C., Wang, P.-H., Tsai, M.-S., Chang, K.-C., & Lee, G. C. (2010). Large-Scale Experimental Study of Precast Segmental Unbonded Posttensioned Concrete Bridge Columns for Seismic Regions. *Journal of Structural Engineering*, *136*(3), 255–264.

Palermo, A., Wotherspoon, L., Hogan, L., Le Heux, M., Camnasio, E., & Brando, M. (2012). *Seismic Performance of Concrete Bridges during Canterbury Earthquakes*. 1080–1091.

Panagiotou, M., Trono, W., Jen, G., Kumar, P., & Ostertag, C. P. (2015). Experimental Seismic Response of Hybrid Fiber-Reinforced Concrete Bridge Columns with Novel Longitudinal Reinforcement Detailing. *Journal of Bridge Engineering*, *20*(7), 04014090.

Peña, F., Lourenço, P. B., & Campos-Costa, A. (2008). Experimental Dynamic Behavior of Free-Standing Multi-Block Structures Under Seismic Loadings. *Journal of Earthquake Engineering*, *12*(6), 953–979.

Priestley, M. J. N., Evison, R. J., & Carr, A. J. (1978). Seismic response of structures free to rock on their foundations. *Bulletin of the New Zealand Society for Earthquake Engineering*, *11*(3), 141–150.

Priestley, M. J. N., Sritharan, S., Conley, J. R., & Pampanin, S. (1999). Preliminary Results and Conclusions from the PRESSS Five-Story Precast Concrete Test Building. *PCI Journal*, *44*(6), 42–67.

Priestley, M. J. N., & Tao, J. R. (1993). Seismic Response of Precast Prestressed Concrete Frames With Partially Debonded Tendons. *PCI Journal*, *38*(1), 58–69.

Salehi, M., Sideris, P., & Liel, A. B. (2021). Experimental testing of hybrid sliding-rocking bridge columns under torsional and biaxial lateral loading. *Earthquake Engineering & Structural Dynamics*, *50*(10), 2817–2837.

Schanack, F., Valdebenito, G., & Alvial, J. (2012). Seismic Damage to Bridges during the 27 February 2010 Magnitude 8.8 Chile Earthquake. *Earthquake Spectra*, *28*(1), 301–315.

Sideris, P., Aref, A. J., & Filiatrault, A. (2014a). Large-Scale Seismic Testing of a Hybrid Sliding-Rocking Posttensioned Segmental Bridge System. *Journal of Structural Engineering*, *140*(6), 04014025.

Sideris, P., Aref, A. J., & Filiatrault, A. (2014b). Quasi-Static Cyclic Testing of a Large-Scale Hybrid Sliding-Rocking Segmental Column with Slip-Dominant Joints. *Journal of Bridge Engineering*, *19*(10), 04014036.

Stone, W. C., Cheok, G. S., & Stanton, J. F. (1995). Performance of Hybrid Moment-Resisting Precast Beam-Column Concrete Connections Subjected to Cyclic Loading. *Structural Journal*, *92*(2), 229–249.

Swiss Seismological Service. (2012). *SED / Basel 1356*. http://www.seismo.ethz.ch/en/knowledge/earthquake-country-switzerland/historical-

earthquakes/basel-1356/

Swiss Seismological Service. (2022). *Earthquake Country Switzerland.* http://www.seismo.ethz.ch/export/sites/sedsite/knowledge/.galleries/pdf_brochures/2021 _SED_Erdbeben_in_der_Schweiz_EN_Web_lowres.pdf_2063069299.pdf.

Thiers-Moggia, R., & Málaga-Chuquitaype, C. (2019). Seismic protection of rocking structures with inerters. *Earthquake Engineering & Structural Dynamics*, *48*(5), 528–547.

Thonstad, T., Kennedy, B. J., Schaefer, J. A., Eberhard, M. O., & Stanton, J. F. (2017). Cyclic Tests of Precast Pretensioned Rocking Bridge-Column Subassemblies. *Journal of Structural Engineering*, *143*(9), 04017094.

Thonstad, T., Mantawy, I. M., Stanton, J. F., Eberhard, M. O., & Sanders, D. H. (2016). Shaking Table Performance of a New Bridge System with Pretensioned Rocking Columns. *Journal of Bridge Engineering*, *21*(4), 04015079.

Trono, W., Jen, G., Panagiotou, M., Schoettler, M., & Ostertag, C. P. (2015). Seismic Response of a Damage-Resistant Recentering Posttensioned-HYFRC Bridge Column. *Journal of Bridge Engineering*, *20*(7), 04014096.

Truniger, R., Vassiliou, M. F., & Stojadinović, B. (2015). An analytical model of a deformable cantilever structure rocking on a rigid surface: Experimental validation. *Earthquake Engineering & Structural Dynamics*, *44*(15), 2795–2815.

United Nations. (2015). *Transforming Our World: The 2030 Agenda for Sustainable Development* (A/RES/70/1).

Vassiliou, M. F., Broccardo, M., Cengiz, C., Dietz, M., Dihoru, L., Gunay, S., Mosalam, K. M., Mylonakis, G., Sextos, A., & Stojadinovic, B. (2021). Shake table testing of a rocking podium: Results of a blind prediction contest. *Earthquake Engineering & Structural Dynamics*, *50*(4), 1043–1062.

Vassiliou, M. F. (2018). Seismic response of a wobbling 3D frame. *Earthquake Engineering & Structural Dynamics*, *47*(5), 1212–1228.

Vassiliou, M. F., Burger, S., Egger, M., Bachmann, J. A., Broccardo, M., & Stojadinovic, B. (2017). The three-dimensional behavior of inverted pendulum cylindrical structures during earthquakes. *Earthquake Engineering & Structural Dynamics*, *46*(14), 2261–2280.

Vassiliou, M. F., Mackie, K. R., & Stojadinović, B. (2017). A finite element model for seismic response analysis of deformable rocking frames. *Earthquake Engineering & Structural Dynamics*, *46*(3), 447–466.

Vassiliou, M. F., & Makris, N. (2015). Dynamics of the Vertically Restrained Rocking Column. *Journal of Engineering Mechanics*, *141*(12), 04015049.

Vlachakis, G., Giouvanidis, A. I., Mehrotra, A., Lourenço, P. B. (2021). Numerical block-based simulation of rocking structures using a novel universal viscous damping model. *Journal of Engineering Mechanics, 147*(11), 04021089.

Wang, J., Wang, Z., Tang, Y., Liu, T., & Zhang, J. (2018). Cyclic loading test of self-centering precast segmental unbonded posttensioned UHPFRC bridge columns. *Bulletin of Earthquake Engineering*, *16*(11), 5227–5255.

Wang, J.-C., Ou, Y.-C., Chang, K.-C., & Lee, G. C. (2008). Large-scale seismic tests of tall concrete bridge columns with precast segmental construction. *Earthquake Engineering & Structural Dynamics*, *37*(12), 1449–1465.

White, S., & Palermo, A. (2016). Quasi-Static Testing of Posttensioned Nonemulative Column-Footing Connections for Bridge Piers. *Journal of Bridge Engineering*, *21*(6), 04016025.

Wittich, C. E., & Hutchinson, T. C. (2015). Shake table tests of stiff, unattached, asymmetric structures. *Earthquake Engineering & Structural Dynamics*, *44*(14), 2425–2443.

Yamashita, R., & Sanders, D. H. (2009). Seismic Performance of Precast Unbonded Prestressed Concrete Columns. *ACI Structural Journal*, *106*(6), 821–830.

Yim, C.-S., Chopra, A. K., & Penzien, J. (1980). Rocking response of rigid blocks to earthquakes. *Earthquake Engineering & Structural Dynamics*, *8*(6), 565–587.

Zhou, Y.-L., Han, Q., Du, X.-L., & Jia, Z. (2019). Shaking Table Tests of Post-Tensioned Rocking Bridge with Double-Column Bents. *Journal of Bridge Engineering*, *24*(8), 04019080.

Zulli, D., Contento, A., & Di Egidio, A. (2012). 3D model of rigid block with a rectangular base subject to pulse-type excitation. *International Journal of Non-Linear Mechanics*, *47*(6), 679–687.

2. Displacement-based analysis and design of rocking structures

Abstract

The response of a rigid rocking block is traditionally described by its tilt angle. This is a correct description, but this paper suggests that describing rocking via displacements is more meaningful, because it uncovers that two geometrically similar blocks of different size will experience the same top displacement, provided that they are not close to overturn. The above is illustrated for both analytical pulse excitations and for recorded ground motions. Thus, the displacement demand of a ground motion on a rocking block is only a function of its slenderness, not of its size. This reduces the dimensionality of the problem and allows for the construction of size-independent rocking demand spectra.

2.1. Introduction

The systematic study of the rocking oscillator started with Housner's seminal paper in 1963 (Housner, 1963). Motivated by the surprising stability that tall slender "golf-ball-on-a-tee" structures presented in the 1960 Chilean earthquake, he showed that (a) out of two geometrically similar planar rigid objects, the larger one is harder to overturn dynamically, and (b) the overturning potential of a ground motion increases with its dominant period.

The interest on the rocking oscillator (Acikgoz & DeJong, 2012; Chopra & Yim, 1985; Ma, 2010; Oliveto et al., 2003; Psycharis, 1991) sources from its ability to describe systems that cannot be described adequately by the classical elastic oscillator (Makris & Konstantinidis, 2003). Indeed, the rocking oscillator can be used to understand the behavior of masonry structures (Casapulla et al., 2017; DeJong, 2012; Kalliontzis & Schultz, 2017; Mehrotra & DeJong, 2018; Stefanou et al., 2011; Tondelli et al., 2016), the seismic behavior of unanchored equipment (Dar et al., 2016, 2018; Di Egidio et al., 2015; Di Sarno et al., 2019; Konstantinidis & Makris, 2010; Mouzakis et al., 2002; Sextos et al., 2017; Voyagaki et al., 2018; Wittich & Hutchinson, 2015), and to explain the stability of ancient Greco-Roman and Chinese temples

that have been standing for more than 2500 years in earthquake prone regions (Mouzakis et al., 2002; Nikolić et al., 2019; Papaloizou & Komodromos, 2009; Papantonopoulos et al., 2002; Vassiliou & Makris, 2012). Rocking motion has also inspired researchers to use inerters as seismic protection devices (Makris & Kampas, 2016; Thiers-Moggia & Málaga-Chuquitaype, 2019). What is not widely known in the western world is that rocking has been used since more than 40 years as a seismic isolation method in the USSR (and now in former USSR countries) (Bachmann et al., 2017). The Soviet system comprises an intentionally designed soft rocking story. The uplift of the rocking columns works as a mechanical fuse and limits the forces transmitted to the superstructure. Rocking has also been suggested as a seismic design method for bridges, either without (Agalianos et al., 2017; Anastasopoulos et al., 2010; Dimitrakopoulos & Giouvanidis, 2015; Makris & Vassiliou, 2013, 2014; Vassiliou, 2018; Vassiliou et al., 2017a; 2017b; Xie et al., 2019) or with (Giouvanidis & Dimitrakopoulos, 2017b; Mander & Cheng, 1997; Thonstad et al., 2016) a restraining system. In New Zealand, a 60-m-tall bridge designed to rock has already been built across the Rangitikei River in 1981 (Beck & Skinner, 1973; Ma & Khan, 2008), and very recently, the Wigram-Magdala restrained rocking bridge has been constructed (Sharpe & Skinner, 1983). Moreover, a 33-m-tall chimney at the Christchurch airport has been designed to uplift (Routledge et al., 2016), and three 30- to 38-m-tall chimneys in Piraeus, Greece, have been retrofitted by allowing them to uplift in case of an earthquake.

Makris & Vassiliou (2015) and Vassiliou & Makris (2015) have suggested that as the size of the rocking system increases, the restraining system can become obsolete and merely increases the design forces of both the superstructure and the foundation. In buildings, rocking walls have been suggested as a resilient design approach (Aghagholizadeh & Makris, 2018; Makris & Aghagholizadeh, 2017, and references therein).

One of the main challenges for the wider adoption of rocking systems stems from their response being absolutely uncorrelated to any elastic system. Therefore, the elastic-based research results are not applicable: e.g., intensity measures, response spectra, motion-to-motion variability, and design ground motions need to be redetermined. To this end, the rocking oscillator should be described with the minimum parameters needed.

This paper suggests that the current state of the art of using the tilt angle θ as the DOF of a rocking system is, of course, correct, but it is not the optimal. Using the top displacement of the oscillator, u, reduces the dimensionality of the problem. Then, the displacement *demand* on a rocking block becomes only slightly dependent on its size and is a function only of its

slenderness.

2.2. Rotation-based dimensional analysis of the rocking oscillator

The equation of in-plane motion for a rigid rectangular rocking column (Figure 2.1) with slenderness α and a semi-diagonal of length R (Figure 2.1) is:

$$\ddot{\theta} = -p^2 \cdot \left(\sin(\pm\alpha - \theta) + \frac{\ddot{u}_g}{g} \cos(\pm\alpha - \theta) \right) \tag{2.1}$$

where

$$p = \sqrt{(3g)/(4R)} \tag{2.2}$$

is the frequency parameter of the rocking column. The upper sign in front of α corresponds to a positive, and the lower to a negative rocking angle θ with respect to the defined coordinate system (Figure 2.1).
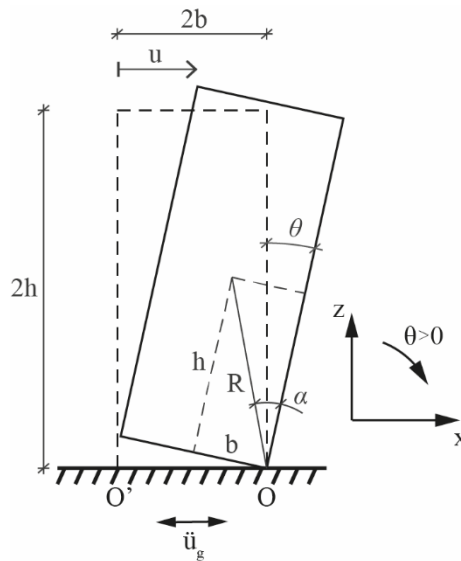
Figure 2.1. Geometric characteristics of the rigid rocking block.

It is assumed that energy is only dissipated during impact. Housner (1963) assumed that (a) the impact is instantaneous and (b) that the impact forces are concentrated on the impacting corner. Under these assumptions, the ratio of postimpact to preimpact rotational velocities is:

$$r = \frac{\dot{\theta}_{after}}{\dot{\theta}_{before}} = 1 - \frac{3}{2} \sin^2 \alpha \tag{2.3}$$

Researchers (including the senior author of this paper) have critically evaluated the

Housner model—especially its damping assumptions (Chatzis et al., 2017; Giouvanidis & Dimitrakopoulos, 2017a; Kalliontzis & Sritharan, 2018; Truniger et al., 2015; Vassiliou et al., 2015). Indeed, while assuming the impact to be instantaneous seems a reasonable assumption, there is no evident reason to assume that the impact forces act on the impacting corner. Given the large sensitivity of the time history response of the rocking oscillator to all the parameters that define it, Housner's model might seem simplistic. However, experimental testing shows that even though it cannot predict the response to an individual ground motion, it can predict the statistics of the response to a set of ground motions (Bachmann et al., 2018). Therefore, we consider it adequate within the scope of earthquake engineering.

By inspecting Equations (2.1) and (2.2), one can conclude that the rotational response of a rocking block to a ground motion is a function of:

$$\theta_{\max} = f_1\left(R, \alpha, g, \ddot{u}_g(t)\right) \tag{2.4}$$

As the gravity acceleration, g, is constant, the rotational response to a given ground motion is a function of two parameters α and R, similarly to the elastic oscillator, in which the response is a function of the eigenperiod, T, and damping ratio ζ. Therefore, by keeping one parameter constant (R or α), one can construct rotational spectra for rocking structures. However, unlike the elastic oscillator, where, for usual structures, one parameter (T) is more influential than the other (ζ), in the case of rocking structures, both R and α strongly influence the rotational response.

Since ground motions containing distinguishable acceleration and/or velocity pulses are particularly destructive (Vassiliou & Makris, 2011, and references therein), Zhang & Makris (2001) have studied the response of a planar rocking block to acceleration pulses given by analytical expressions. A pulse of a given waveform can be described by two parameters. Zhang & Makris (2001) chose the acceleration amplitude a_p and the dominant cyclic frequency ω_p. Then, the response will be a function of:

$$\theta_{\max} = f_2\left(R, \alpha, g, a_p, \omega_p\right) \tag{2.5}$$

Equation (2.5) involves six quantities with two reference dimensions (Time and Length). Therefore, according to the Vaschy-Buckingham Π-Theorem of Dimensional Analysis (Buckingham, 1914; Vaschy, 1892), the number of dimensionless parameters describing the problem is 6–2 = 4. There is not a unique solution for choosing these four parameters. Zhang & Makris (2001) suggested describing the problem as:

$$\theta_{max} = \varphi_1\left(\alpha, \frac{\omega_p}{p}, \frac{a_p}{g\tan\alpha}\right) \tag{2.6}$$

$\dfrac{\omega_p}{p}$ is often called size-frequency parameter and depends on the frequency of the excitation and on the size of the block. $\dfrac{a_p}{g\tan\alpha}$ is usually called nondimensional acceleration, but it can also be perceived as a nondimensional strength parameter, since $mgR\sin\alpha$ is the moment that withstands uplift ("strength") and $ma_pR\cos\alpha$ is the overturning moment.

Therefore, dimensional analysis reduces the dimensionality of the problem from six to four. Hence, by keeping the slenderness parameter α constant, one can produce contour plots of the maximum tilt angle θ as a function of $\dfrac{\omega_p}{p}$ and $\dfrac{a_p}{g\tan\alpha}$, the so-called rocking spectra. It is worth mentioning that Dimitrakopoulos & DeJong (2012) have shown that for small values of α one can drop it as an independent parameter from Equation (2.6) as long as the coefficient of restitution, r, is treated as an extra independent parameter—however, in this section, r is not treated independently.

Figure 2.2 shows the rocking spectra of symmetric and antisymmetric Ricker wavelets. Ricker wavelets are defined as the second and third derivative of the Gaussian:

$$\ddot{u}_g = a_p\left(1 - \frac{2\pi^2 t^2}{T_p^2}\right)e^{-\frac{1}{2}\frac{2\pi^2 t^2}{T_p^2}} \tag{2.7}$$

$$\ddot{u}_g = \frac{a_p}{\beta_r}\left(\frac{4\pi^2 t^2}{3T_p^2} - 3\right)\frac{2\pi t}{\sqrt{3T_P}}e^{-\frac{1}{2}\frac{4\pi^2 t^2}{3T_p^2}} \tag{2.8}$$

where

$$T_p = \frac{2\pi}{\omega_p} \tag{2.9}$$

and $\beta_r = 1.3801$ to enforce that the function maximum is equal to a_p.

The spectra confirm the remarkable observation that larger structures are harder to overturn dynamically and that higher frequency pulses have a lower overturning potential. Interestingly, they show a heavy dependence of the response on both $\dfrac{\omega_p}{p}$ and $\dfrac{a_p}{g\tan\alpha}$.
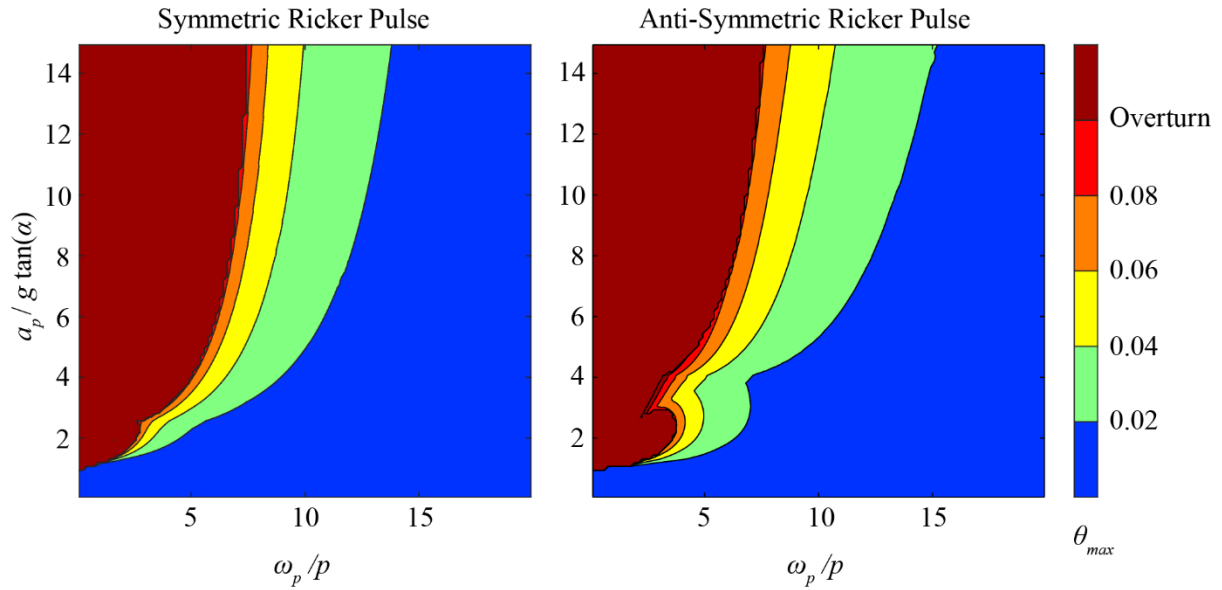
Figure 2.2. Nondimensional rocking spectra based on rotations ($\alpha = 0.1$).

2.3. Displacement-based dimensional analysis of a rocking oscillator excited by analytical pulses

2.3.1. Analysis based on the frequency parameter of the block (p)

The dimensional analysis of the previous section is one of the many correct solutions to describe the problem. It is based on rotations. This section, however, suggests that there is another, displacement-based basis of describing the problem, which is also mathematically correct and more convenient. The convenience does not lie only on the fact that earthquake engineers are more used to displacements than rotations: A displacement-based analysis further reduces the dimensionality of the problem allowing the construction of 2D rocking spectra.

Indeed, the rotation-based analysis of the problem is based on the "recipe for similarity analysis" described in Chapter 5 of the well-known Dimensional Analysis textbook of Barenblatt (1996): "If the problem has an explicit mathematical formulation, the independent variables in the problem and the constant parameters that appear in the equations, boundary conditions and initial conditions, etc., are adopted as the governing parameters". As this section shows, choosing the parameters that appear in the analytical equation might not be the most convenient way of describing this particular problem.

The top displacement of the rocking block can be obtained by a one-to-one mapping on the rotations:

$$u = 2R\sin(\pm\alpha) - 2R\sin(\pm\alpha - \theta) \tag{2.10}$$

The upper sign in front of α corresponds to a positive and the lower sign to a negative tilt angle θ with respect to the defined coordinate system. If we use the top displacement as the single DOF of the problem, then the maximum response can be described as:

$$u_{\max} = f_3\left(R, \alpha, g, a_p, \omega_p\right) \tag{2.11}$$

To numerically compute the response of the block, we will resort to Equation (2.1), which is given in terms of rotation θ. Then, using Equation (2.10), we compute the displacement response.

Applying Buckingham's Π-theorem on Equation (2.11), one possible nondimensionalization is:

$$\frac{u_{\max}\omega_p^2}{a_p} = \varphi_2\left(\alpha, \frac{\omega_p}{p}, \frac{a_p}{g\tan\alpha}\right) \tag{2.12}$$

Figure 2.3 shows the contour plots of $\dfrac{u_{\max}\omega_p^2}{a_p}$ as a function of $\dfrac{\omega_p}{p}$ and $\dfrac{a_p}{g\tan\alpha}$ for a given $\alpha = 0.1$. The remarkable observation is that within the nonoverturning region, the nondimensional displacement depends heavily (and strongly nonlinear) on the nondimensional strength parameter $\dfrac{a_p}{g\tan\alpha}$ but only loosely on the size-frequency parameter $\dfrac{\omega_p}{p}$. When the block is not close to overturning, the influence of $\dfrac{\omega_p}{p}$ is practically negligible.
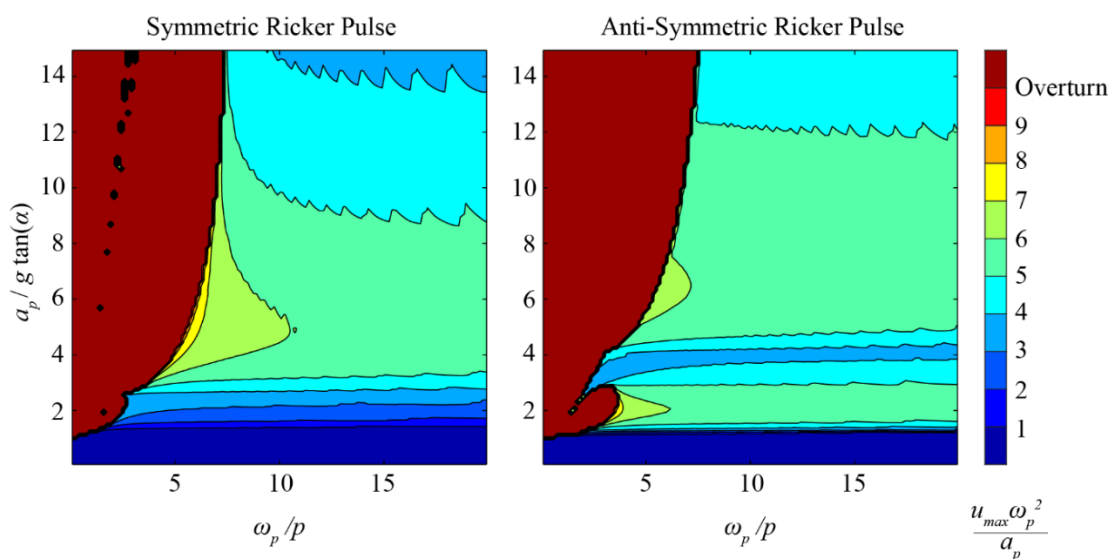
Figure 2.3. Nondimensional rocking spectra based on displacements.

Figure 2.4 plots $\dfrac{u_{\max}\omega_p{}^2}{a_p}$ as a function of $\dfrac{a_p}{g\tan\alpha}$ for different values of $\dfrac{\omega_p}{p}$ (and a

constant slenderness $\alpha = 0.1$). For reasons of figure clarity, only nonoverturning values of

$\dfrac{u_{\max}\omega_p{}^2}{a_p}$ are plot, i.e., not plotting $\dfrac{u_{\max}\omega_p{}^2}{a_p}$ means that the block has overturned. Figure 2.5

plots $\dfrac{u_{\max}\omega_p{}^2}{a_p}$ as a function of $\dfrac{\omega_p}{p}$ for different values of $\dfrac{a_p}{g\tan\alpha}$ (and $\alpha = 0.1$). Again, it is

observed that, as long as the system is away from overturning, the dominant factor that

influences $\dfrac{u_{\max}\omega_p{}^2}{a_p}$ is $\dfrac{a_p}{g\tan\alpha}$, not $\dfrac{\omega_p}{p}$. In fact for small values of nondimensional

acceleration $\dfrac{a_p}{g\tan\alpha}$, the response for all values of size-frequency parameter $\dfrac{\omega_p}{p}$ is practically

the same. The response starts to deviate only when the system is close to overturning—or has

overturned.
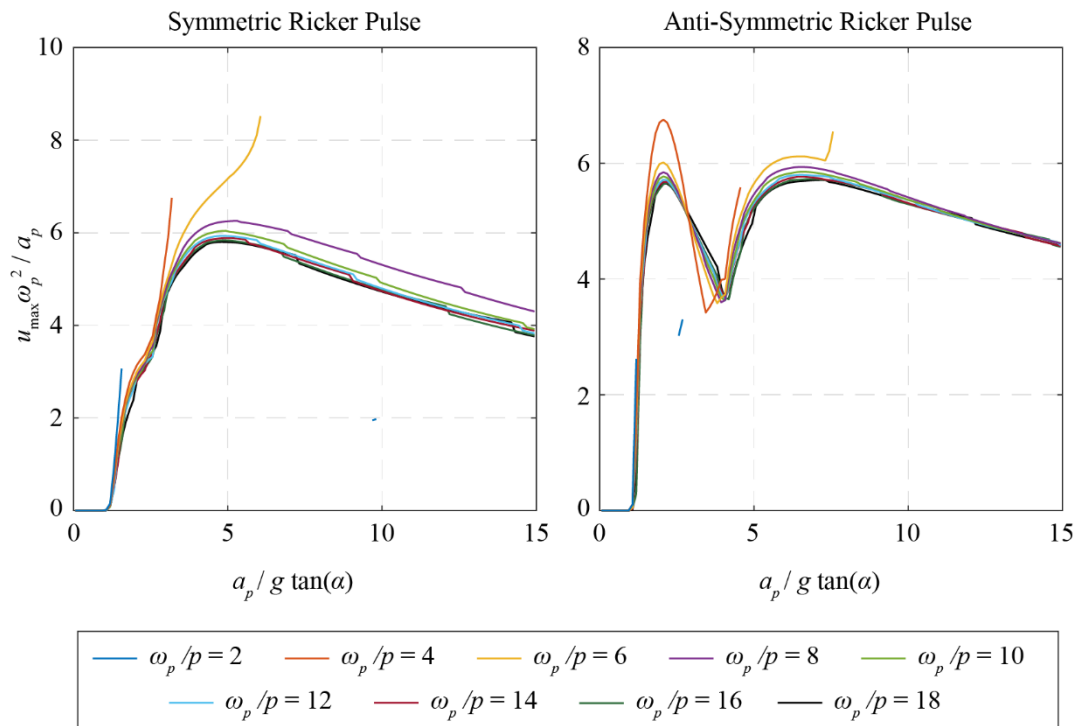
Figure 2.4. $\dfrac{u_{\max}\omega_p{}^2}{a_p}$ vs $\dfrac{a_p}{g\tan\alpha}$ plots for constant $\dfrac{\omega_p}{p}$ ($\alpha = 0.1$).

In other words, a small and a large block, geometrically similar to each other and excited

by analytical pulses, will have roughly equal top displacement, provided that the displacement

is not enough to bring them close to overturn. A given pulse will induce the same *displacement demand*. The larger block is more stable simply because its displacement capacity (i.e., the displacement needed to cause overturn, i.e., its width) is larger.
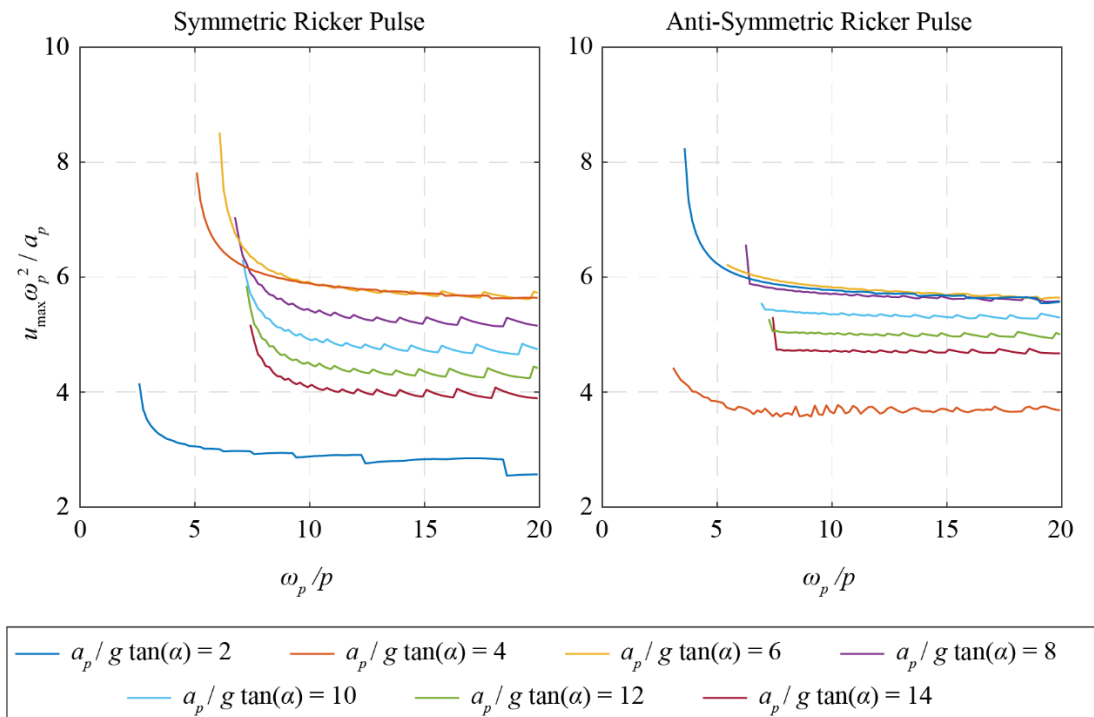
Figure 2.5. $\dfrac{u_{max}\omega_p{}^2}{a_p}$ vs $\dfrac{\omega_p}{p}$ plots for constant $\dfrac{a_p}{g\tan\alpha}$ ($\alpha = 0.1$).

Therefore, using a displacement basis to describe the problem further decreases the number of parameters needed to define it. Practically, the displacement demand on a rocking oscillator excited by a pulse is only a function of its nondimensional strength parameter $\dfrac{a_p}{g\tan\alpha}$, not of its size.

The strongly nonlinear nature of rocking motion is also evident in Figure 2.4 and Figure 2.5. $\dfrac{u_{max}\omega_p{}^2}{a_p}$, which expresses the relation of the rocking displacement to the ground motion displacement, does not depend monotonically on the strength parameter $\dfrac{a_p}{g\tan\alpha}$. In fact, the discontinuities of the $\dfrac{\omega_p}{p} = 2$ line of Figure 2.4 convey that a block can survive a stronger pulse and overturn in a weaker one.

Going back to dimensional quantities, Figure 2.6 plots the displacement response to a symmetric Ricker pulse with $a_p = 1$ g and $T_p = 0.5$ seconds and to an antisymmetric Ricker pulse with $a_p = 1$ g and $T_p = 1$ seconds. The plots confirm that the displacement demand only loosely depends on the size, if the block is not close to overturning. The dominant factor is the slenderness. Therefore, we can define the displacement demand rocking spectrum of a ground motion as a unary function:

$$u_{demand} = f(\alpha) \quad \text{if } u_{demand} \ll 2b \tag{2.13}$$

which is computed via Equations (2.1) and (2.10) for a large enough block size. To check the stability of a block, one has to compute the maximum displacement demand via Equation (2.13) and compare it with the displacement capacity (i.e., the block width).

Therefore, the reduction of the dimension of the problem follows two steps: (a) applying Buckingham's theorem and (b) observing that the displacement demand is roughly independent of the size. The first step is exact and follows from dimensional analysis. The second step is approximate and in this section is illustrated for analytical pulses. Blochlinger (2016) gave a first indication that the approximation also works for recorded ground motions. Further evidence supporting this approximation and highlighting its limitations are given in a next section of this paper.
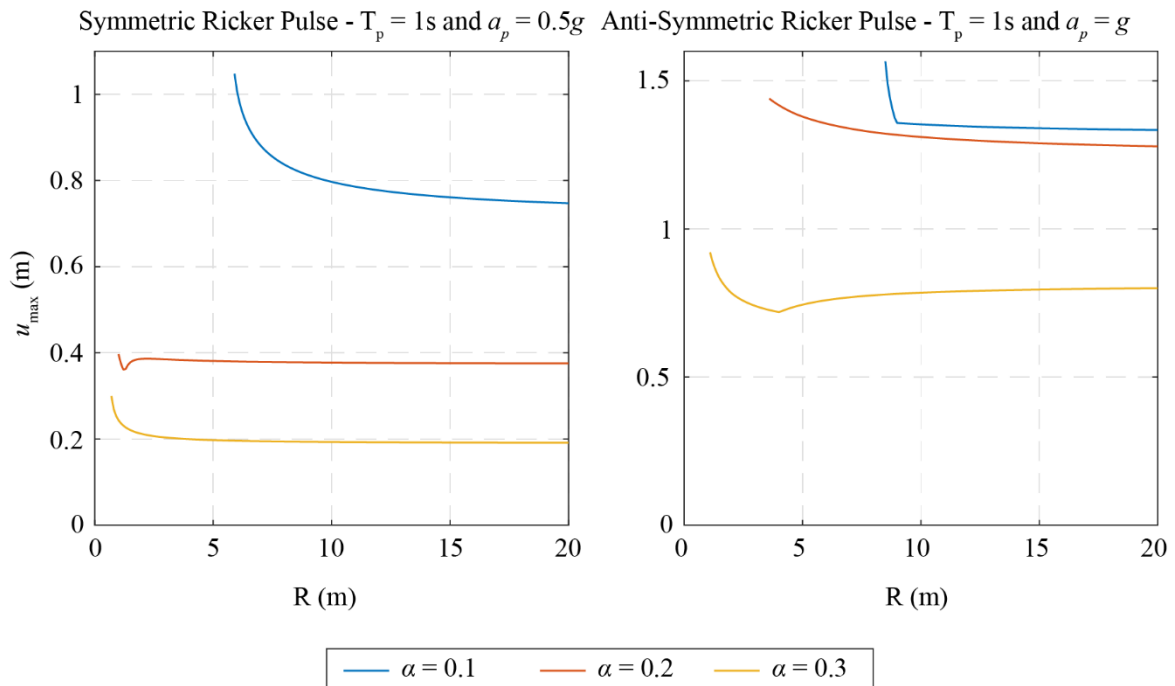
Figure 2.6. Maximum block displacement as a function of block size for symmetric and anti-symmetric Ricker excitation.

2.3.2. Analysis based on the base width of the block (*b*)

The previous section chooses the frequency parameter *p* and the slenderness of the block, *α*, as the two parameters to define it. However, *p* has a physical meaning that is totally unrelated to rocking. It is the natural frequency that the block would have had if it was hanging from its corner (DeJong & Dimitrakopoulos, 2014). But this is merely a coincidence, rocking blocks have no natural frequency (Housner, 1963), and the use of *p* often creates misunderstandings. In this section, we propose to describe the block with two physical parameters that have a clear physical meaning, directly related to the rocking problem. The slenderness *α* is retained, as it controls the uplift of the structure (and could be parallelized with the strength of a system), but *p* is replaced by *b*, which is the halfwidth of the base and exactly equal to one half of its displacement capacity. Then the displacement response will be:

$$u_{max} = f_4\left(b, \alpha, g, a_p, \omega_p\right) \tag{2.14}$$

Using Buckingham's Π theorem, we get:

$$\frac{u_{max}\omega_p^2}{a_p} = \varphi_3\left(\frac{a_p}{g \tan \alpha}, \frac{b\omega_p^2}{a_p}, \alpha\right) \tag{2.15}$$

The term $\dfrac{a_p}{g \tan \alpha}$ would be the reciprocal of the nondimensional strength, $\dfrac{b\omega_p^2}{a_p}$ would be the nondimensional displacement capacity, and *α* (taken as an independent parameter) controls damping, because it controls the coefficient of restitution.

Figure 2.7 plots displacement spectra according to the suggested nondimensionalization. One can observe that for both pulses, a base (i.e., a displacement capacity = 2*b*) of roughly nine times the length scale of the pulse $L_e = \dfrac{a_p}{\omega_p^2}$ is enough to keep the block stable, no matter what the nondimensional strength parameter is.

2.4. Displacement-based analysis of a rocking oscillator excited by recorded ground motions

Analytical pulses can be used to qualitatively study the rocking oscillator. However, as the rocking problem is very sensitive to all of its parameters, pulses would not suffice to prove that the displacement demand on a rocking structure depends only on its slenderness and not on its size. Therefore, this section examines the displacement response of a rocking block excited by

recorded ground motions.
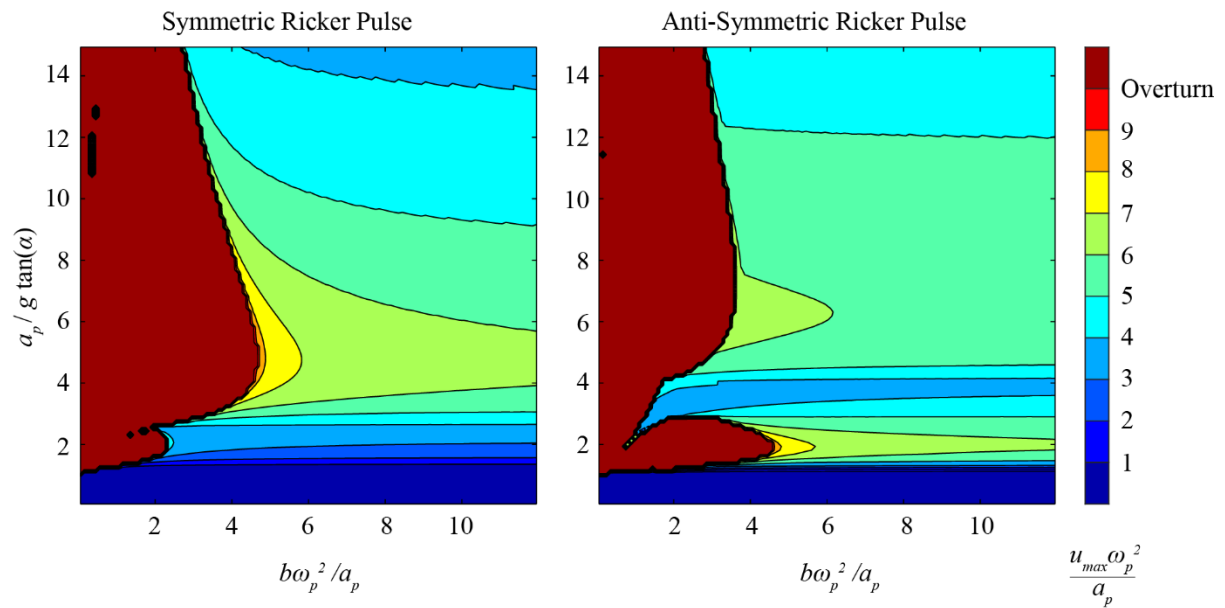
Figure 2.7. Displacement-based nondimensional rocking spectra using the width of the block to characterize its size.

2.4.1. FEMA P695 ground motions

There is no consensus in the engineering community on what ground motions should be used in time history analysis. Several approaches exist including using recorded (scaled or unscaled), artificial, or synthetic ground motions. In this paper, we choose to use the three sets of ground motions proposed by FEMA P695 (FEMA, 2009) (far-field, near-field pulse-like, and near-field non–pulse-like) only as a means to illustrate our rocking-related argument, without taking stance on the debate around ground motions. It is evident that any ground motion selection method based on the response of an elastic system is in principle not applicable in the case of the rocking oscillator, as the elastic and rocking oscillator are uncorrelated. More information on the FEMA P695 ground motions can be found in FEMA (FEMA, 2009).

2.4.2. Equal displacement rule for rocking structures and displacement demand spectra

Vassiliou et al. (2014) have proven that rigid rocking oscillators of equal height attached to massless foundations of the same size behave identically, no matter what their actual column width is (Figure 2.8). Therefore, the design question of a rocking structure would be: Find the size, *2B′*, of the foundation for a given oscillator height *2H*. Hence, it is more meaningful to

use H as a size parameter instead of R, even if the former does not explicitly appear in the equation of motion.
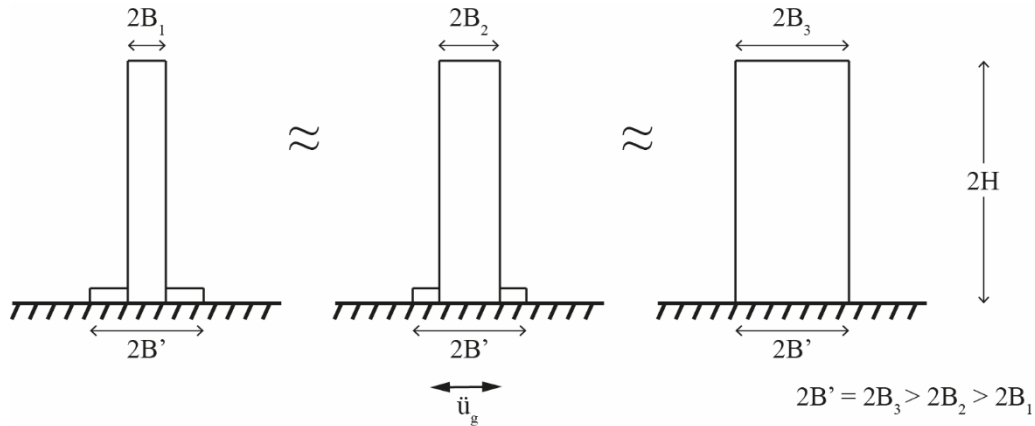
Figure 2.8. Rocking oscillators of equal height.

Figure 2.9 offers the displacement of a rocking oscillator as function of its slenderness α, and for $2H = 2, 4, 10, 20, 80,$ and 1000 m, for a selection of the FEMA P695 ground motions. The $2H = 1000$ m is offered only for reasons of mathematical completeness, to study the limit case of $H \to \infty$. For reasons of plot clarity, each line is plotted only for $\alpha > \alpha_{\text{crit}}$, where α_{crit} is the minimum slenderness angle for which the block overturns. We observe that all blocks of the same slenderness angle present roughly the same displacement, as long as they are not close to overturning. The same observation holds for all the ground motions tested.

As analysis and design of a rocking structure would not involve a single ground motion, but a set of design motions, it makes sense to study the problem by applying sets of multiple excitations and comparing the statistics of the results (e.g., the median displacement among all the ground motions of the excitation set). Figure 2.10 plots displacement spectra of the median of the displacement for seven variations of the near-field pulse-like FEMA P695 set: (a) unscaled ground motions, (b) scaled so that their PGA is equal to $0.5\overline{PGA}$, or $\overline{PGA}$, or $2\overline{PGA}$, (c) scaled so that their PGV is equal to $0.5\overline{PGV}$, or $\overline{PGV}$, or $2\overline{PGV}$, where $\overline{PGA}$ and $\overline{PGV}$ are defined as:

$$\overline{PGA} = \underset{i=1...N}{\text{median}} \left(\sqrt{PGA_{i_x} \times PGA_{i_y}} \right) \tag{2.16}$$

$$\overline{PGV} = \underset{i=1...N}{\text{median}} \left(\sqrt{PGV_{i_x} \times PGV_{i_y}} \right) \tag{2.17}$$

where N is the number of the ground motions and x and y are the two components of each ground motion. Note that each horizontal component of each ground motion is treated as an

independent motion. Figure 2.11 and Figure 2.12 plot the same spectra for the far-field and near-field non–pulse-like ground motions.
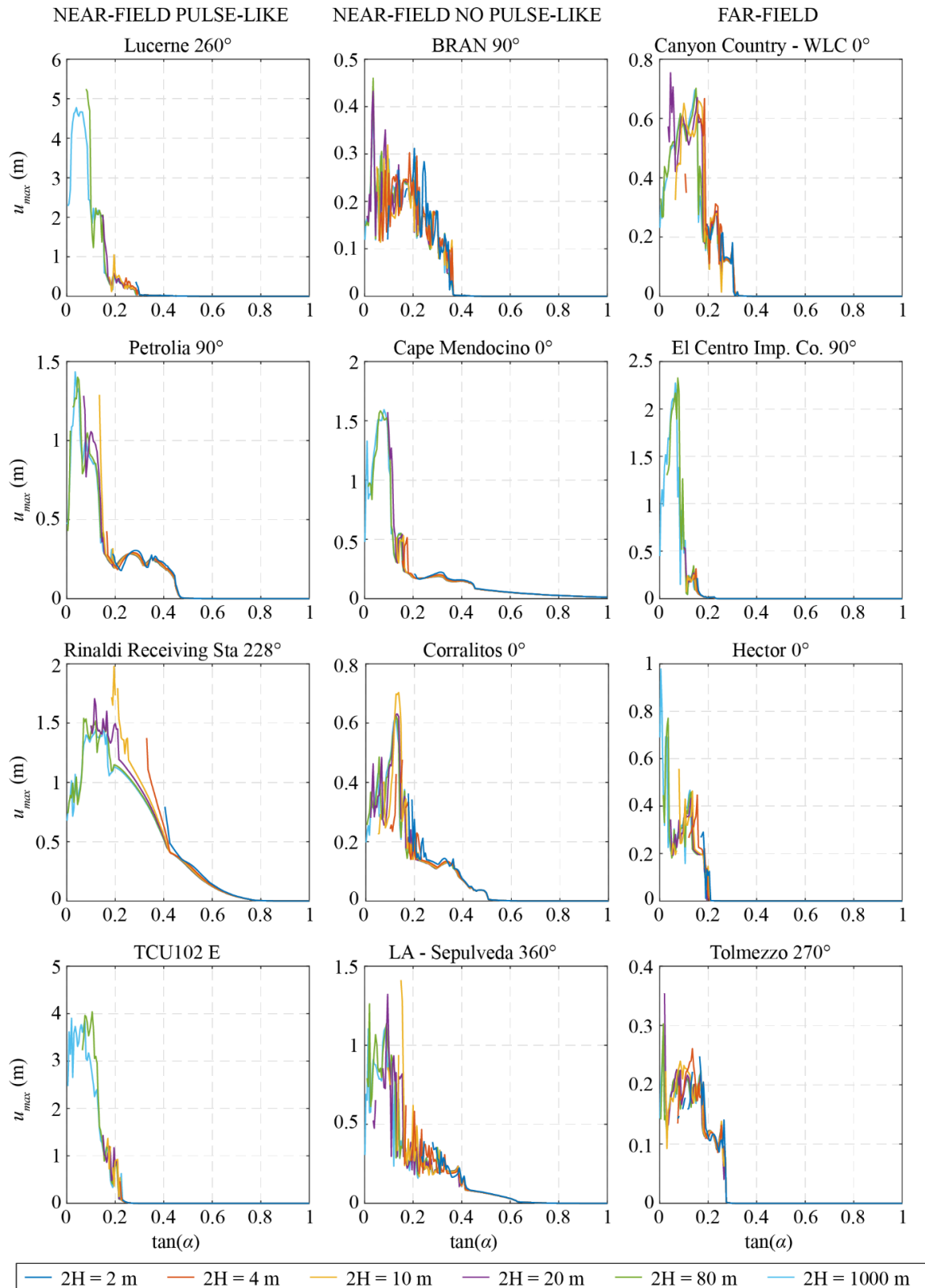
Figure 2.9. Displacement of a rocking oscillator as function of its slenderness α.

The following observations can be made:

(a) The median spectra are smoother, likewise design elastic spectra that were derived by statistical processing of elastic spectra of single ground motions are smoother than single ground motion spectra.

(b) As long as the system is not close to overturning, the displacement does not depend on the size of the block. For this part of the spectrum, instead of computing a different spectrum for each block size, one can compute the design spectrum for $2H \rightarrow \infty$ ($2H = 1000$ m seems an adequate value) and use it to calculate the displacement *demand* on any rocking structure (i.e., $u_{max} = f(\alpha)$). We name the above finding "equal displacement rule" for rocking structures.

(c) As the system gets closer to overturning, the equal displacement rule does not apply: Smaller systems present larger displacements than larger ones. Moreover, as the system approaches overturning, the slope of the spectrum increases dramatically, i.e., a small decrease in tanα leads to very large increase in displacement. This trend dictates that a rational design of a rocking structure would require that this steep part of the spectrum be avoided, because an earthquake slightly stronger than the design one would cause a tremendous increase in displacement. Therefore, the equal displacement rule applies to the rational design region.

(d) The form of the spectrum for all three sets of ground motions presents some repetitive pattern:

    i.   As α tends to zero, u_{max} tends to a finite value. For spectra of individual ground motions, this value is $\frac{3}{2}PGD$. An explanation for this is offered in the next section.

    ii.   As α increases from zero, the displacement demand amplifies 2–2.5 times and reaches a plateau.

    iii.   Further increase of α leads to a monotonic decrease of the displacement demand.

    iv.   Naturally, when tanα reaches PGA/g, the displacement demand becomes zero, as there is no uplift.
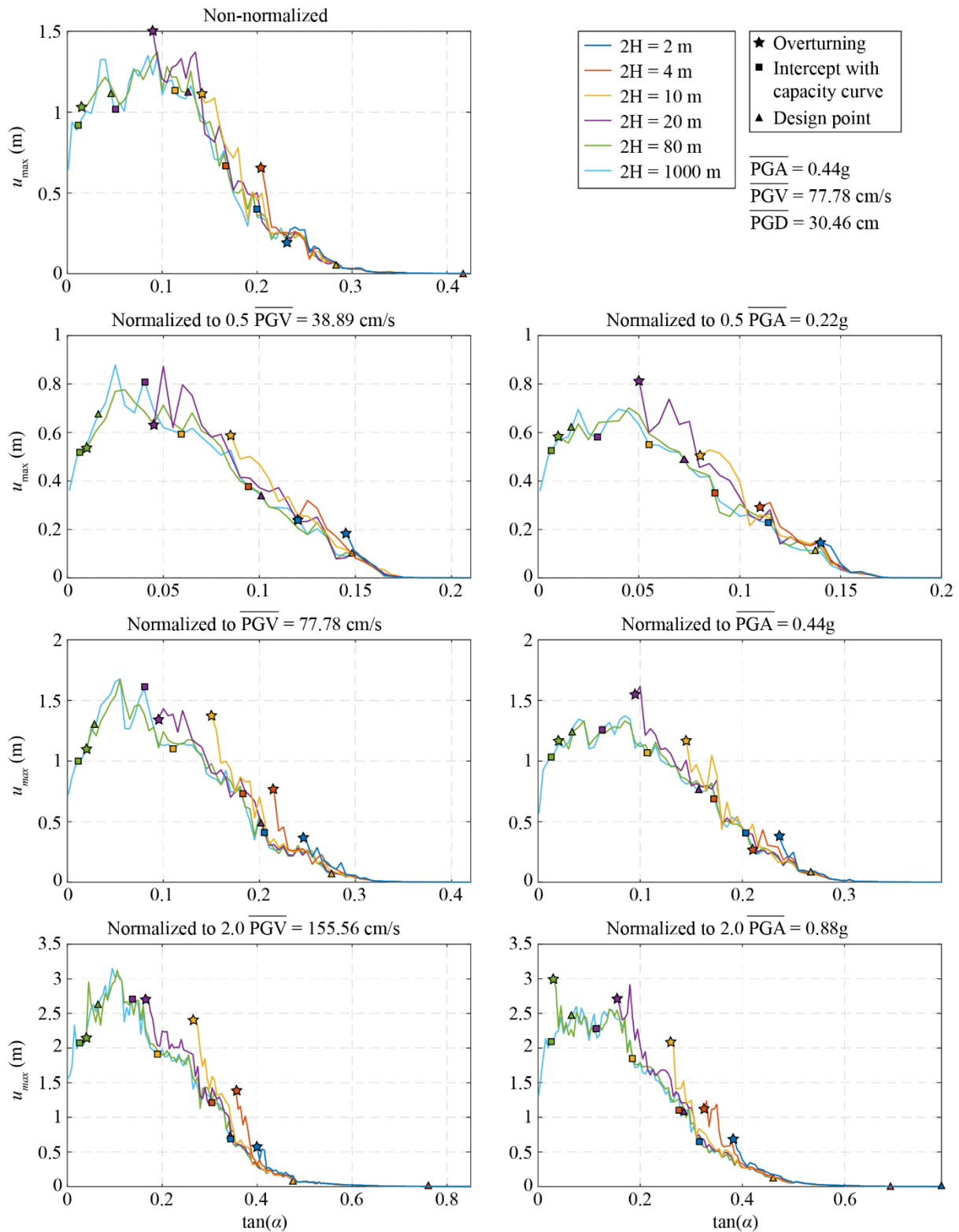
Figure 2.10. Median displacement spectra for near-field pulse-like record set.
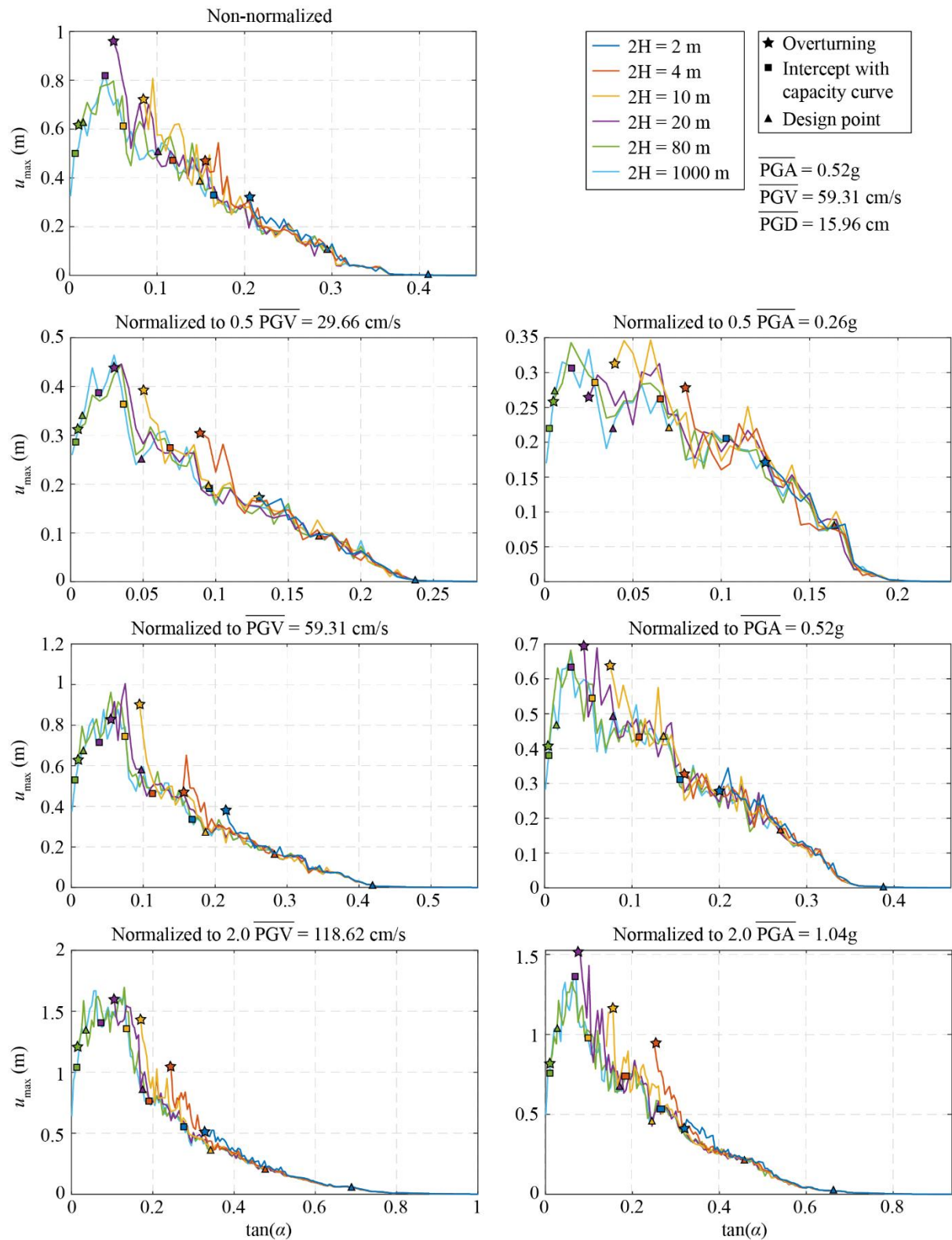
Figure 2.11. Median displacement spectra for near-field non-pulse-like record set.
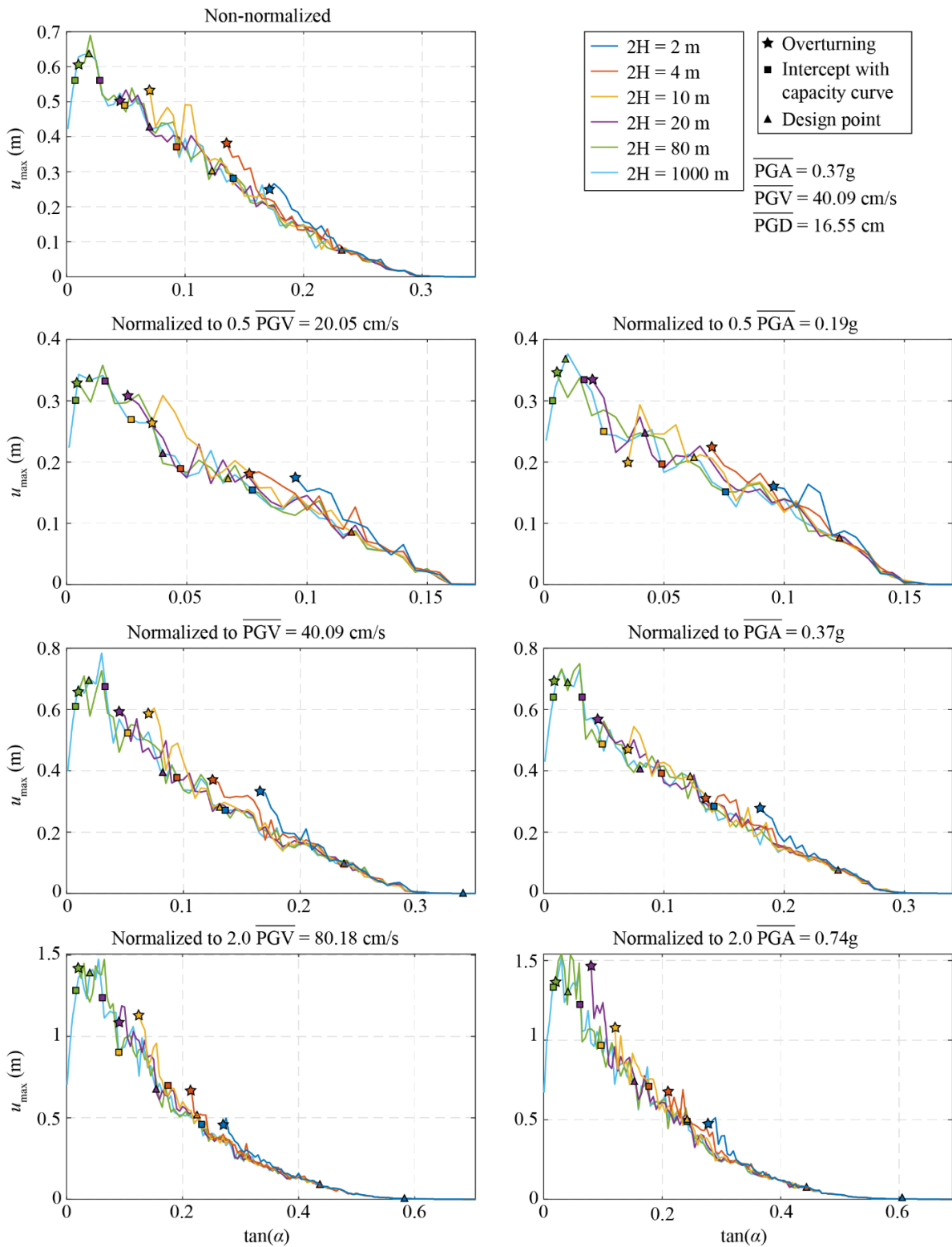
Figure 2.12. Median displacement spectra for near-field non-pulse-like record set.

2.4.3. Preliminary design based on the equal displacement rule

If not for a final design, the equal displacement rule can be used for preliminary calculations. Indeed it is not an exact method, but a preliminary design method that does not aim at being

exact, but at providing a tool for initial calculations, that for certain cases and required degree of accuracy can be enough. The same holds for yielding structures, where the "equal displacement rule" is used for many structural systems, while for more complicated systems, it is used only for preliminary design and then more refined methods are applied. It could be stated that the findings of this paper constitute the generalization of equal displacement rule from yielding to rocking systems. This section proposes a methodology to design a rocking structure based on the equal displacement rule:

(a) On the $u_{\max} - \tan\alpha$ curve, we plot the capacity line $u_c = 2H\tan\alpha$.

(b) We determine the intersection of the capacity line and the $2H = \infty$ line. We define the abscissa of this point as $\tan\alpha_k$.

(c) We use a multiplier of 2.5 to determine the design slenderness: $\tan\alpha_D = 2.5\tan\alpha_k$. The multiplier serves as a safety factor to move the design point away from the steep part of the spectrum.

Figure 2.13 outlines the design procedure applied for a rocking bridge with columns of 6.7 m height ($2H = 6.7$ m). Based on Makris & Vassiliou (2013), the response of the frame is equal to the response of a solitary block of $2H = 10$ m. For this bridge, 21 design scenarios are explored, corresponding to the 21 spectra of Figure 2.10 to Figure 2.12. Table 2.1, Table 2.2, and Table 2.3 and Figure 2.14 summarize the findings for the 21 design scenarios and compare the displacement predicted by the demand spectrum ($2H = 1000$ m) to the displacement predicted by the $2H = 10$ m spectrum. We observe that in all but two cases (near-fault pulse-like scaled to $0.5\overline{PGA}$ and near-fault non–pulse-like scaled to $2\overline{PGA}$), the error in predicting the median displacement is less than 20%. In all cases, the error is smaller than 40%, and no system overturned.
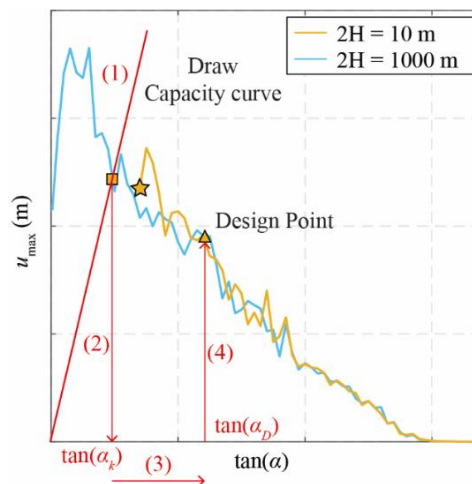
Figure 2.13. Design procedure.

Table 2.1. Near-field pulse-like FS = 2.5.

	Unscaled	$0.5\overline{PGA}$	$\overline{PGA}$	$2\overline{PGA}$	$0.5\overline{PGV}$	$\overline{PGV}$	$2\overline{PGV}$
$\tan(\alpha_D)$	0.2839	0.1378	0.2671	0.4618	0.0596	0.1094	0.1909
$2H = 1000$ m	0.05	0.11	0.08	0.12	0.10	0.07	0.08
$2H = 10$ m	0.06	0.15	0.07	0.13	0.10	0.10	0.08

Table 2.2. Near-field non-pulse-like FS = 2.5.

	Unscaled	$0.5\overline{PGA}$	$\overline{PGA}$	$2\overline{PGA}$	$0.5\overline{PGV}$	$\overline{PGV}$	$2\overline{PGV}$
$\tan(\alpha_D)$	0.1524	0.0708	0.1356	0.2446	0.0916	0.1892	0.3405
$2H = 1000$ m	0.34	0.22	0.44	0.44	0.19	0.27	0.36
$2H = 10$ m	0.41	0.26	0.41	0.69	0.21	0.30	0.38

Table 2.3. Far-field FS = 2.5.

	Unscaled	$0.5\overline{PGA}$	$\overline{PGA}$	$2\overline{PGA}$	$0.5\overline{PGV}$	$\overline{PGV}$	$2\overline{PGV}$
$\tan(\alpha_D)$	0.1228	0.0620	0.1215	0.2411	0.0675	0.1320	0.2249
$2H = 1000$ m	0.30	0.21	0.38	0.52	0.17	0.28	0.52
$2H = 10$ m	0.33	0.20	0.37	0.50	0.19	0.29	0.49

2.5. Interpretation of the equal displacement rule based on the equation of motion

The equal displacement rule can be interpreted by properly manipulating the equation of motion. Assuming small rotation angles ($\sin x = x$ and $\cos x = 1$), Equation (2.1) gives:

$$\ddot{\theta} = -\frac{3g}{4H} \cdot \left(\pm\alpha - \theta + \frac{\ddot{u}_g}{g} \right) \tag{2.18}$$

For small angles, $u = 2H\theta$. Then:

$$\ddot{u} = -\frac{3g\alpha}{2} \cdot \left(\pm 1 - \frac{u}{2b} + \frac{\ddot{u}_g}{g\alpha} \right) \tag{2.19}$$

When $u/2b$ is small (i.e., the block is not close to overturning), the other terms dominate the response and u becomes a function only of α. Furthermore, when $\dfrac{\ddot{u}_g}{g\alpha} \gg 1$, then $\ddot{u} = -\dfrac{3\ddot{u}_g}{2}$.

Therefore, as $\alpha \to 0$ (which can only happen for blocks with $H \to \infty$), $u_{\max} \to 3/2$ PGD.
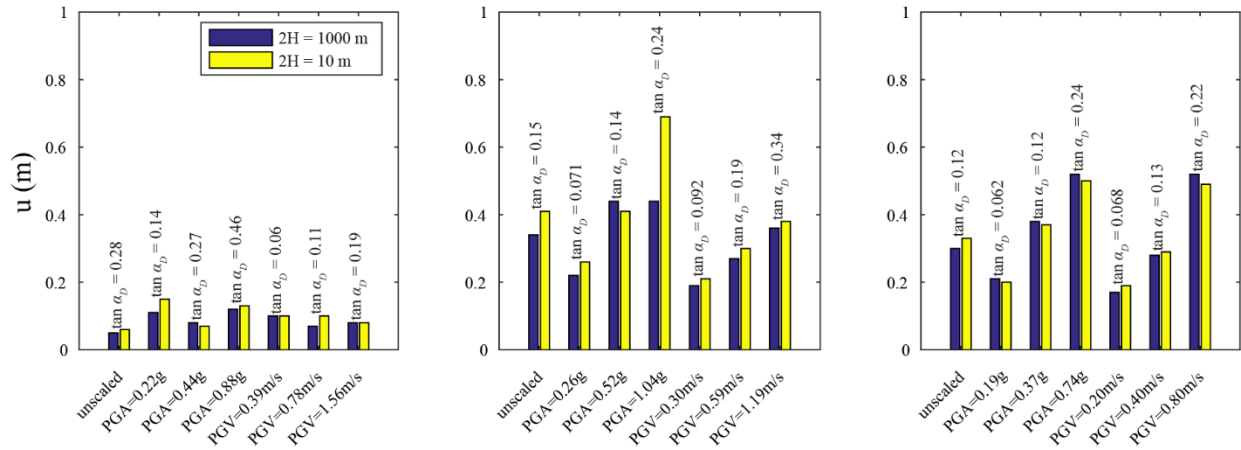
Figure 2.14. Comparison of the displacement response at the design point. Predictions based on the 2*H* = 1000 m and on the 2*H* = 10 m spectra.

2.6. Conclusions

The widely used description of the rocking block via its rotation is correct, but not optimal. It reveals that larger blocks are more stable and that higher frequency pulses present less overturning potential. However, it does not reveal the "equal displacement rule of rocking structures", namely, that a large and a small block of the same aspect ratio will present the same top displacement, if they both are not close to overturning. Not being close to overturning is a design necessity anyway; therefore, for the scope of design, we can claim that the displacement demand is the same, and it only depends on the slenderness, not on the size of the block. The above is illustrated for both analytical pulse excitations and for sets of recorded ground motions. Based on the above, a design method that uses a size-independent rocking spectrum is suggested. This should be taken into account when intensity measures for rocking structures (Dimitrakopoulos & Paraskeva, 2015; Giouvanidis & Dimitrakopoulos, 2018; Kavvadias et al., 2017; Pappas et al., 2017) designed not to get close to overturning are explored.

References

Acikgoz, S., & DeJong, M. J. (2012). The interaction of elasticity and rocking in flexible structures allowed to uplift. *Earthquake Engineering & Structural Dynamics*, *41*(15), 2177–2194.

Agalianos, A., Psychari, A., Vassiliou, M. F., Stojadinovic, B., & Anastasopoulos, I. (2017). Comparative Assessment of Two Rocking Isolation Techniques for a Motorway Overpass Bridge. *Frontiers in Built Environment*, *3*.

Aghagholizadeh, M., & Makris, N. (2018). Earthquake response analysis of yielding structures coupled with vertically restrained rocking walls. *Earthquake Engineering & Structural Dynamics*, *47*(15), 2965–2984.

Anastasopoulos, I., Gazetas, G., Loli, M., Apostolou, M., & Gerolymos, N. (2010). Soil failure can be used for seismic protection of structures. *Bulletin of Earthquake Engineering*, *8*(2), 309–326.

Bachmann, J. A., Strand, M., Vassiliou, M. F., Broccardo, M., & Stojadinović, B. (2018). Is rocking motion predictable? *Earthquake Engineering & Structural Dynamics*, *47*(2), 535–552.

Bachmann, J. A., Vassiliou, M. F., & Stojadinović, B. (2017). Dynamics of rocking podium structures. *Earthquake Engineering & Structural Dynamics*, *46*(14), 2499–2517.

Barenblatt, G. I. (1996). *Scaling, self-similarity, and intermediate asymptotics: Dimensional analysis and intermediate asymptotics* (Vol. 14). Cambridge University Press.

Beck, J. L., & Skinner, R. I. (1973). The seismic response of a reinforced concrete bridge pier designed to step. *Earthquake Engineering & Structural Dynamics*, *2*(4), 343–358.

Blochlinger, P. (2016). *Rigid body rocking spectra for recorded earthquake ground motions* [Masther Thesis]. ETH Zurich.

Buckingham, E. (1914). On Physically Similar Systems; Illustrations of the Use of Dimensional Equations. *Physical Review*, *4*, 345–376.

Casapulla, C., Giresini, L., & Lourenço, P. B. (2017). Rocking and Kinematic Approaches for Rigid Block Analysis of Masonry Walls: State of the Art and Recent Developments. *Buildings*, *7*(3), 69.

Chatzis, M. N., Espinosa, M. G., & Smyth, A. W. (2017). Examining the Energy Loss in the Inverted Pendulum Model for Rocking Bodies. *Journal of Engineering Mechanics*, *143*(5), 04017013.

Chopra, A. K., & Yim, S. C.-S. (1985). Simplified Earthquake Analysis of Structures with Foundation Uplift. *Journal of Structural Engineering*, *111*(4), 906–930.

Dar, A., Konstantinidis, D., & El-Dakhakhni, W. (2018). Seismic response of rocking frames with top support eccentricity. *Earthquake Engineering & Structural Dynamics*, *47*(12), 2496–2518.

Dar, A., Konstantinidis, D., & El-Dakhakhni, W. W. (2016). Evaluation of ASCE 43-05 Seismic Design Criteria for Rocking Objects in Nuclear Facilities. *Journal of Structural Engineering*, *142*(11), 04016110.

DeJong, M. J. (2012). Seismic response of stone masonry spires: Analytical modeling. *Engineering Structures*, *40*, 556–565.

DeJong, M. J., & Dimitrakopoulos, E. G. (2014). Dynamically equivalent rocking structures. *Earthquake Engineering & Structural Dynamics*, *43*(10), 1543–1563.

Di Egidio, A., Alaggio, R., Contento, A., Tursini, M., & Della Loggia, E. (2015). Experimental characterization of the overturning of three-dimensional square based rigid block. *International Journal of Non-Linear Mechanics*, *69*, 137–145.

Di Sarno, L., Magliulo, G., D'Angela, D., & Cosenza, E. (2019). Experimental assessment of the seismic performance of hospital cabinets using shake table testing. *Earthquake*

Engineering & Structural Dynamics, *48*(1), 103–123.

Dimitrakopoulos, E. G., & DeJong, M. J. (2012). Revisiting the rocking block: Closed-form solutions and similarity laws. *Proceedings of the Royal Society A: Mathematical, Physical and Engineering Sciences*, *468*(2144), 2294–2318.

Dimitrakopoulos, E. G., & Giouvanidis, A. I. (2015). Seismic Response Analysis of the Planar Rocking Frame. *Journal of Engineering Mechanics*, *141*(7), 04015003.

Dimitrakopoulos, E. G., & Paraskeva, T. S. (2015). Dimensionless fragility curves for rocking response to near-fault excitations. *Earthquake Engineering & Structural Dynamics*, *44*(12), 2015–2033.

FEMA. (2009). *Quantification of building seismic performance factors* (FEMA-P695). Federal Emergency Management Agency.

Giouvanidis, A. I., & Dimitrakopoulos, E. G. (2017a). Nonsmooth dynamic analysis of sticking impacts in rocking structures. *Bulletin of Earthquake Engineering*, *15*(5), 2273–2304.

Giouvanidis, A. I., & Dimitrakopoulos, E. G. (2017b). Seismic Performance of Rocking Frames with Flag-Shaped Hysteretic Behavior. *Journal of Engineering Mechanics*, *143*(5), 04017008.

Giouvanidis, A. I., & Dimitrakopoulos, E. G. (2018). Rocking amplification and strong-motion duration. *Earthquake Engineering & Structural Dynamics*, *47*(10), 2094–2116.

Housner, G. W. (1963). The behavior of inverted pendulum structures during earthquakes. *Bulletin of the Seismological Society of America*, *53*(2), 403–417.

Kalliontzis, D., & Schultz, A. E. (2017). Characterizing the In-Plane Rocking Response of Masonry Walls with Unbonded Posttensioning. *Journal of Structural Engineering*, *143*(9), 04017110.

Kalliontzis, D., & Sritharan, S. (2018). Characterizing Dynamic Decay of Motion of Free-Standing Rocking Members. *Earthquake Spectra*, *34*(2), 843–866.

Kavvadias, I. E., Papachatzakis, G. A., Bantilas, K. E., Vasiliadis, L. K., & Elenas, A. (2017). Rocking spectrum intensity measures for seismic assessment of rocking rigid blocks. *Soil Dynamics and Earthquake Engineering*, *101*, 116–124.

Konstantinidis, D., & Makris, N. (2010). Experimental and analytical studies on the response of 1/4-scale models of freestanding laboratory equipment subjected to strong earthquake shaking. *Bulletin of Earthquake Engineering*, *8*(6), 1457–1477.

Ma, Q. T., & Khan, M. H. (2008). Free vibration tests of a scale model of the South Rangitikei Railway Bridge. *Proceedings of the New Zealand Society for Earthquake Engineering Annual Conference*. 2008 NZSEE Conference, New Zealand.

Ma, Q. T. M. (2010). *The mechanics of rocking structures subjected to ground motion*. The University of Auckland.

Makris, N., & Aghagholizadeh, M. (2017). The dynamics of an elastic structure coupled with a rocking wall. *Earthquake Engineering & Structural Dynamics*, *46*(6), 945–962.

Makris, N., & Kampas, G. (2016). Seismic Protection of Structures with Supplemental Rotational Inertia. *Journal of Engineering Mechanics*, *142*(11), 04016089.

Makris, N., & Konstantinidis, D. (2003). The rocking spectrum and the limitations of practical design methodologies. *Earthquake Engineering & Structural Dynamics*, *32*(2), 265–289.

Makris, N., & Vassiliou, M. F. (2013). Planar rocking response and stability analysis of an array of free-standing columns capped with a freely supported rigid beam. *Earthquake Engineering & Structural Dynamics*, *42*(3), 431–449.

Makris, N., & Vassiliou, M. F. (2014). Are Some Top-Heavy Structures More Stable? *Journal of Structural Engineering*, *140*(5), 06014001.

Makris, N., & Vassiliou, M. F. (2015). Dynamics of the Rocking Frame with Vertical Restrainers. *Journal of Structural Engineering*, *141*(10), 04014245.

Mander, J. B., & Cheng, C. T. (1997). *Seismic Resistance of Bridge Piers Based on Damage*

Avoidance Design (Techncial Report NCEER-97-0014; pp. 1–144). National Center for Earthquake Engineering Research.

Mehrotra, A., & DeJong, M. J. (2018). The influence of interface geometry, stiffness, and crushing on the dynamic response of masonry collapse mechanisms. *Earthquake Engineering & Structural Dynamics*, *47*(13), 2661–2681.

Mouzakis, H. P., Psycharis, I. N., Papastamatiou, D. Y., Carydis, P. G., Papantonopoulos, C., & Zambas, C. (2002). Experimental investigation of the earthquake response of a model of a marble classical column. *Earthquake Engineering & Structural Dynamics*, *31*(9), 1681–1698.

Nikolić, Ž., Krstevska, L., Marović, P., & Smoljanović, H. (2019). Experimental investigation of seismic behaviour of the ancient Protiron monument model. *Earthquake Engineering & Structural Dynamics*, *48*(6), 573–593.

Oliveto, G., Caliò, I., & Greco, A. (2003). Large displacement behaviour of a structural model with foundation uplift under impulsive and earthquake excitations. *Earthquake Engineering & Structural Dynamics*, *32*(3), 369–393.

Papaloizou, L., & Komodromos, P. (2009). Planar investigation of the seismic response of ancient columns and colonnades with epistyles using a custom-made software. *Soil Dynamics and Earthquake Engineering*, *29*(11), 1437–1454.

Papantonopoulos, C., Psycharis, I. N., Papastamatiou, D. Y., Lemos, J. V., & Mouzakis, H. P. (2002). Numerical prediction of the earthquake response of classical columns using the distinct element method. *Earthquake Engineering & Structural Dynamics*, *31*(9), 1699–1717.

Pappas, A., Sextos, A., da Porto, F., & Modena, C. (2017). Efficiency of alternative intensity measures for the seismic assessment of monolithic free-standing columns. *Bulletin of Earthquake Engineering*, *15*(4), 1635–1659.

Psycharis, I. N. (1991). Effect of Base Uplift on Dynamic Response of SDOF Structures. *Journal of Structural Engineering*, *117*(3), 733–754.

Routledge, P. J., Cowan, M. J., & Palermo, A. (2016). Low-damage detailing for bridges—A case study of Wigram-Magdala Bridge. *Proceedings of the New Zealand Society for Earthquake Engineering Annual Conference*. 2016 NZSEE Conference.

Sextos, A. G., Manolis, G. D., Ioannidis, N., & Athanasiou, A. (2017). Seismically induced uplift effects on nuclear power plants. Part 2: Demand on internal equipment. *Nuclear Engineering and Design*, *318*, 288–296.

Sharpe, R. D., & Skinner, R. I. (1983). The seismic design of an industrial chimney with rocking base. *Bulletin of the New Zealand Society for Earthquake Engineering*, *16*(2), 98–106.

Stefanou, I., Psycharis, I., & Georgopoulos, I.-O. (2011). Dynamic response of reinforced masonry columns in classical monuments. *Construction and Building Materials*, *25*(12), 4325–4337.

Thiers-Moggia, R., & Málaga-Chuquitaype, C. (2019). Seismic protection of rocking structures with inerters. *Earthquake Engineering & Structural Dynamics*, *48*(5), 528–547.

Thonstad, T., Mantawy, I. M., Stanton, J. F., Eberhard, M. O., & Sanders, D. H. (2016). Shaking Table Performance of a New Bridge System with Pretensioned Rocking Columns. *Journal of Bridge Engineering*, *21*(4), 04015079.

Tondelli, M., Beyer, K., & DeJong, M. (2016). Influence of boundary conditions on the out-of-plane response of brick masonry walls in buildings with RC slabs. *Earthquake Engineering & Structural Dynamics*, *45*(8), 1337–1356.

Truniger, R., Vassiliou, M. F., & Stojadinović, B. (2015). An analytical model of a deformable cantilever structure rocking on a rigid surface: Experimental validation. *Earthquake Engineering & Structural Dynamics*, *44*(15), 2795–2815.

Vaschy, A. (1892). Sur les lois de similitude en physique. *Annales Télégraphiques*, *19*, 25–28.

Vassiliou, M. F. (2018). Seismic response of a wobbling 3D frame. *Earthquake Engineering & Structural Dynamics*, *47*(5), 1212–1228.

Vassiliou, M. F., Burger, S., Egger, M., Bachmann, J. A., Broccardo, M., & Stojadinovic, B. (2017a). The three-dimensional behavior of inverted pendulum cylindrical structures during earthquakes. *Earthquake Engineering & Structural Dynamics*, *46*(14), 2261–2280.

Vassiliou, M. F., Mackie, K. R., & Stojadinović, B. (2014). Dynamic response analysis of solitary flexible rocking bodies: Modeling and behavior under pulse-like ground excitation. *Earthquake Engineering & Structural Dynamics*, *43*(10), 1463–1481.

Vassiliou, M. F., Mackie, K. R., & Stojadinović, B. (2017b). A finite element model for seismic response analysis of deformable rocking frames. *Earthquake Engineering & Structural Dynamics*, *46*(3), 447–466.

Vassiliou, M. F., & Makris, N. (2011). Estimating Time Scales and Length Scales in Pulselike Earthquake Acceleration Records with Wavelet Analysis. *Bulletin of the Seismological Society of America*, *101*(2), 596–618.

Vassiliou, M. F., & Makris, N. (2012). Analysis of the rocking response of rigid blocks standing free on a seismically isolated base. *Earthquake Engineering & Structural Dynamics*, *41*(2), 177–196.

Vassiliou, M. F., & Makris, N. (2015). Dynamics of the Vertically Restrained Rocking Column. *Journal of Engineering Mechanics*, *141*(12), 04015049.

Vassiliou, M. F., Truniger, R., & Stojadinović, B. (2015). An analytical model of a deformable cantilever structure rocking on a rigid surface: Development and verification. *Earthquake Engineering & Structural Dynamics*, *44*(15), 2775–2794.

Voyagaki, E., Kloukinas, P., Dietz, M., Dihoru, L., Horseman, T., Oddbjornsson, O., Crewe, A. J., Taylor, C. A., & Steer, A. (2018). Earthquake response of a multiblock nuclear reactor graphite core: Experimental model vs simulations. *Earthquake Engineering & Structural Dynamics*, *47*(13), 2601–2626.

Wittich, C. E., & Hutchinson, T. C. (2015). Shake table tests of stiff, unattached, asymmetric structures. *Earthquake Engineering & Structural Dynamics*, *44*(14), 2425–2443.

Xie, Y., Zhang, J., DesRoches, R., & Padgett, J. E. (2019). Seismic fragilities of single-column highway bridges with rocking column-footing. *Earthquake Engineering & Structural Dynamics*, *48*(7), 843–864.

Zhang, J., & Makris, N. (2001). Rocking Response of Free-Standing Blocks under Cycloidal Pulses. *Journal of Engineering Mechanics*, *127*(5), 473–483.

3. Simplified analysis of bilinear elastic systems exhibiting negative stiffness behavior

Abstract

This work studies the dynamics of the Negative Stiffness Bilinear Elastic (NSBE) oscillator. Such a mathematical idealization can be used to describe deformable rocking systems equipped with restraining tendons or with curved extensions of their bases. First, this paper establishes the characteristic quantities of the bilinear system to make it equivalent to the actual rocking structures. Then, it proceeds by proposing a simpler "equivalent" system that can be used to study the behavior of the NSBE. The equivalent system is not some linear elastic oscillator but a bilinear elastic system with zero stiffness of the second branch: the Zero Stiffness Bilinear Elastic (ZSBE) system. ZSBE is useful because it needs one parameter less than NSBE to be defined. Next, "Equal Displacement" and "Equal Energy" rules that provide estimates of the maximum displacement of the NSBE based on the response of the ZSBE are defined. The concept is similar to the $R\mu T$ relations that provide estimates of the response of bilinear yielding systems based on the response of an equivalent linear elastic system, with one major difference: it does not resort to a linear elastic system but to the ZSBE. The proposed methodology is applied on the FEMA P695 ground motions scaled at three different levels. The results show that ZSBE is a good proxy of NSBE and, hence, indicate that an exhaustive study of the ZSBE is useful for the design of rocking structures.

3.1. Introduction

Rocking has been proposed as a seismic isolation method for both bridges (Agalianos et al., 2017; Bachmann et al., 2018; Dar et al., 2018; Dimitrakopoulos & Giouvanidis, 2015; Giouvanidis & Dimitrakopoulos, 2017b; Kashani et al., 2018; Makris & Vassiliou, 2013, 2014, 2015; Thiers-Moggia & Málaga-Chuquitaype, 2019; Thomaidis et al., 2020; Vassiliou, 2018;

Vassiliou et al., 2017a; Vassiliou et al., 2017b; Vassiliou & Makris, 2015; Xie et al., 2019) and buildings (Aghagholizadeh & Makris, 2018; Bachmann et al., 2017, 2019; Giouvanidis & Dong, 2020; Ríos-García & Benavent-Climent, 2020), because uplift works as a mechanical fuse and limits the design forces of both the superstructure and the foundation. Unlike structures designed to yield, the free rocking rigid block (Housner, 1963) of Figure 3.1a,b exhibits *negative* post-uplift stiffness (Figure 3.1c). Several researchers have used a stiff tendon to keep the post-uplift stiffness positive (Kam et al., 2010; Mahin et al., 2006; Mashal & Palermo, 2019; Palermo et al., 2005; Priestley & Tao, 1993; Routledge et al., 2016; Sakai et al., 2006; Sideris et al., 2014a, 2014b; Thonstad et al., 2016). However, in an attempt to further decrease the design moments, this paper focuses on negative stiffness systems that are designed to sustain rocking motion without sliding (Bao & Konstantinidis, 2020; Dar et al., 2016; Di Sarno et al., 2019; Giouvanidis & Dimitrakopoulos, 2017a; Sextos et al., 2017; Voyagaki et al., 2018). In particular, this paper focuses on negative stiffness systems that do not exhibit hysteretic damping, thus, load and unload on the same branch. These systems do not accumulate displacements as negative stiffness hysteretic systems would. To avoid confusion, note that this paper uses the term "elastic" to describe not only *linear* elastic systems but also all systems that unload on the same branch, linear or nonlinear. Therefore, an unrestrained rocking system is a negative stiffness elastic system.
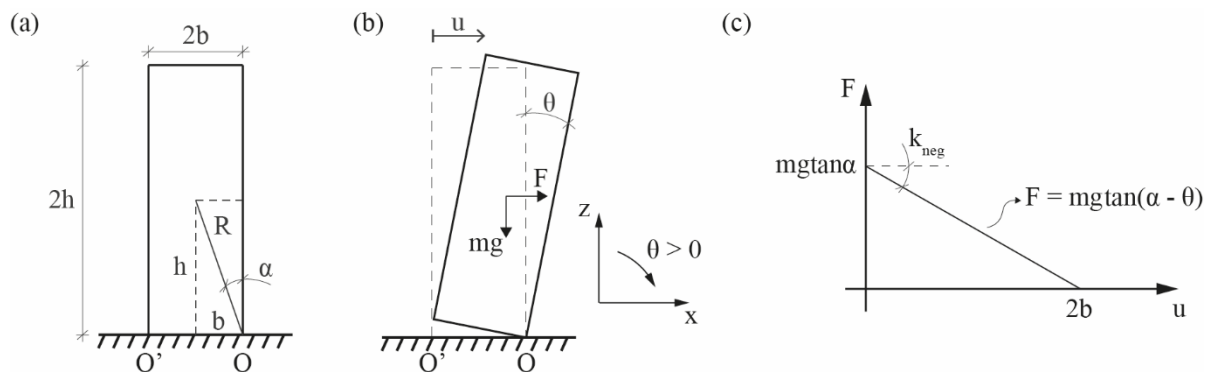
Figure 3.1. (a,b) Geometric characteristics of rigid rocking body, and (c) lateral stiffness of a rigid rocking block.

Plastic design has found its way to practice, partially because a simplified design methodology that is based on the linear elastic response spectrum has been developed. For most structures designed to yield, a time history analysis is not required and an approach based on linear elastic spectra is allowed. This is why in design codes, the hazard is defined through linear elastic response spectra. Even when a nonlinear time history analysis is performed, the

design ground motions are scaled to match the linear elastic response spectrum, implying that there is good correlation between the linear elastic and the elastoplastic oscillator. This convenient design approach was originally developed for elastoplastic systems, including the ones exhibiting post-yield hardening. It has been extended to include recentering (rocking) systems exhibiting positive post-uplift stiffness (Christopoulos et al., 2002). However, it is not applicable to *negative* stiffness rocking systems, because there is no "equivalent linear elastic system" for them (Makris & Konstantinidis, 2003). Therefore, time-consuming time history analysis is required and the linear elastic response spectra that are defined by codes become useless for such structures.

This paper suggests that there can be a simplified design method for Negative Stiffness Bilinear Elastic (NSBE) systems (Figure 3.2, right), based not on an equivalent linear elastic system, but on an equivalent *bilinear* elastic system of constant restoring force (i.e., zero post-uplift stiffness)—a Zero Stiffness Bilinear Elastic (ZSBE) system (Figure 3.3). Even though the equivalent ZSBE system does not present the convenience of a linear elastic system where the response scales proportionally to the excitation, it is useful because it reduces the dimensionality of the problem and it allows for the development of design spectra (*not* linear elastic) for negative stiffness systems. Note that this paper uses the term "spectrum" to refer not only to Biot's *linear elastic* spectrum (Biot, 1932) but also to the collective representation of the maxima of the responses of other nonlinear systems. So "spectrum" does not necessarily mean "*elastic* spectrum".
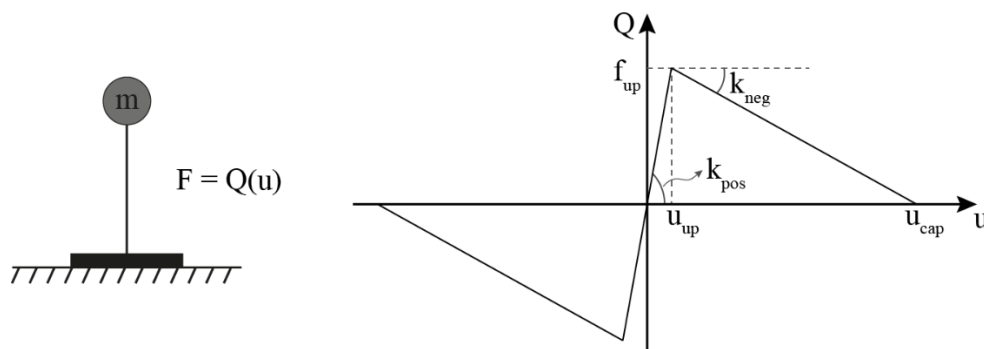
Figure 3.2. Characteristic pushover curve of the Negative Stiffness Bilinear Elastic (NSBE) system. Unloading happens on the same branch.

It should be noted that the results of this study are not directly applicable to design procedures. However, they suggest approaches that might be used to develop a rational design procedure for earthquake resistance of rocking structures.
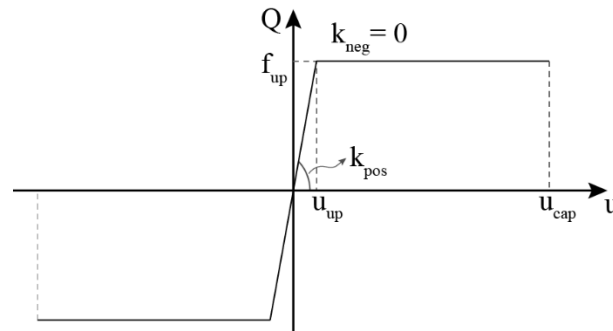
Figure 3.3. Proposed bilinear elastic system of constant restoring force (Zero Stiffness Bilinear Elastic [ZSBE]) system. Unloading happens on the same branch.

3.2. Equivalent description of rocking systems with NSBE systems

One of the challenges in designing a rocking structure is that for a given height of a flat-based unrestrained rocking structure, usually defined by architectural considerations, its displacement capacity (i.e., the displacement that would cause overturn) is coupled to its uplifting force, because they both depend on its slenderness α (or, equivalently, on its base width $2b$) (Figure 3.4). Therefore, extending the base to increase the displacement capacity of the structure causes an increase in the design forces of both the superstructure and the foundation. In an effort to isolate buildings via a rocking story, Soviet engineers (Polyakov, 1974) were the first to suggest a way to decouple the displacement capacity from the uplift acceleration: They extended the base of the block by a curved part (Figure 3.5a). This increases the displacement capacity while keeping the uplifting acceleration constant (Bachmann et al., 2019) (Figure 3.5c). The size and curvature of the extensions control the shape of the post-uplift part of the pushover curve, essentially creating a bilinear or trilinear force-deformation loop, as discussed in detail in Bachmann et al. (2019). The post-uplift stiffness can be positive or negative depending on the curvature of the extension. A similar behavior can be obtained by using a flexible restraining system (Makris & Vassiliou, 2015; Vassiliou & Makris, 2015) (Figure 3.6). For realistic values of column slenderness, steel tendons would have to be used in series with Belleville springs, so that they do not yield. Therefore, *EA* in Figure 3.6 expresses the equivalent stiffness of the restraining system (tendon and springs in series). The softening branches of the force-deformation curves in Figure 3.1 and Figure 3.4-Figure 3.6 are not perfectly linear, but they can be assumed as such by considering $\tan(\alpha-\theta) \approx \alpha - \theta$.

The idealized systems discussed above assume that the structure is rigid—a questionable assumption as the size of the blocks increases. Figure 3.7 shows the force-deformation curve of a rocking structure, when its deformability (or when the deformability of the underlying soil)

is taken into account (Acikgoz & DeJong, 2012; Anastasopoulos et al., 2010, 2012; Avgenakis & Psycharis, 2017, 2019, 2020a, 2020b; Chopra & Yim, 1985; Oliveto et al., 2003; Psycharis, 1991; Sieber et al., 2020; Truniger et al., 2015; Vassiliou et al., 2014, 2015). In this case, the pre-uplift displacement is not zero but takes a finite value u_{up}. Therefore, all systems of Figure 3.1 and Figure 3.4-Figure 3.7 can be described by an elastic bilinear system, up to a linear approximation.
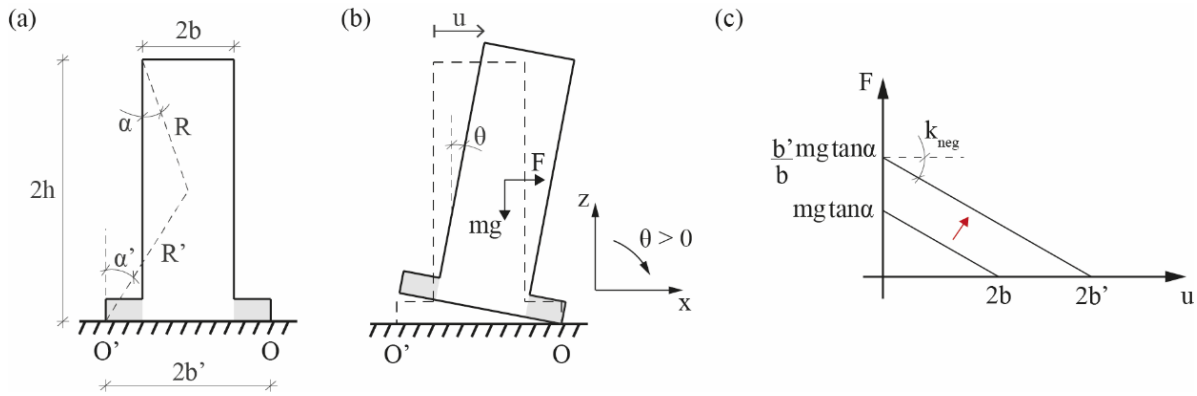
Figure 3.4. (a,b) Geometric characteristics of a flat-based rigid rocking body, and (c) lateral stiffness of a flat-based rigid rocking body.
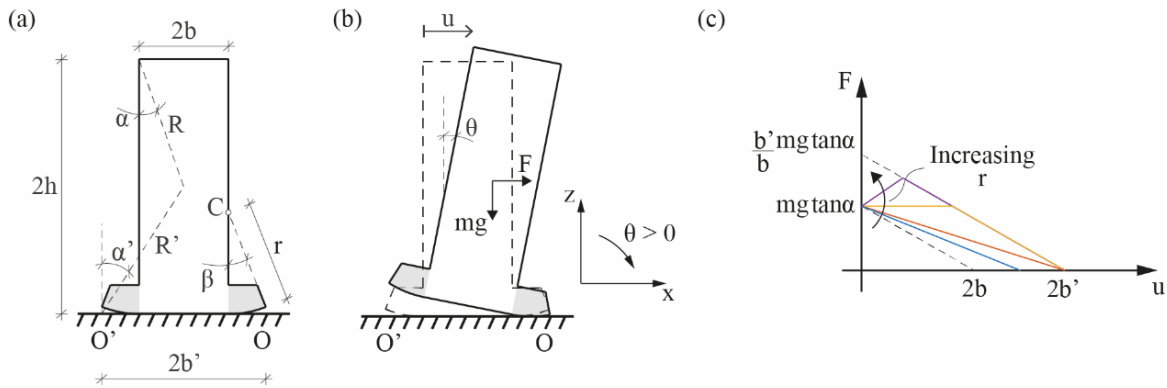
Figure 3.5. (a,b) Geometric characteristics of a curved-based rigid rocking body, and (c) lateral stiffness of a curved-based rigid rocking body.

The SDOF (Diamantopoulos & Fragiadakis, 2019) NSBE studied herein is shown in Figure 3.2 (left). It has a mass m and a restoring force described by Figure 3.2 (right). The initial positive stiffness (k_{pos}) branch represents any pre-uplift deformability. The second branch has negative stiffness (k_{neg}), and it starts at the uplift displacement (u_{up}). The system displacement capacity (u_{cap}) is defined as the displacement that results to zero restoring force, even though there are rare cases where a system can dynamically exceed this displacement

without collapsing.
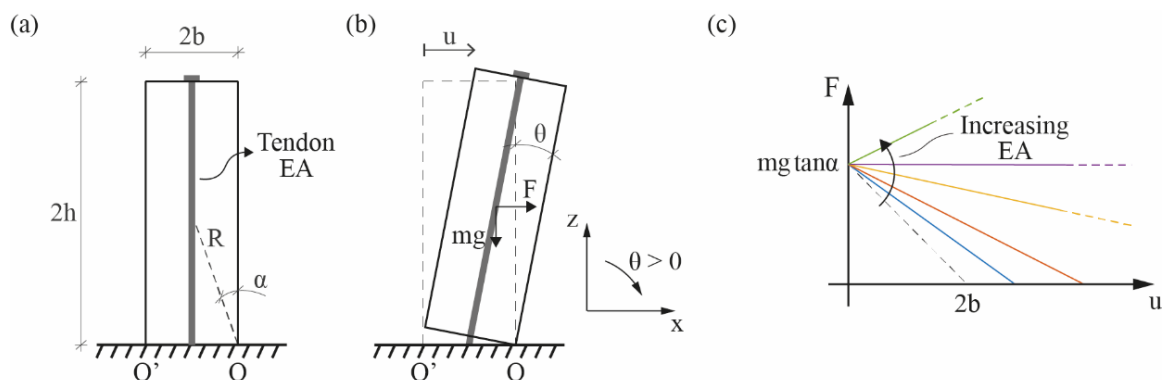
Figure 3.6. (a,b) Restrained rigid rocking body, and (c) lateral stiffness of a restrained rigid rocking body.
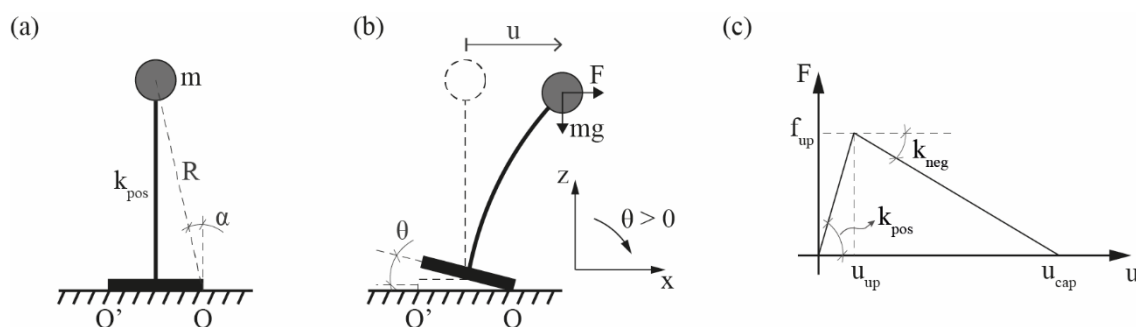
Figure 3.7. (a,b) Deformable rocking body, and (c) lateral stiffness of a deformable rocking body.

Based on its characteristic pushover curve, the oscillator's equation of motion is:

$$m \cdot \ddot{u}(t) + f_{up} \cdot \frac{u(t)}{u_{up}} = -m \cdot \ddot{u}_g(t), \quad |u(t)| \le u_{up} \tag{3.1}$$

$$m \cdot \ddot{u}(t) \pm f_{up} \cdot \left(\frac{u_{cap} - u(t)}{u_{cap} - u_{up}} \right) = -m \cdot \ddot{u}_g(t), \quad |u(t)| > u_{up} \tag{3.2}$$

The upper sign in Equation (3.2) corresponds to a positive displacement and the lower to a negative displacement.

The main source of energy dissipation in rocking structures with protected ends is impact damping—unless extra damping is provided. For this reason, this paper assumes that the proposed NSBE model dissipates energy instantaneously. When the displacement is equal to the uplift displacement (i.e., when there is impact in the case of rocking structures), the

integration is halted, and the post impact velocity is computed by a coefficient of restitution:

$$r_c = \frac{\dot{u}_{postimpact}}{\dot{u}_{preimpact}} \tag{3.3}$$

Herein, the ratio of the preimpact to postimpact velocities will be assumed equal to 0.95. The value can be considered representative of slender structures (Kalliontzis et al., 2016), which are the target systems in this paper. It is well known that energy dissipation due to impact is mainly dependent on the slenderness of the column and hence on its uplift force, f_{up}. Thus, assuming a constant r_c while varying f_{up} is a simplification of the problem. However, f_{up}, can also be varied by applying a prestress to the restraining tendon of the block. Then, at least according to Housner (1963), r_c would not change.

Notably, the system unloads on the same branch and does not dissipate energy while unloading (apart from the instantaneous energy loss when it reaches the yielding displacement). This makes it fundamentally different from the systems studied in previous studies (Pasala et al., 2013; Sarlis et al., 2013; Shu et al., 2017).

For the case of rigid systems, the parameters of the system of Figure 3.2 that make it mathematically equivalent to a variety of rocking systems are given in Table 3.1 and named $\tilde{m}$, $\tilde{f}_{up}$, and $\tilde{u}_{cap}$. Note that in order for the system of Figure 3.2 to be equivalent to these rocking systems, the excitation used for the equivalent bilinear system needs to be multiplied by a factor Γ, also given in Table 3.1. Then, the equation for the equivalent bilinear system becomes:
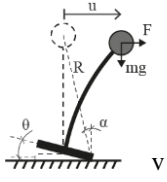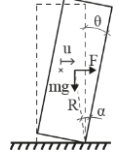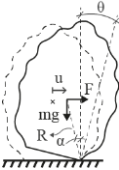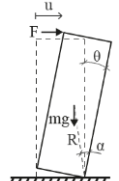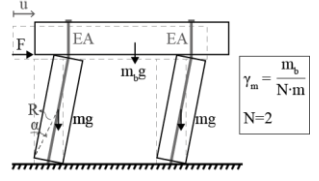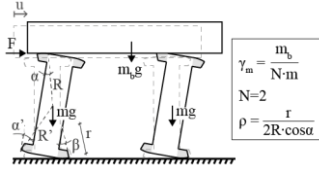
$$\tilde{m} \cdot \ddot{u}(t) + \tilde{f}_{up} \cdot \left(1 - \frac{u}{\tilde{u}_{cap}}\right) = -\Gamma \tilde{m} \cdot \ddot{u}_g(t) \tag{3.4}$$

The derivation of $\tilde{m}$, $\tilde{f}_{up}$, $\tilde{u}_{cap}$, and Γ follows from deriving the equation of motion of each rocking system, linearizing it, and matching the appropriate terms with Equations (3.1) and (3.2). The derivations are not provided herein due to space limitations, but an example is given for clarity. The equation of motion of the rectangular rocking block of Figure 3.1 for positive rotation θ is:

$$\frac{4}{3}mR^2\ddot{\theta} + mgR\sin(\alpha - \theta) = -m\ddot{u}_g R\cos(\alpha - \theta) \tag{3.5}$$

Linearizing Equation (3.5) and expressing it in terms of the top displacement (Row 4 of the Table 3.1) gives:

Table 3.1. Parameters of the bilinear elastic system for different rocking systems.

#	$\tilde{m}$	$\tilde{f}_{up}$	$\tilde{u}_{cap}$	Γ
1	m	$mg\alpha$	$R\sin\alpha$	1
2	$\dfrac{4}{3}m$	$mg\alpha$	$R\sin\alpha$	$\dfrac{3}{4}$
3	$\dfrac{I_o}{R^2}$	$mg\alpha$	$R\sin\alpha$	$\dfrac{mR^2}{I_o}$
4	$\dfrac{m}{3}$	$\dfrac{mg\alpha}{2}$	$2R\sin\alpha$	$\dfrac{3}{2}$
5	$\dfrac{(1+3\gamma_m)Nm}{3}$	$\dfrac{Nmg}{2}(1+2\gamma_m)\alpha$	$\dfrac{\left(\dfrac{1}{2}+\gamma_m\right)}{\left(\dfrac{1}{2}+\gamma_m\right)-\dfrac{EA}{mg}\alpha^2}2b$	$\dfrac{3}{2}\dfrac{(1+2\gamma_m)}{(1+3\gamma_m)}$
6	$\dfrac{(1+3\gamma_m)m}{3}$	Rolling: $\dfrac{mg}{2}(1+2\gamma_m)\alpha$	$\dfrac{2R\sin\alpha}{(1-2\rho)}\le 2R'\sin\alpha'$	$\dfrac{3}{2}\dfrac{(1+2\gamma_m)}{(1+3\gamma_m)}$

$$\frac{m}{3}\ddot{u}+\frac{mg\alpha}{2}\left(1-\frac{u}{2R\sin\alpha}\right)=-\frac{3}{2}\left(\frac{m}{3}\right)\ddot{u}_g \tag{3.6}$$

Matching the terms of Equations (3.6) and (3.2) for $u_{up}=0$ requires that $\tilde{m}=m/3$, $\tilde{f}_{up}=mg\alpha/2$, $\tilde{u}_{cap}=2R\sin\alpha$, and $\Gamma=3/2$.

If a deformable system is studied, assuming large displacements but small deformations, the parameters $\tilde{m}$ and Γ can be picked from the same Table 3.1, but $\tilde{f}_{up}$, $\tilde{u}_{cap}$, and $\tilde{u}_{up}$ should be determined from a nonlinear static analysis.

3.3. Equal displacement and equal energy rules: positive versus negative stiffness systems

3.3.1. Positive stiffness systems

Time history analysis is widely believed to be the most accurate method for the analysis and design of structures. However, despite the increase of the available computational power, it has not replaced simplified approaches based on linear elastic spectra, at least for the vast majority of civil engineering structures. The reason is that linear elastic-spectrum-based methods (a) are often faster and adequately accurate, (b) are needed for preliminary design, and (c) can serve to quickly validate the results of time history analysis.

For *positive* stiffness inelastic structures, the most widely used simplified method is the one based on the so called $R\mu T$ relations, first appearing in the early work of Veletsos & Newmark (1960). The displacement of the nonlinear system $u_{inelastic}$ is computed based on the displacement of a system with the same initial period but infinite strength, that is, a linear elastic system, $u_{elastic}$. There have been numerous papers (Miranda, 2001; Tsiavos et al., 2017, and references therein) attempting to determine the ratio of interest (γ_{PS}):

$$\gamma_{PS} = \frac{u_{inelastic}}{u_{elastic}} \tag{3.7}$$

Some of the most widespread equations to predict γ_{PS} are the "Equal Displacement rule" (i.e., the elastic and the inelastic system exhibit the same maximum displacement, $\gamma_{PS} = 1$, applicable to relatively soft systems, Figure 3.8, left) and the "Equal Energy rule" (i.e., the monotonic loading curves of the elastic and inelastic system produce the same work, $\gamma_{PS} = \mu / \sqrt{2\mu - 1}$, applicable to stiffer systems, Figure 3.8, right).

This correlation between elastic and positive stiffness inelastic systems proved useful for the design of positive stiffness systems, not only because elastic analysis is easier but also because the elastic system is a *two* parameter system with its response depending solely on its period (T) and damping ratio (ζ). In fact, for structures without supplemental damping, the dominant parameter that defines the seismic response of elastic systems is their period. This has allowed for a convenient computation of the response of yielding structures through the nicely visualizable *linear elastic* spectrum.
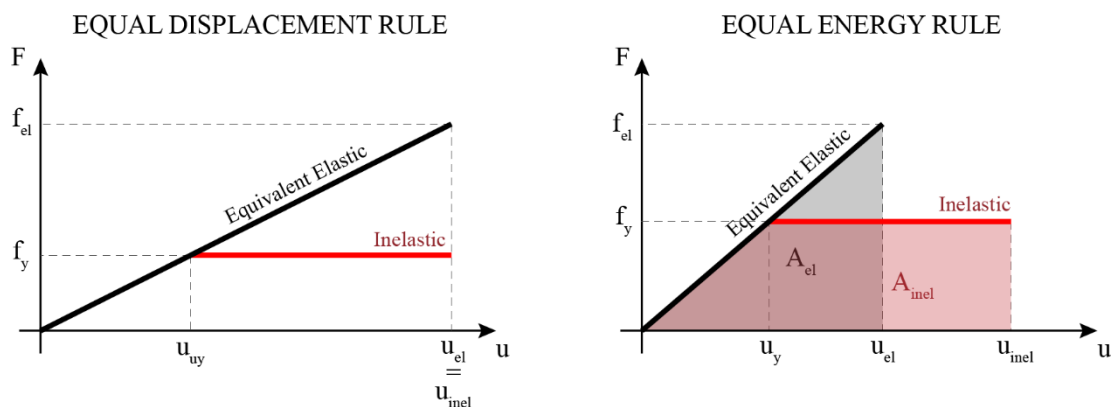
Figure 3.8. Equal Displacement and Equal Energy rules for *positive stiffness* hysteretic systems.

3.3.2. Negative stiffness systems

Using the elastic spectrum for the analysis of *negative* stiffness structures would have been very convenient as engineers are used to it and as elastic spectra for design already exist and are included in codes. However, this is not feasible for NSBE systems, because their response has been proven to be uncorrelated to any "equivalent" elastic system (Makris & Konstantinidis, 2003).

This section defines Equal Displacement and Equal Energy rules that are applied not on an equivalent *elastic* system but on an equivalent ZSBE system (Figure 3.3). We refer to it as "equivalent," but this does not imply that it is *linear* elastic. It is a *bilinear* elastic system with finite pre-uplift displacement and zero post-uplift stiffness system.

To correlate the responses of the NSBE and of the ZSBE, the quantity of interest is the ratio:

$$\gamma = \frac{u_{dem,NS}}{u_{dem,ZS}} \tag{3.8}$$

where $u_{dem,NS}$ and $u_{dem,ZS}$ are the maximum displacements of the NSBE and ZSBE systems, respectively.

The Equal Displacement rule assumes that the NSBE and the equivalent ZSBE system will experience the same maximum displacement (Figure 3.9, left):

$$u_{dem,NS} = u_{dem,ZS} \tag{3.9}$$

and

$$\gamma_{ED} = 1 \tag{3.10}$$
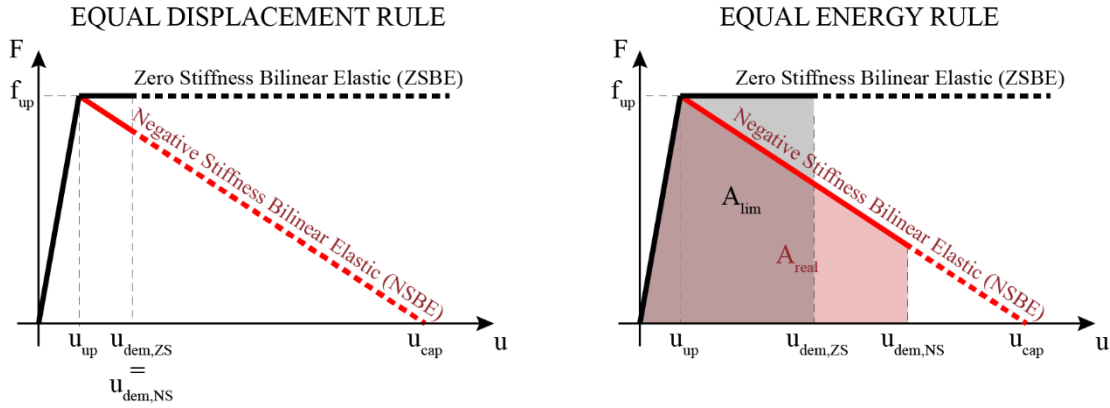
Figure 3.9. Equal Displacement and Equal Energy rules for Negative Stiffness Bilinear Elastic (NSBE) systems.

The Equal Energy rule assumes that the monotonic loading curves of the NSBE and the ZSBE system will produce the same work, that is, the two shaded areas in Figure 3.9 (right) are equal. Based on Figure 3.9, one can compute that the Equal Energy rule gives:

$$\gamma_{EE} = \frac{u_{dem,NS}}{u_{dem,ZS}} = \frac{u_{cap}}{u_{dem,ZS}} - \sqrt{\frac{\left(u_{cap} - u_{up}\right)}{u_{dem,ZS}} \cdot \frac{\left(u_{cap} - 2 \cdot u_{dem,ZS} + u_{up}\right)}{u_{dem,ZS}}} \tag{3.11}$$

Note that $\lim\limits_{\frac{u_{cap}}{u_{dem,ZS}} \to \infty} \gamma_{EE} = 1$, meaning that the Equal Displacement rule is an approximation

of the Equal Energy rule for small values of $\dfrac{u_{dem,NS}}{u_{cap}}$, that is, when the system is away from

collapse. Therefore, the Equal Displacement rule approximates the Equal Energy rule. This is in contrast to the yielding systems, where each rule applies for different period ranges.

3.4. Response of rigid-negative stiffness systems to recorded ground motions

This section explores the accuracy of the rules defined in Section 3.3, when applied to NSBE systems that present minimal pre-uplift displacement, that is, systems with small u_{up}. The influence of pre-uplift displacement will be studied in Section 3.5.

3.4.1. FEMA P695 ground motions

There is no consensus in the engineering community on what ground motions should be used

in time history analysis. Several approaches exist including using recorded (scaled or unscaled), artificial, or synthetic excitations. In this paper, we choose to use the three sets of ground motions proposed by FEMA P695 (FEMA, 2009) (far-field, near-field pulse-like, and near-field no pulse-like) only as a means of illustrating our argument, without taking stance on the debate around ground motion selection. The three sets contain 14, 14, and 21 ground motions, respectively. According to FEMA P695, the far-field set contains 22 ground motions (including #18, Cape Mendocino, Rio Dell Overpass record). However, this was not available in the PEER ground motion database and, thus, was not included in this study. Because this paper examines a planar model, it uses each horizontal component of each ground motion as an independent excitation. Therefore, in total, there are 98 ground motions. It is evident that any ground motion selection method based on the response of an elastic system is in principle not applicable in the case of the NSBE oscillator, as they are uncorrelated (Makris & Konstantinidis, 2003). More information on the FEMA P695 ground motions can be found in FEMA (2009).

3.4.2. Median and 90th percentile displacement spectra

The design of structural systems does not involve a single excitation but a set of excitations that characterize the seismic hazard at a given site. Thus, this paper compares NSBE and ZSBE not by comparing their responses to individual ground motions but by comparing the statistics of the responses to ensembles of ground motions. This statistical rather than motion-by-motion comparison of an approximate and a refined method leads to smoothened results. It is an easier to pass validation test for any seismic design method. A statistical comparison was also followed, for example, by Riddell & Newmark (1979) to produce inelastic spectra for yielding structures, or by Chopra (2012) (section 20.8.3) to evaluate the accuracy of modal pushover analysis. This paper assesses the Equal Displacement and Equal Energy rules by focusing on the median and the 90th percentile displacement spectra for six variations of the near-field pulse-like, near-field no pulse-like, and far-field FEMA P695 sets: (a) scaled so that their PGA is equal to $0.5\overline{\mathrm{PGA}}$, $1.0\overline{\mathrm{PGA}}$, or $2.0\overline{\mathrm{PGA}}$ and (b) scaled so that their PGV is equal to $0.5\overline{\mathrm{PGV}}$, $1.0\overline{\mathrm{PGV}}$, or $2.0\overline{\mathrm{PGV}}$. $\overline{\mathrm{PGA}}$ and $\overline{\mathrm{PGV}}$ are defined as:

$$\overline{\mathrm{PGA}} = \underset{i=1...N}{\mathrm{median}}\left(\sqrt{\mathrm{PGA}_{i_x} \cdot \mathrm{PGA}_{i_y}}\right) \tag{3.12}$$

$$\overline{\mathrm{PGV}} = \underset{i=1...N}{\mathrm{median}}\left(\sqrt{\mathrm{PGV}_{i_x} \cdot \mathrm{PGV}_{i_y}}\right) \tag{3.13}$$

where *N* is the number of ground motions and *x* and *y* are their two components.

The number of ground motions included in each set of excitations would be considered rather low to get an accurate estimate of the 90th percentile of the response. Therefore, the 90th percentile results are reported herein only to provide insight into the dispersion of the results—something that the median response cannot provide on its own. The motion-to-motion variability of the response of rocking oscillator is a subject of future work, and it is required to properly define safety factors for design.

3.4.3. Equal Displacement rule for NSBE systems

Figure 3.10-Figure 3.12 plot the median and 90th percentile of the maximum displacement of the NSBE stiffness system as a function of its strength normalized by the system's self-weight (f_{up}/mg) for several values of the displacement capacity. The uplift displacement is set to $u_{up} = 5 \times 10^{-4}$ m to study quasi-rigid systems. Figure 3.10 plots results for the near-field pulse-like FEMA P695 set, whereas Figure 3.11 and Figure 3.12 for the near-field no pulse-like and far-field sets, respectively. For reasons of plot clarity, each line is plotted only for $f_{up}/mg > (f_{up}/mg)_{crit}$, where $(f_{up}/mg)_{crit}$ is the maximum uplift strength for which there is failure.

In terms of median response, Figure 3.10–Figure 3.12 show that:

(a) As long as the system is not close to failure, the displacement only loosely depends on the displacement capacity. So, when the system is not close to failure, instead of computing a different spectrum for each displacement capacity, one can compute the spectrum for the ZSBE system (i.e., for an NSBE with $u_{cap} \rightarrow \infty$) and use it to calculate the displacement demand on any NSBE of the same strength. This forms a generalization of the *Equal Displacement rule for rocking structures* described in Reggiani Manzo & Vassiliou (2019).

(b) As the system gets closer to collapse, the "Equal Displacement rule" does not apply and is unconservative: Systems with smaller displacement capacity exhibit larger displacements than the ones with larger displacement capacity. Moreover, close to failure, the slope of the spectrum increases dramatically, that is, a small decrease of the system strength would lead to a tremendous increase of the maximum displacement. As in the case of free rocking structures (Reggiani Manzo & Vassiliou, 2019), this trend dictates that a rational design of a negative stiffness system would require that this steep part of the spectrum be avoided, because an earthquake slightly stronger than the design

one would cause a tremendous increase in displacement. Therefore, the Equal Displacement rule is more accurate where it is actually needed: in the rational design region.
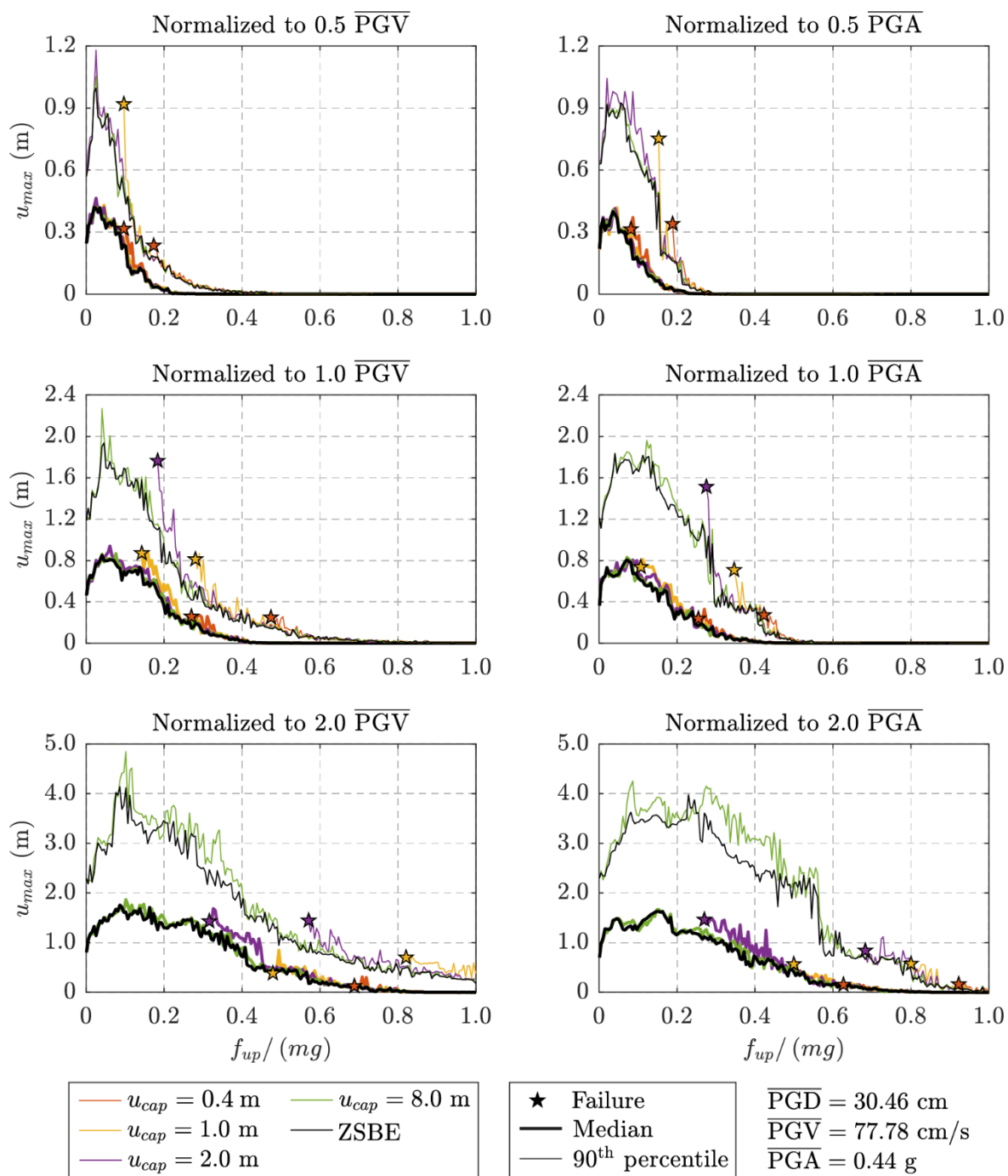
Figure 3.10. Median displacement spectra for near-field pulse-like record set.
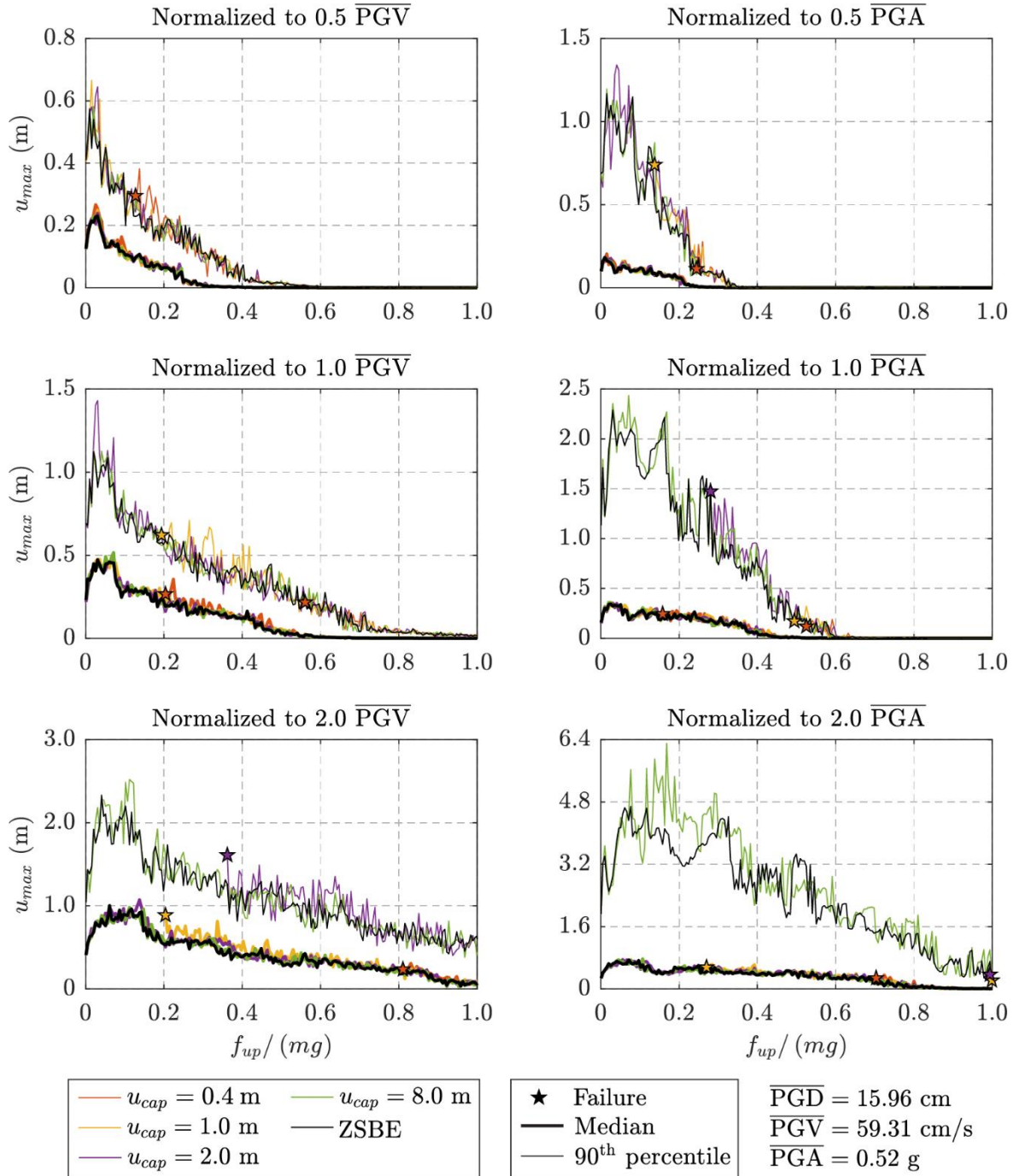
Figure 3.11. Median displacement spectra for near-field no pulse-like record set.

(c) The form of the spectrum for all three sets of ground motion presents a repetitive pattern:

    i. For zero strength ($f_{up} = 0$), the maximum displacement (u_{max}) reaches a finite value. For spectra of individual ground motions, this value is PGD.

    ii. As the strength increases, the maximum displacement initially increases and reaches a maximum of 1.5 to 2.5 times the PGD. Therefore, the maximum

displacement that a ground motion can induce to any negative stiffness elastic bilinear system is 1.5–2.5 times the PGD.

iii. Further increase of the strength leads to a decrease of the maximum displacement.
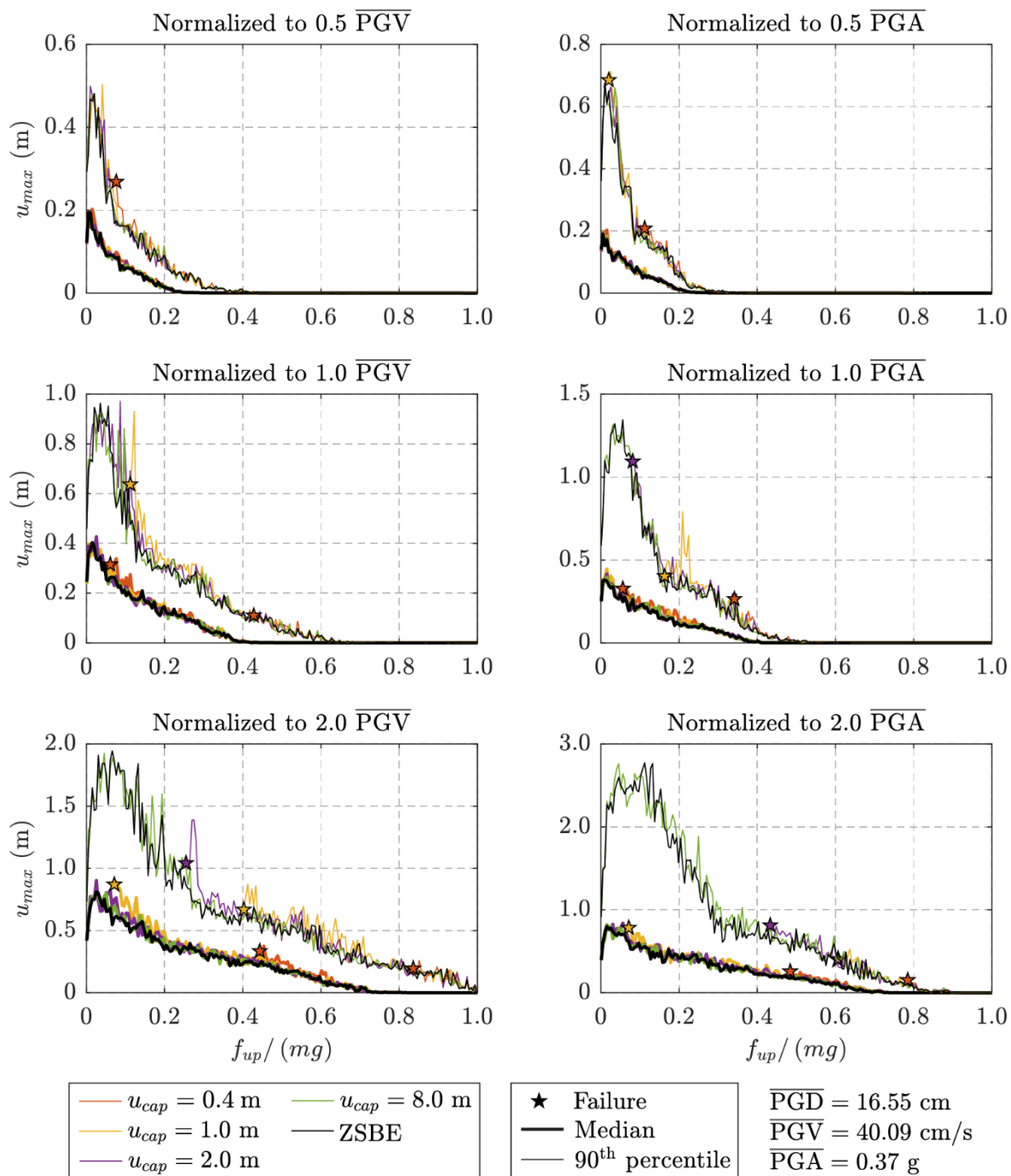
Figure 3.12. Median displacement spectra for far-field record set.

The 90th percentile spectra are often much larger than the median ones, especially for the design scenario where the ground motions are scaled to have the same PGA. This implies that the motion-to-motion variability is relatively large, especially when PGA is used as an intensity measure. This is consistent with the work presented in previous studies (Dimitrakopoulos & Paraskeva, 2015; Giouvanidis & Dimitrakopoulos, 2018; Kavvadias et al., 2017; Pappas et al., 2017; Psycharis et al., 2013) on ground motion intensity measures for rocking structures. The exact quantification of this variability would require more ground motions and lies beyond the scope of this work.

Figure 3.13 offers the displacement of a NSBE oscillator as function of its strength f_{up} for a selection of individual FEMA P695 ground motions. One can observe that the maximum displacement seems independent of the displacement capacity, even if one does not focus on smoothened statistical spectra, but on individual ground motions as well.

The above observations also hold for $u_{up} = 0.005$ and 0.05 m, but the plots are not shown herein due to space limitations.

3.4.4. Equal energy rule for NSBE systems

Figure 3.10–Figure 3.13 show that the Equal Displacement rule is on the unconservative side, especially as the displacement demand approaches the capacity. To examine the performance of the Equal Energy rule, Figure 3.14–Figure 3.16 present the median and 90th percentile of the maximum displacement $u_{\max}$ divided by the factor γ_{EE} (Equation (3.11)) as a function of the system normalized strength f_{up}/mg. The plots are constructed for several values of displacement capacity u_{cap} and for uplift displacement $u_{up} = 5 \times 10^{-4}$ m. Figure 3.14 is plotted for the near-field pulse-like set, whereas Figure 3.15 and Figure 3.16 for the near-field no pulse-like and far-field sets, respectively. According to Equation (3.11), the factor γ_{EE} can only be calculated for systems that satisfy:

$$u_{dem,ZS} \leq \frac{u_{cap} + u_{up}}{2} \approx \frac{u_{cap}}{2} \qquad (3.14)$$

A larger value of $u_{dem,ZS}$ would lead to failure of the negative stiffness system.

The curves for the three sets of recorded ground motions almost collapse to a unique curve, the one that represents the ZSBE system. Notably, this happens for all six different scaling of the ground motions. Hence, the Equal Energy rule gives a good estimate of the maximum displacement of NSBE systems with a finite displacement capacity. Comparing the

Equal Displacement to the Equal Energy rule, the former is simpler, but the latter is overall more conservative, especially for larger displacements. Therefore, unless there is a reason to opt for simplicity, the use of the Equal Energy rule is proposed.
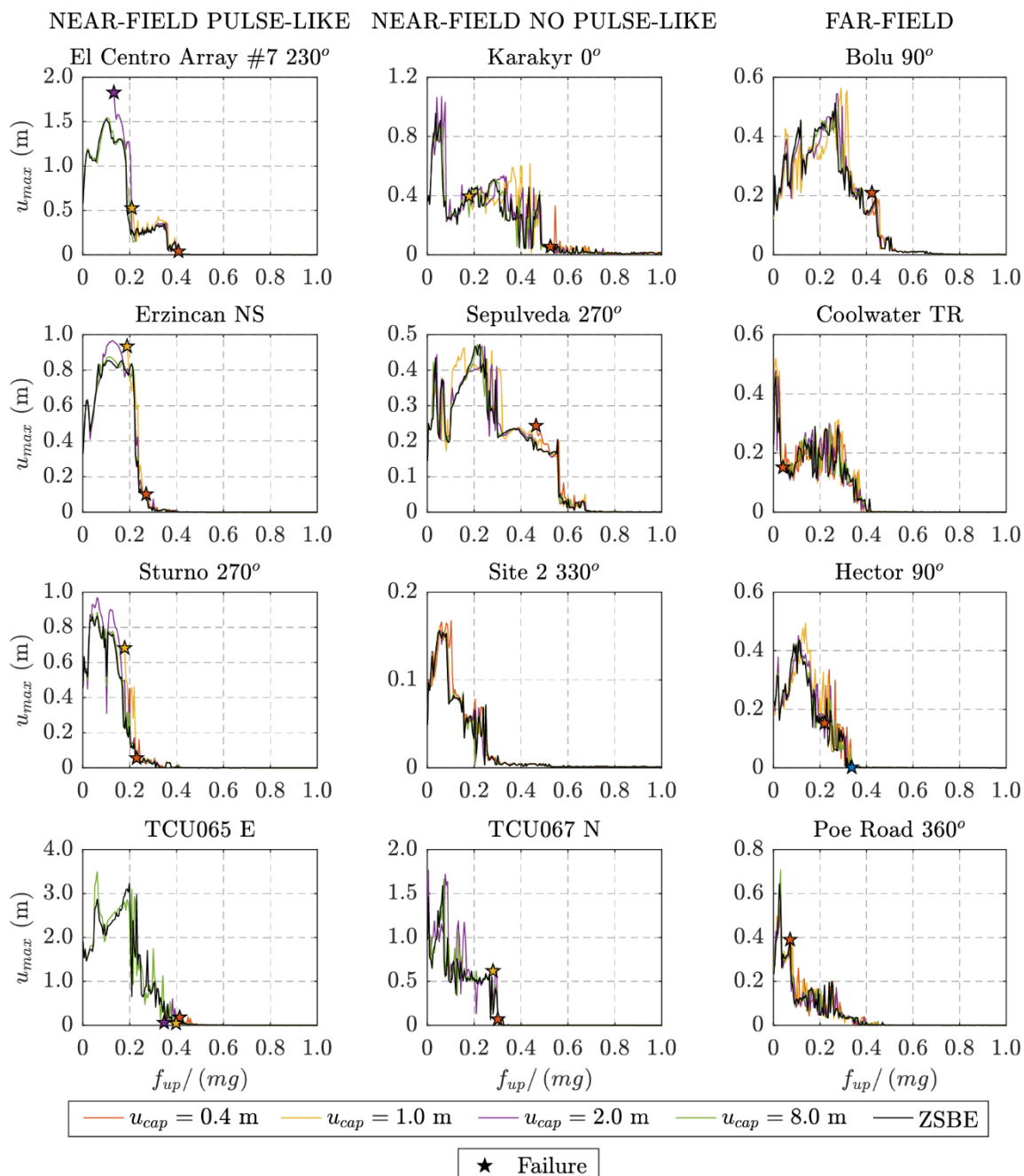
Figure 3.13. Displacement of a Negative Stiffness Bilinear Elastic (NSBE) oscillator as function of its strength f_{up}.
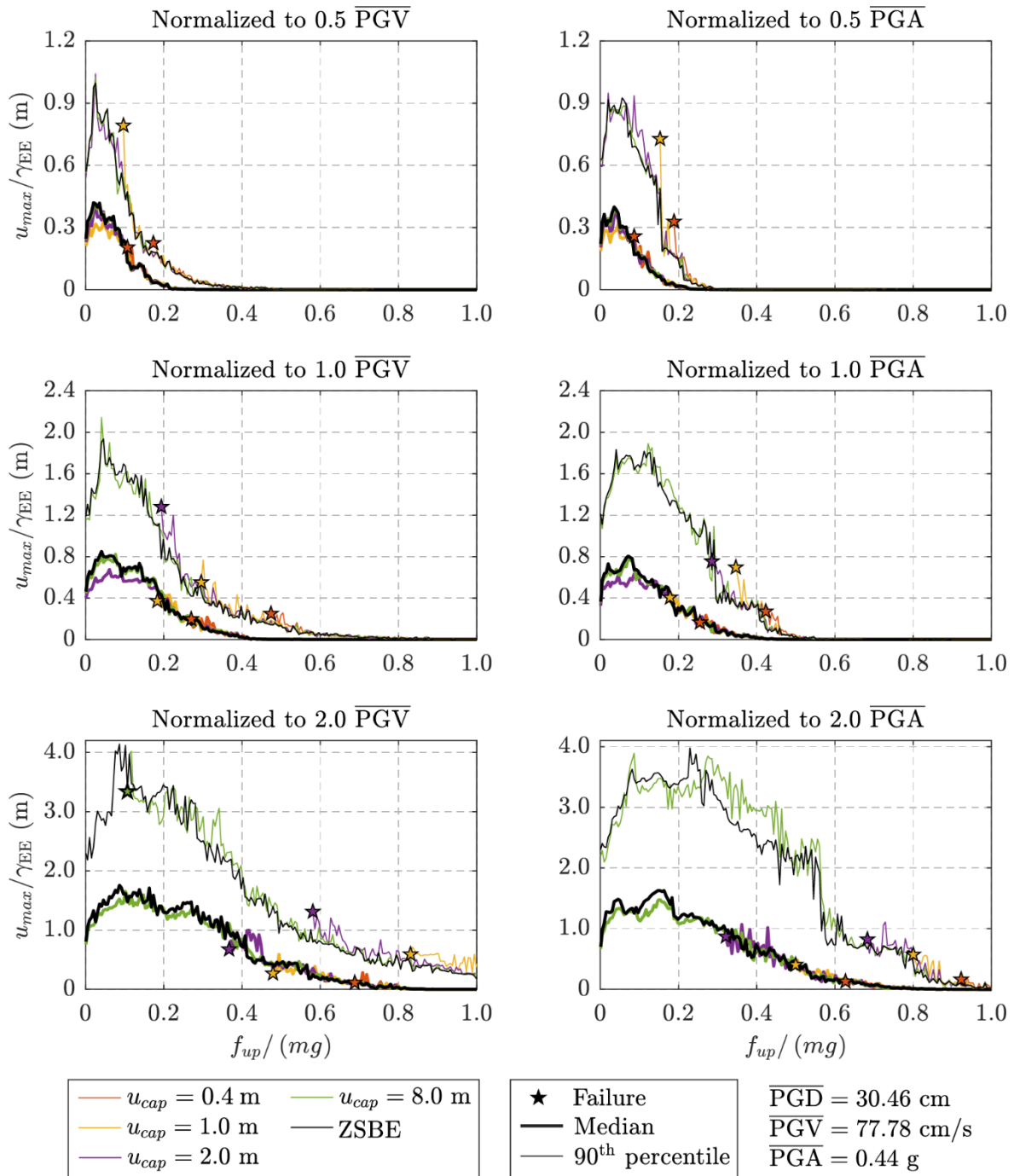
Figure 3.14. Median displacement spectra normalized by *γ_EE* for near-field pulse-like record set.

3.4.5. Design Example

This subsection uses a case study to illustrate a design method based on the Equal Energy and Equal Displacement rules. The method is applied for the design of a rocking bridge equipped with a restraining system that increases the displacement capacity, while keeping the post-uplift stiffness negative (Table 3.1, Row 5 and Makris & Vassiliou (2015)). The geometry of the

bridge is typical of overpass bridges: The columns have a height of 9.6 m and a diameter of 1.6 m, whereas the deck is much heavier than the columns ($\gamma_m \to \infty$). Planar rocking (i.e., one directional excitation) is assumed as a first approximation (even though this has been proven unconservative (Vassiliou, 2018; Vassiliou et al., 2017)). Before the results presented herein find their way to practice, 3D models should be experimentally validated and studied under bidirectional excitation (the vertical excitation has been shown to be insignificant in rocking
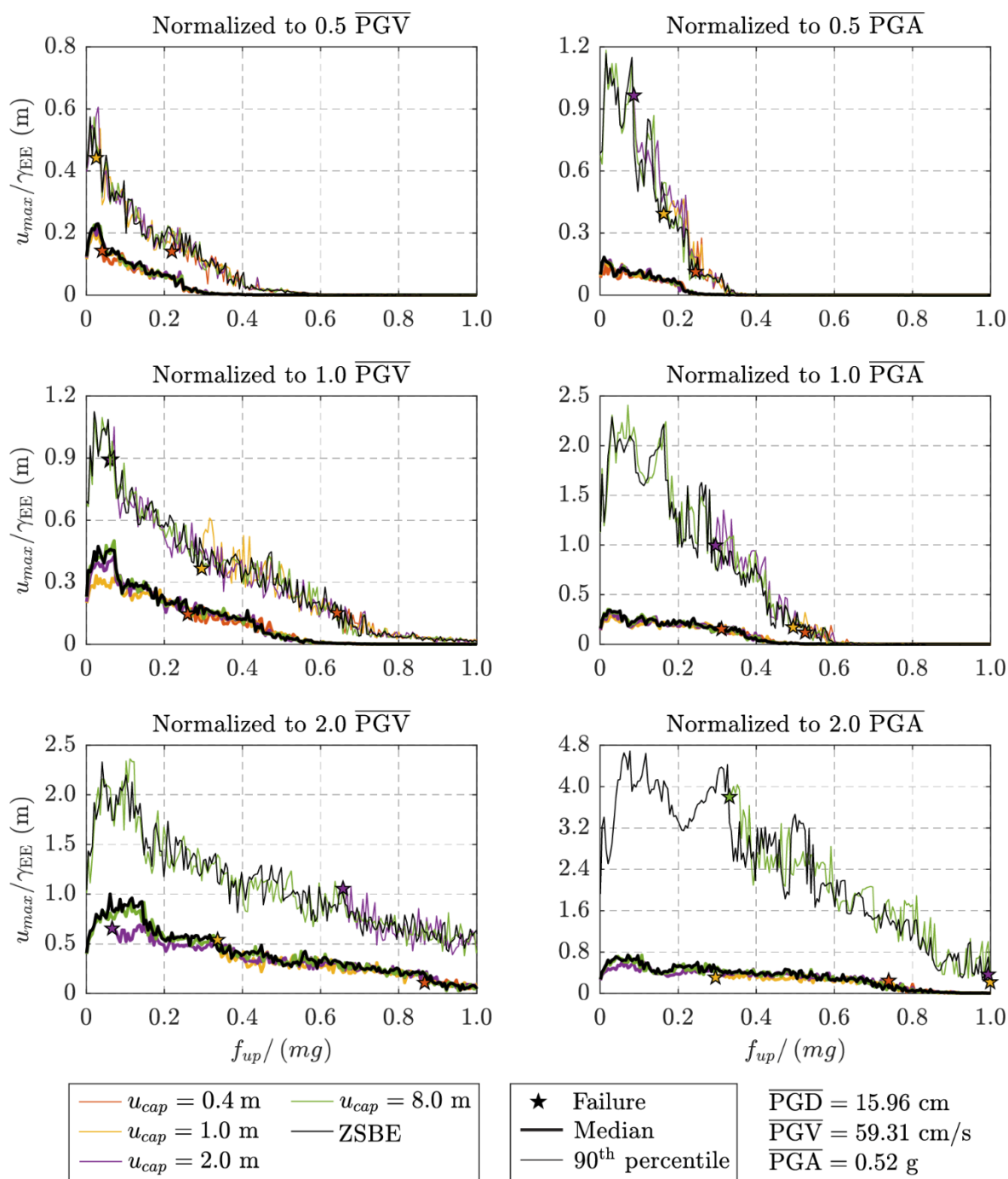
Figure 3.15. Median displacement spectra normalized by γ_{EE} for near-field no pulse-like record set.

motion (Linde et al., 2020; Makris & Kampas, 2016)). Alternatively, the model can be assumed to describe bridges that are only allowed to rock in one dimension. The design quantity of interest is the displacement capacity of the bridge, so that the restraining system is designed accordingly.
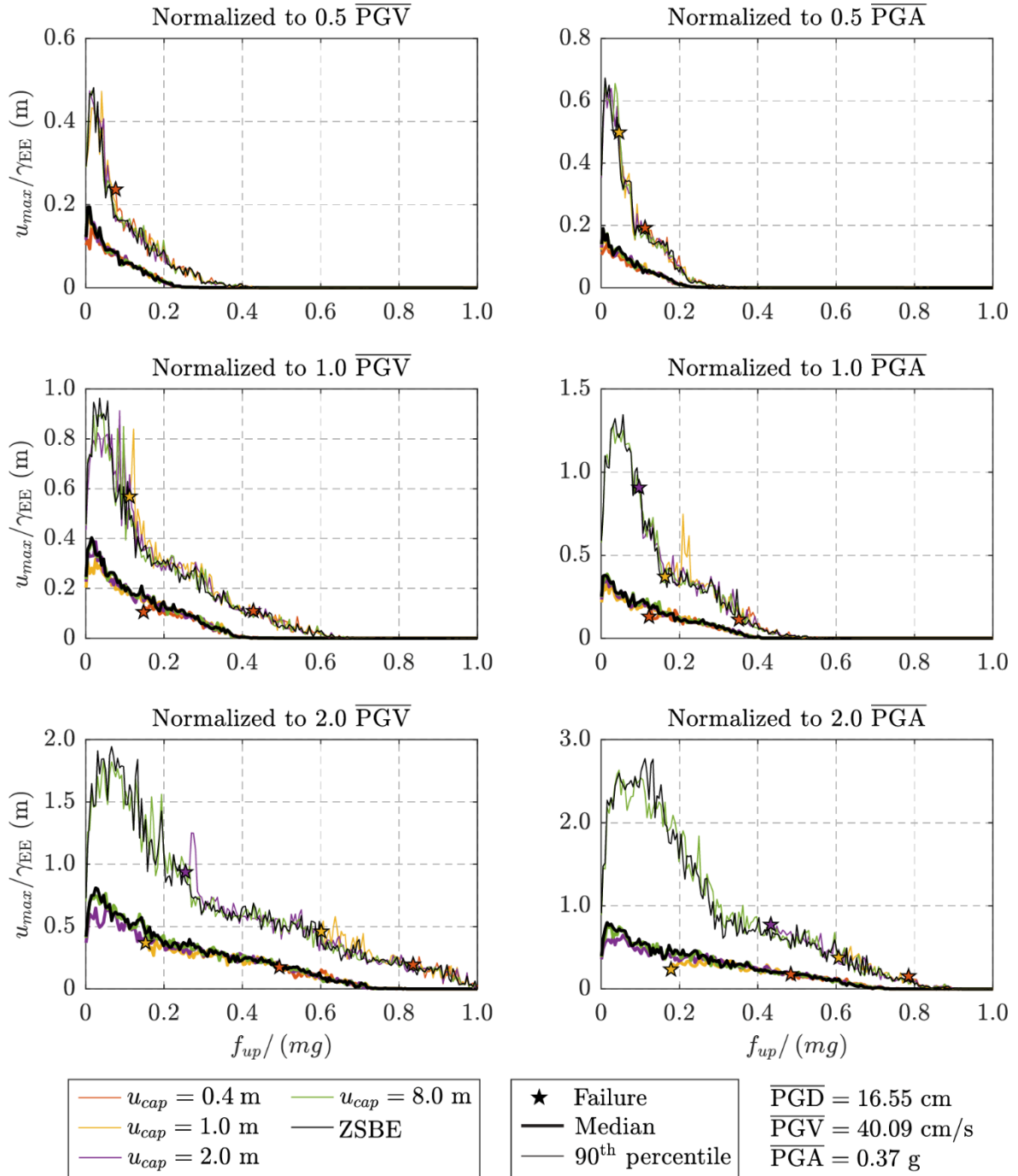
Figure 3.16. Median displacement spectra normalized by γ_{EE} for far-field record set.

Based on Row 5 of Table 3.1 and for $\gamma_m \to \infty$, the properties of the equivalent negative stiffness

system are $\tilde{f}_{up} / \tilde{m}g = \alpha$, $\Gamma = 1$, $u_{cap} = \dfrac{1}{1 - \dfrac{N \cdot EA}{m_b} \alpha^2} 2b$, where N is the number of columns, EA is

the axial stiffness of the restraining system, m_b is the mass of the deck, and α and $2b$ are the slenderness and the width of the columns. Then, the design steps are:

(a) Calculate the normalized yielding strength of the system ($f_{up}/(mg)$). If the restraining tendon is not prestressed, this depends solely on the column geometry and is equal to α.

(b) Obtain the displacement demand for the infinite capacity curve ($u_{dem,ZS}$) using the ZSBE curves of Figure 3.10–Figure 3.12 or Figure 3.14–Figure 3.16.

(c) Calculate the design displacement capacity of the system, as:

$$u_{cap} = FS \cdot u_{dem,NS} = FS \cdot \gamma \cdot u_{dem,ZS} \tag{3.15}$$

in which FS is a safety factor and γ is defined by Equation (3.8). This section evaluates two alternative approaches: One based on the Equal Displacement ($\gamma = 1$) and one on the Equal Energy ($\gamma = \gamma_{EE}$, Equation (3.11)) rule. In both cases, the median response is used.

Table 3.2–Table 3.7 offer the design values when the two rules are applied on the three sets of ground motions under the six different scaling, described in previous sections. u_{cap} is the capacity required for a FS = 2.5 (Equation (3.15)). For a system with a displacement capacity u_{cap}, $u_{dem,TH}$ is the median displacement demand of each set computed with time history analysis. $u_{dem,EE}$ and $u_{dem,ED}$ are equal to $\gamma_{ED} \cdot u_{dem,ZS}$ and $\gamma_{EE} \cdot u_{dem,ZS}$, respectively. $u_{dem,ZS}$ is the median response of the ZSBE system. The error is defined as $error = (u_{dem,ED/EE} - u_{dem,TH})/u_{dem,TH}$.

Table 3.2. Near-field pulse-like: Equal Displacement rule ($\gamma = 1$).

	0.5$\overline{PGA}$	1.0$\overline{PGA}$	2.0$\overline{PGA}$	0.5$\overline{PGV}$	1.0$\overline{PGV}$	2.0$\overline{PGV}$
u_{cap} (m)	1.60	1.60	3.46	1.60	1.60	3.65
$u_{dem,TH}$ (m)	0.030	0.512	1.580	0.056	0.603	1.621
$u_{dem,ED}$ (m)	0.034	0.472	1.382	0.051	0.592	1.459
Error (%)	14.78	-7.67	-12.49	-10.08	-1.80	-10.01

The Equal Displacement rule in general underpredicts the result, with a maximum underprediction error of 18%. The Equal Energy rule is conservative in 14/18 cases. It is

generally more conservative for sets of stronger excitations. Its maximum underprediction error is 9%. None of the rules led to collapse, because of the safety factor FS = 2.5.

Table 3.3. Near-field no pulse-like: Equal Displacement rule ($\gamma = 1$).

	0.5$\overline{PGA}$	1.0$\overline{PGA}$	2.0$\overline{PGA}$	0.5$\overline{PGV}$	1.0$\overline{PGV}$	2.0$\overline{PGV}$
u_{cap} (m)	1.60	1.60	1.60	1.60	1.60	1.83
$u_{dem,TH}$ (m)	0.082	0.201	0.435	0.065	0.264	0.754
$u_{dem,ED}$ (m)	0.080	0.237	0.423	0.068	0.237	0.731
Error (%)	-2.22	17.81	-2.79	3.79	-10.33	-3.08

Table 3.4. Far-field: Equal Displacement rule ($\gamma = 1$).

	0.5$\overline{PGA}$	1.0$\overline{PGA}$	2.0$\overline{PGA}$	0.5$\overline{PGV}$	1.0$\overline{PGV}$	2.0$\overline{PGV}$
u_{cap} (m)	1.60	1.60	1.60	1.60	1.60	1.60
$u_{dem,TH}$ (m)	0.037	0.162	0.536	0.031	0.169	0.447
$u_{dem,ED}$ (m)	0.039	0.165	0.462	0.030	0.152	0.449
Error (%)	5.79	1.63	-13.84	-2.65	-10.56	0.41

Table 3.5. Near-field pulse-like: Equal Energy rule ($\gamma = \gamma_{EE}$).

	0.5$\overline{PGA}$	1.0$\overline{PGA}$	2.0$\overline{PGA}$	0.5$\overline{PGV}$	1.0$\overline{PGV}$	2.0$\overline{PGV}$
u_{cap} (m)	1.60	1.60	4.32	1.60	1.85	4.56
$u_{dem,TH}$ (m)	0.030	0.512	1.514	0.056	0.575	1.669
$u_{dem,ED}$ (m)	0.034	0.576	1.728	0.051	0.740	1.823
Error (%)	16.03	12.59	14.14	-8.61	28.60	9.27

Table 3.6. Near-field no pulse-like: Equal Energy rule ($\gamma = \gamma_{EE}$).

	0.5$\overline{PGA}$	1.0$\overline{PGA}$	2.0$\overline{PGA}$	0.5$\overline{PGV}$	1.0$\overline{PGV}$	2.0$\overline{PGV}$
u_{cap} (m)	1.60	1.60	1.60	1.60	1.60	2.28
$u_{dem,TH}$ (m)	0.082	0.201	0.435	0.065	0.264	0.716
$u_{dem,ED}$ (m)	0.082	0.258	0.501	0.069	0.258	0.914
Error (%)	0.36	28.13	15.25	6.09	-2.47	27.68

Table 3.7. Far-field: Equal Energy rule ($\gamma = \gamma_{EE}$).

	0.5$\overline{PGA}$	1.0$\overline{PGA}$	2.0$\overline{PGA}$	0.5$\overline{PGV}$	1.0$\overline{PGV}$	2.0$\overline{PGV}$
u_{cap} (m)	1.60	1.60	1.60	1.60	1.60	1.60
$u_{dem,TH}$ (m)	0.037	0.162	0.536	0.031	0.169	0.447
$u_{dem,ED}$ (m)	0.039	0.174	0.559	0.030	0.159	0.540
Error (%)	7.11	7.48	4.41	-1.73	-5.87	20.78

3.5. Evaluation of the influence of the pre-uplift deformability u_{up}

Sections 3.4.3–3.4.4 (Figure 3.10–Figure 3.16) focused on the response of a system with an initial quasi-rigid behavior ($u_{up} = 5 \times 10^{-4}$ m). Assuming that the bridge that was studied as a case study in Section 3.4.5 has a fundamental period of 0.3 s, the uplift displacement would be 4×10^{-3} m, which is one order of magnitude larger—and bridges of this or larger size could be even more flexible and have a larger u_{up}. To study the influence of pre-yield deformability, Figure 3.17 plots the displacement of infinite displacement capacity systems for different values of $u_{up} = 5 \times 10^{-4}$ m, 5×10^{-3} m and 5×10^{-2} m. One can observe that:

(a) For small values of uplift strength (f_{up}), u_{up} does not influence the maximum displacement. A limit cannot be clearly established, as it depends on the ground motion set, on its scaling, and on u_{up} itself. Stronger ground motions tend to increase the region in which u_{up} becomes insignificant.

(b) For all ground motion sets and all scaling considered in this study, the response of the $u_{up} = 5 \times 10^{-4}$ m and the $u_{up} = 5 \times 10^{-3}$ m curves are essentially the same, when f_{up}/mg < 0.2. Therefore, the results presented in the case study of Section 3.4.5 are valid (f_{up}/mg $= \tan(1.6/9.6)$), even though a u_{up} one order of magnitude smaller was used.

Another and, maybe, easier to use criterion that defines the region in which u_{up} can be dropped from the analysis is based solely on the displacement predicted by the quasi-rigid analysis: For all the cases considered in this study, whenever the displacement prediction of the quasi-rigid analysis is larger than 0.5 m, all lines practically collapse to one. Therefore, a rigid base analysis predicting $u_{max} > 0.5$ m can be trusted, at least for structures that have $u_{up} <$ 5 cm.

3.6. Conclusions

Rocking systems (free, restrained, or with curved extensions) that exhibit negative post-uplift stiffness can be described as elastic bilinear oscillators with a negative stiffness second branch, herein denoted as NSBE. This description can also take into account their pre-uplift deformability. This paper focused on the seismic behavior of such bilinear systems by using sets of recorded ground motions.

It was found that the strength of the bilinear oscillator is the governing parameter for its response. The slope of the second branch of the bilinear system that controls the displacement

capacity does not influence the response, if the oscillator is not close to collapse. The uplift displacement does not influence the response either, at least for relatively large maximum displacements (larger than 50 cm).
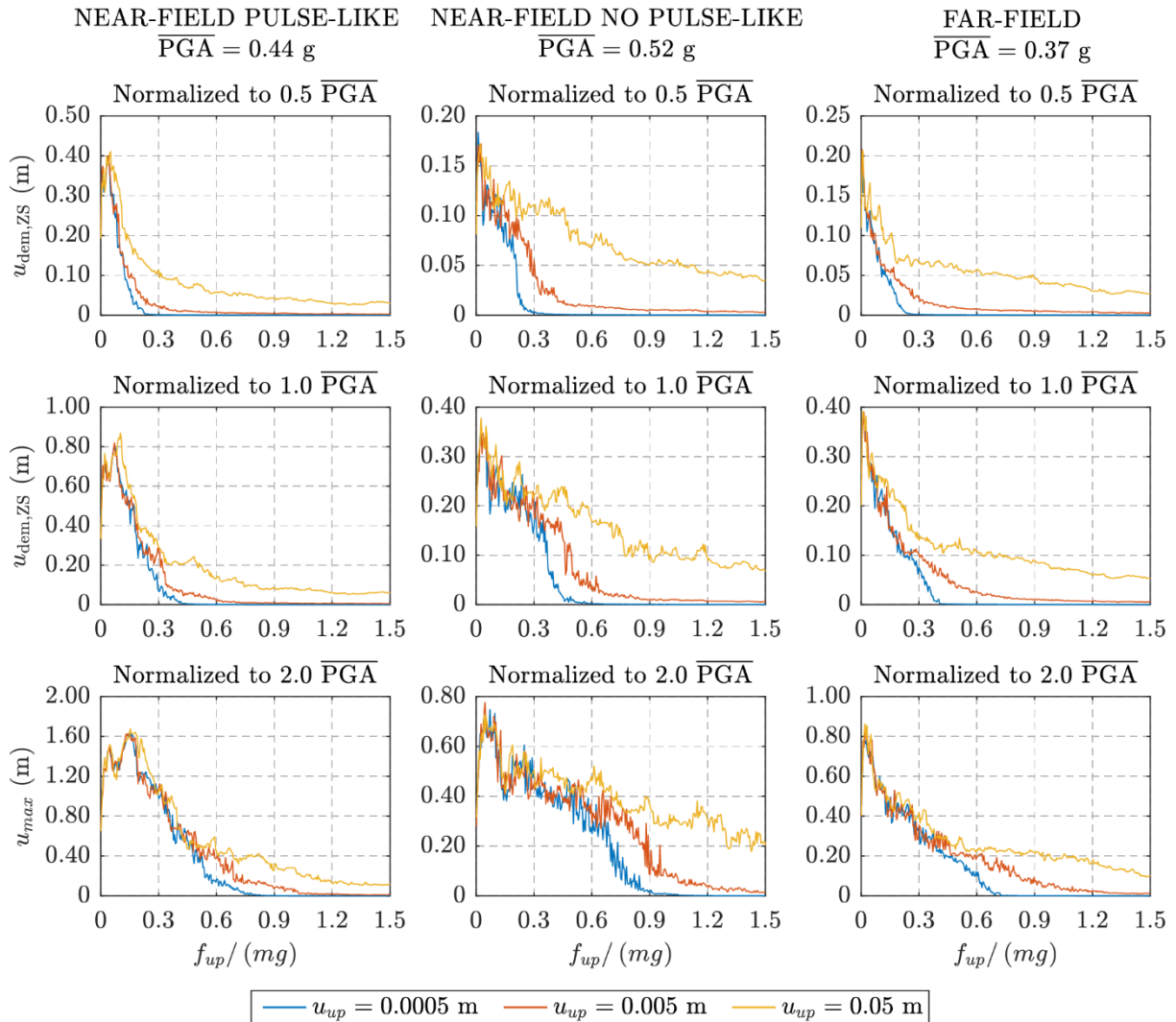
Figure 3.17. Median displacement spectra of systems with infinity capacity and different yielding displacement for multiple record sets.

Acknowledgements

References

Acikgoz, S., & DeJong, M. J. (2012). The interaction of elasticity and rocking in flexible structures allowed to uplift. *Earthquake Engineering & Structural Dynamics*, *41*(15), 2177–2194.

Agalianos, A., Psychari, A., Vassiliou, M. F., Stojadinovic, B., & Anastasopoulos, I. (2017). Comparative Assessment of Two Rocking Isolation Techniques for a Motorway Overpass Bridge. *Frontiers in Built Environment*, *3*.

Aghagholizadeh, M., & Makris, N. (2018). Earthquake response analysis of yielding structures coupled with vertically restrained rocking walls. *Earthquake Engineering & Structural Dynamics*, *47*(15), 2965–2984.

Anastasopoulos, I., Gazetas, G., Loli, M., Apostolou, M., & Gerolymos, N. (2010). Soil failure can be used for seismic protection of structures. *Bulletin of Earthquake Engineering*, *8*(2), 309–326.

Anastasopoulos, I., Kourkoulis, R., Gelagoti, F., & Papadopoulos, E. (2012). Rocking response of SDOF systems on shallow improved sand: An experimental study. *Soil Dynamics and Earthquake Engineering*, *40*, 15–33.

Avgenakis, E., & Psycharis, I. N. (2017). Modeling of Rocking Elastic Flexible Bodies under Static Loading Considering the Nonlinear Stress Distribution at Their Base. *Journal of Structural Engineering*, *143*(7), 04017051.

Avgenakis, E., & Psycharis, I. N. (2019). Determination of the nonlinear displacement distribution of the semi-infinite strip – Application to deformable rocking bodies. *International Journal of Solids and Structures*, *170*, 22–37.

Avgenakis, E., & Psycharis, I. N. (2020a). An integrated macroelement formulation for the dynamic response of inelastic deformable rocking bodies. *Earthquake Engineering & Structural Dynamics*, *49*(11), 1072–1094.

Avgenakis, E., & Psycharis, I. N. (2020b). Modeling of Inelastic Rocking Bodies under Cyclic Loading. *Journal of Engineering Mechanics*, *146*(4), 04020020.

Bachmann, J. A., Strand, M., Vassiliou, M. F., Broccardo, M., & Stojadinović, B. (2018). Is rocking motion predictable? *Earthquake Engineering & Structural Dynamics*, *47*(2), 535–552.

Bachmann, J. A., Vassiliou, M. F., & Stojadinović, B. (2017). Dynamics of rocking podium structures. *Earthquake Engineering & Structural Dynamics*, *46*(14), 2499–2517.

Bachmann, J. A., Vassiliou, M. F., & Stojadinovic, B. (2019). Rolling and rocking of rigid uplifting structures. *Earthquake Engineering & Structural Dynamics*, *48*(14), 1556–1574.

Bao, Y., & Konstantinidis, D. (2020). Dynamics of a sliding-rocking block considering impact with an adjacent wall. *Earthquake Engineering & Structural Dynamics*, *49*(5), 498–523.

Biot, M. A. (1932). *Vibrations of buildings during earthquake (Chapter II in Ph. D. thesis No. 259, entitled "Transient Oscillations in Elastic System")* [Ph. D.]. California Institute of Technology.

Chopra, A. K. (2012). *Dynamics of structures* (4th ed.). Pearson Prentice Hall.

Chopra, A. K., & Yim, S. C.-S. (1985). Simplified Earthquake Analysis of Structures with Foundation Uplift. *Journal of Structural Engineering*, *111*(4), 906–930.

Christopoulos, C., Filiatrault, A., & Folz, B. (2002). Seismic response of self-centring hysteretic SDOF systems. *Earthquake Engineering & Structural Dynamics*, *31*(5), 1131–1150.

Dar, A., Konstantinidis, D., & El-Dakhakhni, W. (2018). Seismic response of rocking frames with top support eccentricity. *Earthquake Engineering & Structural Dynamics*, *47*(12), 2496–2518.

Dar, A., Konstantinidis, D., & El-Dakhakhni, W. W. (2016). Evaluation of ASCE 43-05 Seismic Design Criteria for Rocking Objects in Nuclear Facilities. *Journal of Structural Engineering*, *142*(11), 04016110.

Di Sarno, L., Magliulo, G., D'Angela, D., & Cosenza, E. (2019). Experimental assessment of the seismic performance of hospital cabinets using shake table testing. *Earthquake Engineering & Structural Dynamics*, *48*(1), 103–123.

Diamantopoulos, S., & Fragiadakis, M. (2019). Seismic response assessment of rocking systems using single degree-of-freedom oscillators. *Earthquake Engineering & Structural Dynamics*, *48*(7), 689–708.

Dimitrakopoulos, E. G., & Giouvanidis, A. I. (2015). Seismic Response Analysis of the Planar Rocking Frame. *Journal of Engineering Mechanics*, *141*(7), 04015003.

Dimitrakopoulos, E. G., & Paraskeva, T. S. (2015). Dimensionless fragility curves for rocking response to near-fault excitations. *Earthquake Engineering & Structural Dynamics*, *44*(12), 2015–2033.

FEMA. (2009). *Quantification of building seismic performance factors* (FEMA-P695). Federal Emergency Management Agency.

Giouvanidis, A. I., & Dimitrakopoulos, E. G. (2017a). Nonsmooth dynamic analysis of sticking impacts in rocking structures. *Bulletin of Earthquake Engineering*, *15*(5), 2273–2304.

Giouvanidis, A. I., & Dimitrakopoulos, E. G. (2017b). Seismic Performance of Rocking Frames with Flag-Shaped Hysteretic Behavior. *Journal of Engineering Mechanics*, *143*(5), 04017008.

Giouvanidis, A. I., & Dimitrakopoulos, E. G. (2018). Rocking amplification and strong-motion duration. *Earthquake Engineering & Structural Dynamics*, *47*(10), 2094–2116.

Giouvanidis, A. I., & Dong, Y. (2020). Seismic loss and resilience assessment of single-column rocking bridges. *Bulletin of Earthquake Engineering*, *18*(9), 4481–4513.

Housner, G. W. (1963). The behavior of inverted pendulum structures during earthquakes. *Bulletin of the Seismological Society of America*, *53*(2), 403–417.

Kalliontzis, D., Sritharan, S., & Schultz, A. (2016). Improved Coefficient of Restitution Estimation for Free Rocking Members. *Journal of Structural Engineering*, *142*(12), 06016002.

Kam, W. Y., Pampanin, S., Palermo, A., & Carr, A. J. (2010). Self-centering structural systems with combination of hysteretic and viscous energy dissipations. *Earthquake Engineering & Structural Dynamics*, *39*(10), 1083–1108.

Kashani, M. M., Gonzalez-Buelga, A., Thayalan, R. P., Thomas, A. R., & Alexander, N. A. (2018). Experimental investigation of a novel class of self-centring spinal rocking column. *Journal of Sound and Vibration*, *437*, 308–324.

Kavvadias, I. E., Papachatzakis, G. A., Bantilas, K. E., Vasiliadis, L. K., & Elenas, A. (2017). Rocking spectrum intensity measures for seismic assessment of rocking rigid blocks. *Soil Dynamics and Earthquake Engineering*, *101*, 116–124.

Linde, S. A., Konstantinidis, D., & Tait, M. J. (2020). Rocking Response of Unanchored Building Contents Considering Horizontal and Vertical Excitation. *Journal of Structural Engineering*, *146*(9), 04020175.

Mahin, S., Sakai, J., & Jeong, H. (2006). *Use of partially prestressed reinforced concrete columns to reduce post-earthquake residual displacements of bridges*. 5th National Seismic Conference on Bridges & Highways, San Francisco, USA.

Makris, N., & Kampas, G. (2016). Size Versus Slenderness: Two Competing Parameters in the Seismic Stability of Free-Standing Rocking Columns. *Bulletin of the Seismological Society of America*, *106*(1), 104–122.

Makris, N., & Konstantinidis, D. (2003). The rocking spectrum and the limitations of practical design methodologies. *Earthquake Engineering & Structural Dynamics*, *32*(2), 265–289.

Makris, N., & Vassiliou, M. F. (2013). Planar rocking response and stability analysis of an array of free-standing columns capped with a freely supported rigid beam. *Earthquake Engineering & Structural Dynamics*, *42*(3), 431–449.

Makris, N., & Vassiliou, M. F. (2014). Are Some Top-Heavy Structures More Stable? *Journal of Structural Engineering*, *140*(5), 06014001.

Makris, N., & Vassiliou, M. F. (2015). Dynamics of the Rocking Frame with Vertical

Restrainers. *Journal of Structural Engineering*, *141*(10), 04014245.

Mashal, M., & Palermo, A. (2019). Low-Damage Seismic Design for Accelerated Bridge Construction. *Journal of Bridge Engineering*, *24*(7), 04019066.

Miranda, E. (2001). Estimation of Inelastic Deformation Demands of SDOF Systems. *Journal of Structural Engineering*, *127*(9), 1005–1012.

Oliveto, G., Caliò, I., & Greco, A. (2003). Large displacement behaviour of a structural model with foundation uplift under impulsive and earthquake excitations. *Earthquake Engineering & Structural Dynamics*, *32*(3), 369–393.

Palermo, A., Pampanin, S., & Calvi, G. M. (2005). Concept and development of hybrid solutions for seismic resistant bridge systems. *Journal of Earthquake Engineering*, *09*(06), 899–921.

Pappas, A., Sextos, A., da Porto, F., & Modena, C. (2017). Efficiency of alternative intensity measures for the seismic assessment of monolithic free-standing columns. *Bulletin of Earthquake Engineering*, *15*(4), 1635–1659.

Pasala, D. T. R., Sarlis, A. A., Nagarajaiah, S., Reinhorn, A. M., Constantinou, M. C., & Taylor, D. (2013). Adaptive Negative Stiffness: New Structural Modification Approach for Seismic Protection. *Journal of Structural Engineering*, *139*(7), 1112–1123.

Polyakov, S. V. (1974). *Design of Earthquake Resistant Structures*. MIR Publishers.

Priestley, M. J. N., & Tao, J. R. (1993). Seismic Response of Precast Prestressed Concrete Frames With Partially Debonded Tendons. *PCI Journal*, *38*(1), 58–69.

Psycharis, I. N. (1991). Effect of Base Uplift on Dynamic Response of SDOF Structures. *Journal of Structural Engineering*, *117*(3), 733–754.

Psycharis, I. N., Fragiadakis, M., & Stefanou, I. (2013). Seismic reliability assessment of classical columns subjected to near-fault ground motions. *Earthquake Engineering & Structural Dynamics*, *42*(14), 2061–2079.

Reggiani Manzo, N., & Vassiliou, M. F. (2019). Displacement-based analysis and design of rocking structures. *Earthquake Engineering & Structural Dynamics*, *48*(14), 1613–1629.

Riddell, R., & Newmark, N. M. (1979). *Statistical analysis of the response of nonlinear systems subjected to earthquakes*. University of Illinois Engineering Experiment Station. College of Engineering. University of Illinois at Urbana-Champaign.

Ríos-García, G., & Benavent-Climent, A. (2020). New rocking column with control of negative stiffness displacement range and its application to RC frames. *Engineering Structures*, *206*, 110133.

Routledge, P. J., Cowan, M. J., & Palermo, A. (2016). Low-damage detailing for bridges—A case study of Wigram-Magdala Bridge. *Proceedings of the New Zealand Society for Earthquake Engineering Annual Conference*. 2016 NZSEE Conference.

Sakai, J., Jeong, H., & Mahin, S. (2006). *Reinforced concrete bridge columns that re-center following earthquakes*. 8th U.S. National Conference on Earthquake Engineering, San Francisco, USA.

Sarlis, A. A., Pasala, D. T. R., Constantinou, M. C., Reinhorn, A. M., Nagarajaiah, S., & Taylor, D. P. (2013). Negative Stiffness Device for Seismic Protection of Structures. *Journal of Structural Engineering*, *139*(7), 1124–1133.

Sextos, A. G., Manolis, G. D., Ioannidis, N., & Athanasiou, A. (2017). Seismically induced uplift effects on nuclear power plants. Part 2: Demand on internal equipment. *Nuclear Engineering and Design*, *318*, 288–296.

Shu, Z., Zhang, J., & Nagarajaiah, S. (2017). Dimensional Analysis of Inelastic Structures with Negative Stiffness and Supplemental Damping Devices. *Journal of Structural Engineering*, *143*(3), 04016184.

Sideris, P., Aref, A. J., & Filiatrault, A. (2014a). Large-Scale Seismic Testing of a Hybrid Sliding-Rocking Posttensioned Segmental Bridge System. *Journal of Structural*

Engineering, *140*(6), 04014025.

Sideris, P., Aref, A. J., & Filiatrault, A. (2014b). Quasi-Static Cyclic Testing of a Large-Scale Hybrid Sliding-Rocking Segmental Column with Slip-Dominant Joints. *Journal of Bridge Engineering*, *19*(10), 04014036.

Sieber, M., Klar, S., Vassiliou, M. F., & Anastasopoulos, I. (2020). Robustness of simplified analysis methods for rocking structures on compliant soil. *Earthquake Engineering & Structural Dynamics*, *49*(14), 1388–1405.

Thiers-Moggia, R., & Málaga-Chuquitaype, C. (2019). Seismic protection of rocking structures with inerters. *Earthquake Engineering & Structural Dynamics*, *48*(5), 528–547.

Thomaidis, I. M., Kappos, A. J., & Camara, A. (2020). Dynamics and seismic performance of rocking bridges accounting for the abutment-backfill contribution. *Earthquake Engineering & Structural Dynamics*, *49*(12), 1161–1179.

Thonstad, T., Mantawy, I. M., Stanton, J. F., Eberhard, M. O., & Sanders, D. H. (2016). Shaking Table Performance of a New Bridge System with Pretensioned Rocking Columns. *Journal of Bridge Engineering*, *21*(4), 04015079.

Truniger, R., Vassiliou, M. F., & Stojadinović, B. (2015). An analytical model of a deformable cantilever structure rocking on a rigid surface: Experimental validation. *Earthquake Engineering & Structural Dynamics*, *44*(15), 2795–2815.

Tsiavos, A., Mackie, K. R., Vassiliou, M. F., & Stojadinović, B. (2017). Dynamics of inelastic base-isolated structures subjected to recorded ground motions. *Bulletin of Earthquake Engineering*, *15*(4), 1807–1830.

Vassiliou, M. F. (2018). Seismic response of a wobbling 3D frame. *Earthquake Engineering & Structural Dynamics*, *47*(5), 1212–1228.

Vassiliou, M. F., Burger, S., Egger, M., Bachmann, J. A., Broccardo, M., & Stojadinovic, B. (2017a). The three-dimensional behavior of inverted pendulum cylindrical structures during earthquakes. *Earthquake Engineering & Structural Dynamics*, *46*(14), 2261–2280.

Vassiliou, M. F., Mackie, K. R., & Stojadinović, B. (2014). Dynamic response analysis of solitary flexible rocking bodies: Modeling and behavior under pulse-like ground excitation. *Earthquake Engineering & Structural Dynamics*, *43*(10), 1463–1481.

Vassiliou, M. F., Mackie, K. R., & Stojadinović, B. (2017b). A finite element model for seismic response analysis of deformable rocking frames. *Earthquake Engineering & Structural Dynamics*, *46*(3), 447–466.

Vassiliou, M. F., & Makris, N. (2015). Dynamics of the Vertically Restrained Rocking Column. *Journal of Engineering Mechanics*, *141*(12), 04015049.

Vassiliou, M. F., Truniger, R., & Stojadinović, B. (2015). An analytical model of a deformable cantilever structure rocking on a rigid surface: Development and verification. *Earthquake Engineering & Structural Dynamics*, *44*(15), 2775–2794.

Veletsos, A. S., & Newmark, N. M. (1960). *Effect of inelastic behavior on the response of simple systems to earthquake motions*. Department of Civil Engineering, University of Illinois.

Voyagaki, E., Kloukinas, P., Dietz, M., Dihoru, L., Horseman, T., Oddbjornsson, O., Crewe, A. J., Taylor, C. A., & Steer, A. (2018). Earthquake response of a multiblock nuclear reactor graphite core: Experimental model vs simulations. *Earthquake Engineering & Structural Dynamics*, *47*(13), 2601–2626.

Xie, Y., Zhang, J., DesRoches, R., & Padgett, J. E. (2019). Seismic fragilities of single-column highway bridges with rocking column-footing. *Earthquake Engineering & Structural Dynamics*, *48*(7), 843–864.

4. Uniform Risk Spectra for Rocking Structures

Abstract

This paper presents uniform risk spectra for Zero Stiffness Bilinear Elastic (ZSBE) systems. The ZSBE oscillator is a bilinear elastic system with zero post-"yield" stiffness that satisfactorily predicts the response of different systems with negative lateral stiffness (e.g. free-standing or restrained rocking blocks). It can be described by a single parameter; thus, it is simpler to produce its spectrum. Using the ZSBE proxy, this paper provides the uniform risk spectra for sites in six locations in Europe. The spectra are constructed using two distinct intensity measures (IMs): Peak Ground Velocity and Peak Ground Acceleration. The efficiency of both IMs at different ranges of displacement demands is discussed and analytical approximations of the spectra are proposed.

4.1. Introduction

In the last half century, rocking has been extensively studied and it was proposed as an alternative seismic design method (Agalianos et al., 2017; Aghagholizadeh & Makris, 2018; Dar et al., 2018; Dimitrakopoulos & Giouvanidis, 2015; Giouvanidis & Dimitrakopoulos, 2017; Makris & Vassiliou, 2013, 2014; Ríos-García & Benavent-Climent, 2020; Sieber et al., 2020; Thomaidis et al., 2020; Vassiliou, 2018; Vassiliou et al., 2017a, 2017b; Zhang et al., 2019). Rocking isolation is a resilient design alternative that has the potential of reducing the cost of conventionally designed bridges: it reduces the forces transmitted to the foundation and it can present low-damage even after being subjected to design level events, provided that adequate detailing of the columns ends is employed (Mashal & Palermo, 2019; Reggiani Manzo & Vassiliou, 2022; Thonstad et al., 2016).

A free-standing rocking block subjected to a lateral excitation has infinite lateral stiffness until uplifting. After uplift, the block has a negative stiffness defined solely by its geometric

properties and it becomes statically unstable at a maximum top horizontal displacement equal to its base size (Figure 4.1a). The stability of the rocking block can be improved without changing its uplifting force by the introduction of axially flexible non-prestressed restrainers. Prestressing the restrainers would also change the uplifting force (Figure 4.1b) (Cohagen et al., 2008; Kashani et al., 2018; Liu & Palermo, 2017; Makris & Vassiliou, 2015; Mander & Cheng, 1997; Marriott et al., 2009; Mashal & Palermo, 2019; Motaref et al., 2014; Reggiani Manzo & Vassiliou, 2022; Sakai et al., 2006; Sideris et al., 2014a, 2014b, 2015; Thomaidis et al., 2020, 2022; Thonstad et al., 2016; Vassiliou & Makris, 2015; Zhou et al., 2019). A more stable system can also be achieved without changing the uplifting force by extending the block ends in a curved shape (Figure 4.1c) (Bachmann et al., 2017, 2019) or by adding damping or inerter devices (Aghagholizadeh, 2020; Makris & Aghagholizadeh, 2019; Thiers-Moggia & Málaga-Chuquitaype, 2019, 2020, 2021).

Among other reasons, rocking isolation has not been widely adopted in practice because of its high nonlinearity (Makris & Konstantinidis, 2003). Small changes in the excitation or any imperfection in the system can lead to a completely different response. Since ground excitations cannot be predicted in advance, available analytical and numerical models have been considered insufficient for designing rocking structures.
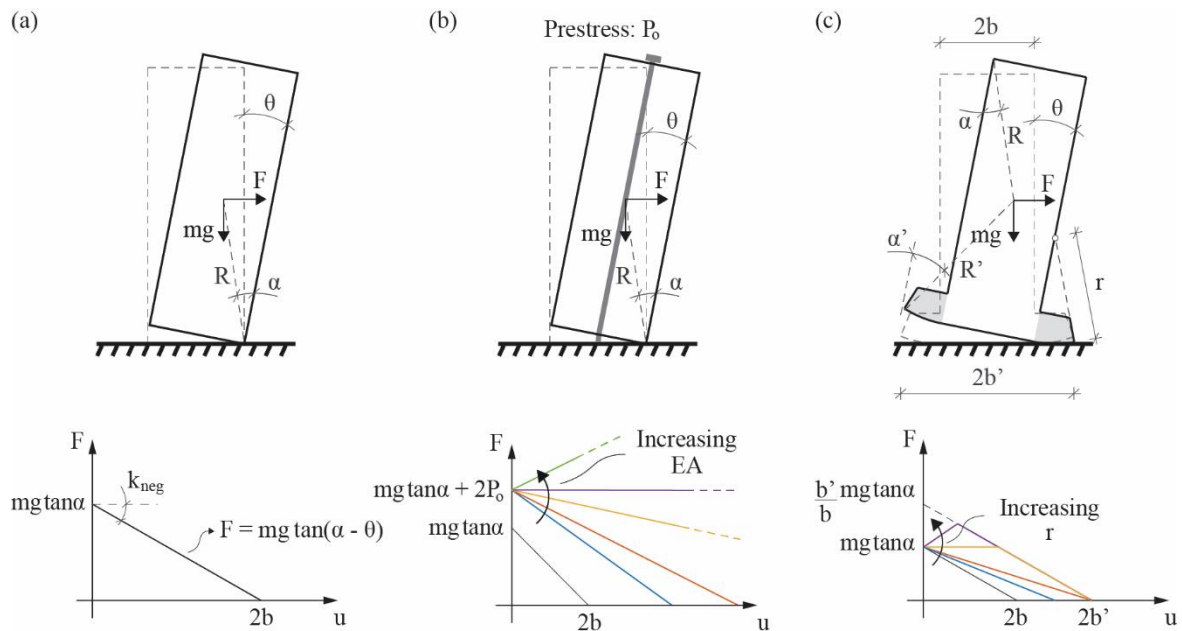
Figure 4.1. (a) Free-standing rigid rocking block; (b) restrained rigid rocking block; and (c) curved-base rigid rocking block.

To overcome the limitations of the deterministic approaches (i.e. of trying to predict the

response of a system to an individual ground motion), Bachmann et al. (2018) compared the statistics of the experimental and numerical response of a rocking structure subjected to several ground excitations. Although they could not match individual experimental and numerical time histories, the authors have shown that the experimental and numerical cumulative distribution function (CDF) of the normalized maximum tilt angle experienced by the specimen are in good agreement.

Although the use of probabilistic tools to seismically assess the behaviour of structures has become increasingly popular with the advent of performance-based earthquake engineering (Cornell & Krawinkler, 2000), addressing the rocking problem in a probabilistic manner is not something new. In 1980, Yim et al. (1980) have already treated the problem statistically and presented probability curves for the overturning of rigid rocking blocks. In recent years, several authors have proposed fragility curves for rocking structures (Acikgoz & DeJong, 2014; Dimitrakopoulos & Paraskeva, 2015; Ebad Sichani et al., 2018; Giouvanidis & Dimitrakopoulos, 2018; Giouvanidis & Dong, 2020; Kafle et al., 2011; Kavvadias et al., 2017; Kazantzi et al., 2021; Petrone et al., 2017; Psycharis et al., 2013; Roh & Cimellaro, 2011; Xie et al., 2019). However, the optimal intensity measure (IM) to construct such curves is still an open discussion. Giouvanidis & Dimitrakopoulos (2018) have extensively studied the most "efficient", "sufficient" and "hazard computable" IMs for rocking. They observed that the best IM for predicting rocking response and overturning are not the same. Rocking response can be better predicted using the dimensionless duration-based IMs, while overturning is well predicted using dimensionless IMs based on the Peak Ground Velocity (*PGV*), as firstly suggested by Dimitrakopoulos & Paraskeva (2015). Kavvadias et al. (2017) also studied the efficiency of several IMs and proposed two spectral IMs based on rocking structures. Although the proposed spectral IMs are reported to outperform other IMs, they require extra computational effort and would also need the development of new ground motion prediction equations (GMPEs), which is a non-trivial undertaking. Among the other IMs, their study shows that the *PGV* has also a good performance.

Currently, there is no established simplified method to design rocking structures; an equivalent elastic system does not exist (Makris & Konstantinidis, 2003). To address this issue, Kazantzi et al. (2021) have offered normalized response prediction and fragility assessment expressions that can be employed within a probabilistic framework to assess or design simple rocking systems (Vamvatsikos & Aschheim, 2016). Following another approach, Reggiani Manzo & Vassiliou (2019, 2021) have observed that rocking systems having the same uplift

force and being far from their failure point, exhibit roughly the same displacement demand, independently of their post uplift stiffness. Therefore, the displacement of rocking structures of uplift force f_{up} can be computed using as a proxy the displacement of a bilinear oscillator of uplift force f_{up} and infinite displacement capacity (Zero Stiffness Bilinear Elastic (ZSBE) oscillators). This simplification reduces the number of variables in the rocking problem and allows the construction of a single spectrum for a range of negative stiffness systems: free-standing rocking frames, restrained rocking frames, or rocking frames with curved ends.

This paper further develops this simplified spectrum by considering the uncertainties inherent to seismic actions. It presents uniform risk spectra for six locations with different seismicity in Europe (Vamvatsikos et al., 2020), constructed using the ZSBE proxy, as well as the step-by-step methodology for constructing them. The spectra for each location were constructed using two distinct IMs: namely the Peak Ground Acceleration (*PGA*) and *PGV*. Thus, using bootstrapping technique (Efron & Tibshirani, 1993), the paper follows on indirectly assessing the efficiency (as firstly defined in Luco & Cornell (2007)) of each IM. Finally, it provides analytical functions that can estimate the displacement demand of rocking structures.

4.2. The Zero Stiffness Bilinear Elastic System (ZSBE) as a proxy for Negative Stiffness Biliner Elastic Systems (NSBE)

4.2.1. The Negative Stiffness Bilinear Elastic System

The Negative Stiffness Bilinear Elastic (NSBE) system can describe the dynamics of free-standing (Figure 4.1a), restrained (Figure 4.1b), and curved-based (Figure 4.1c) rocking structures, or any other deformable system that presents negative post-uplift stiffness and does not exhibit hysteretic damping. Figure 4.2 presents the NSBE oscillator, and its displacement-restoring force relationship. Up until uplift, the system behaves as a linear single degree-of-freedom (SDOF) system, representing any deformability the system might present before uplifting. After uplifting, the tangent stiffness becomes negative (k_{neg}). The displacement capacity (u_{cap}) is defined not by material failure, but by the displacement that causes a zero restoring force. Therefore, the displacement capacity of an unrestrained column measured at its top is equal to its width.

Based on its displacement-force relationship (Figure 4.2c), the oscillator's equation of motion is:

$$m \cdot \ddot{u}(t) + f_{up} \cdot \frac{u(t)}{u_{up}} = -m \cdot \ddot{u}_g(t) , \quad |u(t)| \le u_{up} \tag{4.1}$$

$$m \cdot \ddot{u}(t) + \mathrm{sgn}(u(t)) \cdot f_{up} \cdot \left(\frac{u_{cap} - u(t)}{u_{cap} - u_{up}} \right) = -m \cdot \ddot{u}_g(t) , \quad |u(t)| > u_{up} \tag{4.2}$$
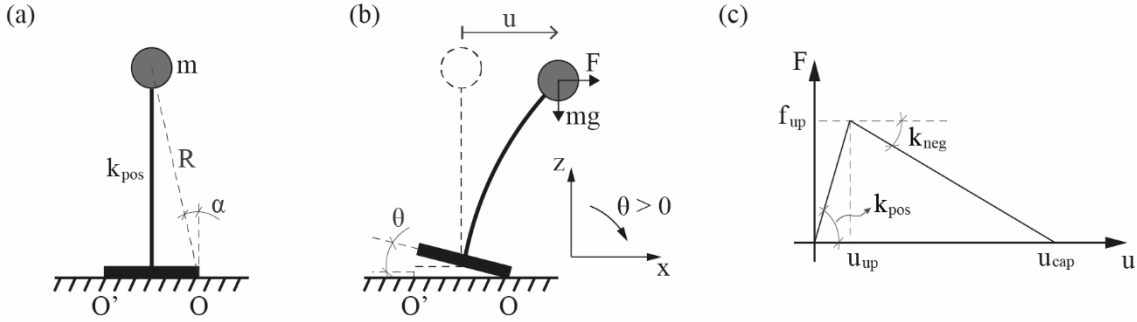
Figure 4.2. (a, b) NSBE system representation; and (c) its displacement-restoring force relationship.

The only source of energy dissipation in the system is impact damping, which is assumed to happen instantaneously. This assumption is valid for rocking structures with protected ends and no extra damping mechanism but might deviate from reality when the column ends are not protected (Kalliontzis et al., 2016; Kalliontzis & Sritharan, 2020). When the system is returning to its original position and its displacement equals to the uplift displacement (u_{up}) (i.e. when the system is "downcrossing" u_{up}), the integration is halted, and its post-impact velocity is calculated by a coefficient of restitution (r_c):

$$r_c = \frac{\dot{u}_{post-impact}}{\dot{u}_{pre-impact}} \tag{4.3}$$

A coefficient of restitution equal to 0.95 is assumed, corresponding to relatively slender structures. It is known that the coefficient of restitution, as defined in Equation (4.3) and by Housner (1963), depends mainly on the slenderness of the column and consequently on the column's uplifting force. However, the uplifting force can also be changed without varying the coefficient of restitution by prestressing the rocking column (Makris & Vassiliou, 2015; Vassiliou & Makris, 2015).

4.2.2. The Zero Stiffness Bilinear Elastic System

Figure 4.3a presents the displacement-force relationship of the Zero Stiffness Bilinear Elastic

(ZSBE) system (loading and unloading in the same curve). The system follows the same equation of motion and assumptions of the NSBE system when its displacement capacity tends to infinity, resulting in a system with zero post-uplift stiffness ($k_{neg} = 0$).
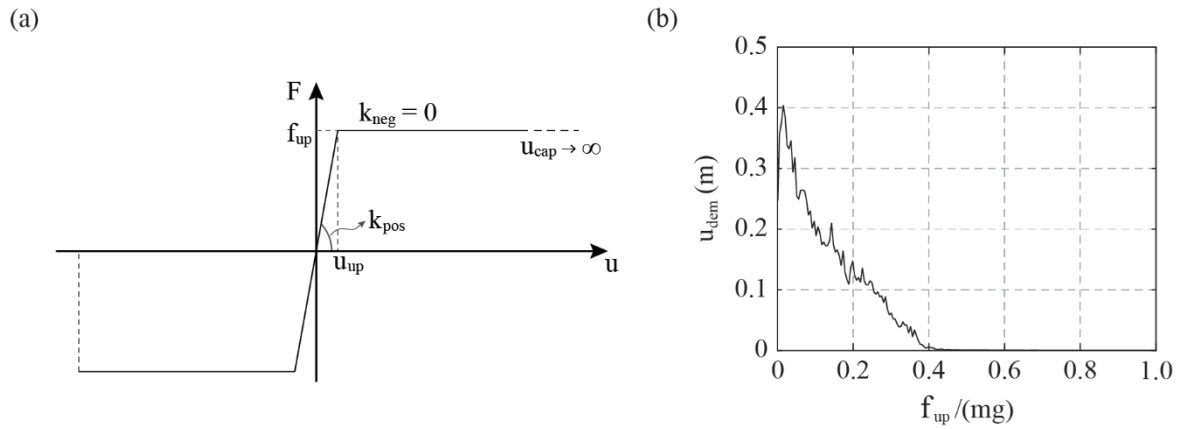
Figure 4.3. (a) Displacement-restoring force relationship of the ZSBE system; and (b) spectrum obtained using the ZSBE proxy.

The ZSBE oscillator can be used as a proxy for the prediction of the response of the NSBE oscillator (Reggiani Manzo & Vassiliou, 2019, 2021). Hence, studying the response of a ZSBE system of a given f_{up} and u_{up} suffices for the description of the response of all NSBE of the same f_{up} and u_{up}, independently of their u_{cap}. Therefore, spectra providing the maximum horizontal displacement (u_{dem}) of the ZSBE system as a function of f_{up} for a given u_{up} can be used for the design of NSBE systems. Figure 4.3b presents such a spectrum, extracted from Reggiani Manzo & Vassiliou (2021). It refers to $u_{up} = 0.0005$ m and it gives the median response for a set of ground motions selected and scaled as discussed in Reggiani Manzo & Vassiliou (2021). Herein, a $u_{up} = 0.0005$m was also used to denote a quasi-rigid ZSBE system.

4.3. Methodology for constructing the uniform risk spectra for rocking structures

Uniform hazard spectra (UHS) are widely adopted in seismic codes for the design of conventional structures. The UHS provides values of the (pseudo)spectral acceleration with an equal mean annual frequency (MAF) of exceedance. SDOF structures of a given period designed to reach "failure" (e.g. significant damage or life safety) at precisely the spectral acceleration value denoted by the UHS for this period would do so with the MAF (or equivalently the return period) that characterizes the UHS, assuming their response could be

calculated without any uncertainty (Luco et al., 2007); typically, however, this is only the case for elastic oscillators. Any deviation from this strict norm results in increased MAFs, i.e., unconservative designs. Given the significant uncertainties inherent in nonlinear response, record-to-record variability, higher modes, geometry, and materials, this has become a well-known problem of intensity-based approaches. It is traditionally tackled by conventional design codes through ad hoc safety factors and overdesign, leading to the advent of performance-based seismic design (PSBD, (Krawinkler et al., 2006; Vamvatsikos & Aschheim, 2016)).

Given the computational complexity of early PSBD approaches, Luco et al. (2007) tried to strike a middle ground by proposing the Risk-Targeted or Uniform Risk Spectrum (URS). The URS provides seismic actions that at least results in elastoplastic single-degree-of-freedom systems with uniform risk of damage or collapse, partially mitigating some of the inaccuracies of the UHS when applied to realistic systems (Spillatura, 2017). Therefore, given the practicality of the URS for seismic design, this paper demonstrates how to produce them for ZSBE systems.

Using the ZSBE proxy, the proposed URS is a plot of the displacement demand of the system as a function of its normalized strength, in which all ordinates of the plot present the same MAF of exceedance (Figure 4.4b). The URS can also be interpreted as an iso-MAF contour plot of the seismic risk surface, which is a 3D plot of the annual probability of exceeding a displacement demand for a range of systems with different normalized uplifting forces (Figure 4.4a).
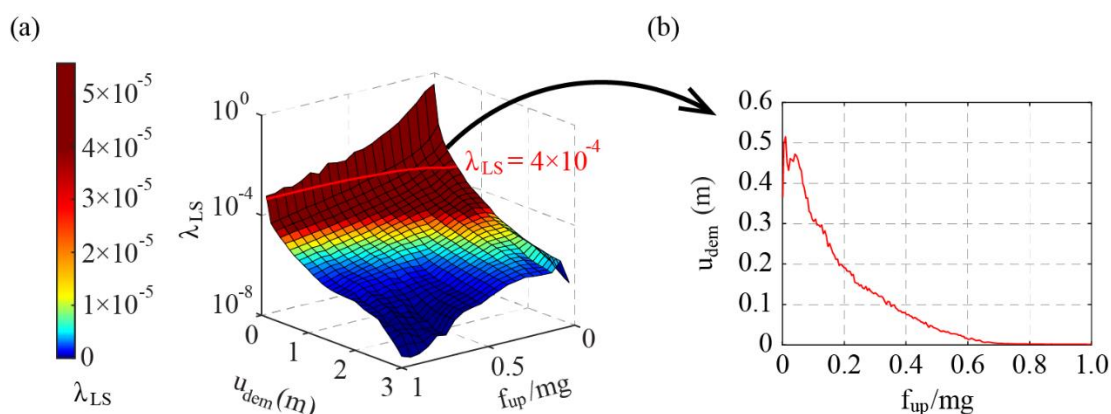
Figure 4.4. (a) Seismic risk surface with an iso-MAF contour plot highlighted; and (b) Uniform Risk Spectrum.

The calculation of the probability of exceedance is performed using the risk integral (Cornell et al., 2002):

$$\lambda_{LS} = \lambda\left(EDP > EDP_C\right) = \int P\left(EDP > EDP_C \mid \mathrm{IM}\right) \cdot \left|d\lambda\left(\mathrm{IM}\right)\right| \tag{4.4}$$

in which λ_{LS} is the MAF of exceeding (i.e., violating) a limit state (LS), $P(EDP > EDP_C \mid IM)$ is the fragility function, which represents the probability that the engineering demand parameter (*EDP*) exceeds the capacity threshold of EDP_C associated with *LS* for any given level of the ground motion intensity measure (IM) and $\lambda(IM)$ is the MAF of exceeding a given value of IM, which can be retrieved from the site-specific seismic hazard curve. Note that Equation (4.4) gives a single-point of the seismic risk surface. To construct the complete surface, the equation has to be evaluated for several limit states and a range of systems with different normalized uplifting force, $f_{up} / (mg)$.

4.3.1. Intensity measures

Given that all outputs of the risk assessment are conditioned on the chosen IM, it is extremely important to choose it wisely (Kazantzi & Vamvatsikos, 2015). The performance of an IM is commonly defined by its efficiency, sufficiency and hazard computability (Giouvanidis & Dimitrakopoulos, 2018; Kazantzi & Vamvatsikos, 2015; Luco & Cornell, 2007). Efficiency is related to the record-to-record variability; the more efficient an IM is, the lower is the dispersion of the predicted *EDP* along the full range of the evaluated IM. Sufficiency requires that the IM offers an unbiased prediction of the *EDP* that is not influenced by other seismological or ground motion characteristics (e.g. magnitude, distance from the rupture, etc.). Lastly, an IM is defined as hazard computable if there are reliable GMPEs for this IM. Without GMPEs, an IM is essentially useless for risk calculations.

To guarantee hazard computability, two commonly used IMs in vulnerability studies are employed herein, namely the *PGA* and *PGV*. Both are employed in their geomean form, denoted henceforth as $\overline{PGA}$ and $\overline{PGV}$, and calculated as the geometric mean of the *PGA* and *PGV*, respectively, from the two horizontal components (*x*, *y*) of the ground motions:

$$\overline{PGA} = \sqrt{PGA_x \cdot PGA_y} \tag{4.5}$$

$$\overline{PGV} = \sqrt{PGV_x \cdot PGV_y} \tag{4.6}$$

The use of the geomean instead of the arbitrary component spectral ordinates (i.e., randomly taking one of the two, usually the one applied in the 2D system) is preferable as most modern GMPEs refer to the former rather than the latter. Hence, convolving fragility functions

via Equation (4.4) based on arbitrary-component IMs with hazard curves defined on the respective geomean components would yield biased risk estimates due to the obvious incompatibility (Baker & Cornell, 2006). To this end, the geomean IM values are used also for the analysis, by employing IDA in discrete steps of $\overline{PGA}$ and $\overline{PGV}$, even if for the planar model at hand only one arbitrary component is assigned to the model per run. In a later section, the efficiency of both IMs is briefly discussed. Their sufficiency, however, is not evaluated herein, as the goal of the paper is not to evaluate the performance of the IMs, but to propose and discuss the construction of the URS, using the ZSBE proxy.

4.3.2. Site-specific seismic hazard curves

The risk assessment was conducted for six locations in Europe: Aachen (Germany), Athens (Greece), Baden bei Wien (Austria), Focşani (Romania), Montreux (Switzerland), and Perugia (Italy) (Vamvatsikos et al., 2020). The seismic hazard curves for both IMs were assessed via Probabilistic Seismic Hazard Analysis (PSHA (Cornell, 1968)). For the hazard calculations, the open-source platform OpenQuake was used (Global Earthquake Model (GEM), 2016) with the 2013 European seismic hazard model (ESHM13 (Woessner et al., 2015)). From the available logic tree branches of ESHM13 only the area source model and the Boore Atkinson 2008 GMPE (Boore & Atkinson, 2008) were employed. Since no site-specific data for the soil condition were available, a uniform "rock" soil type was assumed (V_{S30} = 800 m/s) in all sites under investigation.

Figure 4.5a points out the location of the six sites in Europe, while Figure 4.5b,c presents the seismic hazard curves obtained using $\overline{PGV}$ and $\overline{PGA}$ as IM, respectively. From Figure 4.5b,c, it can be noted that Athens, Focşani, and Perugia have a higher seismicity than Aachen, Baden bei Wien, and Montreux.

4.3.3. Fragility curves

Incremental dynamic analyses (IDA) (Vamvatsikos & Cornell, 2002) were carried out to obtain the fragility functions for each predefined limit state and system. A set of 105 firm-soil ordinary (no-pulse, no-long-duration) ground motions were selected from the PEER database (Chiou et al., 2008; Pacific Earthquake Engineering Research Center). They all come from events with moment magnitude (M_w) higher than 6.2 and $\overline{PGA}$ higher than 0.14g. When adopting $\overline{PGV}$ as IM, the ground motions were gradually scaled in $\overline{PGV}$ levels of:

$\overline{PGV} = \left[(1:0.5:20), (25:5:200) \right]$ cm/s. For the $\overline{PGA}$, scaling was employed in specific

levels of: $\overline{PGA} = \left[0.001, (0.0025:0.0025:0.0225), (0.025:0.005:0.195), (0.20:0.05:2) \right]$ g.
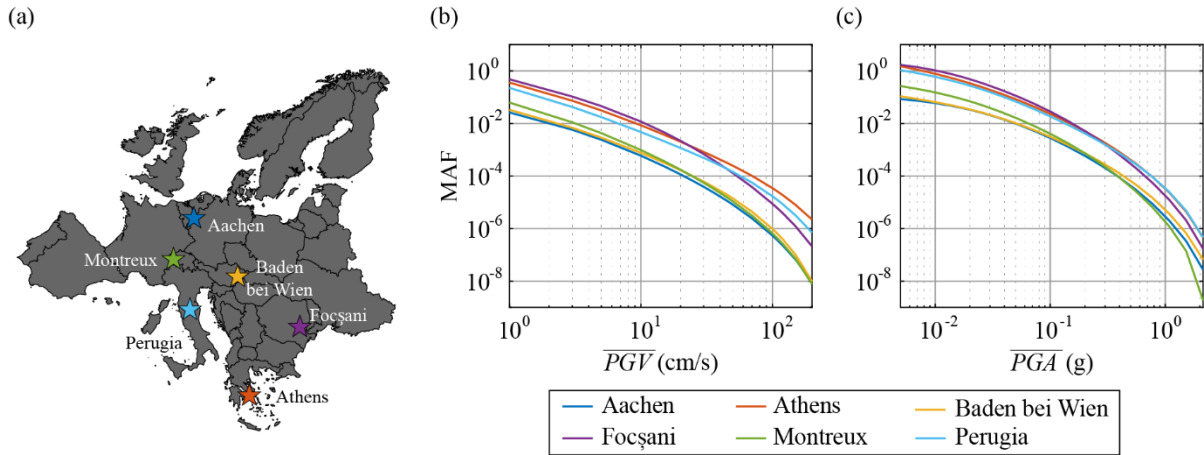
Figure 4.5. (a) Europe map indicating the six locations for which the risk assessment was carried out; and seismic hazard curves for (b) $\overline{PGV}$ and (c) $\overline{PGA}$.

The ZSBE system model considers only planar response. Therefore, the nonlinear dynamic analysis was carried out using one of the two components of the ground motion. After carrying out the analyses for all different scales and ground motions, the fragility function per limit state and system can be easily obtained either on an *EDP* or on an IM-basis approach (Kazantzi & Vamvatsikos, 2015). In this paper, the former was employed. For each IM-step value (horizontal stripe), the probability of exceeding the deterministic EDP capacity threshold was calculated as:

$$P\left(EDP > EDP_C \mid IM \right) = \frac{\text{number of records with } EDP > EDP_C}{\text{total number of records}} \tag{4.7}$$

Note that for smaller values of $\overline{PGV}$ and $\overline{PGA}$, a finer discretization was adopted because low *PGV* or *PGA* ground motions might lead to smaller EDP values, but they also have large probability of occurrence, hence resulting in significant contribution to the convolution of the risk integral (Equation (4.4)). Moreover, alike rigid rocking systems (Psycharis et al., 2000), the typical ZSBE IDA curve (not shown here for reasons of conciseness) shows highly weaving behaviour. However, for the fragility definition herein and the horizontal statistics approach at hand (Equation (4.7)), no inversion of the curves is needed and the raw analysis is used (Lachanas & Vamvatsikos, 2022).

The maximum horizontal displacement of the system (u_{dem}) was adopted as the *EDP*. To

construct the seismic risk surface (Figure 4.4a), fragility curves were constructed for several limit states and a range of systems with different normalized uplifting force. Herein, 3002 thresholds were evaluated, ranging from 0 to 3 m, in steps of 0.001 m. To be able to depict uplift, the threshold 0.0005 m was also included (see Section 4.2.2). The nonlinear analyses were carried out for systems with normalized uplifting force varying from 0.1 to 1.0, in steps of 0.05.

4.3.4. Risk Integral

The last step for obtaining the MAF of exceedance (λ_{LS}, Equation (4.4)) was to combine the structural response (i.e. fragility curves) with the seismic hazard at each location. Evaluating the risk integral for all 3002 thresholds and 301 systems with distinct normalized uplifting force, resulted in the seismic risk surface. Herein, the URS with 2%, 10% and 50% probability of exceedance in 50 years are presented for the six locations. These probabilities correspond to a MAF of 0.0004, 0.0021 and 0.0139 per year, as given by Equation (4.8), in which MAF can be converted to probability of exceedance (P_T) in a specific period of time (T), and vice versa, via the cumulative distribution function of the exponential distribution:

$$\text{MAF} = \frac{-\ln\left(1 - P_T\right)}{T} \tag{4.8}$$

4.4. Uniform Risk Spectra

Figure 4.6 and Figure 4.7 present the URS with $P_{50} = 2\%$, 10% and 50% probability of exceedance in 50 years, constructed using $\overline{PGV}$ and $\overline{PGA}$ as IM, respectively. As expected, for all locations and IMs, the displacement demands are increased when moving from the less frequent hazard levels (i.e., $P_{50} = 2\%$) to the most (i.e., $P_{50} = 50\%$). Moreover, the differences in the seismicity between the six locations at hand are also captured in the risk spectrum, whereas for the places of higher seismicity (i.e., Athens) notably higher demand values are calculated in comparison with lower seismicity places (i.e., Aachen).

Observing the spectra constructed for the same location and probability of exceedance, but different IMs, one can infer that the spectra constructed using $\overline{PGA}$ as IM predict larger displacement demands than the spectra that adopt $\overline{PGV}$ as IM. The larger displacement demands could be a consequence of the higher variance that GMPEs for $\overline{PGA}$ present in

comparison to GMPEs for $\overline{PGV}$. From Equation (4.4) it follows that distributions with fatter tails, once convolved with the fragility curves, lead to larger risk values.
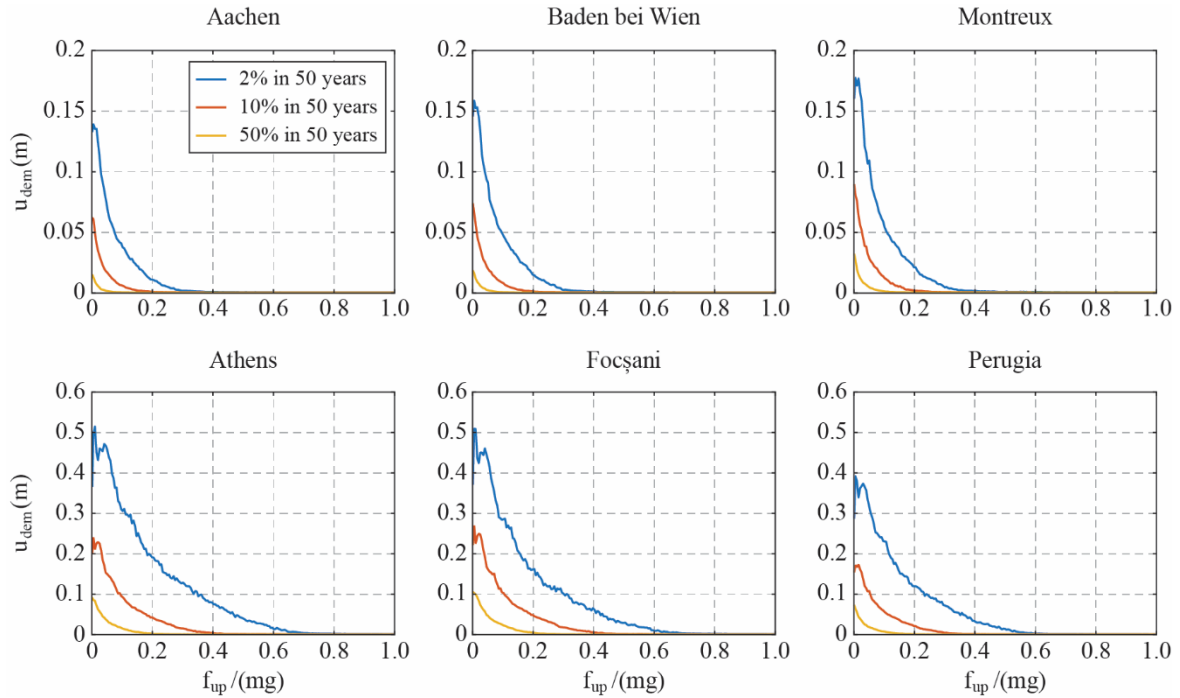
Figure 4.6. Uniform risk spectra for ZSBE systems with 2%, 10% and 50% probability of exceedance in 50 years, constructed using $\overline{PGV}$ as IM.

However, it is important to note that the fragility curves used to construct the spectra with different IMs were computed by performing two distinct incremental dynamic analyses. For the risk assessment using $\overline{PGV}$ as IM, the ground motions are scaled to levels of $\overline{PGV}$, while for the assessment that uses $\overline{PGA}$ as IM, the ground motions are scaled to levels of $\overline{PGA}$. While in theory the result of Equation (4.4) should be the same (within statistical significance) regardless of the IM used, this only holds if the IMs are sufficient. Thus, one should be careful in comparing the spectra with different IMs. In any case, the spectra developed using $\overline{PGV}$ are considered to be more reliable than the ones developed using $\overline{PGA}$ because the fragility curves when $\overline{PGA}$ was used (not shown here for reason of conciseness) had larger dispersion, which is indicative of lower sufficiency in practical terms (Kazantzi & Vamvatsikos, 2015).

4.5. IM-based uncertainty in uniform risk spectra

Given the discrepancy between the displacement demand predicted by the risk assessment conducted with both IMs (Figure 4.6 and Figure 4.7), bootstrapping (Efron & Tibshirani, 1993)

was employed to evaluate the dispersion of the spectra and indirectly check the efficiency of the intensity measures through the following steps:

(a) Choosing a (re)sampling size. Herein, sample sizes of 20, 40, 60, 80, and 105 ground motions were adopted.

(b) Randomly sampling with substitution per selected size from the total of 105 ground motions and reconstructing the uniform risk spectra with the desired probability of exceedance.

(c) Repeat step (a) N times, each time with a new random sample. In this paper, $N=1000$ repetitions were performed leading to $N=1000$ samples for each sample size.

(d) Estimate the statistical parameters of interest (i.e. median, 5%-quantile, 95%-quantile) over the N samples of the same size.

The above described bootstrapping technique was performed for the spectra with probabilities of exceedance of $P_{50} = 2\%$, 10% and 50% in 50 years. However, for the sake of brevity, only the results for the spectra with 2% in 50 years probability of exceedance are presented and discussed.
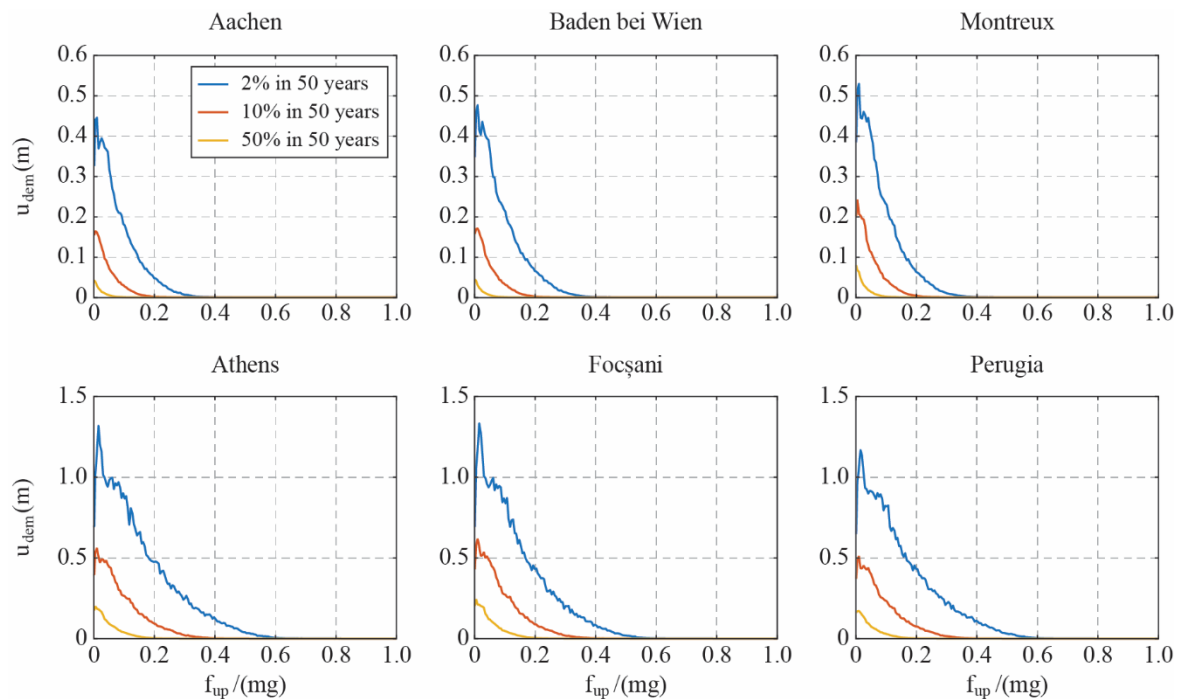
Figure 4.7. Uniform risk spectra for rocking structures with 2%, 10% and 50% probability of exceedance in 50 years, constructed using $\overline{PGA}$ as IM.

4.5.1. Peak rocking response

Figure 4.8 presents the obtained median spectra (solid lines) and their 90% bootstrap percentile confidence interval (CI, shown as a shaded area) for all sample sizes. The spectra presented in Section 4.4 (black dashed line) are also plotted for reference. Table 4.1 quantitatively compares the curves of Figure 4.8 presenting the error (e_{median}) of the median spectra and the maximum range of the 90% confidence interval (r_{90CI}). The quantities are defined as:

$$e_{median} = \frac{\max\left(\left|u_{median}\left(f_{up}\right) - u_{105GM}\left(f_{up}\right)\right|\right)}{u_{105GM}\left(f_{up,umax,1}\right)} \tag{4.9}$$

$$r_{90CI} = \frac{\max\left(\left|u_{95}\left(f_{up}\right) - u_{5}\left(f_{up}\right)\right|\right)}{u_{median}(f_{up,umax,2})} \tag{4.10}$$

in which, u_5, u_{median} and u_{95} are 5%-, 50%- and 95% quantiles of the displacement demand given by the bootstrapping analysis, respectively; u_{105GM} is the displacement demand given by the spectra obtained in Section 4.4; and $f_{up,umax,1}$ and $f_{up,umax,2}$ are the values of f_{up} that maximize the numerators of Equation (4.9) and (4.10), respectively.

Figure 4.8 and Table 4.1 show that, when using $\overline{PGV}$ as IM, the median spectra provide a good estimation of the original spectra for all locations, independently of the sample size. The maximum e_{median} for all locations and sample sizes are smaller or equal to 10%, even when the smallest sample size of the bootstrapping analysis (i.e. 20 ground motions) is adopted. These low differences that are captured for $\overline{PGV}$ stem from its efficiency, and are also indicative of high sufficiency by virtue of reducing the magnitude of any bias that can be attributed to non-captured seismological characteristics (Kazantzi & Vamvatsikos, 2015).

Although the sample size does not have a significant influence on the median of the $N = 1000$ estimated spectra, increasing the sample size leads to overall tighter estimates, and thus narrower confidence intervals on the estimated spectra. As shown in Equation (4.10), the maximum r_{90CI} range describes how wide the confidence interval is. For most locations, the spectra obtained with a sample size of 20 ground motions have a wide variability, in which r_{90CI} can be as high as 74%. Once the sample size is increased to 80 or more ground motions, the maximum r_{90CI} among all locations drops to 40%.
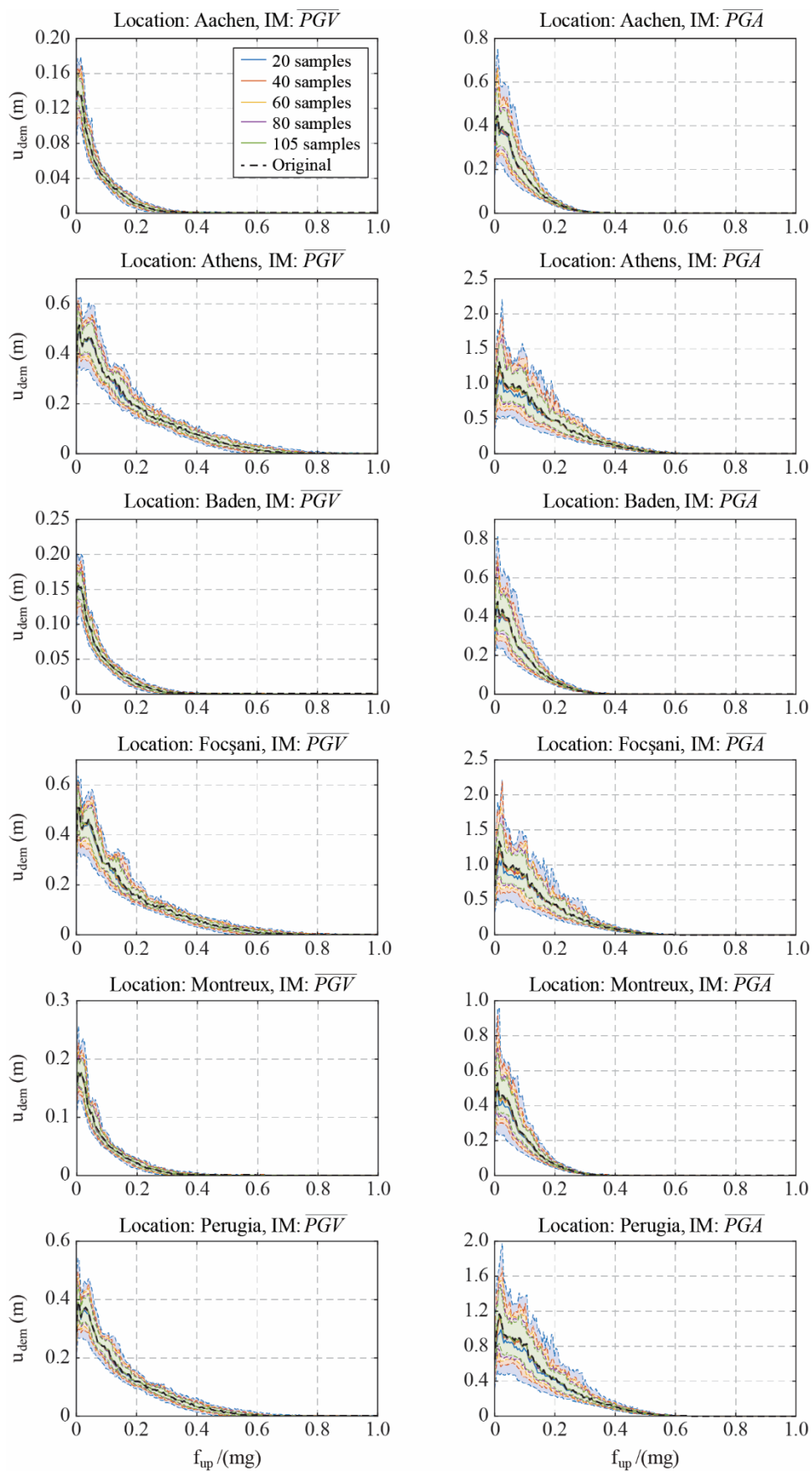
Figure 4.8. Median and 90% confidence interval for the spectra with 2% in 50 years probability of exceedance.

Table 4.1. Maximum error of the median spectra (e_{median}) and maximum range of the 90% confidence interval (r_{90CI}).

Place	Sample Size	$\overline{PGV}$		$\overline{PGA}$	
		e_{median} (%)	r_{90CI} (%)	e_{median} (%)	r_{90CI} (%)
Aachen	20	3.9	63	10.3	127
	40	2.5	46	6.0	98
	60	1.2	40	4.3	91
	80	1.6	36	4.4	69
	105	1.5	32	3.0	63
Athens	20	10.2	70	20.0	155
	40	5.5	47	11.7	123
	60	5.0	40	9.4	91
	80	4.9	35	5.0	89
	105	1.5	31	5.7	71
Baden bei Wien	20	2.8	69	11.1	126
	40	2.2	43	5.9	95
	60	1.5	36	6.1	80
	80	1.9	34	4.7	77
	105	0.5	27	2.5	59
Focşani	20	4.5	74	22.4	159
	40	3.6	56	17.5	149
	60	2.4	40	10.6	98
	80	2.1	36	8.4	88
	105	1.7	33	6.4	72
Montreux	20	7.2	72	13.7	181
	40	2.6	47	8.5	125
	60	1.4	45	5.0	88
	80	1.7	39	3.6	74
	105	1.7	35	3.4	60
Perugia	20	3.8	71	19.4	160
	40	5.4	51	12.5	112
	60	1.8	42	5.1	82
	80	1.8	33	4.5	74
	105	2.0	29	2.6	62

On the other hand, for the less efficient and sufficient $\overline{PGA}$, the median of the $N = 1000$ spectra obtained from the bootstrapping analysis still remains close to the original spectra, presented in Section 4.4. The e_{median} for different locations and sample sizes may appear to be uniformly higher for $\overline{PGA}$ than those calculated for $\overline{PGV}$, yet this difference should be viewed in light of the significantly higher dispersion of the results in the former case. Even so, e_{median} is again considerably reduced with the increase of the sample size. Lachanas & Vamvatsikos (2022) have suggested that for the case of *PGA* a sample size of 40 records is a robust lower limit for applying IDA to simple rocking systems, which also seems to hold for ZSBE systems,

especially if $\overline{PGV}$ is employed as the IM.

Additionally, the high levels of record-to-record variability that is captured in the IDA when employing $\overline{PGA}$ as IM and moving away from the deterministic rocking initiation threshold, lead to large values of r_{90CI}. Even when samples of 105 ground motions are used, r_{90CI} is still in the range of 60-70%, an r_{90CI} value that was only observed for the $\overline{PGV}$-based spectra with the smallest sample size adopted herein (i.e. 20 ground motions).

Figure 4.9 reproduces again the median $\overline{PGA}$-based spectra and its 90% CI, as well as the median $\overline{PGV}$-based spectra, both calculated with the largest sample size. Note that, for all locations, the median spectra obtained for $\overline{PGV}$ are not even contained in the confidence interval of the $\overline{PGA}$-based spectra, indicating that there is little statistical evidence to support the hypothesis that the two results are equivalent. Given that in both cases, the hazard was estimated on the basis of the same family of GMPEs (Boore & Atkinson, 2008), the same source model and software platform, this glaring difference is another indication that $\overline{PGA}$ should not be trusted as IM for predicting the peak rocking response, even if structural codes implicitly provide it as the Spectral Acceleration for *T*=0. Therefore, based on the above and the large record-to-record variability of the $\overline{PGA}$-based spectra, it can be concluded that $\overline{PGV}$ is a more efficient intensity measure than $\overline{PGA}$, as also observed by (Acikgoz & DeJong, 2014; Dimitrakopoulos & Paraskeva, 2015; Giouvanidis & Dimitrakopoulos, 2018; Kavvadias et al., 2017; Kazantzi et al., 2021; Petrone et al., 2017; Xie et al., 2019).

4.5.2. Rocking initiation

Although $\overline{PGV}$ is considered as a uniformly efficient rocking IM, showing relative low record-to-record variability in the full range of the response, $\overline{PGA}$ is reported to present a better performance in predicting rocking initiation of free-standing blocks (Kazantzi et al., 2021; Petrone et al., 2017). This follows directly from the uplift condition for rocking, that is completely controlled by *PGA* (i.e. there is uplift when $PGA > f_{up}/m$). Figure 4.8 gives a first evidence that this is reflected in the simplified spectra constructed herein. One can observe that the confidence interval of the spectra constructed using $\overline{PGA}$ narrows when approaching systems with large uplifting force and smaller displacement demands, in which rocking is minimal, while narrowing of the confidence interval of the spectra constructed using $\overline{PGV}$ cannot be observed.
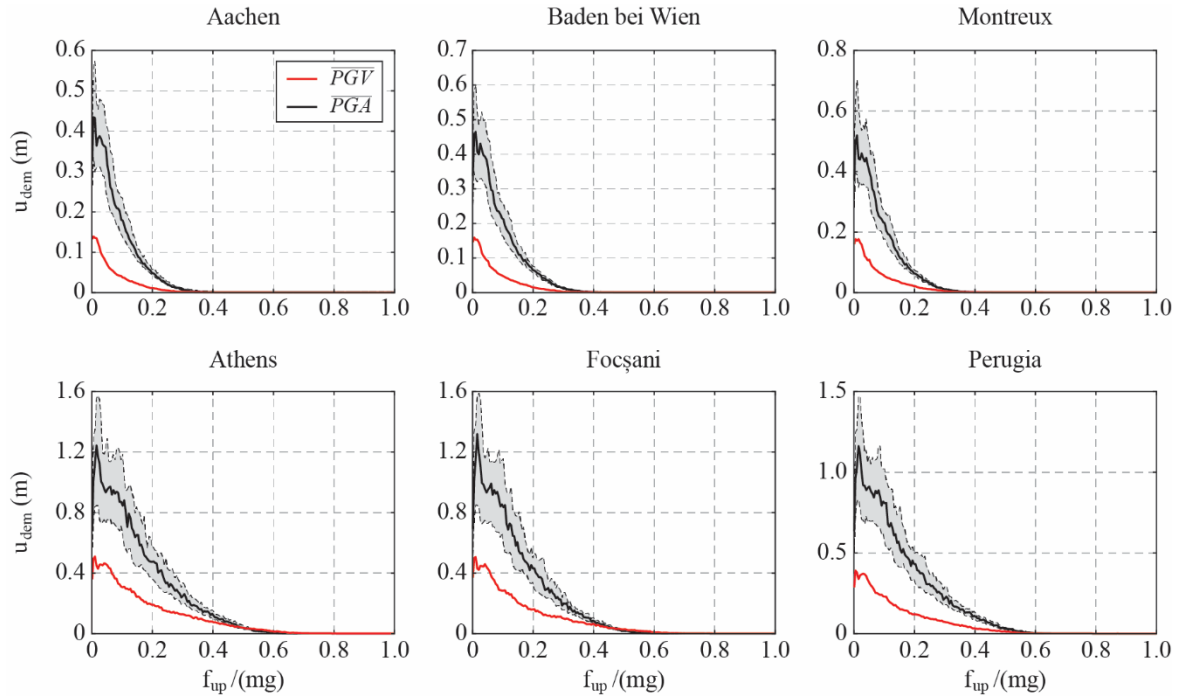
Figure 4.9. Median and 90% confidence interval for the spectra with 2% in 50 years probability of exceedance and sample size of 105 ground motions.

Figure 4.10 presents the median and 90% confidence interval of the spectra with 50% in 50 years probability of exceedance for sites in Baden and Montreux, which predict displacement demands smaller than the adopted uplift displacement (i.e. $u_{up} = 0.0005$m). The plots only show the curves for the range of displacement demands close to rocking initiation. The spectra with 2% in 50 years probability of exceedance are not shown because they predict displacement demands larger than the uplift displacement, and therefore cannot be used for assessing the dispersion of the spectra at the verge of rocking initiation.

In contrast to what was observed in Figure 4.8, one can note that after zooming in on small displacement demands, the spectra constructed using $\overline{PGA}$ present smaller dispersion than the spectra constructed using $\overline{PGV}$. Therefore, it can be suggested that, contrary to what was observed for the peak rocking response, $\overline{PGA}$ is a more efficient IM than $\overline{PGV}$ in predicting uplift. This also follows directly from the uplifting condition for rocking systems: In the general case, this would be $PGA > f_{up}/m$, while in the case without a restrainer this would be $PGA > g\tan\alpha$ (α defined in Figure 4.1 and Figure 4.2). This means that out of all the characteristics of a ground motion, PGA is the one that completely controls uplift.
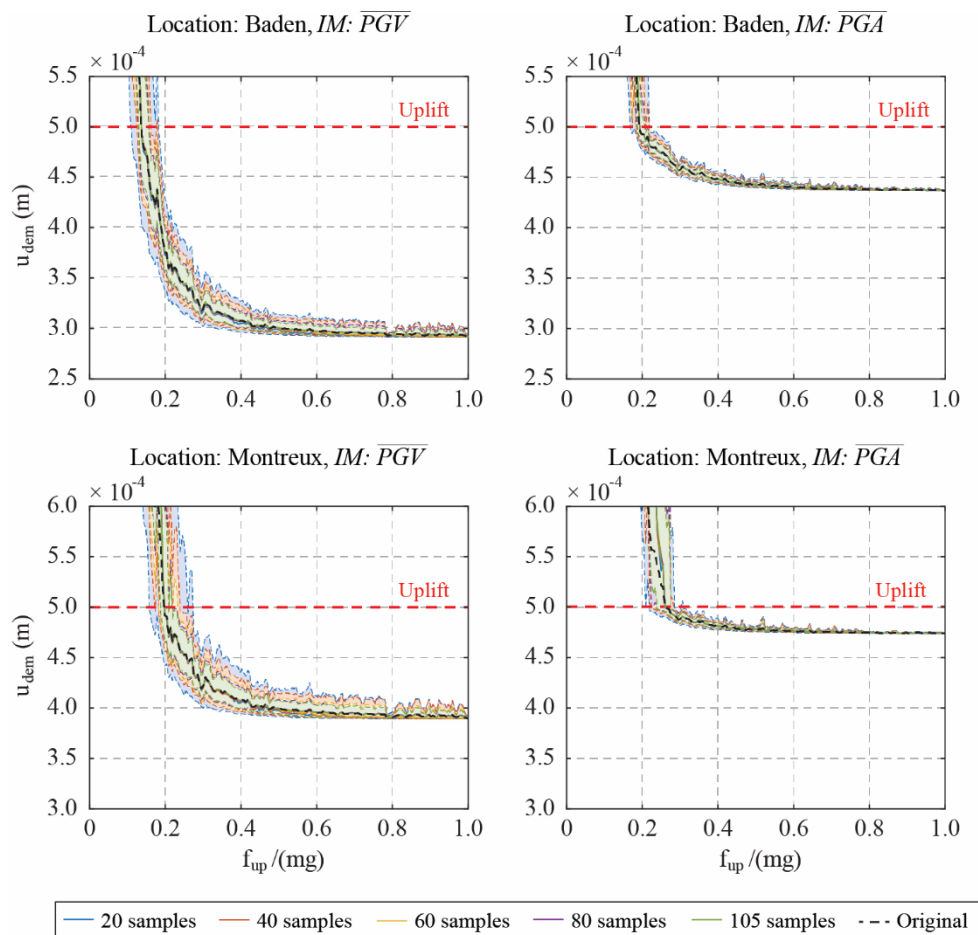
Figure 4.10. Median and 90% confidence interval for the spectra with 50% in 50 years probability of exceedance for sites in Baden and Montreux.

4.6. Regression analysis on the $\overline{PGV}$ -based spectra

Similarly to analytical approximations of conventional UHS, this section derives analytical approximations of URS for ZSBE structures that were developed in the previous sections. Nonlinear regression analysis was conducted to fit a function to the $\overline{PGV}$ -based spectra, and estimate the displacement demand of the rocking systems. Because of the low efficiency of the $\overline{PGA}$ in predicting the peak rocking response, no attempt was made to find a function that fit well to the $\overline{PGA}$ -based spectra. Herein, an exponential function with the general format shown below was adopted.

$$u_{dem}\left(f_{up}/(mg)\right) = c_0 \cdot \exp\left(c_1 \cdot f_{up}/(mg)\right) + c_2 \tag{4.11}$$

The function has three constant parameters that were fitted to the individual spectra corresponding to distinct probabilities of exceedance and location. Table 4.2 presents the fitted parameters, as well as the Root Mean Squared Error (RMSE) returned by the fitting algorithm.

Table 4.2. Fitted parameters to predict the displacement demand using Equation (4.11).

Place	Prob. of Exceedance	c_0	c_1	c_2	RMSE
Aachen	2% in 50 years	0.1557	-14.3419	0.0007	0.0017
	10% in 50 years	0.0635	-26.8763	0.0006	0.0006
	50% in 50 years	0.0147	-43.0825	0.0002	0.0001
Athens	2% in 50 years	0.5651	-5.2976	0	0.0089
	10% in 50 years	0.2643	-9.9605	0.0006	0.0033
	50% in 50 years	0.0939	-19.2313	0.0005	0.0007
Baden	2% in 50 years	0.1759	-13.0488	0.0007	0.0019
	10% in 50 years	0.0718	-24.9015	0.0006	0.0006
	50% in 50 years	0.0191	-46.1140	0.0003	0.0001
Focşani	2% in 50 years	0.5452	-5.9908	0	0.0087
	10% in 50 years	0.2834	-9.5306	0.0007	0.0037
	50% in 50 years	0.1116	-16.4333	0.0005	0.0009
Montreux	2% in 50 years	0.2022	-12.5980	0.0009	0.0024
	10% in 50 years	0.0889	-21.0858	0.0006	0.0007
	50% in 50 years	0.0311	-40.2362	0.0004	0.0003
Perugia	2% in 50 years	0.4356	-6.4190	0	0.0059
	10% in 50 years	0.1967	-12.1549	0.0006	0.0021
	50% in 50 years	0.0708	-26.5297	0.0006	0.0007

The RMSE values and Figure 4.11 show that the chosen exponential function fits well the spectra for all locations and probabilities of exceedance. However, in the range of systems with $f_{up}/(mg) < 0.05$, the displacement demand is overestimated. As it can be depicted on the original spectra (Figure 4.6, and reproduced in Figure 4.11), moving from $f_{up}/(mg) = 0$ to larger values the spectra present the following pattern:

(a) At $f_{up}/(mg) = 0$, the spectra start from a finite value, which for individual ground motions would be equivalent to the Peak Ground Displacement (PGD). This is consistent with the physics of the problem, as $f_{up}/(mg) = 0$ means that the mass is not connected to the ground and it stays still.

(b) Then, the spectra rapidly increase and reach a plateau.

(c) After the plateau, the displacement demand seems to decrease exponentially, being in good agreement with the proposed analytical exponential function.

This paper did not try to capture the rapid increase and the plateau observed in the original spectra because it would require a three-fold equation to better represent a region that it is not even meaningful for practical applications. In the case of the free-standing block, $f_{up}/(mg) = 0.05$ would lead to a block 1m-wide and 20m-high. Therefore, to keep the analytical function as simple as possible, the exponential function was fitted in the $f_{up}/(mg) > 0.05$ and extrapolated

in the range of $f_{up}/(mg) < 0.05$. This leads to overestimating the displacement demand for $f_{up}/(mg) < 0.05$.
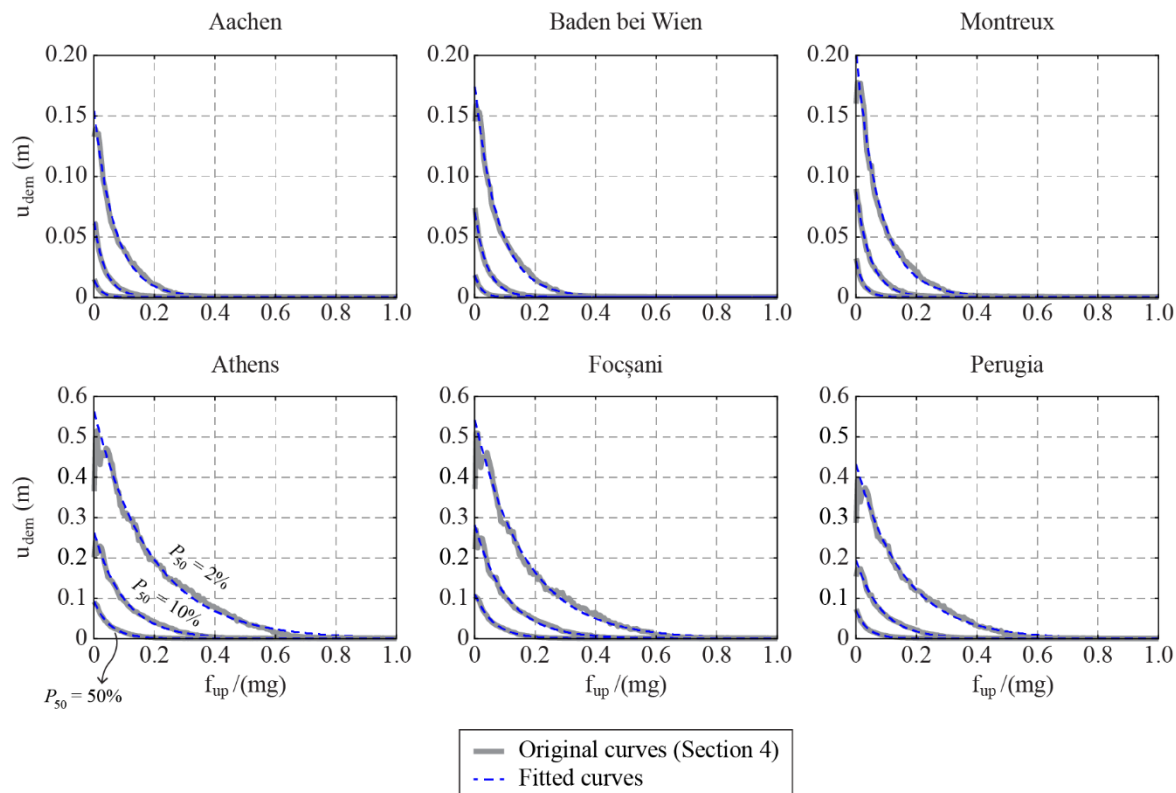
Figure 4.11. Proposed analytical functions and the original spectra.

4.7. Conclusions

This paper constructed uniform risk displacement demand spectra for rocking structures, which could be used for their design. To this end, it used the Zero Stiffness Bilinear Elastic system as a proxy of rocking systems. The methodology for constructing the spectra was firstly explained in detail. Then, spectra for six locations in Europe, using two distinct IMs ($\overline{PGA}$ and $\overline{PGV}$), were presented and discussed.

The two explored intensity measures perform differently depending on the objective they are used for. $\overline{PGA}$ is excellent in predicting uplift – as was expected based on the physics of the problem. However, for systems that displace into the "rocking region" (i.e. more than the displacement needed to uplift) $\overline{PGA}$ shows high response dispersion, while $\overline{PGV}$ manages to reduce this record-to-record variability, hence becoming more efficient.

The paper also approximated the $\overline{PGV}$-based spectra with exponential analytical curves. The proposed functions overestimate the displacement demand of systems with low uplift force (i.e.

$f_{up}/(mg) < 0.05$), this being a choice of simplicity over accuracy on a range of systems that do not have a real practical application. For all remaining systems (i.e. $f_{up}/(mg) > 0.05$), the displacement demands are well predicted.

Acknowledgements

References

Acikgoz, S., & DeJong, M. J. (2014). The rocking response of large flexible structures to earthquakes. *Bulletin of Earthquake Engineering*, *12*(2), 875–908.

Agalianos, A., Psychari, A., Vassiliou, M. F., Stojadinovic, B., & Anastasopoulos, I. (2017). Comparative Assessment of Two Rocking Isolation Techniques for a Motorway Overpass Bridge. *Frontiers in Built Environment*, *3*.

Aghagholizadeh, M. (2020). A finite element model for seismic response analysis of vertically-damped rocking-columns. *Engineering Structures*, *219*, 110894.

Aghagholizadeh, M., & Makris, N. (2018). Earthquake response analysis of yielding structures coupled with vertically restrained rocking walls. *Earthquake Engineering & Structural Dynamics*, *47*(15), 2965–2984.

Bachmann, J. A., Strand, M., Vassiliou, M. F., Broccardo, M., & Stojadinović, B. (2018). Is rocking motion predictable? *Earthquake Engineering & Structural Dynamics*, *47*(2), 535–552.

Bachmann, J. A., Vassiliou, M. F., & Stojadinović, B. (2017). Dynamics of rocking podium structures. *Earthquake Engineering & Structural Dynamics*, *46*(14), 2499–2517.

Bachmann, J. A., Vassiliou, M. F., & Stojadinovic, B. (2019). Rolling and rocking of rigid uplifting structures. *Earthquake Engineering & Structural Dynamics*, *48*(14), 1556–1574.

Baker, J. W., & Cornell, C. A. (2006). Which Spectral Acceleration are you Using? *Earthquake Spectra*, *22*(2), 293–312.

Boore, D. M., & Atkinson, G. M. (2008). Ground-Motion Prediction Equations for the Average Horizontal Component of PGA, PGV, and 5%-Damped PSA at Spectral Periods between 0.01 s and 10.0 s. *Earthquake Spectra*, *24*(1), 99–138.

Chiou, B., Darragh, R., Gregor, N., & Silva, W. (2008). NGA Project Strong-Motion Database. *Earthquake Spectra*, *24*(1), 23–44.

Cohagen, L. S., Pang, J. B. K., Stanton, J. F., & Eberhard, M. O. (2008). *A Precast Concrete Bridge Bent Designed to Re-Center after an Earthquake* (Rep No. WA-RD 684.3/TNW 2008-09). Washington State Department of Transportation.

Cornell, C. A. (1968). Engineering seismic risk analysis. *Bulletin of the Seismological Society of America*, *58*(5), 1583–1606.

Cornell, C. A., Jalayer, F., Hamburger, R. O., & Foutch, D. A. (2002). Probabilistic Basis for 2000 SAC Federal Emergency Management Agency Steel Moment Frame Guidelines.

Journal of Structural Engineering, *128*(4), 526–533.

Cornell, C. A., & Krawinkler, H. (2000). Progress and challenges in seismic performance assessment. *PEER Center News*, *3*(2).

Dar, A., Konstantinidis, D., & El-Dakhakhni, W. (2018). Seismic response of rocking frames with top support eccentricity. *Earthquake Engineering & Structural Dynamics*, *47*(12), 2496–2518.

Dimitrakopoulos, E. G., & Giouvanidis, A. I. (2015). Seismic Response Analysis of the Planar Rocking Frame. *Journal of Engineering Mechanics*, *141*(7), 04015003.

Dimitrakopoulos, E. G., & Paraskeva, T. S. (2015). Dimensionless fragility curves for rocking response to near-fault excitations. *Earthquake Engineering & Structural Dynamics*, *44*(12), 2015–2033.

Ebad Sichani, M., Padgett, J. E., & Bisadi, V. (2018). Probabilistic seismic analysis of concrete dry cask structures. *Structural Safety*, *73*, 87–98.

Efron, B., & Tibshirani, R. (1993). *An introduction to the bootstrap*. Chapman & Hall.

Giouvanidis, A. I., & Dimitrakopoulos, E. G. (2017). Seismic Performance of Rocking Frames with Flag-Shaped Hysteretic Behavior. *Journal of Engineering Mechanics*, *143*(5), 04017008.

Giouvanidis, A. I., & Dimitrakopoulos, E. G. (2018). Rocking amplification and strong-motion duration. *Earthquake Engineering & Structural Dynamics*, *47*(10), 2094–2116.

Giouvanidis, A. I., & Dong, Y. (2020). Seismic loss and resilience assessment of single-column rocking bridges. *Bulletin of Earthquake Engineering*, *18*(9), 4481–4513.

Global Earthquake Model (GEM). (2016). *OpenQuake Engine User Instruction Manual*.

Housner, G. W. (1963). The behavior of inverted pendulum structures during earthquakes. *Bulletin of the Seismological Society of America*, *53*(2), 403–417.

Kafle, B., Lam, N. T. K., Gad, E. F., & Wilson, J. (2011). Displacement controlled rocking behaviour of rigid objects. *Earthquake Engineering & Structural Dynamics*, *40*(15), 1653–1669.

Kalliontzis, D., & Sritharan, S. (2020). Dynamic response and impact energy loss in controlled rocking members. *Earthquake Engineering & Structural Dynamics*, *49*(4), 319–338.

Kalliontzis, D., Sritharan, S., & Schultz, A. (2016). Improved Coefficient of Restitution Estimation for Free Rocking Members. *Journal of Structural Engineering*, *142*(12), 06016002.

Kashani, M. M., Gonzalez-Buelga, A., Thayalan, R. P., Thomas, A. R., & Alexander, N. A. (2018). Experimental investigation of a novel class of self-centring spinal rocking column. *Journal of Sound and Vibration*, *437*, 308–324.

Kavvadias, I. E., Papachatzakis, G. A., Bantilas, K. E., Vasiliadis, L. K., & Elenas, A. (2017). Rocking spectrum intensity measures for seismic assessment of rocking rigid blocks. *Soil Dynamics and Earthquake Engineering*, *101*, 116–124.

Kazantzi, A. K., Lachanas, C. G., & Vamvatsikos, D. (2021). Seismic response distribution expressions for on-ground rigid rocking blocks under ordinary ground motions. *Earthquake Engineering & Structural Dynamics*, *50*(12), 3311–3331.

Kazantzi, A. K., & Vamvatsikos, D. (2015). Intensity measure selection for vulnerability studies of building classes. *Earthquake Engineering & Structural Dynamics*, *44*(15), 2677–2694.

Krawinkler, H., Zareian, F., Medina, R. A., & Ibarra, L. F. (2006). Decision support for conceptual performance-based design. *Earthquake Engineering & Structural Dynamics*, *35*(1), 115–133.

Lachanas, C. G., & Vamvatsikos, D. (2022). Rocking incremental dynamic analysis. *Earthquake Engineering & Structural Dynamics*, *51*(3), 688–703.

Liu, R., & Palermo, A. (2017). Quasi-Static Testing of a 1/3 Scale Precast Concrete Bridge

Utilising a Post-Tensioned Dissipative Controlled Rocking Pier. *Proceedings of 16th World Conference on Earthquake Engineering*. 16th World Conference on Earthquake Engineering, Santiago, Chile.

Luco, N., & Cornell, C. A. (2007). Structure-Specific Scalar Intensity Measures for Near-Source and Ordinary Earthquake Ground Motions. *Earthquake Spectra*, *23*(2), 357–392.

Luco, N., Ellingwood, B. R., Hamburger, R. O., Hooper, J. D., Kimball, J. K., & Kircher, C. A. (2007). Risk-targeted versus current seismic design maps for the conterminous United States. *Struct. Eng. Assoc. Calif. 2007 Conv. Proc.*

Makris, N., & Aghagholizadeh, M. (2019). Effect of Supplemental Hysteretic and Viscous Damping on Rocking Response of Free-Standing Columns. *Journal of Engineering Mechanics*, *145*(5), 04019028.

Makris, N., & Konstantinidis, D. (2003). The rocking spectrum and the limitations of practical design methodologies. *Earthquake Engineering & Structural Dynamics*, *32*(2), 265–289.

Makris, N., & Vassiliou, M. F. (2013). Planar rocking response and stability analysis of an array of free-standing columns capped with a freely supported rigid beam. *Earthquake Engineering & Structural Dynamics*, *42*(3), 431–449.

Makris, N., & Vassiliou, M. F. (2014). Are Some Top-Heavy Structures More Stable? *Journal of Structural Engineering*, *140*(5), 06014001.

Makris, N., & Vassiliou, M. F. (2015). Dynamics of the Rocking Frame with Vertical Restrainers. *Journal of Structural Engineering*, *141*(10), 04014245.

Mander, J. B., & Cheng, C. T. (1997). *Seismic Resistance of Bridge Piers Based on Damage Avoidance Design* (Techncial Report NCEER-97-0014; pp. 1–144). National Center for Earthquake Engineering Research.

Marriott, D., Pampanin, S., & Palermo, A. (2009). Quasi-static and pseudo-dynamic testing of unbonded post-tensioned rocking bridge piers with external replaceable dissipaters. *Earthquake Engineering & Structural Dynamics*, *38*(3), 331–354.

Mashal, M., & Palermo, A. (2019). Low-Damage Seismic Design for Accelerated Bridge Construction. *Journal of Bridge Engineering*, *24*(7), 04019066.

Motaref, S., Saiidi, M. S., & Sanders, D. (2014). Shake Table Studies of Energy-Dissipating Segmental Bridge Columns. *Journal of Bridge Engineering*, *19*(2), 186–199.

Pacific Earthquake Engineering Research Center. *PEER NGA Database*. Retrieved 27 July 2021, from http://peer.berkeley.edu/nga/

Petrone, C., Di Sarno, L., Magliulo, G., & Cosenza, E. (2017). Numerical modelling and fragility assessment of typical freestanding building contents. *Bulletin of Earthquake Engineering*, *15*(4), 1609–1633.

Psycharis, I. N., Fragiadakis, M., & Stefanou, I. (2013). Seismic reliability assessment of classical columns subjected to near-fault ground motions. *Earthquake Engineering & Structural Dynamics*, *42*(14), 2061–2079.

Psycharis, I. N., Papastamatiou, D. Y., & Alexandris, A. P. (2000). Parametric investigation of the stability of classical columns under harmonic and earthquake excitations. *Earthquake Engineering & Structural Dynamics*, *29*(8), 1093–1109.

Reggiani Manzo, N., & Vassiliou, M. F. (2019). Displacement-based analysis and design of rocking structures. *Earthquake Engineering & Structural Dynamics*, *48*(14), 1613–1629.

Reggiani Manzo, N., & Vassiliou, M. F. (2021). Simplified analysis of bilinear elastic systems exhibiting negative stiffness behavior. *Earthquake Engineering & Structural Dynamics*, *50*(2), 580–600.

Reggiani Manzo, N., & Vassiliou, M. F. (2022). Cyclic tests of a precast restrained rocking system for sustainable and resilient seismic design of bridges. *Engineering Structures*, *252*, 113620.

Ríos-García, G., & Benavent-Climent, A. (2020). New rocking column with control of negative

stiffness displacement range and its application to RC frames. *Engineering Structures*, *206*, 110133.

Roh, H., & Cimellaro, G. P. (2011). Seismic Fragility Evaluation of RC Frame Structures Retrofitted with Controlled Concrete Rocking Column and Damping Technique. *Journal of Earthquake Engineering*, *15*(7), 1069–1082.

Sakai, J., Jeong, H., & Mahin, S. (2006). *Reinforced concrete bridge columns that re-center following earthquakes*. 8th U.S. National Conference on Earthquake Engineering, San Francisco, USA.

Sideris, P., Aref, A. J., & Filiatrault, A. (2014a). Large-Scale Seismic Testing of a Hybrid Sliding-Rocking Posttensioned Segmental Bridge System. *Journal of Structural Engineering*, *140*(6), 04014025.

Sideris, P., Aref, A. J., & Filiatrault, A. (2014b). Quasi-Static Cyclic Testing of a Large-Scale Hybrid Sliding-Rocking Segmental Column with Slip-Dominant Joints. *Journal of Bridge Engineering*, *19*(10), 04014036.

Sideris, P., Aref, A. J., & Filiatrault, A. (2015). Experimental Seismic Performance of a Hybrid Sliding–Rocking Bridge for Various Specimen Configurations and Seismic Loading Conditions. *Journal of Bridge Engineering*, *20*(11), 04015009.

Sieber, M., Klar, S., Vassiliou, M. F., & Anastasopoulos, I. (2020). Robustness of simplified analysis methods for rocking structures on compliant soil. *Earthquake Engineering & Structural Dynamics*, *49*(14), 1388–1405.

Spillatura, A. (2017). *From record selection to risk targeted spectra for risk based assessment and design* [Ph. D.]. Scola Universitaria Superiore Pavia.

Thiers-Moggia, R., & Málaga-Chuquitaype, C. (2019). Seismic protection of rocking structures with inerters. *Earthquake Engineering & Structural Dynamics*, *48*(5), 528–547.

Thiers-Moggia, R., & Málaga-Chuquitaype, C. (2020). Seismic control of flexible rocking structures using inerters. *Earthquake Engineering & Structural Dynamics*, *49*(14), 1519–1538.

Thiers-Moggia, R., & Málaga-Chuquitaype, C. (2021). Effect of Base-Level Inerters on the Higher Mode Response of Uplifting Structures. *Journal of Engineering Mechanics*, *147*(8), 04021041.

Thomaidis, I. M., Camara, A., & Kappos, A. J. (2022). Dynamics and Seismic Performance of Asymmetric Rocking Bridges. *Journal of Engineering Mechanics*, *148*(3), 04022003.

Thomaidis, I. M., Kappos, A. J., & Camara, A. (2020). Dynamics and seismic performance of rocking bridges accounting for the abutment-backfill contribution. *Earthquake Engineering & Structural Dynamics*, *49*(12), 1161–1179.

Thonstad, T., Mantawy, I. M., Stanton, J. F., Eberhard, M. O., & Sanders, D. H. (2016). Shaking Table Performance of a New Bridge System with Pretensioned Rocking Columns. *Journal of Bridge Engineering*, *21*(4), 04015079.

Vamvatsikos, D., & Aschheim, M. A. (2016). Performance-based seismic design via yield frequency spectra‡. *Earthquake Engineering & Structural Dynamics*, *45*(11), 1759–1778.

Vamvatsikos, D., Bakalis, K., Kohrangi, M., Pyrza, S., Castiglioni, C. A., Kanyilmaz, A., Morelli, F., Stratan, A., D' Aniello, M., Calado, L., Proença, J. M., Degee, H., Hoffmeister, B., Pinkawa, M., Thanopoulos, P., & Vayas, I. (2020). A risk-consistent approach to determine EN1998 behaviour factors for lateral load resisting systems. *Soil Dynamics and Earthquake Engineering*, *131*, 106008.

Vamvatsikos, D., & Cornell, C. A. (2002). Incremental dynamic analysis. *Earthquake Engineering & Structural Dynamics*, *31*(3), 491–514.

Vassiliou, M. F. (2018). Seismic response of a wobbling 3D frame. *Earthquake Engineering & Structural Dynamics*, *47*(5), 1212–1228.

Vassiliou, M. F., Burger, S., Egger, M., Bachmann, J. A., Broccardo, M., & Stojadinovic, B.

(2017a). The three-dimensional behavior of inverted pendulum cylindrical structures during earthquakes. *Earthquake Engineering & Structural Dynamics*, *46*(14), 2261–2280.

Vassiliou, M. F., Mackie, K. R., & Stojadinović, B. (2017b). A finite element model for seismic response analysis of deformable rocking frames. *Earthquake Engineering & Structural Dynamics*, *46*(3), 447–466.

Vassiliou, M. F., & Makris, N. (2015). Dynamics of the Vertically Restrained Rocking Column. *Journal of Engineering Mechanics*, *141*(12), 04015049.

Woessner, J., Laurentiu, D., Giardini, D., Crowley, H., Cotton, F., Grünthal, G., Valensise, G., Arvidsson, R., Basili, R., Demircioglu, M. B., Hiemer, S., Meletti, C., Musson, R. W., Rovida, A. N., Sesetyan, K., Stucchi, M., & The SHARE Consortium. (2015). The 2013 European Seismic Hazard Model: Key components and results. *Bulletin of Earthquake Engineering*, *13*(12), 3553–3596.

Xie, Y., Zhang, J., DesRoches, R., & Padgett, J. E. (2019). Seismic fragilities of single-column highway bridges with rocking column-footing. *Earthquake Engineering & Structural Dynamics*, *48*(7), 843–864.

Yim, C.-S., Chopra, A. K., & Penzien, J. (1980). Rocking response of rigid blocks to earthquakes. *Earthquake Engineering & Structural Dynamics*, *8*(6), 565–587.

Zhang, J., Xie, Y., & Wu, G. (2019). Seismic responses of bridges with rocking column-foundation: A dimensionless regression analysis. *Earthquake Engineering & Structural Dynamics*, *48*(1), 152–170.

Zhou, Y.-L., Han, Q., Du, X.-L., & Jia, Z. (2019). Shaking Table Tests of Post-Tensioned Rocking Bridge with Double-Column Bents. *Journal of Bridge Engineering*, *24*(8), 04019080.

5. Cyclic tests of a precast restrained rocking system for sustainable and resilient seismic design of bridges

Abstract

Letting a column uplift and sustain rocking motion has been suggested as a seismic design method for bridges. In an effort to increase the redundancy of a rocking bridge, most researchers use ungrouted restraining tendons passing through the columns. However, it has been argued that these tendons unnecessarily increase the design forces of the superstructure and of the foundation, and that rocking systems should be designed to be unrestrained.

In an effort to combine the benefits of both approaches this paper suggests the use of flexible restraining systems comprising a tendon in series with disc springs, essentially forming a seismic isolation method for precast structures. It presents cyclic tests of two 1:5 scale RC columns with ends protected either with steel jackets or with steel discs. The columns are able to sustain drifts of more than 15% (and in some cases 30%) without any significant damage – hence they are resilient. The behavior of the disc springs is well predicted by analytical models. The strength (i.e. uplift force) and post uplift stiffness of the system can be predicted with a reasonable accuracy using a rigid body model. However, the rigid body model does not predict well the pre-uplift behavior. As the tendon is anchored within the column, the design moment of the foundation drastically decreases, therefore costly and material intensive pile foundations could be avoided – hence the design concept contributes to sustainability.

5.1. Introduction

Modern seismic design of bridges is based on the dogma that the columns should be firmly connected to the ground. The survival of ancient Greco-Roman temples that are supported by columns that are allowed to uplift indicates that this dogma might be unnecessary. Moreover, not only it is unnecessary but fixing the columns to the ground results in large design moments

for both the columns and the foundation. As designing for elastic behavior under these design moments seemed an expensive approach, plastic design of bridges has been the state of the practice for the last decades. This implies that bridges are designed to sustain non-repairable damage under the design earthquake. Moreover, this approach often results in huge pile foundations that can comprise up to 50% of the Reinforced Concrete of the total structure. As an example, the bents of a bridge in Egnatia Highway in Northern Greece are less than 12.5 m tall, while the piles of the foundation are 36 m long and governed by the seismic loading.

To avoid plastic design and the expected damage that it implies, a very efficient way of using the reinforcement has been proposed: an unbonded tendon passes along the length of the column and is anchored at the cap beam and the foundation. Hence, its strain equals to its deformation divided by its whole length and a much larger column drift is required to yield the tendon. To provide energy dissipation, yielding reinforcement is used either grouted within the column, or connected to it in the side. Proper dimensioning of the unbonded tendon and yielding reinforcement results in the so-called "flag shaped" (Christopoulos, 2004; Giouvanidis & Dimitrakopoulos, 2017) hysteresis loops and recentering performance. The concept is based on the early work of Priestley & Tao (1993), Stanton et al. (1997), and the PREcast Seismic Structural Systems project (Nakaki et al., 1999; Priestley et al., 1999). Different names have been used for similar concepts: Damage Avoidance Design (Mander & Cheng, 1997), Controlled Rocking (Calvi et al., 2004; Liu & Palermo, 2017, 2020; Marriott et al., 2009; Mashal & Palermo, 2019; Palermo et al., 2005, 2007; White & Palermo, 2016), Self-Centering System (Cheng, 2008; Christopoulos et al., 2008; Cohagen et al., 2008; ElGawady & Sha'lan, 2011; Guerrini et al., 2015; Kashani et al., 2018; Li et al., 2019; Restrepo & Rahman, 2007; Sakai et al., 2006; Trono et al., 2015; Wang et al., 2018), Precast Hybrid Systems (Billington & Yoon, 2004; Bu et al., 2016; Motaref et al., 2014; Ou et al., 2010; Panagiotou et al., 2015), Restrained Rocking (Makris & Vassiliou, 2015; Vassiliou & Makris, 2015), Hybrid Sliding-Rocking System (Sideris et al., 2014a, 2014b, 2015), Pretensioned Rocking (Thonstad et al., 2016, 2017; Yamashita & Sanders, 2009, among others), Unbonded Post-Tensioned Systems (Chou et al., 2013; Chou & Chen, 2006; Chou & Hsu, 2008), and it has recently found its way to practice in New Zealand (Routledge et al., 2016) and China (Qu et al., 2018). This concept is a breakthrough, because it addresses the societal call for not only avoiding collapse, but for reducing damage and increasing post disaster functionality as well.

However, the current state of the art in restrained rocking bridges still results in large

design moments for the foundation. Hence, large pile foundations only to take the overturning moment are often needed. The foundation often comprises up to 50% of the total Reinforced Concrete (RC) used in the project. To address this waste of material, Agalianos et al. (2017), Chen & Li (2021), Dimitrakopoulos & Giouvanidis (2015), Giouvanidis & Dimitrakopoulos (2018), Giouvanidis & Dong (2020), Makris & Vassiliou (2013), Thomaidis et al. (2020), Vassiliou et al. (2017a,b), Vassiliou (2018), Xie et al. (2019) have proposed that a rocking system without a tendon (a "free rocking" system – Figure 5.1) is stable enough and leads to much smaller design moments for the foundation. The analysis of such a system is fundamentally different to elastic and positive stiffness elastoplastic or flag-shaped systems, because it exhibits a negative post uplift stiffness – that is, after uplift the restoring force decreases as displacement increases. Therefore, any analysis based on the elastic spectrum is not applicable (Makris & Konstantinidis, 2003) and a different simplified design method has been proposed (Reggiani Manzo & Vassiliou, 2019, 2021). The main counter argument against free rocking systems is that they have no redundancy, especially redundant parallel mechanisms that engage in a beyond design event. Psychological aspects regarding building a freestanding structure should not be disregarded.
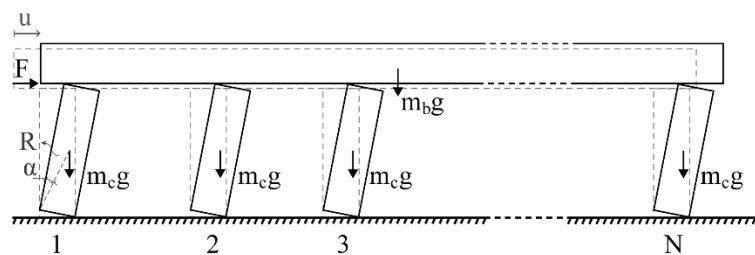
Figure 5.1. Free-standing rocking frame.

In an effort to combine the low foundation design moment of a free rocking system with the redundancy provided by restrainers, this paper suggests the use of a spring in series with the restraining tendon (Figure 5.2). Then, the post uplift stiffness of the system is negative, the design moment remains small, the overturning displacement is increased, while the redundancy of the system can be enhanced by adding a spring stopper that can engage when the spring reaches a critical displacement. This paper discusses cyclic tests that have been performed on 2 RC precast columns equipped with a tendon-spring restraining system (Figure 5.3). As the springs are used to make the system more flexible and, consequently, to decrease the design forces, the idea could be perceived as a seismic isolation method for the controlled rocking systems.
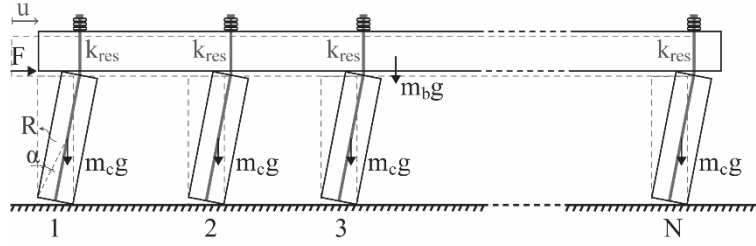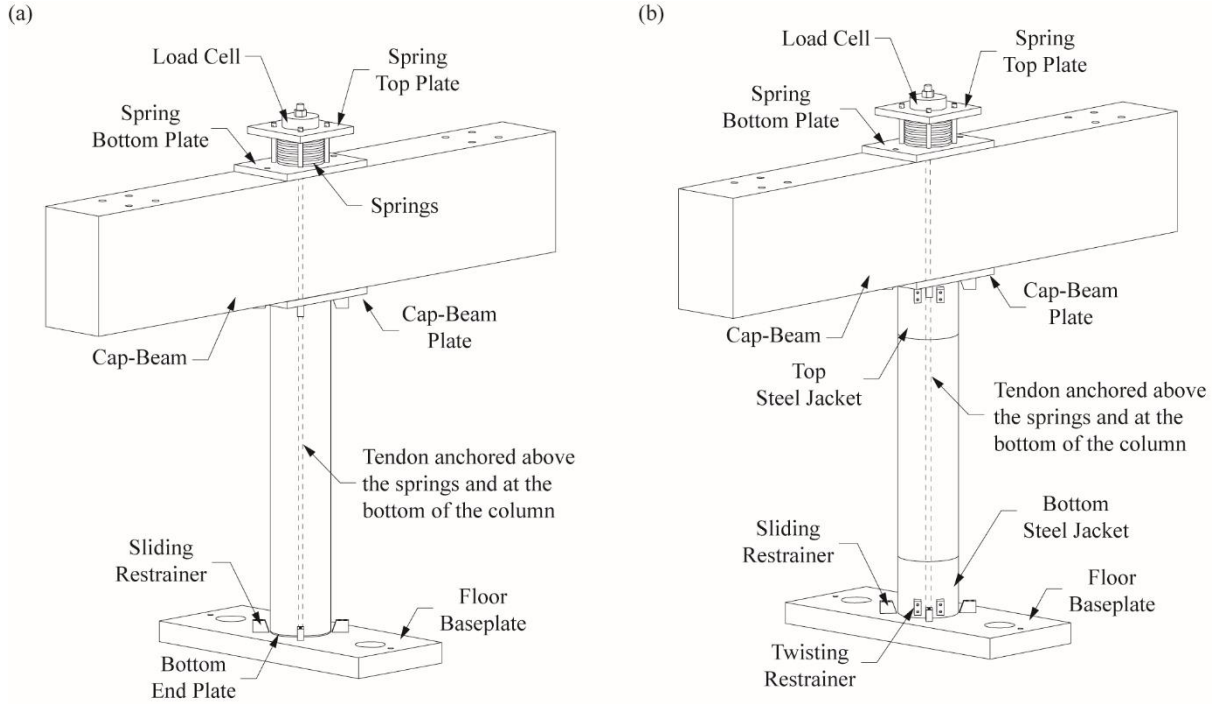
Figure 5.2. Restrained rocking frame.

Figure 5.3. Specimen with: (a) circular end plate (Column D), and (b) steel jacket (column J).

5.2. Mechanics of the restrained rocking column

Assume the rocking column presented in Figure 5.4a. The column has a mass m_c and carries a vertical constant load $F_1 + F_2 + m_b \cdot g = P$. It is restrained via an unbonded restraining system having overall stiffness k_{res} and zero prestress. Assuming no sliding and rigid behavior of the column, and following an approach similar to Makris & Vassiliou (2015) and Vassiliou & Makris (2015), the horizontal force–displacement relation is:

$$F = \left(P + \frac{m_c g}{2} \right) \tan(\alpha - \theta) + \frac{1}{2} k_{res} R \sin^2 \alpha \frac{\sin \theta}{\cos(\alpha - \theta)} \qquad (5.1)$$

where R is the semidiagonal of the column and θ its tilt angle.
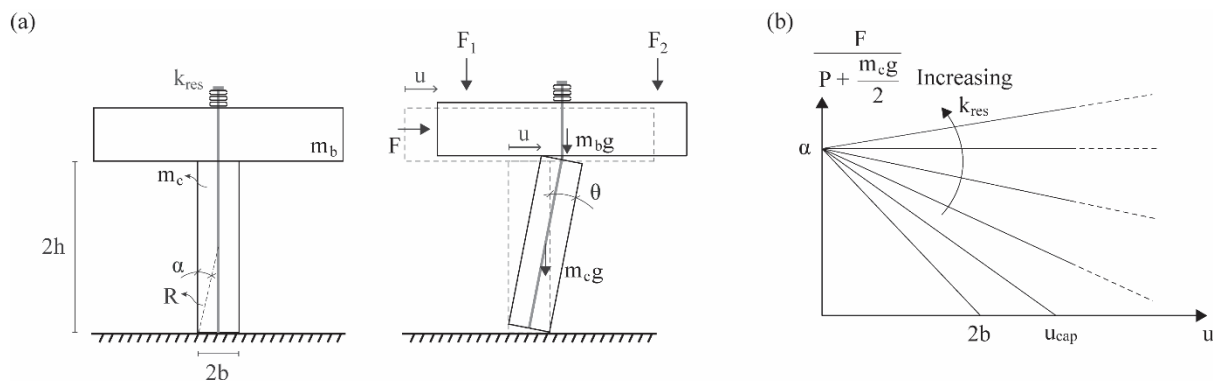
Figure 5.4. (a) Rocking Column; (b) Restoring force versus displacement diagram of the rocking column.

For small α and θ, it becomes:

$$\frac{F}{P + \frac{m_c g}{2}} = \frac{b}{h} - \left(1 - \frac{k_{res}\alpha b}{2\left(P + \frac{m_c g}{2}\right)}\right)\frac{u}{2h} \qquad (5.2)$$

Figure 5.4b shows a plot of $\dfrac{F}{P + \dfrac{m_c g}{2}}$ as a function of u for different values of k_{res}. For

$k_{res} = 0$ (i.e. no restraining system), the system presents a negative post uplift stiffness. The restoring force becomes negative at the point of unstable equilibrium, i.e. $\theta = \alpha$, or, in terms of displacement, $u = 2b$. This point defines collapse under static loading. In traditional RC columns, collapse is defined as a deformation that has damaged the column enough to lose its vertical bearing capacity. On the contrary, in rocking columns with protected ends collapse occurs because of a geometric instability, not because of material damage.

The presence of the non-prestressed tendon (i.e. $k_{res} > 0$), increases the post uplift

stiffness, without affecting the uplift force. When $k_{res} < \dfrac{2\left(P + \dfrac{m_c g}{2}\right)}{R\alpha^2}$ the overall post uplift

stiffness remains negative. The displacement of unstable equilibrium now increases to:

$$u_{cap} = 2b\left(1 - \frac{\dfrac{1}{k_{res}R\alpha^2}}{2\left(P + \dfrac{m_c g}{2}\right)}\right) \qquad (5.3)$$

When $k_{res} > \dfrac{2\left(P + \dfrac{m_c g}{2}\right)}{R\alpha^2}$, Equation (5.2) gives positive post uplift stiffness, hence there

exists no point of unstable equilibrium and a rigid column restrained by an elastic system does not fail.

Designing a precast rocking column would require the determination of the section moment and shear forces, so that the column is appropriately reinforced. To this end, the tendon force, T, is computed as:

$$T = \frac{k_{res}\alpha}{2}u \tag{5.4}$$

The critical cross section is the top most. There, for small θ, the axial load, moment and shear applied on this cross section is:

$$N = F_1 + F_2 + T = F_1 + F_2 + \frac{k_{res}\alpha}{2}u \tag{5.5}$$

$$M = Nb = \left(F_1 + F_2 + \frac{k_{res}\alpha}{2}u\right)b \tag{5.6}$$

$$V = F + \left(F_1 + F_2\right)\frac{u}{2h} \tag{5.7}$$

The above analysis is highly idealized because:

a) Usually a restraining system comprises solely a tendon that has a finite yield strain. For a tendon strength of 1800 MPa, the yield strain is 9×10^{-3}. Assuming a bridge column of 9.6×1.6 m, rigid body analysis shows that the tendon will yield at a drift ratio of 11%.

b) The column is not rigid, but will sustain flexural deformation along its length and local deformation at the column-foundation and column-cap beam contact zones.

c) There might be sliding at the interfaces between the column and the cap beam or foundation.

However, the experimental results presented in this paper show that the rigid body model provides a good approximation for large displacements, at least in the case where a) the restraining system is made relatively flexible by adding a spring and b) the column ends are protected with steel jackets or steel plates.

Concerning the dynamic response of negative stiffness restrained rocking systems,

Vassiliou (2010) and Reggiani Manzo & Vassiliou (2019, 2021) have shown that the presence of a non-prestressed tendon increases the post uplift stiffness and the displacement capacity without affecting the displacement demand – as long as the post uplift stiffness remains negative.

5.3. Design of the test specimens

Two column specimens of the same geometry were tested: One had its ends protected with steel jackets (column J) and one with steel annular (top) or disc (bottom) plates (column D). The geometry of the specimens was not chosen to represent a specific bridge, but rather fall in the range of typical columns used in bridge design in seismic prone areas. The scale of the specimen was 1:5 and was controlled by the stroke of the available actuator. Scale effects on the compressive strength of concrete are not quantified in this paper. Column elevations and critical cross sections are shown in Figure 5.5.

The ungrouted tendon passed through the centerline of the column. One end was anchored in the bottom plate of the column via a threaded socket, providing no connection between the foundation and the column. The other end was anchored above the beam, in series with the disc springs (Figure 5.2). A minimal prestress loading of 2 kN was applied to the restraining system to remove the slack of the restraining system.

Steel plates were also fixed to the floor and to the cap beam to avoid damage due to stress concentrations (Figure 5.3). The plates were equipped with sliding restrainers, which limited the sliding motion of the column. A restrainer was also provided to avoid twisting of the columns.

5.3.1. Casting of the columns and concrete mix

The columns were cast in-house using a commercial dry mixture of self-compacting concrete of strength class C30/37 ($f_{ck} = 30$ MPa). Although the water/cement ratio suggested in the pack of the dry mixture was initially respected, the concrete workability was not the one expected, and more water had to be added to the mixture. Three standard cylindrical specimens of 150 mm-diameter and 300 mm-height were cast to define the strength and Young's modulus of the concrete. The measured mean (standard deviation) 28-day strength and Young's modulus of the specimen were 45.4 (12.5) MPa and 29.9 (4.2) GPa, respectively. Therefore, assuming a lognormal distribution, the characteristic compressive strength of the concrete (5%-quantile) is

f_{ck} = 28.9 MPa.
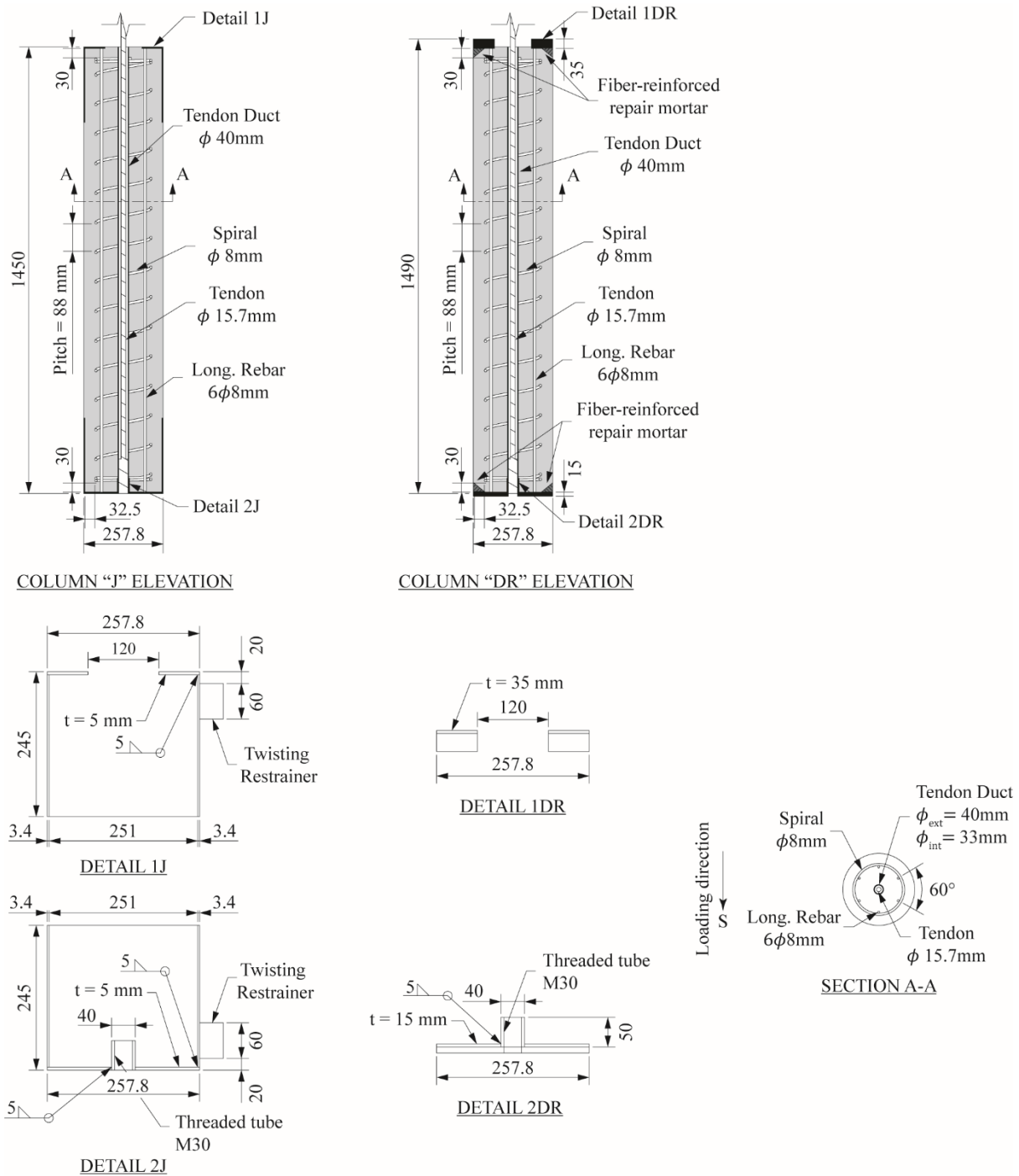
Figure 5.5. Column elevation and critical cross-sections (dimensions in mm).

The concrete was cast from the top, and compacted from the side with a mallet. Because the workability of the concrete remained relatively low, after removing the formwork it was observed that there were voids at the ends of the column D, especially at the top end, which is also the most critical cross-section (Figure 5.6). The voids were repaired with mortar. One

could not see whether there were voids within the jackets of column J, but it is reasonable to assume so. However, after the tests, column J had sustained only minimal damage (see section 5.5.2), so even if there were voids, it seems that the jackets were strong enough to protect the column. This did not hold for column D.


Figure 5.6. Voids created while casting at the top end of column D.

After the first test, the repair mortar that was used had failed and the steel plates were clearly bent. The column's voids were filled using a "Sika Monotop − 412 NFG" fiber-reinforced, low shrinkage repair mortar with 48 MPa compressive strength at 28 days (Sika). This time 30 mm and 10 mm thickness plates were welded on the top and bottom of the bent plates. The column was retested as column DR (R for "repaired"). Based on the above, the columns should either be cast from the side as in Thonstad et al. (2016, 2017), or a more workable mix should be used.

5.3.2. Steel jackets and end plates

S355 steel was used for the protection of the ends of both columns. The ends of column J were protected with a tube having 3.4 mm thickness, 245 mm height, and 257.8 mm external diameter (see Figure 5.5, Figure 5.7a). The steel tube was welded at its base to a steel plate of 5 mm thickness. The detailing of the steel plate is different in the bottom and top part of the column to allow for casting from the top. A threaded steel tube was welded at the bottom steel plate to allow for anchoring the tendon. In the top part, a circular annular plate with internal diameter of 120 mm was used.

The ends of column D were protected solely with a 5 mm thick disc plate (bottom) and an annular plate (top). The top and bottom repair plates (DR) had a thickness of 30 and 10 mm resulting in a total thickness of 35 and 15 mm respectively (Figure 5.5, Figure 5.7b). The addition of the repair plates increased the total height of column DR to 1490 mm.

(a)   (b)
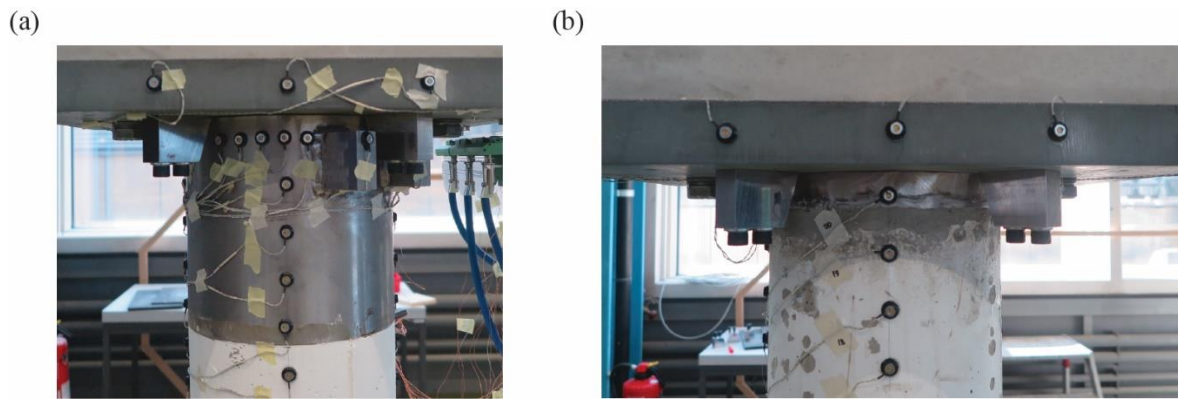
Figure 5.7. Column end protection. (a) Steel Jacket of column J; (b) Repaired discs of column DR.

To limit sliding, the steel plates fixed to the ground and to the cap-beam were equipped with restrainers that limited sliding to 5 mm in each direction (Figure 5.8). Column J was also equipped with a twist restrainer (Figure 5.8).
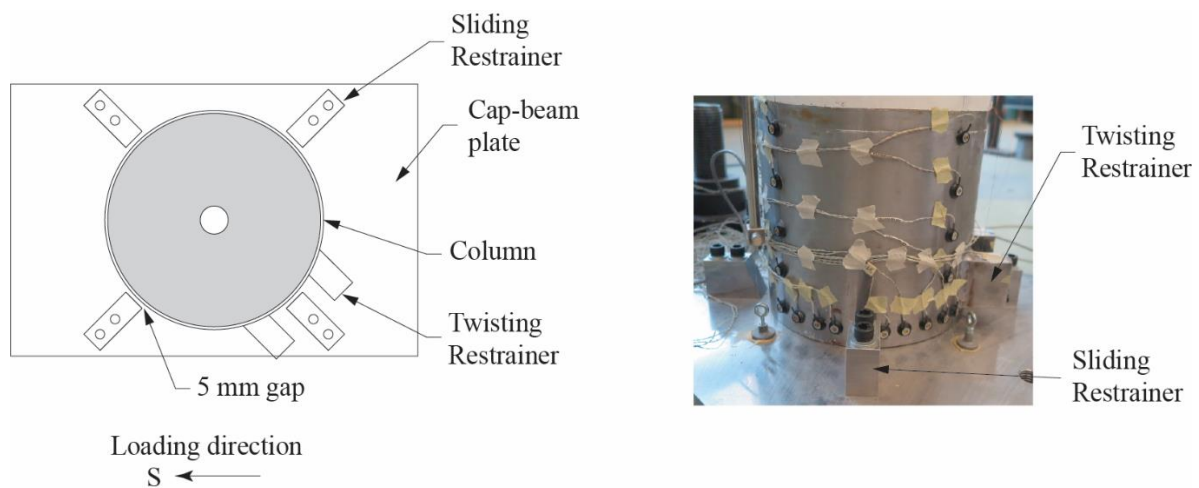
Figure 5.8. Schematic illustration (left) and photo (right) of the motion restrainers.

5.3.3. Restraining system

The tests were performed under a vertical load $V = 52.2$ kN that would correspond to a normalized axial load ($v = N/(A_c \times f_{cd})$) of 5% in the columns, which is on the low side but typical for bridge columns (Mashal & Palermo, 2019). The target stiffness of the restraining system was obtained by setting $u_{cap} = 4b = 515$ mm. In the prototype scale this corresponds to an enormous displacement capacity of 2.58 m, but seismic joints of this capacity can be manufactured. Based on these properties, Equation (5.3) gives a target stiffness of the restraining system of $k_{res} = 2302$ kN/m.

The restraining system comprised a tendon in series with a spring system.

The unbonded tendon had a nominal cross-section area of 150 mm^2, a Young's modulus of 190 GPa, and total length of 2352 mm. Thus, its axial stiffness is 12,117 kN/m. Its yield and ultimate characteristic strength are 1590 MPa and 1770 MPa. It had threaded sockets at its ends and it was anchored in the bottom end of the column, as Detail 1 of Figure 5.5 shows. The other end was anchored at the top of the springs with a nut.

The spring system comprised disc springs, also known as "Belleville washers", i.e. conical shells that are loaded along their axis (Figure 5.9a). Multiple disc springs may be stacked to modify the total stiffness of the spring assembly. Stacking in the same direction results in a system with stiffness equal to the sum of the component springs (like adding helical springs in parallel). Stacking in an alternating direction is the same as adding helical springs in series, resulting in a system with total flexibility equal to the sum of the component springs (like adding helical springs in series). Mixing and matching directions allow a specific spring constant and deflection capacity to be designed. This can be proven useful in designing systems with adaptable stiffness, like e.g. the double and triple concave spherical isolation bearings (Becker & Mahin, 2012; Fenz & Constantinou, 2006, 2008). The force–deformation relation of each spring is given in closed form by Almen & Laszlo (1936). Each spring can present hardening, softening or linear behavior, depending on each geometry.

In this work, 11 disc springs having dimensions 200/92/10 mm (external diameter / internal diameter / thickness) were used, all stacked in alternate direction (Figure 5.9a). The displacement capacity of each spring was 5.6 mm, resulting in a displacement capacity of the stack equal to 61.6 mm.

The force–deformation diagram of the stack of the springs, as predicted by the Almen & Laszlo (1936) equations, presents a mild softening behaviour and is shown in Figure 5.9b. The same plot shows the force–deformation curves of the assembly of the springs (as measured during the tests) and of the spring-tendon system, as predicted by Almen & Laszlo (1936) and assuming linear behavior of the tendon. The secant stiffness of the system at 45 mm (which is roughly equal to the restraining system deformation when the column tilts to the target displacement of 515 mm) is 2,500kN/m, which is 9% larger than the 2,300kN/m target value.
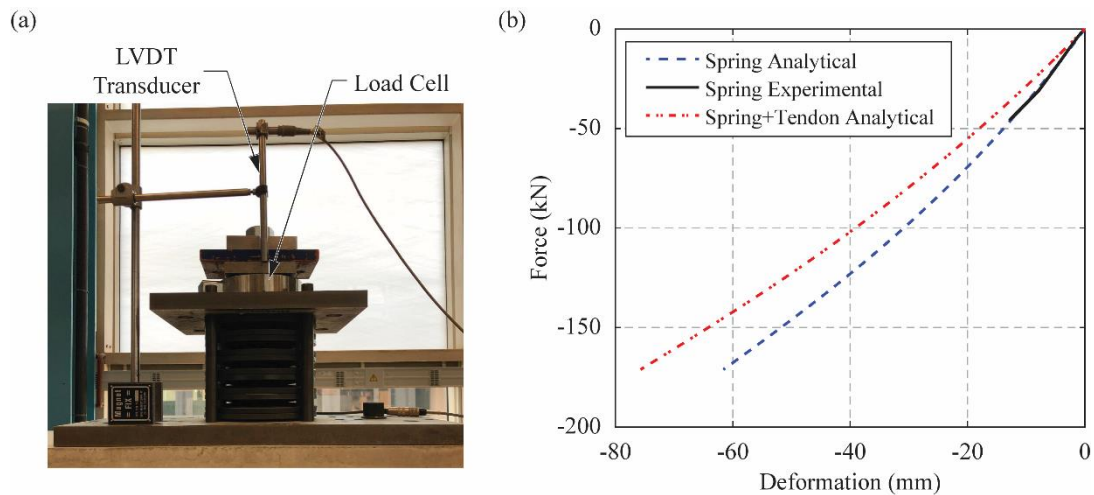
Figure 5.9. Left: Disc Springs used in the test; Right: Force-deformation diagrams for the assembly of all 11 springs.

5.3.4. Steel reinforcement

Columns J and D had identical reinforcement that was designed to resist the internal moment and shear generated when the column rotates to a displacement equal to *4b* = 515.6 mm. The internal moment and shear generated at this rotation were computed using Equations (5.5)-(5.7) to determine the acting internal forces and moments and the Eurocode 2 (EC2), EN-1992–1–1 Design of Concrete Structures (CEN, 2004) to determine the resistance. This resulted in a longitudinal reinforcement composed of 6 B500B rebars of 8 mm-diameter (A_s = 3.02 cm^2) distributed uniformly along the circular perimeter of the column. The longitudinal reinforcement was welded on the steel plate at the column ends.

The transverse reinforcement comprised an 8 mm-diameter B500B spiral, only to satisfy the minimum transverse reinforcement ratio required by the Eurocode 2 (A_{sw}/s = 0.022 cm^2/cm).

The contribution of the jacket on both the moment and the shear strength was neglected.

5.4. Test setup and instrumentation

Figure 5.10a schematically shows the test setup. It consisted of two vertical and a horizontal actuator. The three actuators can apply forces or displacements to a steel beam, which was connected to the cap-beam with short wide flange steel beams. The steel beam is constrained, and its out-of-plane displacement is not allowed.
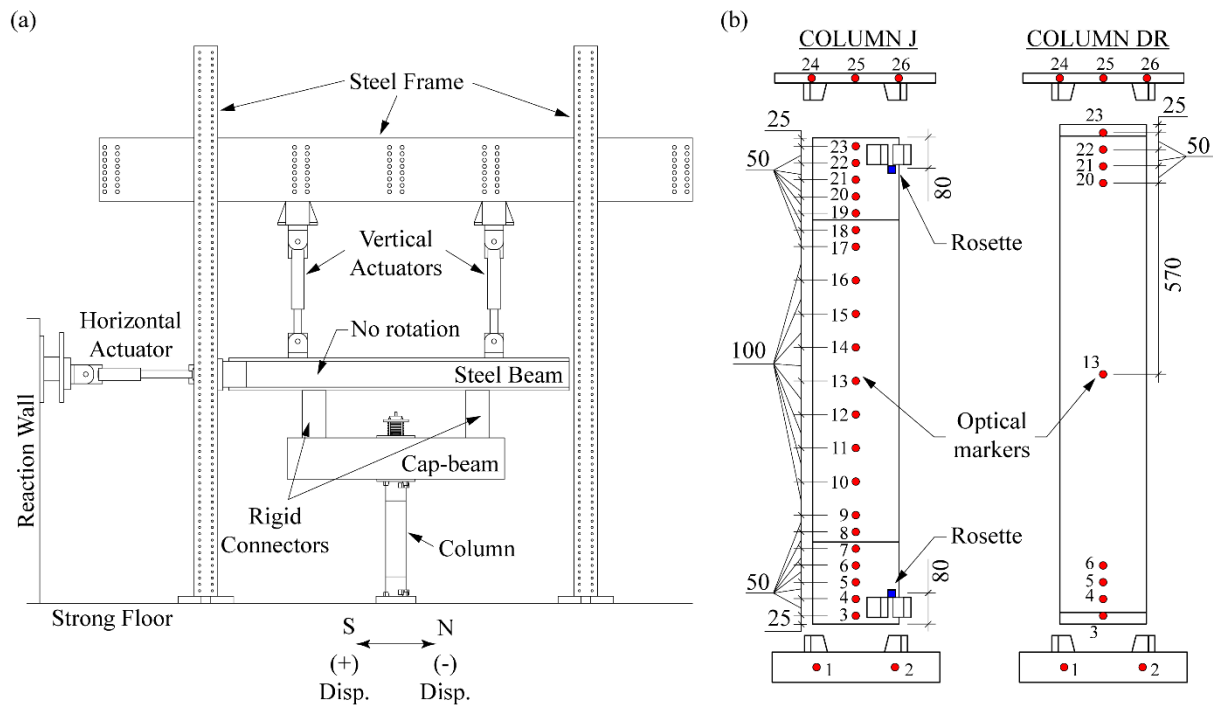
Figure 5.10. (a) Test setup and (b) position of the optical markers and rosettes installed on columns J and DR.

The setup kept the vertical force applied to the column constant and equal to 52.20 kN, simulating the gravitational loads of the super-structure. The axial load that was applied during testing was chosen so that the normalized axial load $v = N/(f_{cd} \times A_c)$ falls within the range of tests performed on rocking bridge columns. Mashal & Palermo (2019) tested under $v = 2\%$ which they consider representative of a typical highway bridge in New Zealand, while Thonstad et al. (2017) tested under $v = 7.5\%$. The axial load of the tests presented in this paper gives $v = 5\%$.

Using an Inova EU 3000 RTC control system, the difference of the stroke of the vertical actuators was kept constant and equal to zero. This constraint guaranteed that the cap and steel beam could move up and down without rotating.

For the cyclic test, the horizontal actuator applied the displacements defined in the loading protocol shown in Figure 5.11. The loading protocol consisted of two consecutive cycles of the same drift ratio, followed by a subsequent cycle of 1.25 times the previous drift ratio. In total, the columns were subjected to 18 sets of two cycles each. The loading protocol was based on the American Concrete Institute recommendations. Since the most recent report (ACI, 2013) specifies that the drift ratio must be increased based on the yield strain (not applicable in this case), the increase of the drift ratios was based on an older report (ACI, 2001)

and the first cycle had a drift of 0.36%. The maximum drift ratio for the cyclic tests was 15%, as this reached the stroke of the horizontal actuator. The drift was applied at 1.38×10^{-4}/s rate.
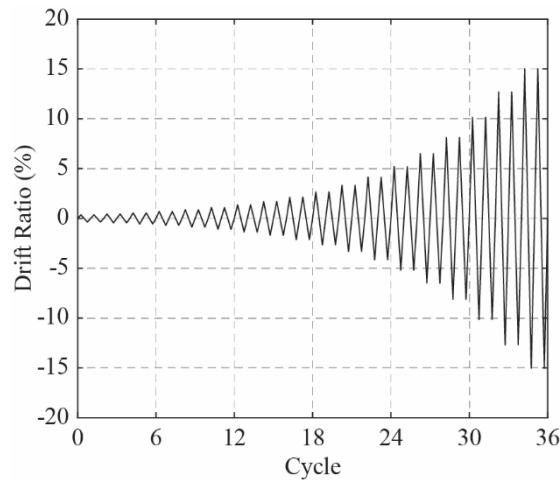
Figure 5.11. Cyclic Loading Protocol.

To explore the behaviour to even larger drift ratios, column J was subjected to a monotonic test up to 30% drift, applied at a 1.38×10^{-4}/s rate.

The displacements of the column and cap-beam were measured by an optical measurement device that tracks the positions of markers fixed in the specimen. Column J was tested first and it was observed that flexural deformation was minimal. Therefore, less markers along the height of the column were used when testing column DR. The forces and strokes of all actuators were recorded by load cells and integrated displacement sensors installed on them. A load cell and a Linear Variable Differential Transformer (LVDT) were also installed in series with the springs and tendon, recording the forces in the restraining system and the springs deformation, respectively. Rosettes measured the strain in the steel jacket.

5.5. Results

5.5.1. Force-drift loops

This paper only reports the results of columns J and DR. The results of column D (i.e. the one that was damaged because of problematic casting) are not discussed.

Figure 5.12-Figure 5.13 present the force-drift response for low drift ratios (up to 1.1%), medium drift ratios (up to 4.2%), and high drift ratios (up to 15%). The drift ratio is defined herein as the ratio between the horizontal displacement of the beam and the height of the

column (1450 mm and 1490 mm for the J and DR columns, respectively). Positive drifts are towards the South (Figure 5.10).
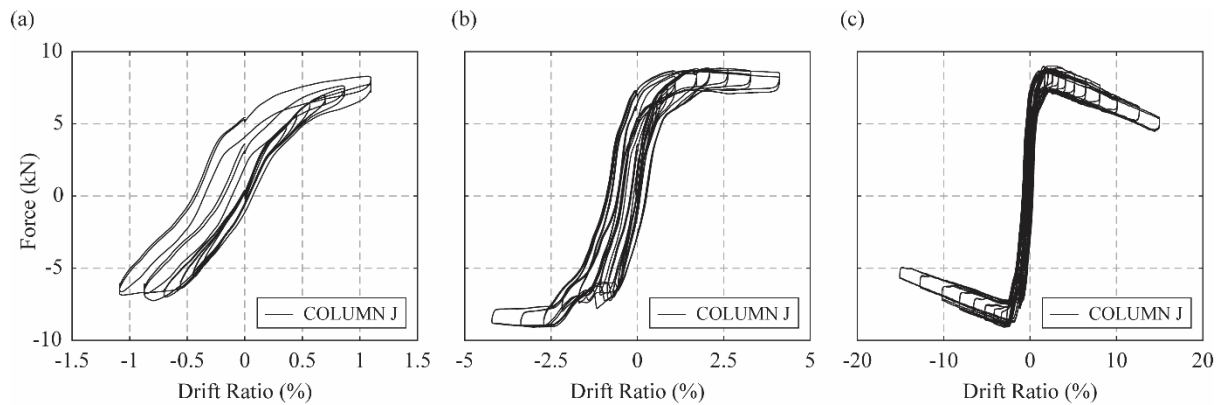
Figure 5.12. Force-drift relation for: (a) low drift ratio, (b) medium drift ratio, and (c) high drift ratio.
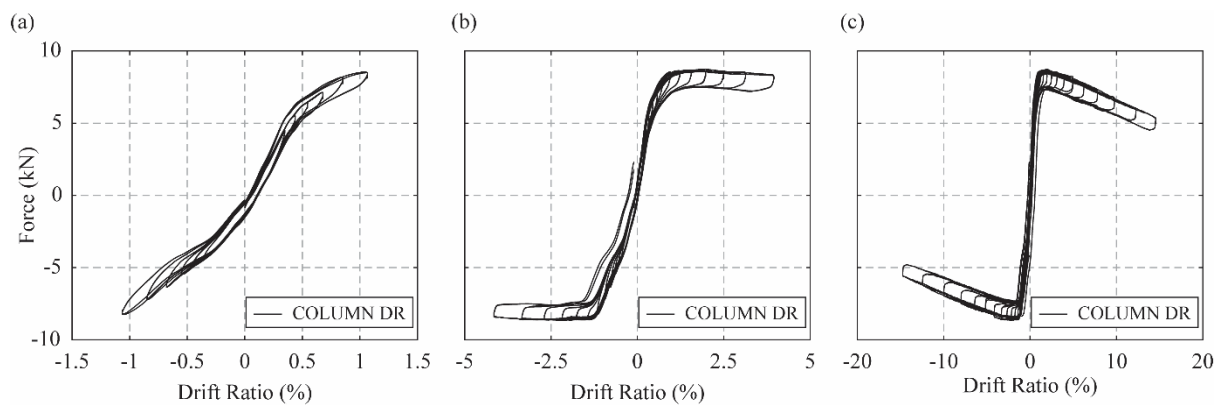
Figure 5.13. Force-drift relation for: (a) low drift ratio, (b) medium drift ratio, and (c) high drift ratio.

Both columns present almost no strength reduction even when tested up to 15%. Apparently, there is some energy dissipation as the loops do encompass some area. However, as a) there is no damage to the columns and b) energy dissipation is present even in small amplitude cycles where there was no sliding, there seems to be no physically plausible energy dissipation mechanism apart of setup internal friction, mainly at the actuator clevises.

In future tests, a 3DOF load cell should be used underneath the column to measure the horizontal force that is actually applied to the column (without the setup friction), as typically done when testing seismic isolation devices (e.g. Cilsalar & Constantinou (2019)).

Sliding did occur (as can be seen in Figure 5.12a,b and Figure 5.13b) but it was smaller

than 5 mm and the sliding restrainers did not engage. Due to setup imperfections, some out-of-plane motion (on the order of 10% of the in-plane) occurred when the specimen moved towards the negative displacement. This caused some minor twisting and this is the reason for the slight asymmetry of the force deformation loops (Figure 5.12-Figure 5.13).

Figure 5.14 compares the force-drift response predicted by rigid-body calculations, and the obtained response at the largest drift ratio (15%). Two curves are presented for the force-drift response of the rigid-body: assuming that the restraining system (1) exhibits the force deformation curve given by the analytical curve of Figure 5.9 ("Analyt. Restr."); (2) exhibits the force deformation curve obtained experimentally ("Exp. Restr."). In both curves the gap between the tendon and the duct is neglected, as it is less than 9 mm while the halfwidth of the column is 129 mm. The column is assumed rigid with dimensions equal to the dimensions of the tested columns (257.8 mm-diameter and 1450 mm-height, and 257.8 mm-diameter and 1490 mm-height for columns J and DR, respectively), and constant vertical load of 52.20 kN.
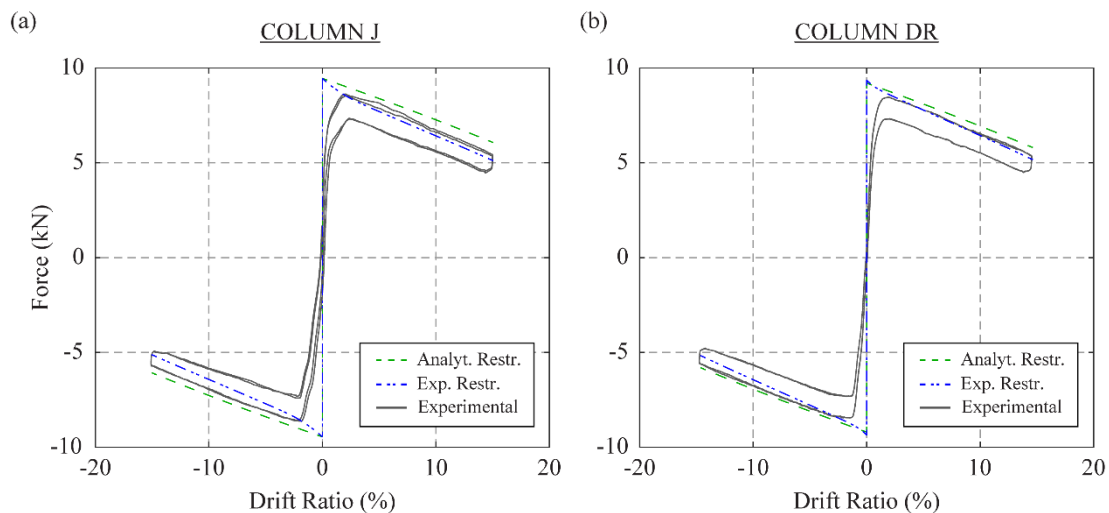
Figure 5.14. Force-drift envelopes for: (a) Column J, and (b) Column DR.

Figure 5.14 shows that there exists some deviation between the predicted behavior of the restraining system, and the one observed experimentally, apparently contradicting the good approximation stated in Figure 5.9. However, Figure 5.9 compares only the behavior of the springs with its analytical equation, and not of the complete restraining system. Therefore, the deviation observed in the response could be related to the tendon, which might be more flexible than predicted by its specifications.

Table 5.1 offers a comparison between tests and the different variations of the analytical model in terms of peak load, drift at peak load, and post uplift stiffness. For the experimental

tests, the post uplift stiffness is defined as the slope of the loading branch between 3% and 15% drift ratio.

Table 5.1. Comparison between tests and the different variations of the analytical model in terms of peak load, drift at peak load, and post uplift stiffness.

|		Tests (+drift/ -drift)	Analyt. Restr.	Exp. Restr.
Colum J	Peak load (kN)	8.57/-8.62	9.45	9.45
	Drift at peak load (%)	1.81/-1.95	0	0
	Post uplift stiffness (kN/m)	-17.54/-15.87	-15.49	-18.42
Column DR	Peak load (kN)	8.46/-8.43	9.45	9.45
	Drift at peak load (%)	1.90/-1.83	0	0
	Post uplift stiffness (kN/m)	-17.19/-16.23	-15.49	-18.42

Overall, the flexibility of the tested system only causes a slight deviation from the rigid body model, that is non-negligible only for drift ratios smaller than 2–3%, essentially before the column uplifts. For design level earthquakes the displacement is expected to be more than the threshold of 2–3% that corresponds to 15–20 cm of displacement in the prototype scale. This shows that a) The displacement of the column sourcing from flexural deformation is minimal compared to the one sourcing from rigid body rotation and b) That the compression zone at the column protected ends is essentially a compression point, as visible during the tests. The above is confirmed by the deflection shapes that are offered in Figure 5.15 in increments of 3% drift ratio.

5.5.2. Observed damage

At the end of the test, a very slight dent caused by local buckling could be noticed at the top jacket of column J (Figure 5.16b). The dent resulted in minor gap between the column end and the steel plate of the beam (Figure 5.16a). Judging by the voids caused by trapped air pockets in column D, it is reasonable to assume that the dent is due to non visible air pockets trapped inside the jackets. The dent first appeared at a drift of 12.7%. The influence of the dent in the overall behavior of the column is negligible, as the force–deformation loops show no deterioration. No cracks or concrete spalling of the column was observed. The bottom steel jacket did not present any damage visually observed, as a smaller moment is acting on it. Peeling of the concrete paint was observed at the end of the steel jacket (Figure 5.17a). Column DR, presented no observable damage.
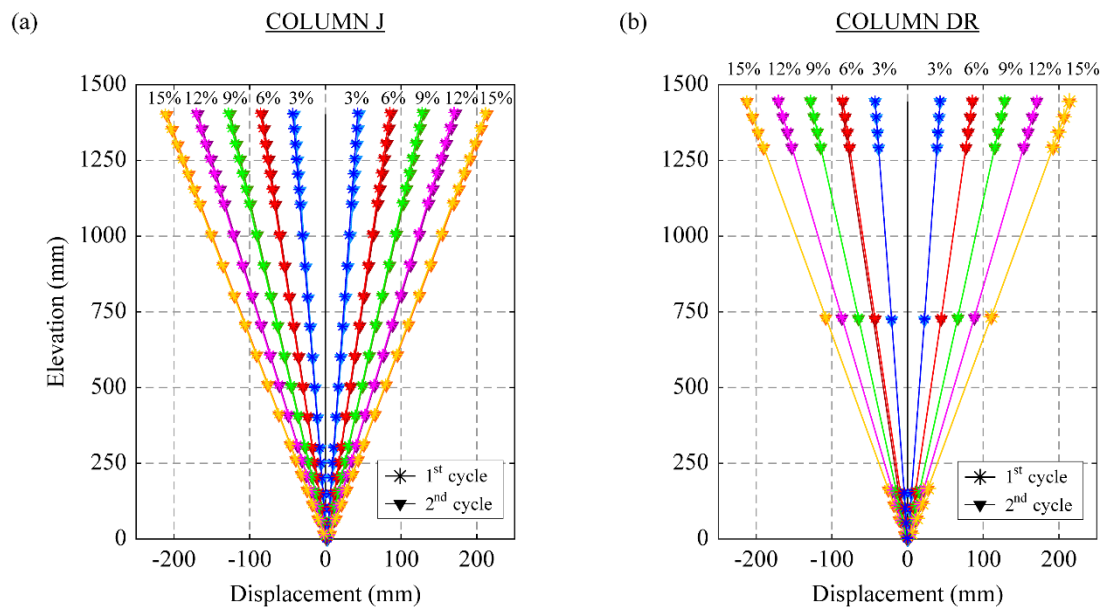
Figure 5.15. Deflection shapes of the columns for several drift amplitudes.
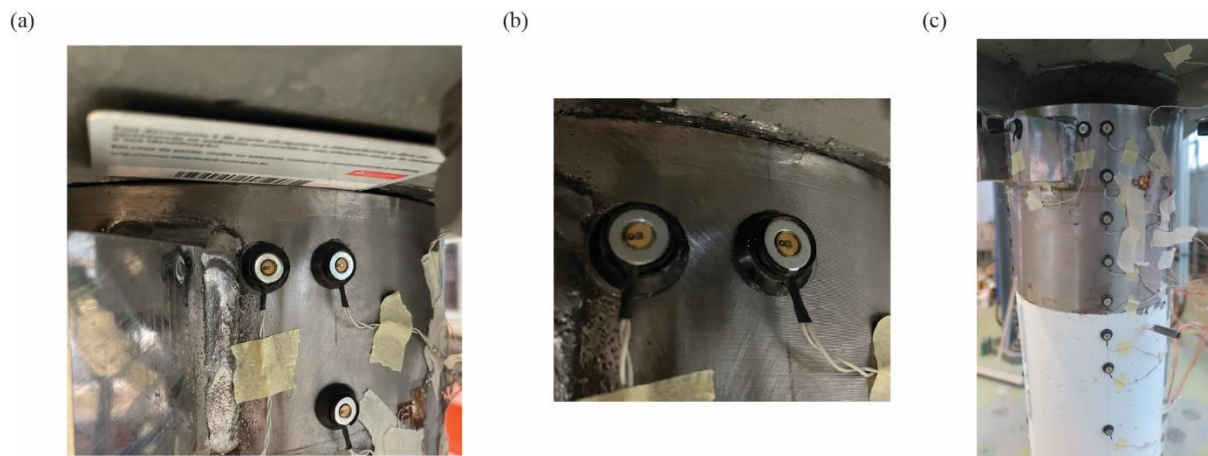
Figure 5.16. Dent observed at the top end of column J. a) A 1 mm thickness card can fit in between the column and the cap beam in the at-rest position b) Close view of the dent c) Side view of the jacket that shows that there is no other damage apart from the dent.

5.5.3. Strain in the steel jackets

Rosettes were placed in both steel jackets at their north side and at 8 cm from the column ends (Figure 5.17a). Figure 5.17b presents the envelope of the normalized longitudinal and hoop strain in both steel jackets. The strains were normalized to the unidirectional yield strain of the steel.
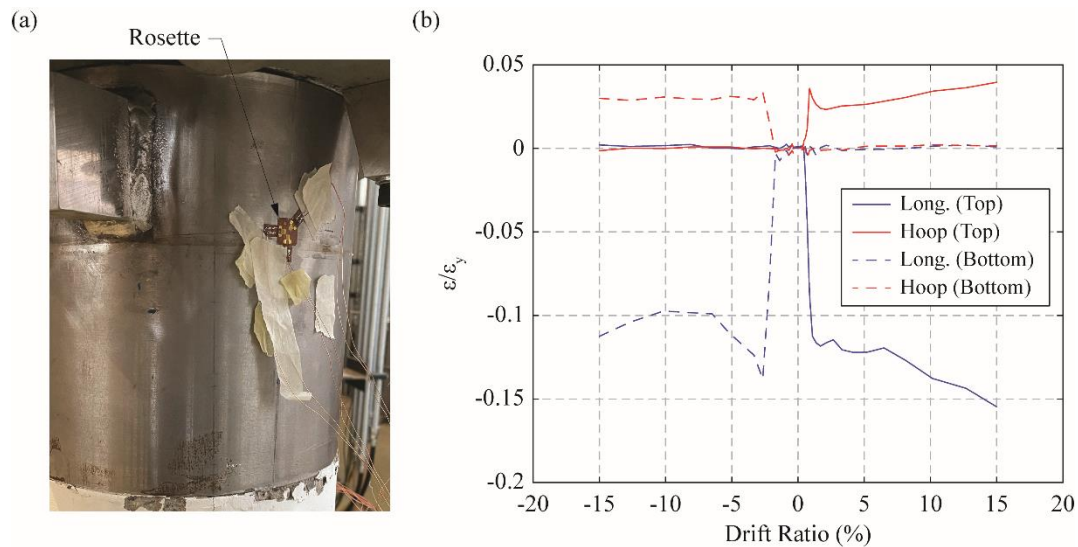
Figure 5.17. (a) Rosettes used to measure strain (b) Envelopes of normalized stress at the steel jackets of column J.

There was zero longitudinal and hoop strain in both steel jackets when their north edge was not in contact with the steel plates fixed to ground or cap-beam. Once the north edge was in contact with the plates, the steel jackets presented compressive strains in the longitudinal direction, and tensile strains in the hoop direction.

Until the system went into the negative stiffness region, the strain magnitude in the top and bottom steel jacket is the same and increases with drift. Once the column enters the negative stiffness region (i.e. when there is a clear uplift), the strain magnitude in the top steel jacket continues to increase, although at a smaller rate. This increase is due to the extra compressive force acting at the edge of the column, applied by the beam to equilibrate the tendon force. On the contrary, the strain at the bottom does not significantly change, as the tendon is anchored within the column and at the center of the cross section.

The strain magnitudes reached 4% and 15% of the steel unidirectional yield strain in the hoop and longitudinal direction, respectively.

5.5.4. Load in the restraining system

Figure 5.18 presents the envelope of the load in the restraining system (tendon plus springs) as measured in the tests and as predicted using Almen & Laszlo (1936) equations. The measured load increased linearly with the drift ratio, and it is in good agreement with the one calculated. It can be noted that the restraining system is more flexible than predicted analytically. This is

in agreement with the steeper force–deformation curve observed in Figure 5.14, when the drift-force response is calculated using the experimental force deformation curve of the restraining system.
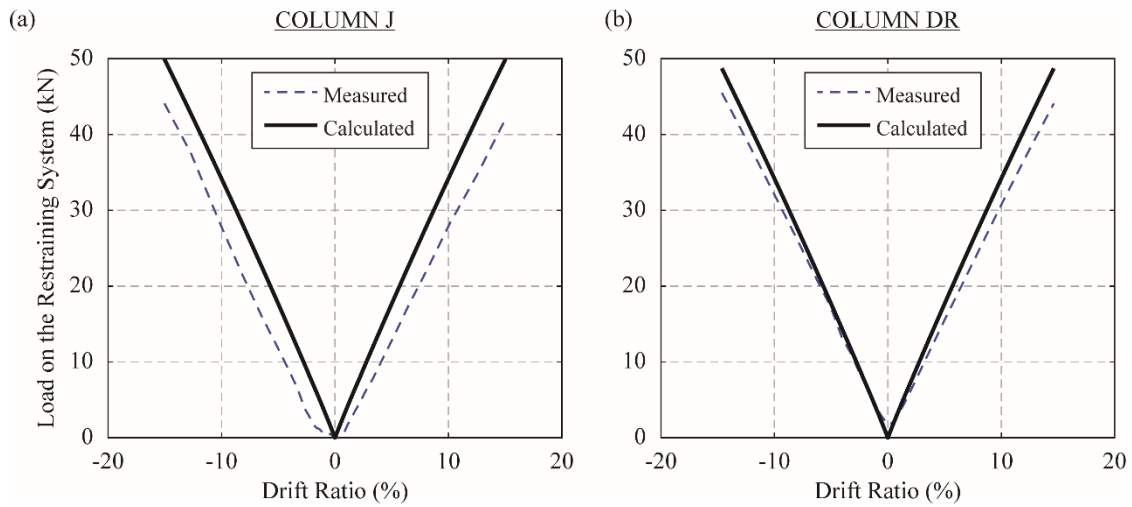
**Figure 5.18.** Measured and calculated load in the restraining system.

Since the yielding load of the tendon is 238 kN, it did not exceed its linear range during the cyclic tests. The springs also did not reach their load capacity of 171.2 kN.

5.5.5. One direction monotonic loading

In order to test for larger drift rates, the test setup was reconfigured so that the stroke of the actuator is −240 mm when the column is vertical. With this configuration, the system was subjected to a drift ratio of 31.8% (Figure 5.19). Similarly to the cyclic test, the vertical force was constant and equal to 52.2 kN during the entire test.

Figure 5.20a presents the measured force–deformation curve. The measured system's strength was 8.77 kN, which is almost equal to the strength observed in the cyclic test (8.90 kN). In the pushover test, the system was pulled to the south direction, which led the contact region at the interface between the column and the cap-beam to be the north-edge, the same that presented the dent at the end of the cyclic test (Figure 5.16b). Hence, it can be concluded that the minor dent did not affect the strength of the system.

Figure 5.20b shows the column after the test to 31.8% drift ratio. No further damage, other than the one observed at the end of the cyclic test, could be noticed. No spalling of the concrete was observed.
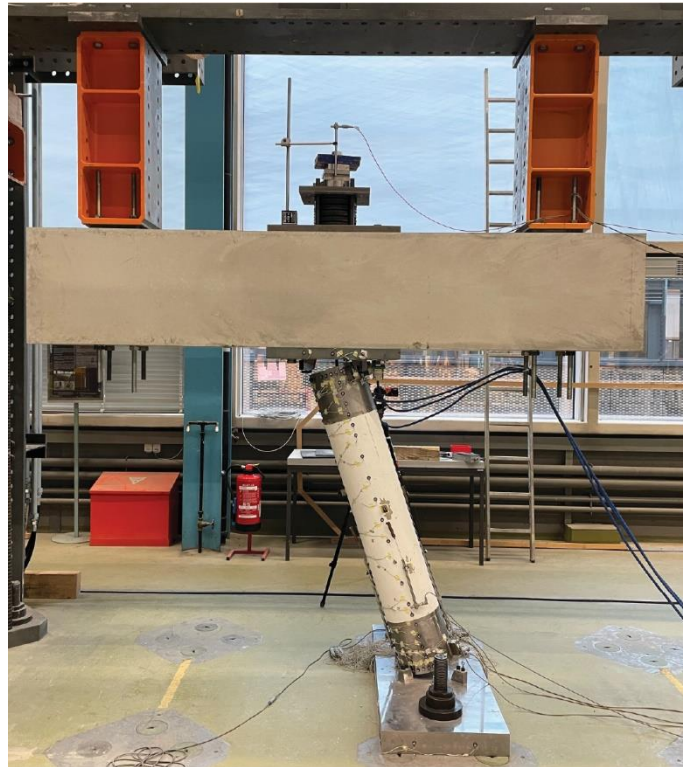
Figure 5.19. Column J subjected to a drift ratio of 31.8%.
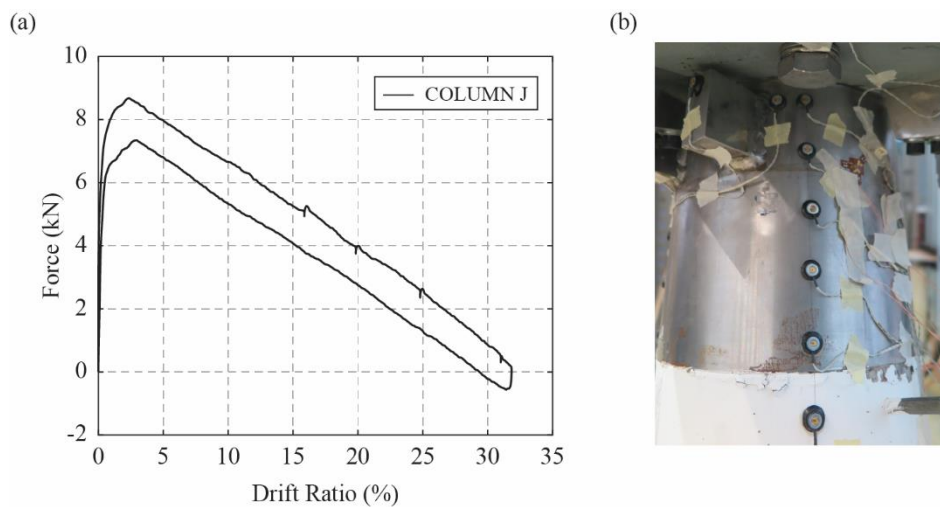
Figure 5.20. (a) Pushover curve of Column J; (b) Column J at 31.8% drift ratio.

The restraining system reached a maximum force of 86.3 kN, a value that it is still in the elastic range of the tendon. Only the rosette at the top of the steel jacket measured non-zero strain. The strains followed the same pattern observed in the cyclic tests, reaching 6% and 20% of the unidirectional yield strain of the steel in the hoop and longitudinal direction, respectively.

5.6. Conclusions

A subassembly comprising a restrained (or "controlled") rocking column and a beam was tested. The column was equipped with an unbonded tendon in series with disc springs. The bottom end of the tendon was anchored at the bottom of the column, while the top end was anchored at the top of the cap beam, in series with the springs. The restraining system was designed to be flexible enough, so that the overall post uplift stiffness of the system remains negative. This approach reduces the design forces and moments of bridge foundations and can lead to the reduction of their size, which can lead to a significant save of material – hence contribute to sustainable design of bridges. It could be perceived as a seismic isolation method for restrained rocking structures, in the sense that it uses a device (i.e. the springs) to make the system more flexible and reduce the design forces at the expense of larger displacements.

Two variations of the columns were tested: One had steel jackets at its ends, while the other annular steel plates.

The steel jacketed column was tested to a 30% drift, while the column with steel plates to 15% drift without any damage. The only observable damage was a slight dent in the column with the steel jackets. The dent was likely due to improper casting that left voids within the jackets. Hence, the system is resilient.

The strain at the steel jacket was smaller than 20% of the yield strain (where it was measured), even though it is expected that it was larger closer to the column end.

The behavior of the restraining system is simple and predictable by an analytical model used for disc springs.

Sliding was smaller than 5 mm, hence the sliding restrainers did not engage in these tests. However, sliding could be larger in 3D shake table testing, because the objects slide more easily during 3D rocking motion.

A Housner-like (Housner, 1963) rigid body model that assumes a contact point rather than a contact region between the column and the base or the foundation was able to capture the behavior of the system with reasonable accuracy for drifts larger than 2–3%. In prototype scale this corresponds to 15–20 cm, which is smaller than the displacement expected for the design level earthquake for such a system. The influence of the deviation of the analytical and experimental curves during the first 2–3% of drift on the dynamic response of such a system needs to be furtherly studied.

Declaration of Competing Interest

The authors declare that they have no known competing financial interests or personal relationships that could have appeared to influence the work reported in this paper.

Acknowledgment

References

ACI. (2001). *Acceptance criteria for moment frames based on structural testing* (Rep. No. ACI T1.1-01).

ACI. (2013). *Guide for Testing Reinforced Concrete Structural Elements under Slowly Applied Simulated Seismic Loads* (Rep. No. ACI 374.2R-13).

Agalianos, A., Psychari, A., Vassiliou, M. F., Stojadinovic, B., & Anastasopoulos, I. (2017). Comparative Assessment of Two Rocking Isolation Techniques for a Motorway Overpass Bridge. *Frontiers in Built Environment*, *3*.

Almen, J. O., & Laszlo, A. (1936). The uniform-section disk spring. *Trans. Am. Soc. Mech. Eng.*, *58*(4).

Becker, T. C., & Mahin, S. A. (2012). Experimental and analytical study of the bi-directional behavior of the triple friction pendulum isolator. *Earthquake Engineering & Structural Dynamics*, *41*(3), 355–373.

Billington, S. L., & Yoon, J. K. (2004). Cyclic Response of Unbonded Posttensioned Precast Columns with Ductile Fiber-Reinforced Concrete. *Journal of Bridge Engineering*, *9*(4), 353–363.

Bu, Z.-Y., Ou, Y.-C., Song, J.-W., & Lee, G. C. (2016). Hysteretic Modeling of Unbonded Posttensioned Precast Segmental Bridge Columns with Circular Section Based on Cyclic Loading Test. *Journal of Bridge Engineering*, *21*(6), 04016016.

Calvi, G., Palermo, A. G., & Pampanin, S. (2004). *Use of 'controlled rocking' in the seismic design of bridges*. 13th World Conference on Earthquake Engineering (13 WCEE), Vancouver, Canada.

CEN. (2004). *Eurocode 2: Design of concrete structures—Part 1-1: General rules and rules for buildings*. Comité Européen de Normalisation.

Chen, X., & Li, J. (2021). Seismic fragility analysis for tall pier bridges with rocking foundations. *Advances in Bridge Engineering*, *2*(1), 7.

Cheng, C.-T. (2008). Shaking table tests of a self-centering designed bridge substructure. *Engineering Structures*, *30*(12), 3426–3433.

Chou, C.-C., Chang, H.-J., & Hewes, J. T. (2013). Two-plastic-hinge and two dimensional finite element models for post-tensioned precast concrete segmental bridge columns. *Engineering Structures*, *46*, 205–217.

Chou, C.-C., & Chen, Y.-C. (2006). Cyclic tests of post-tensioned precast CFT segmental bridge columns with unbonded strands. *Earthquake Engineering & Structural Dynamics*, *35*(2), 159–175.

Chou, C.-C., & Hsu, C.-P. (2008). Hysteretic model development and seismic response of

unbonded post-tensioned precast CFT segmental bridge columns. *Earthquake Engineering & Structural Dynamics*, *37*(6), 919–934.

Christopoulos, C. (2004). Frequency Response of Flag-Shaped Single Degree-of-Freedom Hysteretic Systems. *Journal of Engineering Mechanics*, *130*(8), 894–903.

Christopoulos, C., Tremblay, R., Kim, H.-J., & Lacerte, M. (2008). Self-Centering Energy Dissipative Bracing System for the Seismic Resistance of Structures: Development and Validation. *Journal of Structural Engineering*, *134*(1), 96–107.

Cilsalar, H., & Constantinou, M. C. (2019). *Development and Validation of a Seismic Isolation System For Lightweight Residential Construction* (Rep. No. MCEER.19-0001).

Cohagen, L. S., Pang, J. B. K., Stanton, J. F., & Eberhard, M. O. (2008). *A Precast Concrete Bridge Bent Designed to Re-Center after an Earthquake* (Rep No. WA-RD 684.3/TNW 2008-09). Washington State Department of Transportation.

Dimitrakopoulos, E. G., & Giouvanidis, A. I. (2015). Seismic Response Analysis of the Planar Rocking Frame. *Journal of Engineering Mechanics*, *141*(7), 04015003.

ElGawady, M. A., & Sha'lan, A. (2011). Seismic Behavior of Self-Centering Precast Segmental Bridge Bents. *Journal of Bridge Engineering*, *16*(3), 328–339.

Fenz, D. M., & Constantinou, M. C. (2006). Behaviour of the double concave Friction Pendulum bearing. *Earthquake Engineering & Structural Dynamics*, *35*(11), 1403–1424.

Fenz, D. M., & Constantinou, M. C. (2008). Spherical sliding isolation bearings with adaptive behavior: Experimental verification. *Earthquake Engineering & Structural Dynamics*, *37*(2), 185–205.

Giouvanidis, A. I., & Dimitrakopoulos, E. G. (2017). Seismic Performance of Rocking Frames with Flag-Shaped Hysteretic Behavior. *Journal of Engineering Mechanics*, *143*(5), 04017008.

Giouvanidis, A. I., & Dimitrakopoulos, E. G. (2018). Rocking amplification and strong-motion duration. *Earthquake Engineering & Structural Dynamics*, *47*(10), 2094–2116.

Giouvanidis, A. I., & Dong, Y. (2020). Seismic loss and resilience assessment of single-column rocking bridges. *Bulletin of Earthquake Engineering*, *18*(9), 4481–4513.

Guerrini, G., Restrepo, J. I., Massari, M., & Vervelidis, A. (2015). Seismic Behavior of Posttensioned Self-Centering Precast Concrete Dual-Shell Steel Columns. *Journal of Structural Engineering*, *141*(4), 04014115.

Housner, G. W. (1963). The behavior of inverted pendulum structures during earthquakes. *Bulletin of the Seismological Society of America*, *53*(2), 403–417.

Kashani, M. M., Gonzalez-Buelga, A., Thayalan, R. P., Thomas, A. R., & Alexander, N. A. (2018). Experimental investigation of a novel class of self-centring spinal rocking column. *Journal of Sound and Vibration*, *437*, 308–324.

Li, C., Bi, K., & Hao, H. (2019). Seismic performances of precast segmental column under bidirectional earthquake motions: Shake table test and numerical evaluation. *Engineering Structures*, *187*, 314–328.

Liu, R., & Palermo, A. (2017). Quasi-Static Testing of a 1/3 Scale Precast Concrete Bridge Utilising a Post-Tensioned Dissipative Controlled Rocking Pier. *Proceedings of 16th World Conference on Earthquake Engineering*. 16th World Conference on Earthquake Engineering, Santiago, Chile.

Liu, R., & Palermo, A. (2020). Multi-"Hinge" Hierarchical Activation to Improve Structural Robustness of Post-tensioned Rocking Piers. *Special Publication*, *341*, 202–225.

Makris, N., & Konstantinidis, D. (2003). The rocking spectrum and the limitations of practical design methodologies. *Earthquake Engineering & Structural Dynamics*, *32*(2), 265–289.

Makris, N., & Vassiliou, M. F. (2013). Planar rocking response and stability analysis of an array of free-standing columns capped with a freely supported rigid beam. *Earthquake Engineering & Structural Dynamics*, *42*(3), 431–449.

Makris, N., & Vassiliou, M. F. (2015). Dynamics of the Rocking Frame with Vertical Restrainers. *Journal of Structural Engineering*, *141*(10), 04014245.

Mander, J. B., & Cheng, C. T. (1997). *Seismic Resistance of Bridge Piers Based on Damage Avoidance Design* (Techncial Report NCEER-97-0014; pp. 1–144). National Center for Earthquake Engineering Research.

Marriott, D., Pampanin, S., & Palermo, A. (2009). Quasi-static and pseudo-dynamic testing of unbonded post-tensioned rocking bridge piers with external replaceable dissipaters. *Earthquake Engineering & Structural Dynamics*, *38*(3), 331–354.

Mashal, M., & Palermo, A. (2019). Low-Damage Seismic Design for Accelerated Bridge Construction. *Journal of Bridge Engineering*, *24*(7), 04019066.

Motaref, S., Saiidi, M. S., & Sanders, D. (2014). Shake Table Studies of Energy-Dissipating Segmental Bridge Columns. *Journal of Bridge Engineering*, *19*(2), 186–199.

Nakaki, S. D., Stanton, J. F., & Sritharan, S. (1999). An Overview of the PRESSS Five-Story Precats Test Building. *PCI Journal*, *44*(2), 26–39.

Ou, Y.-C., Tsai, M.-S., Chang, K.-C., & Lee, G. C. (2010). Cyclic behavior of precast segmental concrete bridge columns with high performance or conventional steel reinforcing bars as energy dissipation bars. *Earthquake Engineering & Structural Dynamics*, *39*(11), 1181–1198.

Palermo, A., Pampanin, S., & Carr, A. J. (2005). *Efficiency of simplified alternative modelling approaches to predict the seismic response of precast concrete hybrid systems*. fibSymposium "Keep Concrete Attractive".

Palermo, A., Pampanin, S., & Marriott, D. (2007). Design, Modeling, and Experimental Response of Seismic Resistant Bridge Piers with Posttensioned Dissipating Connections. *Journal of Structural Engineering*, *133*(11), 1648–1661.

Panagiotou, M., Trono, W., Jen, G., Kumar, P., & Ostertag, C. P. (2015). Experimental Seismic Response of Hybrid Fiber-Reinforced Concrete Bridge Columns with Novel Longitudinal Reinforcement Detailing. *Journal of Bridge Engineering*, *20*(7), 04014090.

Priestley, M. J. N., Sritharan, S., Conley, J. R., & Pampanin, S. (1999). Preliminary Results and Conclusions from the PRESSS Five-Story Precast Concrete Test Building. *PCI Journal*, *44*(6), 42–67.

Priestley, M. J. N., & Tao, J. R. (1993). Seismic Response of Precast Prestressed Concrete Frames With Partially Debonded Tendons. *PCI Journal*, *38*(1), 58–69.

Qu, H., Li, T., Wang, Z., Wei, H., Shen, J., & Wang, H. (2018). Investigation and verification on seismic behavior of precast concrete frame piers used in real bridge structures: Experimental and numerical study. *Engineering Structures*, *154*, 1–9.

Reggiani Manzo, N., & Vassiliou, M. F. (2019). Displacement-based analysis and design of rocking structures. *Earthquake Engineering & Structural Dynamics*, *48*(14), 1613–1629.

Reggiani Manzo, N., & Vassiliou, M. F. (2021). Simplified analysis of bilinear elastic systems exhibiting negative stiffness behavior. *Earthquake Engineering & Structural Dynamics*, *50*(2), 580–600.

Restrepo, J. I., & Rahman, A. (2007). Seismic Performance of Self-Centering Structural Walls Incorporating Energy Dissipators. *Journal of Structural Engineering*, *133*(11), 1560–1570.

Routledge, P. J., Cowan, M. J., & Palermo, A. (2016). Low-damage detailing for bridges—A case study of Wigram-Magdala Bridge. *Proceedings of the New Zealand Society for Earthquake Engineering Annual Conference*. 2016 NZSEE Conference.

Sakai, J., Jeong, H., & Mahin, S. (2006). *Reinforced concrete bridge columns that re-center following earthquakes*. 8th U.S. National Conference on Earthquake Engineering, San Francisco, USA.

Sideris, P., Aref, A. J., & Filiatrault, A. (2014a). Large-Scale Seismic Testing of a Hybrid

Sliding-Rocking Posttensioned Segmental Bridge System. *Journal of Structural Engineering*, *140*(6), 04014025.

Sideris, P., Aref, A. J., & Filiatrault, A. (2014b). Quasi-Static Cyclic Testing of a Large-Scale Hybrid Sliding-Rocking Segmental Column with Slip-Dominant Joints. *Journal of Bridge Engineering*, *19*(10), 04014036.

Sideris, P., Aref, A. J., & Filiatrault, A. (2015). Experimental Seismic Performance of a Hybrid Sliding–Rocking Bridge for Various Specimen Configurations and Seismic Loading Conditions. *Journal of Bridge Engineering*, *20*(11), 04015009.

Sika. *Sika Monotop -412 NFG*. https://swe.sika.com/content/dam/dms/se01/7/SikaMonoTop-412%20NFG%20PB%20ENG.pdf

Stanton, J. F., Stone, W. C., & Cheok, G. S. (1997). A hybrid reinforced precast frame for seismic regions. *PCI Journal*, *42*(2), 20–23.

Thomaidis, I. M., Kappos, A. J., & Camara, A. (2020). Dynamics and seismic performance of rocking bridges accounting for the abutment-backfill contribution. *Earthquake Engineering & Structural Dynamics*, *49*(12), 1161–1179.

Thonstad, T., Kennedy, B. J., Schaefer, J. A., Eberhard, M. O., & Stanton, J. F. (2017). Cyclic Tests of Precast Pretensioned Rocking Bridge-Column Subassemblies. *Journal of Structural Engineering*, *143*(9), 04017094.

Thonstad, T., Mantawy, I. M., Stanton, J. F., Eberhard, M. O., & Sanders, D. H. (2016). Shaking Table Performance of a New Bridge System with Pretensioned Rocking Columns. *Journal of Bridge Engineering*, *21*(4), 04015079.

Trono, W., Jen, G., Panagiotou, M., Schoettler, M., & Ostertag, C. P. (2015). Seismic Response of a Damage-Resistant Recentering Posttensioned-HYFRC Bridge Column. *Journal of Bridge Engineering*, *20*(7), 04014096.

Vassiliou, M. F. (2010). *Analytical investigation of the dynamic response of a pair of columns capped with a rigid beam and of the effect of seismic isolation on rocking structures* [Ph. D.]. University of Patras.

Vassiliou, M. F. (2018). Seismic response of a wobbling 3D frame. *Earthquake Engineering & Structural Dynamics*, *47*(5), 1212–1228.

Vassiliou, M. F., Burger, S., Egger, M., Bachmann, J. A., Broccardo, M., & Stojadinovic, B. (2017a). The three-dimensional behavior of inverted pendulum cylindrical structures during earthquakes. *Earthquake Engineering & Structural Dynamics*, *46*(14), 2261–2280.

Vassiliou, M. F., Mackie, K. R., & Stojadinović, B. (2017b). A finite element model for seismic response analysis of deformable rocking frames. *Earthquake Engineering & Structural Dynamics*, *46*(3), 447–466.

Vassiliou, M. F., & Makris, N. (2015). Dynamics of the Vertically Restrained Rocking Column. *Journal of Engineering Mechanics*, *141*(12), 04015049.

Wang, J., Wang, Z., Tang, Y., Liu, T., & Zhang, J. (2018). Cyclic loading test of self-centering precast segmental unbonded posttensioned UHPFRC bridge columns. *Bulletin of Earthquake Engineering*, *16*(11), 5227–5255.

White, S., & Palermo, A. (2016). Quasi-Static Testing of Posttensioned Nonemulative Column-Footing Connections for Bridge Piers. *Journal of Bridge Engineering*, *21*(6), 04016025.

Xie, Y., Zhang, J., DesRoches, R., & Padgett, J. E. (2019). Seismic fragilities of single-column highway bridges with rocking column-footing. *Earthquake Engineering & Structural Dynamics*, *48*(7), 843–864.

Yamashita, R., & Sanders, D. H. (2009). Seismic Performance of Precast Unbonded Prestressed Concrete Columns. *ACI Structural Journal*, *106*(6), 821–830.

6. Shaking table tests of a resilient bridge system with precast reinforced concrete columns equipped with springs

Abstract

This paper presents the shake table test results of a novel system for the design of precast reinforced concrete bridges. The specimen comprises a slab and four precast columns. The connections are dry and the columns are connected to the slab by an ungrouted tendon. One of the tendon ends is anchored above the slab, in series with a stack of washer springs, while the other end is anchored at the bottom of the column. The addition of such a flexible restraining system increases the stability of the system, while keeping it relatively flexible allowing it to experience negative post-uplift stiffness. It is a form of seismic isolation. Anchoring the tendon within the column, caps the design moment of the foundation, and reduces its size. One hundred and eighty-one shake table tests were performed. The first 180 caused negligible damage to the specimen, mainly abrasion at the perimeter of the column top ends. Hence, the system proved resilient. The 181st excitation caused collapse, because the tendons unexpectedly failed at a load less than 50% of their capacity (provided by the manufacturer), due to the failure of their end socket. This highlights the importance of properly designing the tendons. The tests were used to statistically validate a rigid body model. The model performed reasonably well never underestimating the median displacement response of the center of mass of the slab by more than 30%. However, the model cannot predict the torsion rotation of the slab that was observed in the tests and is due to imperfections.

6.1. Introduction

Modern bridge design should fulfill a number of requirements. Modern bridges should often (a) be constructed quickly; (b) be resilient, that is, not only avoid collapse, but also suffer minimal or no damage under the design (or even a larger) earthquake.

Prefabrication can conform to the above requirements and offers a number of advantages, namely (a) reduced overall construction time, (b) reduced on-site construction time, and (c) better quality control and improved safety for the workers. In places where labor cost is high, prefabrication can be more competitive than on-site construction, as it requires less labor. On the other hand, prefabrication requires well-qualified labor, and the transport of large elements might require special vehicles.

Prefabrication has not been widely used in seismic regions because the state of the practice has been to try to emulate cast-in-place structures by connecting prefabricated elements with cast in situ concrete, in an effort to create monolithic connections—and this is neither always cost-effective nor presents optimal behavior. However, research and, recently, practice has proven that there are alternative design and construction methods that, apart from preventing collapse, they also provide re-centering. Engineers in New Zealand, the United States, and China have suggested connecting precast elements via ungrouted post-tensioned tendons, forming dry connections. Mild reinforcement can be added to provide extra energy dissipation. The seismic behavior of such systems is superior not only to precast elements with emulated connections, but also to cast-in-place systems. The reason is that the elongation of the reinforcement is distributed along all its length and therefore it does not yield. Hence the tendon offers a recentering mechanism and the structure does not exhibit damage. In fact, the widespread belief that the Achilles' heel of precast structures is their seismic behavior is wrong: precast structures can be designed to be more resilient than cast in place.

The above concept is based on the early work of Priestley & Tao (1993), Stanton et al., (1997), and the PREcast Seismic Structural Systems (PRESSS) project (Nakaki et al., 1999; Priestley et al., 1999). Different names have been used for similar concepts: damage avoidance design (Mander & Cheng, 1997), controlled rocking (Calvi et al., 2004; Liu & Palermo, 2017, 2020; Marriott et al., 2009; Mashal & Palermo, 2019; Palermo et al., 2005, 2007; White & Palermo, 2016), self-centering system (Cheng, 2008; Christopoulos et al., 2008; Cohagen et al., 2008; ElGawady & Sha'lan, 2011; Guerrini et al., 2015; Kashani et al., 2018; Li et al., 2019; Restrepo & Rahman, 2007; Sakai et al., 2006; Trono et al., 2015; Wang et al., 2018), precast hybrid systems (Billington & Yoon, 2004; Bu et al., 2016; Motaref et al., 2014; Ou et al., 2010; Panagiotou et al., 2015), hybrid sliding–rocking system (Salehi et al., 2021; Sideris et al., 2014a, 2014b, 2015), pre- or post-tensioned rocking (Thonstad et al., 2016, 2017; Yamashita & Sanders, 2009), and it has recently found its way to practice in New Zealand (Routledge et al., 2016) and China (Qu et al., 2018).

Soviet engineers have been using prefabricated elements dried connected as a seismic

isolation method for buildings as referred elsewhere (Bachmann et al., 2017; Bantilas et al., 2021a, 2021b; Cherepinskiy, 2004; Uzdin et al., 2009). The concept has a seismic behavior similar to the one of ancient Greco-Roman temples (Konstantinidis & Makris, 2005; Makris & Vassiliou, 2013, 2014; Mouzakis et al., 2002; Papaloizou & Komodromos, 2009; Papantonopoulos et al., 2002).

All the above references focus on the superstructure. However, in seismic-prone regions, the foundation of conventional bridges can comprise up to 50% of the reinforced concrete used for the project. The design dogma that the superstructure should not be allowed to uplift often results in large design moments for the foundation that governs its size. This paper claims that this dogma is not necessary, hence it results in unnecessarily large pile foundations. It presents shake table tests of a slab supported on four precast columns. Ungrouted restraining tendons in series with washer springs (also known as Belleville washers or Belleville springs) connect the columns with the slab. The columns are freely supported on the shake table, that is, the tendon is anchored within the column, so that the design moment of the foundation is minimized (Figure 6.1a,b). The flexibility of the restraining system is governed by the flexibility of the springs, which make the system more deformable and reduce the design forces, at the expense of increasing displacements. To clarify the concept, Figure 6.2a,b shows such a column that was previously tested cyclically in the ETH Zurich (Reggiani Manzo & Vassiliou, 2021a).
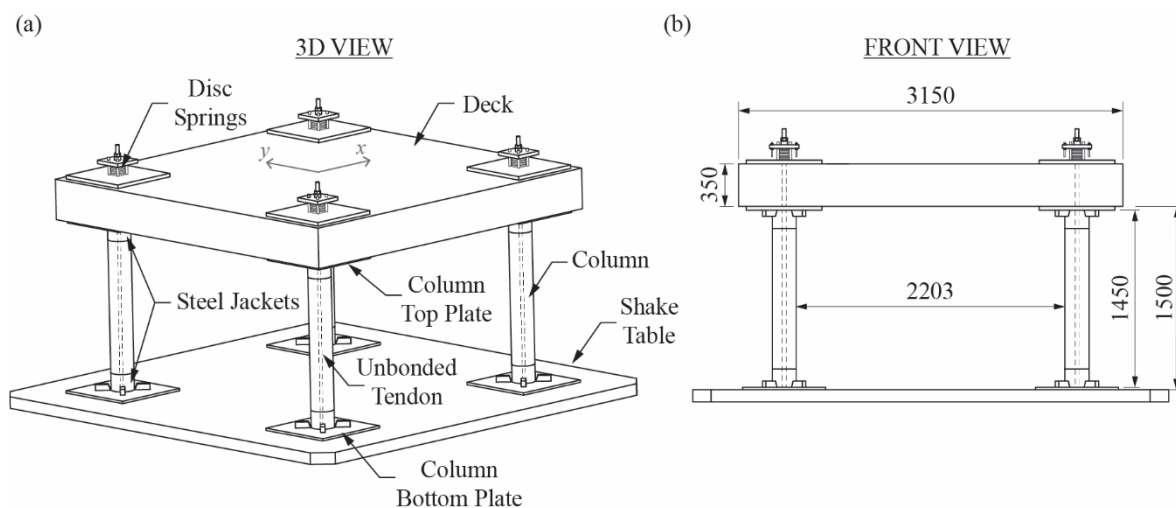
Figure 6.1. Schematic drawing of specimen in (a) 3D View, and (b) Front View.

To the authors' knowledge, this is the first paper that discusses shake table tests of a system that uses such a spring system for isolation. The proposed concept can be perceived as seismic isolation (Buckle et al., 2006; Konstantinidis et al., 2008; Tsopelas et al., 1996) for precast structures. However, a detailed cost/performance comparison of conventional seismic

isolation (i.e., spherical sliding or rubber bearings, which also reduce the design shear and moment of bridge piers) and the suggested approach lies beyond the scope of this paper.
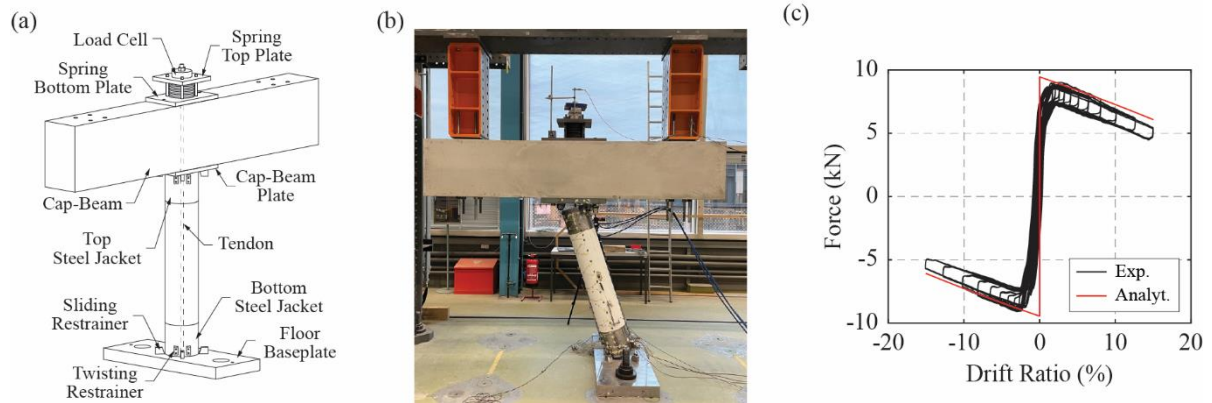
Figure 6.2. (a) Schematic illustration of the tested specimen; (b) Specimen tested at ETH Zürich.

6.2. Mechanics of the rocking frame

6.2.1. Static planar behavior

Figure 6.3 presents two variations of a rocking frame comprising N rigid columns of total mass $N \times m_c$ and a rigid beam of mass m_b. The columns are able to uplift but not slide at any end. They are restrained with a perfectly elastic restraining system. In both variations, the top end of the tendon is anchored above the beam, in series with a spring. The total stiffness of the restraining system (i.e., spring + tendon) is k_{res}. In Figure 6.3a, the bottom end of the tendon is anchored at the foundation, while in Figure 6.3b, it is anchored at the bottom end of the column.

Assuming a horizontal force F applied at the beam, the linearized lateral force–deformation relation ("pushover curve") when the frame is anchored at the foundation is (Makris & Vassiliou, 2015; Vassiliou & Makris, 2015):

$$F = \underbrace{\left(\frac{1}{2} + \gamma\right) N m_c g\, \alpha\, \mathrm{sgn}(u)}_{gravity\ at\ initial\ position} + \left(\underbrace{2 N k_{res} b \alpha}_{tendon} - \underbrace{\left(\frac{1}{2} + \gamma\right) N m_c g}_{P-\Delta}\right)\frac{u}{2h} \qquad (6.1)$$

where γ is defined in Figure 6.3.

When the tendon is anchored within the column (Figure 6.3b) the linearized pushover curve becomes:

$$F = \underbrace{\left(\frac{1}{2}+\gamma\right)Nm_c g\alpha\,\mathrm{sgn}(u)}_{gravity\ at\ initial\ position} + \left(\underbrace{\frac{Nk_{res}b\alpha}{2}}_{tendon} - \underbrace{\left(\frac{1}{2}+\gamma\right)Nm_c g}_{P-\Delta}\right)\frac{u}{2h} \tag{6.2}$$
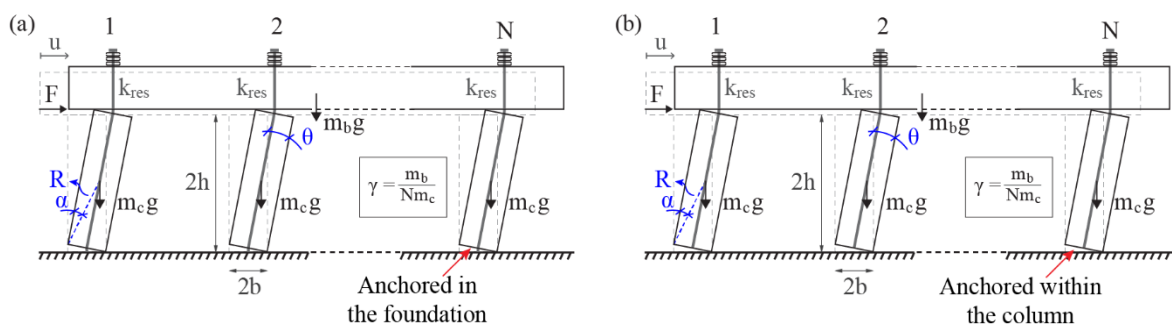

Figure 6.3. Rocking frame with vertical restrainers. Tendon anchored (a) in the foundation; (b) within the column.

The stiffness originating from the restraining system is four times larger if the tendon is anchored in the foundation, rather than within the column. Figure 6.4a plots Equations (6.1) and (6.2) for different values of k_{res}. For all values of k_{res}, the system presents a bilinear elastic behavior. There is no hysteresis, and unloading follows the same branch.
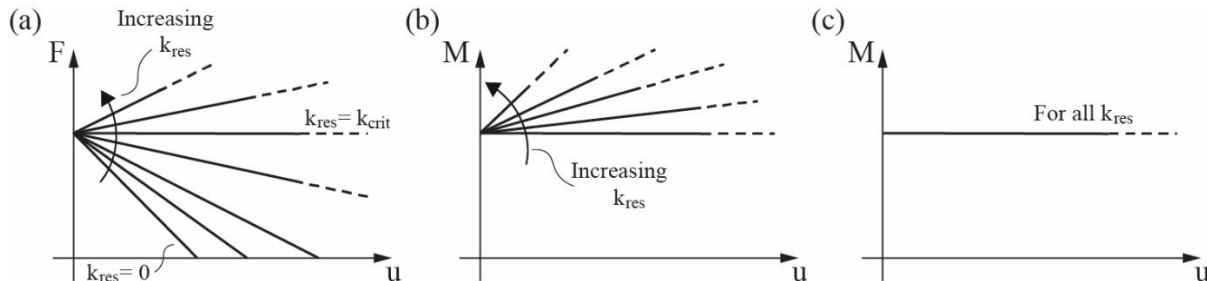
Figure 6.4. (a) *F–u* relationship for the cases of Figure 6.3a,b; (b) M_{base}–*u* relationships for the case of Figure 6.3a; (c) M_{base}–*u* relationship for the case of Figure 6.3b.

When $k_{res} = 0$ (i.e., no tendon), the post-uplift stiffness of the system is negative. Collapse is reached not because of material failure, but when the restoring force becomes zero, that is, when the columns reach the point of neutral equilibrium. This defines the displacement capacity.

Adding a non-prestressed tendon algebraically increases the post-uplift stiffness. When the stiffness remains below k_{crit}, where $k_{crit} = \dfrac{(1+2\gamma)m_c g}{4b\alpha}$ or $k_{crit} = \dfrac{(1+2\gamma)m_c g}{b\alpha}$ depending on whether the tendon is anchored within the foundation or at the column, the post-uplift

stiffness of the system remains negative, the slope of the second branch is milder and the displacement capacity increases (Makris & Vassiliou, 2015; Vassiliou & Makris, 2015).

When the stiffness of the tendon becomes larger than k_{crit}, the post-uplift stiffness becomes positive and the system never becomes instable, given the assumption of no sliding.

By choosing appropriate restraining systems, the pushover curves of the two variations of the rocking frame can be made identical. This is not the case for the base moment—top displacement curve: when the tendon is anchored in the foundation, the base moment increases with displacement (Figure 6.4b). However, if the tendon is anchored within the column, the base moment is capped and equal to the load carried by the column times its halfwidth (Figure 6.4c). As the goal is to reduce the base moment, this paper will focus only on the latter case.

The above analysis is highly idealized because:

(a) Usually, a restraining system comprises solely a tendon that has a finite yield strain, and no spring is used. For a tendon strength of 1800 MPa, the yield strain is 9×10^{-3}. Assuming a bridge column of 9.6×1.6 m, rigid body analysis shows that the tendon will yield at a drift ratio of 11%, if the tendon is anchored in the bottom of the column and 5.5%, if it is anchored in the foundation.

(b) The column is not rigid, but will sustain flexural deformation along its length and local deformation at the column–foundation and column–cap beam contact zones. If a relatively stiff tendon is used and the column ends are not protected, the deformation will cause concrete spalling.

(c) There might be sliding at the interfaces between the column and the cap beam or foundation.

To test the validity of the static analysis presented above, cyclic tests on a 1:5 scaled precast RC column (not of the same dimensions as the one used for the shake table tests) were performed in the laboratory of the Institute of Structural Engineering (IBK) of the ETH Zurich (Reggiani Manzo & Vassiliou, 2021a). To avoid damage to the column, its ends were protected with steel jackets. The restraining system comprised unbonded tendons in series with disc springs (Figure 6.2a,b). The column was subjected to a normalized axial load of 52.2 kN that would correspond to a normalized axial load ($v = N/(A_c \times f_{cd})$) of 5% and then laterally loaded in cycles up to 15% drift. No damage was observed and the force–deformation loops (Figure 6.2c) showed no deterioration. The energy dissipation implied from the loops is due to friction of the setup, not damage to the column. Note, that the columns were not identical to the ones

tested on the shake table due to lab constraints.

6.2.2. Dynamics of the planar rocking frame

Based on Makris & Vassiliou (2015), and assuming that the columns are always in contact with the ground (i.e. they never fly), the equation of motion of the restrained rocking frame of Figure 6.3b is:

$$\ddot{\theta} = -\frac{1+2\gamma}{1+3\gamma} p^2 \left(\sin(\alpha \operatorname{sgn} \theta - \theta) + \frac{\ddot{u}_g}{g} \cos(\alpha \operatorname{sgn} \theta - \theta) \right) - \frac{1}{1+3\gamma} p^2 \sin \alpha \frac{k_{res} b}{m_c g} \sin \theta \quad (6.3)$$

where $p = \sqrt{\dfrac{3g}{4R}}$ and θ is the tilt angle shown in Figure 6.3.

Linearizing Equation (6.3) gives:

$$\ddot{u} + \underbrace{\frac{1+2\gamma}{1+3\gamma}\frac{3g}{2}\alpha \operatorname{sgn} u}_{gravity\ at\ initial\ position} + \left(\frac{3}{2} \underbrace{\frac{1}{1+3\gamma}\frac{\alpha k_{res} b}{m_c}}_{tendon} - \underbrace{\frac{3g}{2}\frac{1+2\gamma}{1+3\gamma}}_{P-\Delta} \right)\frac{u}{2h} = -\frac{3}{2}\frac{1+2\gamma}{1+3\gamma}\ddot{u}_g \quad (6.4)$$

Unless extra yielding reinforcement is provided internally or externally, energy is only dissipated during impact, and it is usually taken into account via a coefficient of restitution (Housner, 1963) defined as:

$$r = \frac{\dot{\theta}_{after}}{\dot{\theta}_{before}} \quad (6.5)$$

When the stiffness of the restraining system is positive, extra damping can be provided to the system in the form of extra yielding bars, and the force deformation loop takes a characteristic flag shape (Christopoulos, 2004; Giouvanidis & Dimitrakopoulos, 2017). Then the dynamic response of the system can be approximated by an equivalent elastic oscillator, and the design follows the standard elastic spectrum-based approach.

However, when the stiffness of the bilinear oscillator is negative, there is no equivalent elastic system and the elastic spectrum cannot be used (Makris & Konstantinidis, 2003). To avoid time history analysis, Reggiani Manzo & Vassiliou (2019, 2021b) proposed simplified design methods.

6.2.3. Extension in three dimensions

Figure 6.5 shows a 3D extension of the rocking frame model (Vassiliou et al., 2017; Vassiliou, 2018). The assumptions made for the planar frame (rigid bodies, no sliding or "flying" allowed, pointwise contact) are extended to include the following:

(a) The columns are constrained not to roll-out of its initial position.

(b) The columns are always in contact with the support and the slab (i.e., they never fly). Therefore, the contact force is always compressive.

(c) No damping mechanism is included.

(d) The tendon is anchored above the spring and within the column.
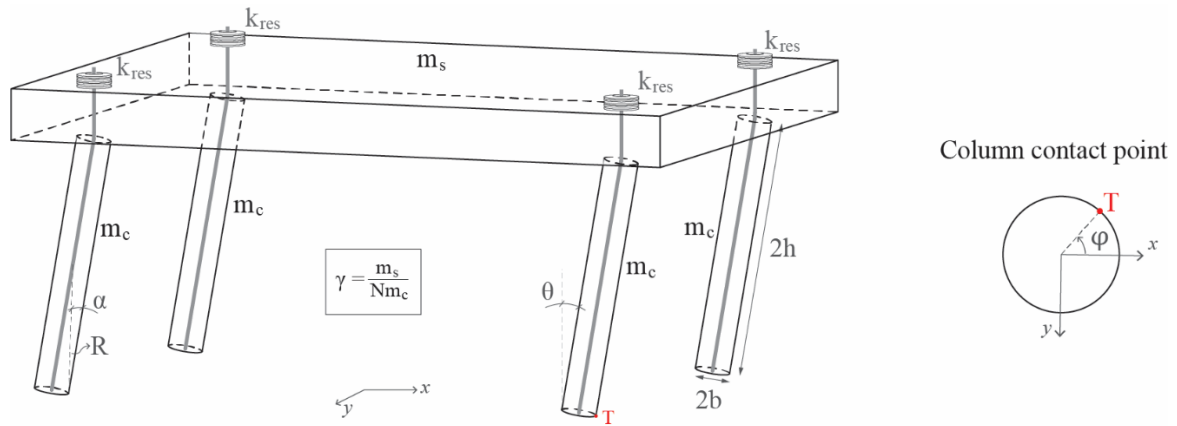
Figure 6.5. Three-dimensional wobbling frame. The columns are allowed to uplift. Twist and roll out of the columns are constrained.

Then the equations of motion become:

$$\ddot{\theta} = -\hat{p}^2 \left(\sin(\alpha-\theta) + \cos(\alpha-\theta)\left(\frac{\ddot{u}_g}{g}\cos\varphi + \frac{\ddot{v}_g}{g}\sin\varphi \right) + \frac{k_{res}\cdot 2h}{m_c g}\frac{1}{2(2\gamma+1)}\sin\alpha\tan\alpha\sin\theta \right) +$$

$$+\ddot{\varphi}^2 \left(\begin{array}{l} \sin\theta\sin^2\alpha\left(4\gamma+\dfrac{3}{2}\right) + \cos\alpha\sin\alpha(4\gamma+1)(1+\cos\theta-2\cos^2\theta) + \\ \sin\theta\cos\theta\left(\dfrac{4}{3}\cos^2\alpha - \dfrac{5}{4}\sin^2\alpha + 4\gamma(\cos^2\alpha-\sin^2\alpha)\right) \end{array} \right) \frac{12}{48\gamma+15+\cos^2\alpha} \qquad (6.6)$$

$$\begin{pmatrix} \left(\left(\frac{4}{3}\cos^2\alpha - \frac{5}{4}\sin^2\alpha + 4\gamma\left(\cos^2\alpha - \sin^2\alpha\right)\right)\sin^2\theta + \\ (3+8\gamma)(1-\cos\theta)\sin^2\alpha + 2\sin\alpha\cos\alpha\sin\theta(1+4\gamma)(1-\cos\theta) \end{pmatrix}\ddot\varphi +$$

$$+ \begin{pmatrix} (3+8\gamma)\sin^2\alpha\sin\theta + \left(\frac{8}{3}\cos^2\alpha - \frac{5}{2}\sin^2\alpha + 8\gamma\left(\cos^2\alpha - \sin^2\alpha\right)\right)\sin\theta\cos\theta \\ +2\cos\alpha\sin\alpha(1+4\gamma)(2\sin^2\theta + \cos\theta - 1) \end{pmatrix}\dot\varphi\cdot\dot\theta = \qquad (6.7)$$

$$= (2\gamma+1)\left(\sin\alpha + \sin(\theta-\alpha)\right)\frac{\left(\ddot u_{g_x}\sin\varphi - \ddot u_{g_y}\cos\varphi\right)}{R}$$

where

$$\hat p^2 = \frac{12(2\gamma+1)}{48\gamma + 15 + \cos^2\alpha}\frac{g}{R} \qquad (6.8)$$

θ is the tilt angle. φ is the angle defining the contact point, T, between the column and the support (Figure 6.5).

6.3. Shake table testing

A series of tests was performed at the Laboratory for Earthquake Engineering (LEE) of the National Technical University of Athens (NTUA). The objectives of the tests were two: (a) to evaluate the seismic performance of a precast system based on the concept of Section 6.2 and (b) to validate the numerical model presented in Section 6.2.3. The tested specimen consisted of four reinforced concrete columns supporting a reinforced concrete slab (Figure 6.1). The columns were connected to the slab via unbonded non-prestressed restraining tendons in series with washer springs, but were freely standing on the shake table. The end of each tendon was anchored to the bottom of its corresponding column using a threaded socket at the base.

6.3.1. Column design and casting

The model was designed around the limitations of the shake table of the LEE and was not designed to represent a specific prototype bridge, as this was impossible at a scale larger than or equal to 1:5. However, at a 1:5 scale, the tested specimen will have a height of 7.25 m in the prototype scale that falls within the range of typical heights of columns of highway bridges, although on the lower end. The column aspect ratio (height to width) was slightly larger than typical highway bridges. The aspect ratio and the height chosen were controlled by the limitations of the shaking table. Moreover, the slab had a mass that leads to a normalized load

in the columns of $v = N/(A_c \cdot f_{cd}) = 3.3\%$, where N is the axial load and A_c and f_{cd} are the column cross-sectional area and the design compressive strength of the concrete, respectively. This value is larger than the value used by Mashal & Palermo (2019) and Mashal (2015) who tested a bridge bent of a typical highway bridge in New Zealand. It lies within the typical design range of overpass bridges, but still is relatively low. Such a low value was dictated by the capacity of the shake table. So, more tests with larger loads are needed.

Figure 6.6 shows an elevation of the columns and their critical sections. The columns were 1450-mm high and 197 mm in diameter. The ends of the columns were protected with steel jackets.
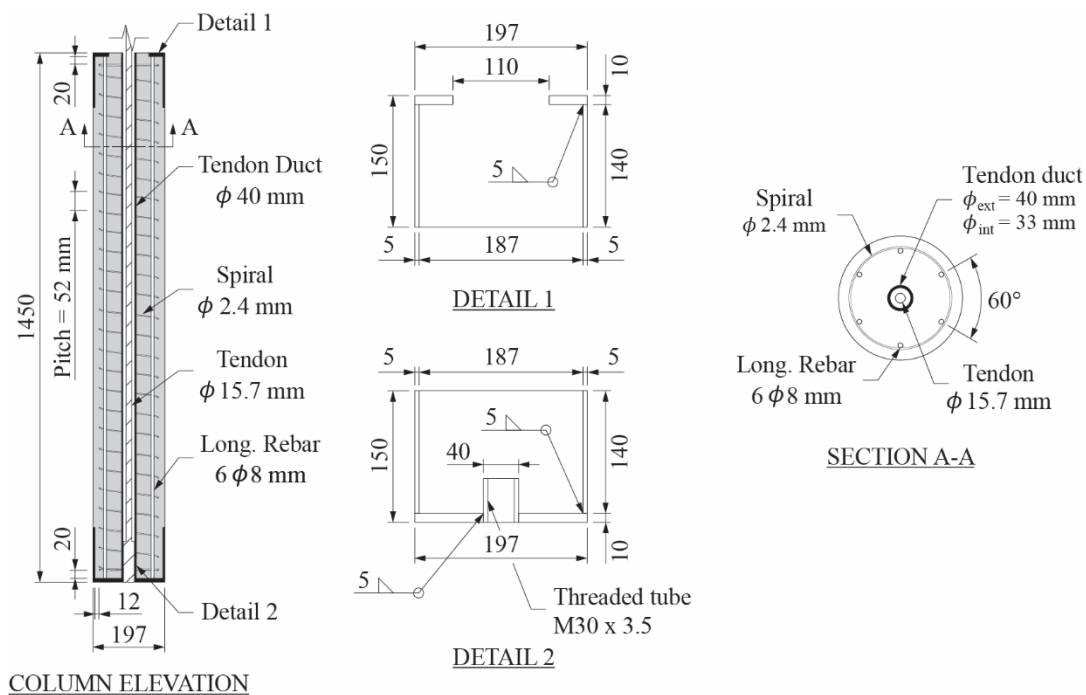
Figure 6.6. Column elevation and critical cross sections (dimensions in mm).

Longitudinal reinforcement was provided by $6\phi8$ B500 rebars that were welded to the top and bottom jacket plates. This resulted in a reinforcement ratio of $\rho_l = 1.00\%$. Transverse reinforcement was provided by a spiral wire of 2.4-mm diameter and 400-MPa yield strength. This creates a distortion in the physical model as the steel is annealed and smooth, unlike standard rebars used in construction. However, the shear behavior is not expected to be critical and confinement to the critical sections is anyways provided by the steel jackets. The pitch of the spires was 52 mm providing a transverse reinforcement ratio of $\rho_s = 0.23\%$. S355 steel was used for the protection of both ends of the columns.

The columns were cast in the Laboratory of Reinforced Concrete of NTUA. The concrete was sampled in cubes of 100-mm edge, and the average compressive strength at the age of 28 days was measured at 44.5 ± 0.74 MPa. Therefore, the characteristic value of concrete's compressive strength was estimated at $f_{ck} = 41.2$ MPa, classifying the concrete at the C30/37 strength class. The Young's modulus of the specimen is considered to be 33 GPa, according to EC2 (CEN, 2004a). The column was cast from the top and compacted with a vibrator that barely passed through the opening between the top steel jacket and the tendon duct. To avoid forming voids right below the end steel plate, the mixture was manually pushed towards the perimeter. Therefore, it is recommended that either the columns be cast from the lateral side (Thonstad et al., 2016), or that the initial high workability of the mixtures be retained during the casting time, using the appropriate dosage of retarder.

The ends of columns were protected with a tube having 5-mm thickness, 140-mm height, and 197-mm external diameter (Figure 6.6). The steel tube was welded at its base to a steel plate of 10-mm thickness. No particular methodology was used for the design of the tube, as existing methodologies are based on the beam theory, which is not applicable in this case, because of the strong discontinuity caused by uplifting. To dimension the steel jacket, the jacket tested by Thonstad et al. (2017) was approximately scaled down from 1:2 to 1:5 scale. The detailing of the steel plate is different in the bottom and top part of the column to allow for casting from the top. A threaded steel tube (Figure 6.6) was welded at the bottom steel plate to allow for anchoring the tendon (see Section 6.3.3). In the top part, a circular annular plate with an internal diameter of 110 mm was used.

6.3.2. End plates

In order to avoid damage to the slab or the column ends due to stress concentrations, S355 steel plates were placed at the interfaces of the column with the slab and the shake table. The steel plates were equipped with restrainers that limited sliding to 5 mm in each direction (Figure 6.7).

6.3.3. Restraining system

The model was designed to keep the post-uplift stiffness negative while providing a displacement capacity (i.e., displacement to reach the point of neutral equilibrium) of $u_{cap} = 4b$ = 394 mm, which corresponds to doubling the displacement capacity of the equivalent

unrestrained system. Using this value and Equation (6.2), the target stiffness calculated for the restraining system was k_{res} = 1,808 kN/m.
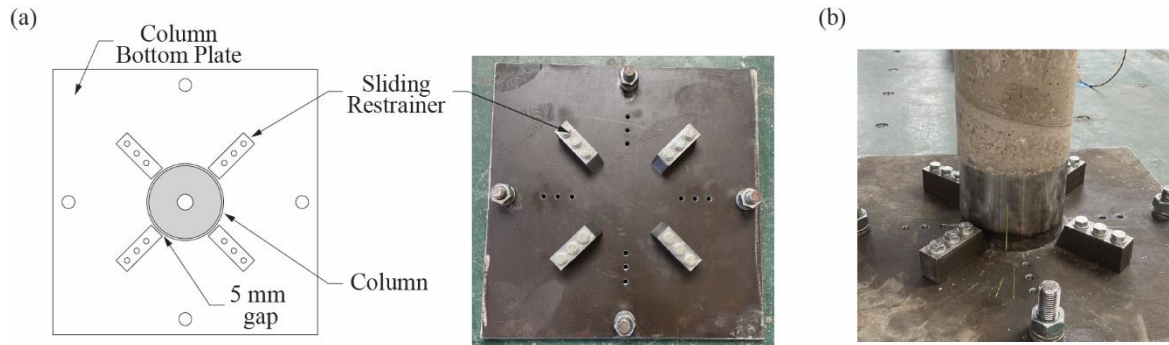

Figure 6.7. (a) Schematic illustration (left) and picture (right) of the end plates; (b) end plates with the column.

To obtain the target stiffness, the restraining system was composed of an unbonded tendon in series with washer springs. The tendon cross section was dictated by the market availability of materials. Tendons with threaded connections at their ends (Figure 6.8a) were only available as seven-wire strands with nominal cross-sectional area of 150 mm^2 and Young's Modulus of 190 GPa. The tendons were 2134-mm long, resulting in an axial stiffness of 13,318 kN/m. One end was anchored at the bottom of the column using a threaded tube welded to the steel jacket and the other one was anchored at the top of the springs with a nut.

The spring system consisted of washer springs, also known as disc springs or "Belleville springs". Washer springs are conical shells loaded along their axis. Similar to helical springs, they can be combined to achieve a desired total stiffness. However, unlike helical springs, the stacking direction of the springs affects the total stiffness. Stacking the washer springs in the same direction results in a stiffer system, while stacking them in alternate directions makes the system more flexible. An analytical expression describing the force–deformation relationship of a single spring was derived by Almen & Laszlo (1936). The springs can exhibit hardening, softening, or linear behavior, depending on their geometry.

The washers of the spring system were not custom-made, because they are available in the market at specific dimensions and their manufacturer provides the force–deformation curve of each washer based on Almen & Laszlo (1936). So, the design of the stack of the springs involved determining the target stiffness and displacement capacity and choosing the appropriate size and number of washers from the manufacturer's catalog: ten washer springs of $125 \times 61 \times 6$ mm (external diameter/internal diameter/thickness) were stacked in alternate

directions (Figure 6.8b). Each washer could deform to a maximum of 3.6 mm, corresponding to a load of 64 kN. Figure 6.8c plots the force–deformation relation of the spring stack, as predicted by Almen & Laszlo (1936). At the target displacement capacity of the specimen, the spring stack deforms by 21.5 mm and its secant stiffness is 1975 kN/m. Figure 6.8c also presents the force–deformation curve of the restraining system, assuming linear behavior of the tendon. At the displacement capacity of the specimen, the secant stiffness of the restraining system was 1720 kN/m, 5% smaller than the target stiffness of 1808 kN/m.
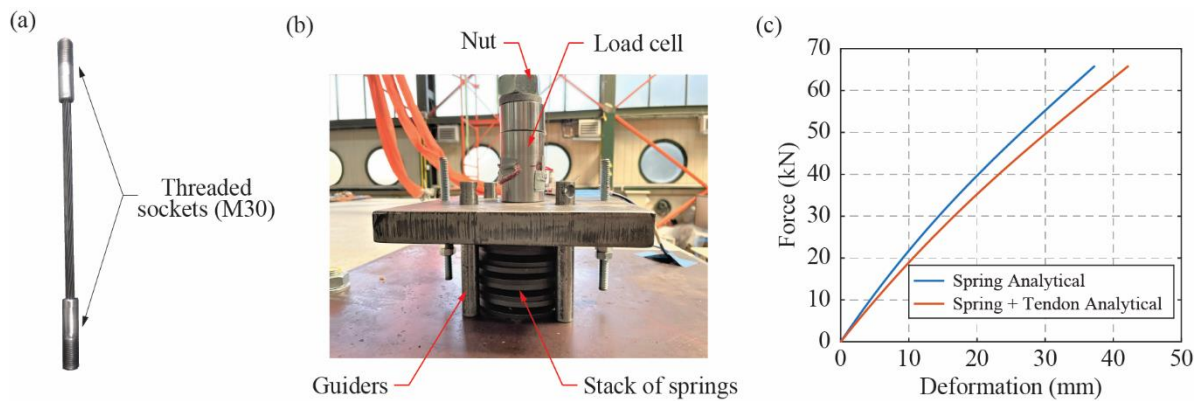
Figure 6.8. (a) Threaded sockets fixed to the tendon (sample tendon of smaller length than the one used in the tests); (b) stack of springs; and (c) force-deformation relation for the stack of springs.

As shown in Figure 6.6, there was a gap of 8.7 mm between the tendon and tendon duct. The large internal diameter of the tendon duct (33 mm) was necessary for passing the 30-mm diameter threaded sockets through the duct. Although unavoidable, this detailing resulted in a different lateral force–displacement relation for the specimen than what Equation (6.2) predicts. Figure 6.9 presents the two curves: the one predicted by Equation (6.2), assuming that the tendon does not move from the centerline of the duct and one that considers that the tendon will move away from the duct's centerline until it touches the duct's wall (for the derivation, please refer to Appendix 2 - Derivation of the planar lateral load-deformation response of the system with shifted tendon). The adjusted curve presents a displacement capacity of 333 mm, 11% smaller than the predicted displacement capacity of 374 mm. In the future, it is recommended that a spacer be fixed in the top of the end of the duct to guarantee that the tendon will stay in the duct's centerline.
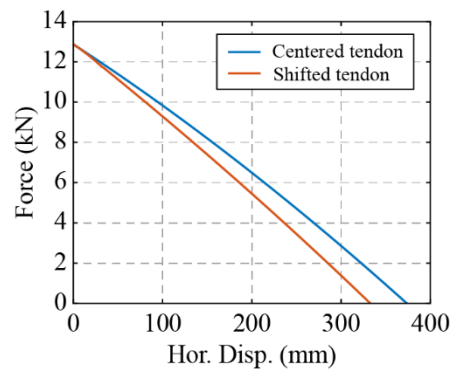
Figure 6.9. Lateral force–displacement relation for the tendon fixed to the centerline of the duct and for shifted tendon.

6.3.4. Redundant mechanism

The specimen was designed with a redundant mechanism to prevent the toppling of the columns while protecting the tendons from exceeding their capacity. The redundant mechanism, "stoppers", consisted of two M12 threaded rods of Grade 4.8 placed in parallel with each stack of springs (Figure 6.8b and Figure 6.10a,b). The stoppers engage only if the slab experiences large displacements. In this case, the load in the restraining system increases. To protect the tendons, which could not be easily replaced without disassembling the specimen, the stoppers were designed as sacrificial elements, yielding at a load of 54.0 kN. In this experimental campaign, the stoppers engage after a 15-mm deformation of the stack of springs. Using the model that takes into account the gap between the tendon and the duct, this deformation of the spring system corresponds to a displacement of the slab of 280 mm. The force at the tendon when the stoppers engage is computed to be 31.2 kN. Therefore, when they yield, the tendon force is 85.2 kN, which is smaller than the yielding load of the tendons (237 kN).
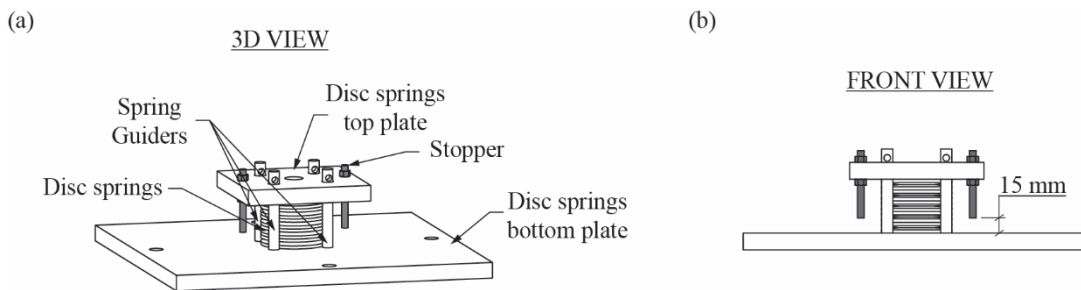
Figure 6.10. Detailing of the redundant mechanism. (a) 3D view; (b) front view.

6.4. Test setup and excitations

6.4.1. Shaking table specifications

The tests were performed in the 4×4-m six degree-of-freedom shaking table of NTUA. The maximum stroke and velocity of the simulator in the three axes are ± 100 mm and 1000 mm/s, respectively. Under 10 tons of payload, the maximum acceleration of the horizontal axes is $2g$, while a $4g$ acceleration is permitted in the vertical direction.

6.4.2. Construction

Figure 6.11a-d shows key stages of the construction process. The steel jackets were fabricated in a workshop and the reinforcement was welded to them. The spiral was placed by hand, the tendon was screwed to the bottom threaded tube, and a steel duct was welded around the threaded tube. The columns were cast in the LRC of NTUA using carton formwork and 48 days after casting, when the concrete had developed an average compressive strength of 47.6 $\pm$ 2.4 MPa, the columns were placed on the shake table, and the slab was placed on top with a crane. Then, the spring stack was placed and the top nut was screwed at the top end of the tendon. Safety steel columns (in red in Figure 6.11c,d) were installed on the shake table to prevent crashing of the slab onto the shake table, in case of specimen collapse. A minimal prestress of 2 kN was applied to the columns to ensure that they are not loose.

6.4.3. Excitation selection and scaling

Usually, shake table tests are performed under a handful of ground motions of increasing intensity because the tests are expected to cause damage to the specimen. However, the structure discussed in this paper is designed not to suffer from any major damage. Therefore, it can be tested under multiple ground motions, thus allowing for a better understanding of its behavior and for the evaluation of its resilience. Moreover, testing under sets of multiple ground motions allows for numerical models to be evaluated in the statistical sense, that is, be evaluated according to their ability to predict the cumulative distribution function (CDF) of the time maxima of the responses to sets of ground motions that characterize the seismic hazard (Bachmann et al., 2018; Del Giudice et al., 2020; Vassiliou et al., 2021a, 2021b, 2021c).

Therefore, the specimen was subjected to all three sets of ground motions proposed by FEMA P695 (FEMA, 2009) (near-field pulse-like (NFP), near-field no pulse-like (NF), and far-field (FF)). The sets are composed of 14 NFP, 14 NF, and 22 FF ground motions. In addition

to the ground motions proposed by FEMA, an extra 12 NFP, 12 NF, and 21 FF ground motions were included. According to FEMA, the original FF set of ground motions includes Cape Mendocino, Rio Dell Overpass record. However, this was not available in the PEER ground motion database and, thus, was not included in this study.
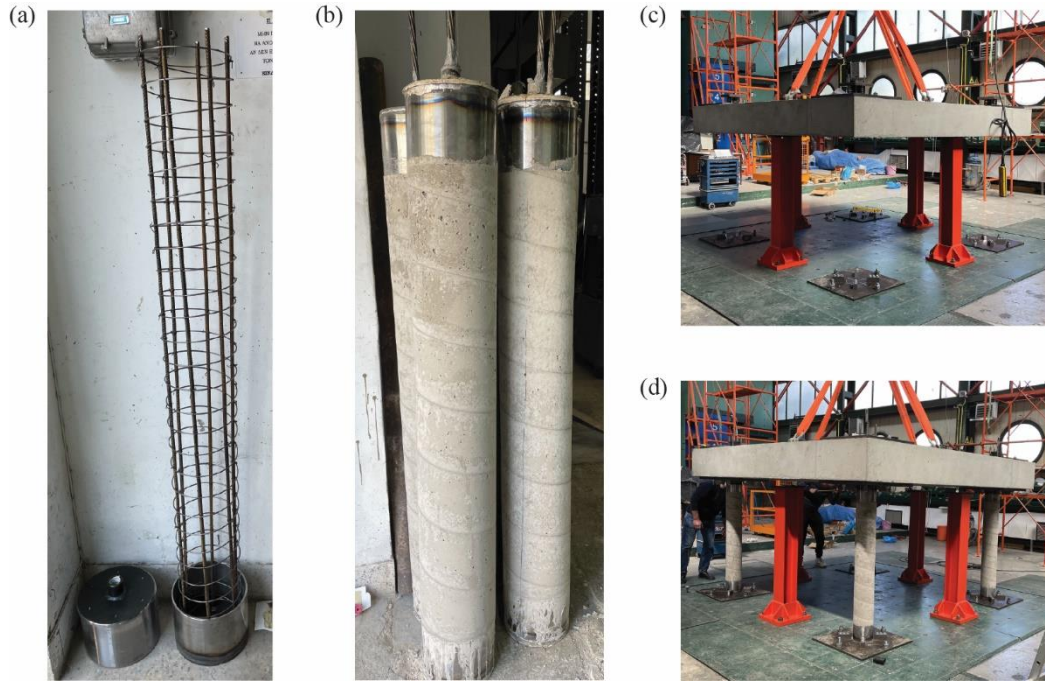
Figure 6.11. (a) Column cage partially assembled; (b) cast columns; (c) slab placed on top of the safety columns for the later assemblage of the reinforced concrete columns; (d) columns and slab assembled on top of the shaking table platform.

In total, this experimental campaign consisted of 26 NFP, 26 NF, and 42 FF ground motions. The specific records, along with the adopted numbering scheme, are provided in Table A1.1 of the appendix for reference.

All sets of ground motions were scaled to have the same $\overline{\text{PGV}}$ defined as:

$$\overline{\text{PGV}} = \sqrt{\left(\text{PGV}_x\right)^2 + \left(\text{PGV}_y\right)^2} \tag{6.9}$$

where PGV_x and PGV_y are the peak ground velocities along the x and y directions. According to the capacity of the shake table, two different $\overline{\text{PGV}}$ levels were selected (in the model scale): (a) low $\overline{\text{PGV}} = 16.75$ cm/s and (b) a high $\overline{\text{PGV}} = 33.5$ cm/s. Overall, there were three different ground motion sets (NFP, NF, and FF) scaled at two different $\overline{\text{PGV}}$s resulting in 188 ground motions. The ground motions are provided in the Appendix 1, together with their $\overline{\text{PGA}}$, after they were scaled to the high $\overline{\text{PGV}}$. The longitudinal, lateral, and vertical components of each

ground motion were simulated by the shake table.

The specimen was constructed assuming a 1:5 scale for the column height. Therefore, to preserve similitude of time, the excitations were scaled in time to $S_T = \sqrt{S_L}$, in which S_L is the length scale equal to 1/5. Therefore, the $\overline{PGV}$ of the high- and low-intensity sets in the prototype scale is 75 and 37.5 cm/s, respectively. Figure 6.12a-l plots the linear 5% damped spectra for the excitations, as they were recorded on the shake table. It also includes the design spectrum for a site in Athens, Greece (in model scale), assuming soil type C and importance factor 1, according to EC8 (CEN, 2004b).

The order of the tests was defined based on the system's response predicted using the analytical model proposed by Vassiliou (2018), sorting them from low to high expected response. Some ground motions could not be simulated either because the structure failed before its execution or because the shake table could not reproduce them sufficiently accurately. The loading protocol is also given in the Appendix 1.

6.4.4. Instrumentation

Figure 6.13 presents the location of all instruments installed on the specimen. The horizontal displacements of the slab were measured using draw-wire sensors, the vertical displacements using cable-extension position transducers, and the accelerations using accelerometers. Load cells were also installed in series with the tendons of each column (Figure 6.8b). The deformation of the spring system of column C2 was recorded using a string potentiometer. Furthermore, the sensors integrated into the actuators of the shaking table recorded the displacement and acceleration of the table platform.

6.5. Response Quantities

The horizontal displacement of the slab and the base shear of the system were the two quantities of interest in this experimental campaign.

6.5.1. Horizontal displacement of the deck

Assuming that the slab is a rigid body and neglecting vertical displacements, the displacement

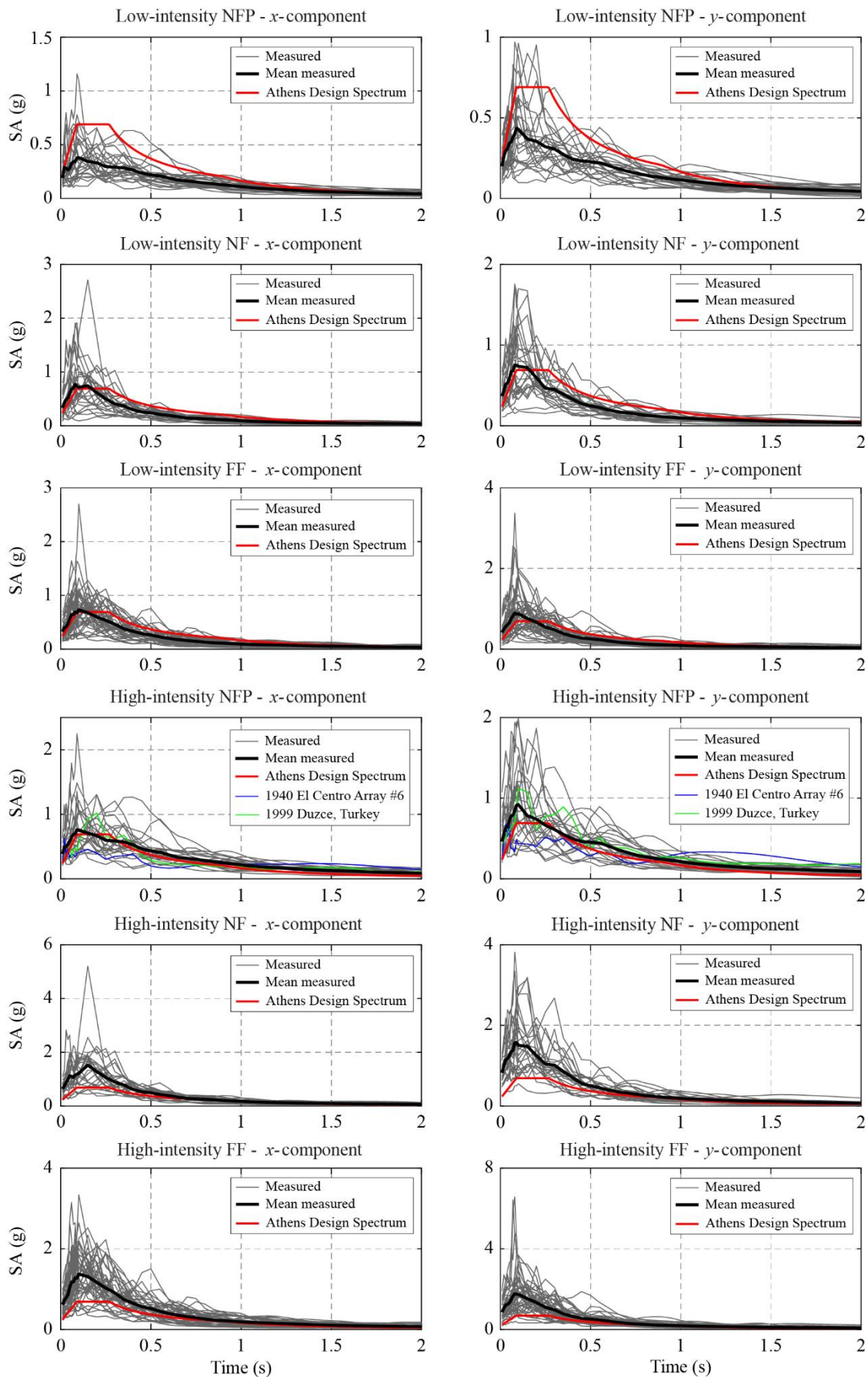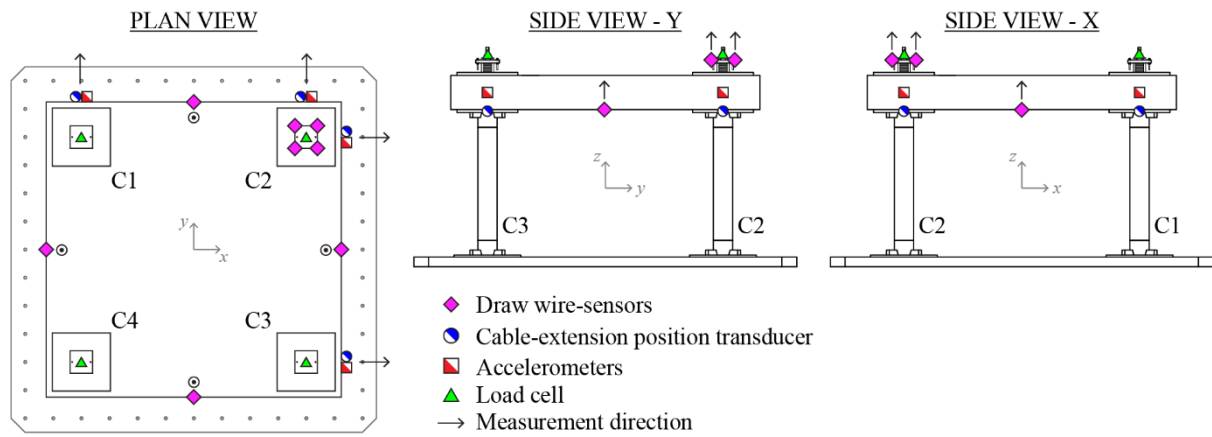**Figure 6.12.** Linear spectra (ζ = 5%), as recorded on the shake table.

Figure 6.13. Instrumentation location.

and torsion at the center of mass of the slab were calculated using the elongation/shortening measured by the four-string potentiometers fixed to it. The horizontal projection of the displacement of the center of mass of the slab is defined as *U*. The specimen was symmetric and the slab was not supposed to sustain torsion. However, due to small imperfections, torsion could be observed during the tests. *U* is not affected by the torsion of the slab. This slab torsion needs further experimental study, as a real bridge would most likely have eccentricity by design, so more tests need to be performed with an eccentric mass placed on top.

6.5.2. Base shear of the system

The base shear of the system was estimated based on the inertial resistance of the slab:

$$V_{base}(t) = m_{slab} \cdot \left(\sqrt{\ddot{u}_{x,slab}^{2}(t) + \ddot{u}_{y,slab}^{2}(t)} \right) \tag{6.10}$$

in which m_{slab} is the mass of the slab, $\ddot{u}_{x,slab}$ and $\ddot{u}_{y,slab}$ are the total longitudinal and lateral acceleration of the slab at its center of mass.

The mass of slab was measured during assembling of the system and it weighed 9435 kg (including the concrete, the steel plates, the springs, and the mounting screws).

6.6. Insight on the behavior

To gain insight in the response, this section presents the results of two tests that caused significant displacements: the 1940 El Centro Array #6 record (Exc. ID 1) and the 1999 Duzce, Turkey record (Exc. ID 14), both belonging to the high-intensity NFP set of ground motions

(Figure 6.12). The former did not engage the stoppers, while the latter did.

Figure 6.14a shows the recorded base shear–drift ratio response. The drift ratio was defined herein as the ratio between the U displacement of the slab and the height of the columns (1450 mm). The system has an initial branch with positive stiffness, which is followed by a second branch with negative stiffness. The finite stiffness of the initial branch sources from the system's pre-uplift flexibility that is ignored by rigid body models. The system's uplifting force can be estimated around 10 kN, which is 22% lower than the value predicted by the rigid body approximation (12.9 kN). Apparently, the pre-uplift flexibility influences the strength of the system. Figure 6.14a (right) shows that the base shear reaches a plateau at a drift ratio of 20%, which indicates that the stoppers of at least one of the columns engaged. Their engagement was visually confirmed after the test, even though the stoppers did not yield (in all but the 181st test, which cause collapse).

Figure 6.14b shows the time history of the loads recorded in the restraining system of each column. The tendons of the columns clearly exhibit different loads. The main reason for this is the torsion of slab that causes each column to displace differently. This is shown in Figure 6.14c that plots the time histories of the displacements of the vertical projections of the center of the column cross sections at the top surface of the slab. Figure 6.14d plots the twist rotation (torsion) time history. Figure 6.15 shows some snapshots of the horizontal position of the slab, during the 1940 El Centro Array #6 ground motion. Evidently, columns exhibit a different displacement because of the torsion of the slab.

Figure 6.14e presents the time history of the horizontal displacement of the center of the slab (U) for both tests. It also presents a numerical prediction of the time history, discussed in Section 6.8. It shows that because of torsion, U can be much larger than the maximum displacement of the columns. However, torsion on its own cannot justify such large differences in the tendon forces, because the load differences (Figure 6.14b) seem to be larger than the displacement differences (Figure 6.14c). Part of the discrepancy can be attributed to some tendons having slack after the top nut becoming loose and to the tolerances of the restraining system being larger than necessary. Therefore, in future tests, the tendon should be checked for becoming loose, and smaller construction tolerances should be applied.

Moreover, Figure 6.14b (right) shows that when the system was subjected to the 1999 Duzce, Turkey record, at around 5–6 s the forces in the restraining systems of columns C2 and C3 started becoming significantly larger than the forces of the tendons of the other columns,
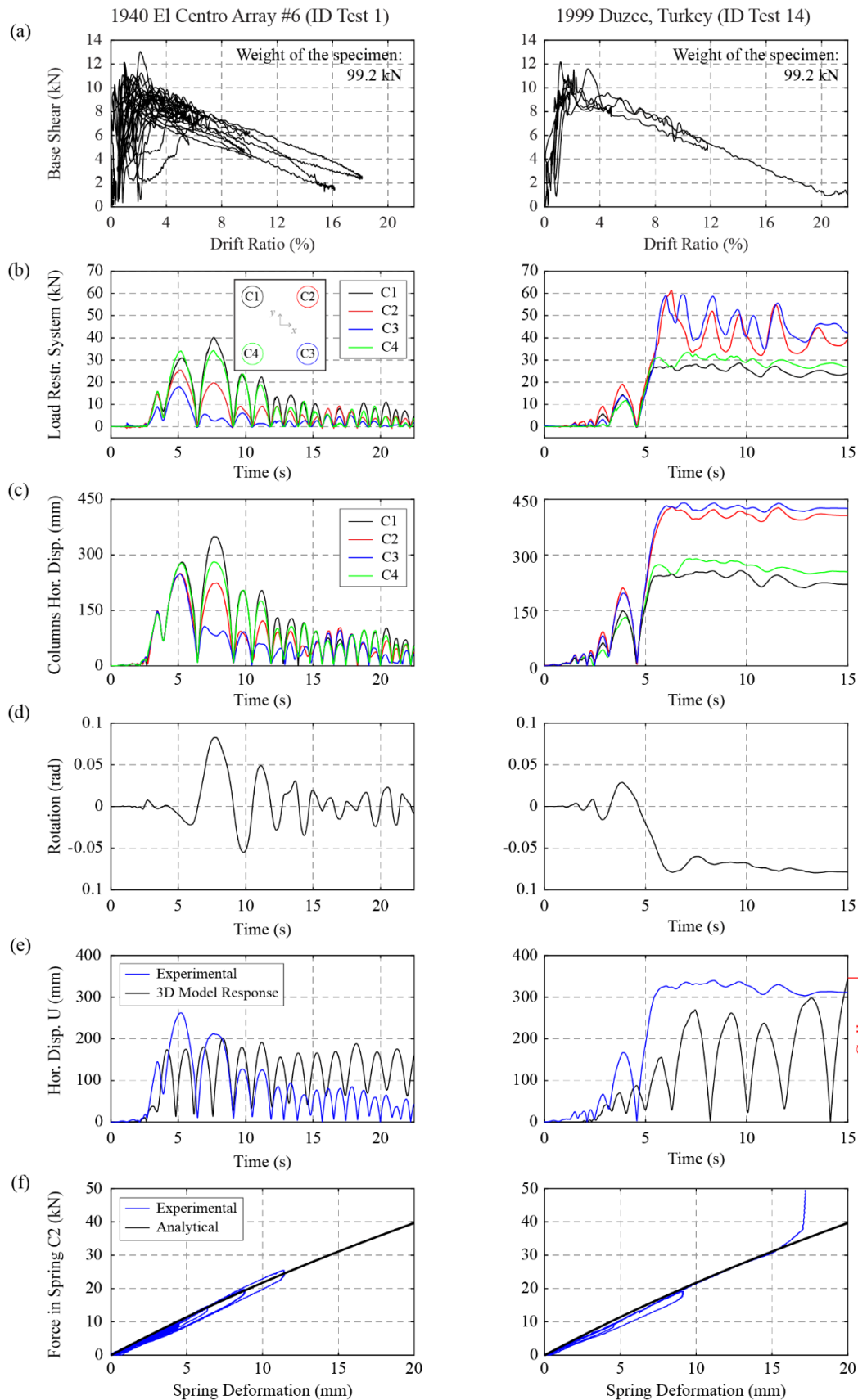
Figure 6.14. (a) Base shear–drift response (*U*/column height); (b) time history of the loads recorded in the restraining system of each column; (c) time history of the slab displacement right above each column; (d) time history of twist rotation (torsion) of the slab; (e) the time

history of the absolute horizontal displacement of the slab; (f) force–deformation relation of the stack of springs composing the restraining system of column C2.
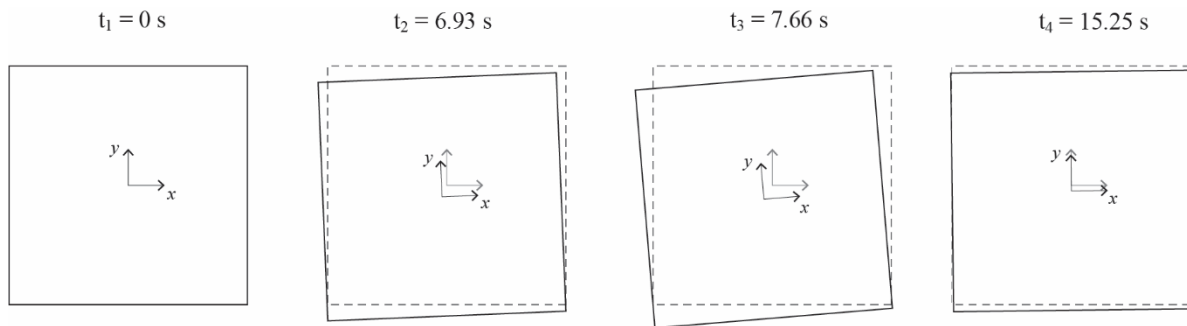
Figure 6.15. Snapshots of the slab for the High-Intensity 1940 El Centro Array #1 excitation.

indicating that the stoppers of these two columns engaged. Not all columns engaged simultaneously, because of the torsion of the slab.

Figure 6.14f plots the force–deformation relation of the tendon of column C2 as recorded and as predicted by Almen & Laszlo (1936) equations. The plot in the right presents further evidence that the stoppers of column C2 engaged: at a deformation of around 15 mm, the system becomes much stiffer. As mentioned in Section 6.3.4, the stoppers were designed to provide redundancy to the system, to prevent collapse under extreme events, even at the cost of permanent deformation. In this particular test, they were successful, as they prevented collapse, even though there was a permanent displacement, not in the form of damage but in the form of the columns ending up tilted and being held by the stoppers. The specimen was recentered using the lab crane. The tendon was not damaged. In the other tests where the stoppers engaged, the system was still able to recenter—with the exception of the case where there was collapse (see Section 6.7.2).

The recorded force–deformation curves in both tests show that the stack of springs dissipates some minimal energy. Possible sources of energy dissipation are friction of the springs with the external guiders and friction of the spring with the end plates. A comparison of the experiment and analytical curve shows that the analytical curve predicts the behavior of the spring reasonably well, despite its inability to model the minimal damping that was experimentally observed.

6.7. Experimental results

This section collectively presents the results to all 181 excitations.

6.7.1. Measured displacements

Figure 6.16 presents the maximum drift ratio of the slab (U/1450 mm) for each excitation in ascending order. This was not the order by which the tests were performed. Different curves are shown for low and high-intensity sets of excitations. Some of the planned excitations were not run and the results for these excitations are not shown in the plots.

The system experienced drift ratios smaller than 5% when subjected to most of the low-intensity excitations. The stoppers engaged for the motions 14 and 16 of the high-intensity NFP set and for the motions 72 and 88 of the high-intensity FF set.

The maximum twisting (torsion) angle observed during the tests was 0.115 rad (6.59°) for the motion 72 of the high-intensity FF set.

6.7.2. Eventual collapse

The system eventually collapsed when it was excited by ground motion 1987, Superstition Hills-02 (Exc. ID 88) scaled to the high-intensity set. The collapse was caused by the unexpected failure of the tendon of column C1 that was followed by the failure of tendon of column C2. The collapse was unexpected because the tendons failed prematurely: C1 broke at 98.8 kN and C2 at 105.4 kN. Both tendons failed at their sockets, indicating some unexpected stress concentration during the manufacturing process. This highlights the importance of the tendon design, as the stability of the whole system relies on them. Therefore, not only the tendons of this system need to be designed with large safety factors, but they should be able to hold the structure even if some of them fail.

6.7.3. Observed damage and performance of the slider restrainers

The specimen was visually inspected after each excitation and after an eventual collapse. No cracks and concrete spalling could be observed in the columns and steel jacket. The only observed damage was abrasion of the edges of the top (Figure 6.17a) and bottom (Figure 6.17b) steel jacket. Figure 6.17 shows that the abrasion of the top steel jacket is more pronounced than the abrasion of the bottom one—something expected as the top end of the column develops a

larger bending moment. What looks like damage in the top steel jacket of C4 was made with the cutting wheel while cutting the duct that was sticking out of the column after casting. Interestingly, the abrasion was not caused by any impacts, but by the forces that were developed at large displacements, when the stoppers engage. Therefore, the steel jacket was enough to protect the specimens from the impacts, and what governs damage and design is the maximum moment applied at the top cross section, which occurs under maximum displacement.
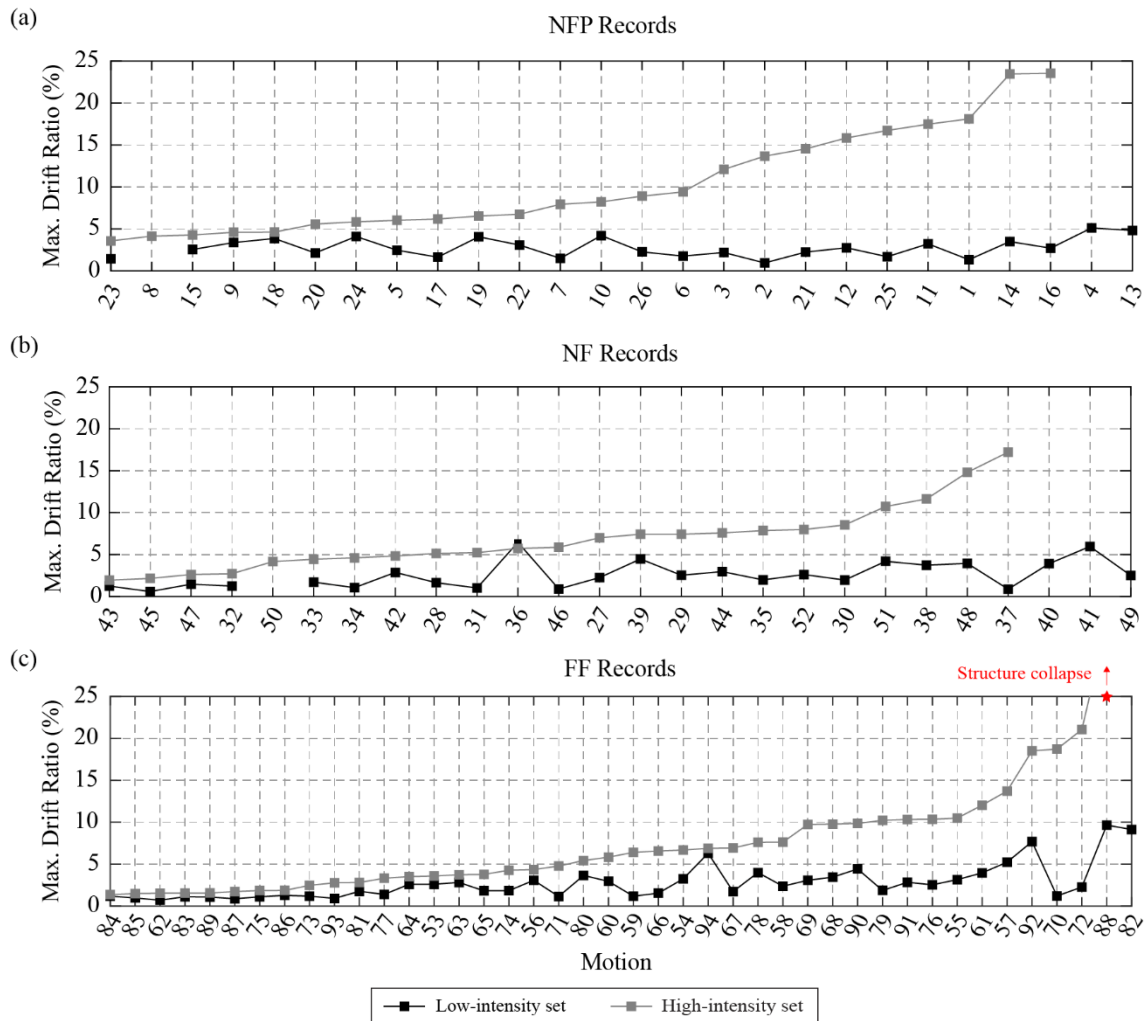
Figure 6.16. Maximum drift ratio for: (a) the near-field pulse-like (NFP) set, (b) the near-field (NF) set, and (c) the far-field (FF) set.

The sliding restrainers managed to restrain sliding in all cases (but the one that the system collapsed). In several cases, the columns impacted on the restrainers, in some cases, they climbed up their inclined surface, but eventually, they slid back to the bottom steel plate.
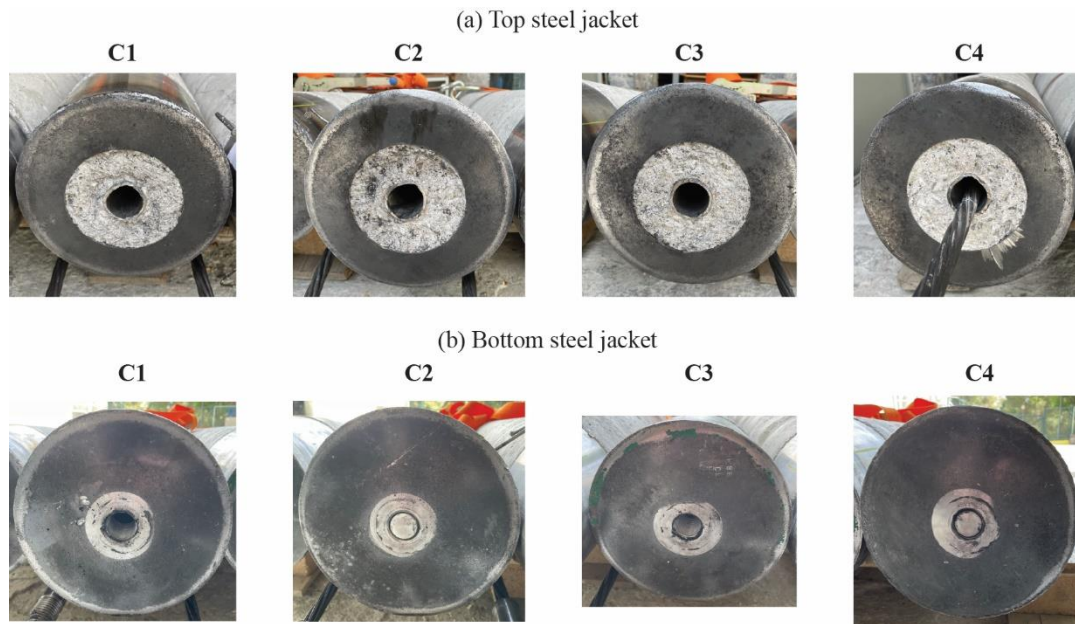
Figure 6.17. Observed damage at the (a) top surface and (b) bottom surface of the columns.

## 6.8. Statistical validation of a rigid body model

Seismic response is inherently stochastic. Therefore, Bachmann and colleagues (Bachmann et al., 2018; Del Giudice et al., 2020; Vassiliou et al., 2021a, 2021b, 2021c) have claimed that, in earthquake engineering, structural model validation should follow a stochastic procedure. More specifically, the validation test of predicting the response to an individual ground motion is sufficient for a structural model, but it is not necessary. Models need to be able to predict the CDF of the time maxima of the responses to a set of ground motions that characterize the seismic hazard. This is a weaker but sufficient validation procedure. It is often the only possible one, as shake table tests are often not repeatable—especially for rocking structures (Bachmann et al., 2016; Vassiliou et al., 2021b). In such cases, trying to predict the response to an individual ground motion is meaningless.

This section attempts to statistically validate the model presented in Section 6.2.3 (without taking into account the nonlinearity of the spring or the presence of the duct) by comparing its predictions to the shake table tests results. The analytical model assumes that the columns do not slide or twist. In addition, the model also does not account for torsion of the slab, which was observed in this experimental campaign and is generated by any small imperfections in the specimen. Thus, it is a very simple model—to the point of being simplistic, as it grossly overestimated the response of a rocking system in the PEER 2019 blind prediction contest (Malomo et al., 2021; Vassiliou et al., 2021a; Zhong & Christopoulos, 2021). With

reference to Equations (6.7) and (6.8) and Figure 6.5, the model parameters that were used are: $2R = 1.463$ m, $\alpha = 0.1359$, $m_c g = 1.22$ kN, $m_s g = 94.35$ kN, and $k_{res} = 1720$ kN/m. Indicatively, Figure 6.14e (left) shows that the model underpredicts the response to this individual ground motion by roughly 35%.

Figure 6.18 presents the experimental and numerical CDFs of the displacement of the center of mass *U*. Figure 6.18a presents the data clustered in bins of low and high intensity, while Figure 6.18b-d presents bins of different excitation types (NFP, NF, FF). Figure 6.18 also plots 95% confidence intervals of the experimentally obtained *U*. The model performs reasonably well, as it generally lies within the 95% CI. To statistically validate the analytical model, a two-sample Kolmogorov–Smirnov test was conducted using the built-in Matlab routine "kstest2" (*MATLAB*, 2019). This test rejects or accepts the null hypothesis (H_o) that both data are from the same distribution. The null hypothesis H_o is rejected when the *p*-value is lower than a given statistical significance value α_s. The *p*-value is a measure of the evidence against H_o and it does not represent the probability that H_o is true (Wasserman, 2013). In this work, a fairly large value of statistical significance of 0.1 is used to allow for a nuanced qualification of null hypothesis validity using an evidence classification scale shown in Table 6.1. A detailed explanation of the hypothesis testing procedure can be found in Wasserman (2013). Table 6.2 provides the *p*-values for all eight sets shown in Figure 6.18. The numerical CDF is compared to the experimental CDF of *U*. In 7/8 cases there is small to none evidence against both data coming from the same distribution, while in 1/8 there is medium–weak. Hence, this statistical test shows that the analytical model is a good predictor of the response of the center of mass of the slab.

As *p*-values are not often used in earthquake engineering practice, Table 6.2 also presents the error of the median of *U*. In 7/8 cases, the error lies below 30%. In the high-intensity FF, the error is 47%—but the model is conservative. In no case did the model underestimate the median response by more than 30%. However, as the model disregards a number of physical mechanisms (e.g., energy dissipation, flexibility of the columns, geometric imperfections that lead to torsion), one cannot generalize, and more tests under more complicated and realistic geometries should be performed for its validation. Moreover, the model cannot predict the torsion of the slab and therefore it can only be used for the prediction of the center of the mass of the slab; not for the column drift ratios.
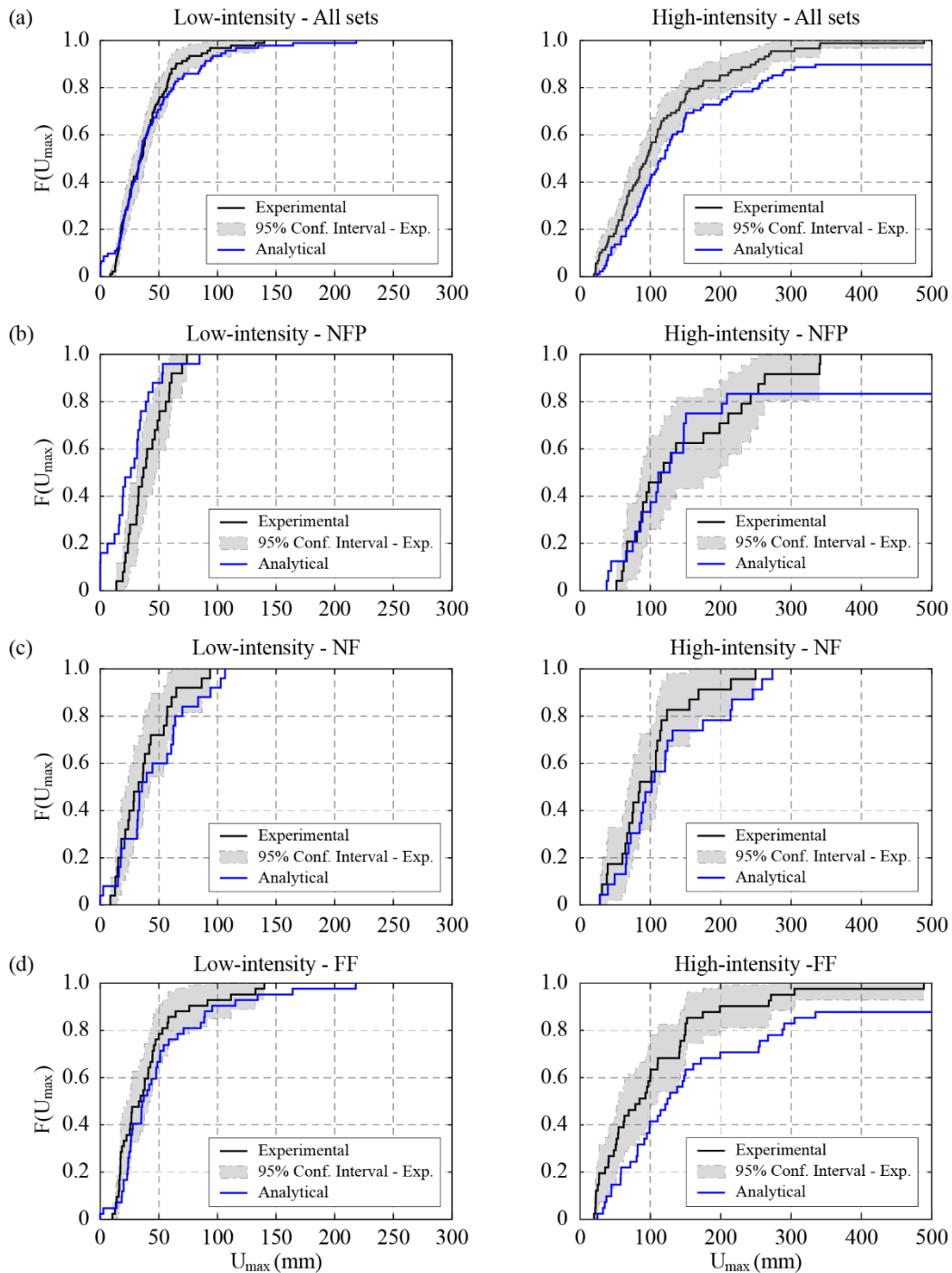
Figure 6.18. CDF plots obtained from the experimental data and CDF obtained using the analytical model with data clustered in (a) low- and high-intensity sets; (b) low- and high-intensity NFP sets; (c) low- and high-intensity NF sets; and (d) low- and high-intensity FF sets.

**Table 6.1.** Evidence classification *p*-value scale (Wasserman, 2013)**.**

p-value	Evidence
<0.01	Very strong against H_o
0.01-0.05	Strong against H_o
0.05-0.10	Medium – weak against H_o
>0.10	Small or none against H_o

Table 6.2. Statistical comparison of the analytical model and the experimental data.

Set	*p*-value	$e_{50} = \dfrac{\left\| u_{50,ana} - u_{50,\exp} \right\|}{u_{50,\exp}}$
Low-intensity (All)	0.75	0.04
High-intensity (All)	0.14	0.24
Low-intensity (NFP)	0.06	0.29
High-intensity (NFP)	0.86	0.02
Low-intensity (NF)	0.65	0.09
High-intensity (NF)	0.59	0.20
Low-intensity (FF)	0.26	0.09
High-intensity (FF)	0.15	0.47

Abbreviations: FF, far field; NF, near field; NFP, near-field pulse-like.

Figure 6.19 presents a scatter plot that gives a motion-by-motion comparison of the maximum *U* of the columns obtained experimentally and by the analytical model. The correlation coefficients between the experimental and numerical *U* are also shown in the same figure. The calculated correlation coefficients range from $\rho = 0.65$ to 0.04 indicating that the model cannot predict the response to individual ground motions. However, as a designer would design for sets of ground motion (not for individual excitations), this paper claims that the statistical validation approach is the appropriate one.
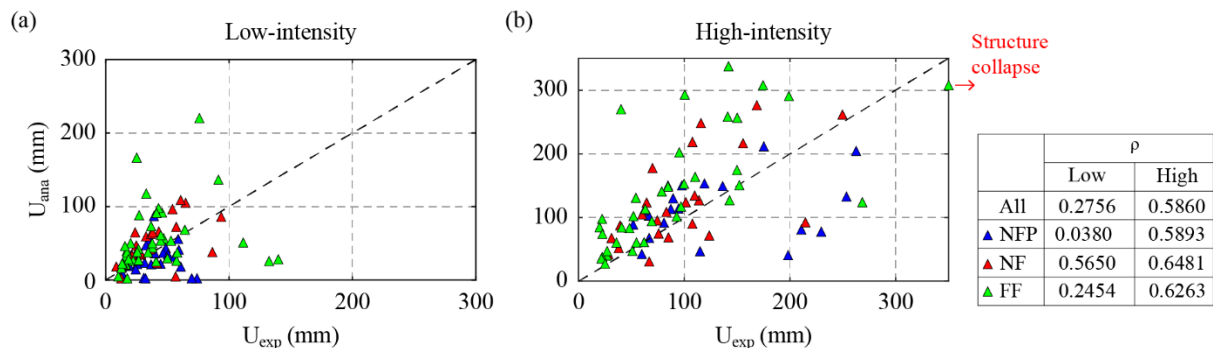
Figure 6.19. Motion-by-motion comparison of the experimental response and the response predicted by the analytical model for the (b) low-intensity and (b) high-intensity set.

6.9. Conclusions

A system for the seismic protection of precast bridges was suggested and tested on a shake table. Precast elements are connected with ungrouted tendons in series with washer springs. The bottom end of the tendon is anchored within the column, and the whole system is freely standing on its foundation. This kind of support minimizes the design moment of the foundation, thus reducing the need for piles, which can comprise up to 50% of the RC of the project.

The spring increases both the flexibility and the displacement capacity of the system. In that sense, it can be perceived as a form of seismic isolation using only steel and concrete. In the performed tests, the spring was designed to keep the post-uplift stiffness of the system negative. However, a negative stiffness is not a necessity—a stiffer spring can be used that would increase the post-uplift stiffness to positive values.

After 180 excitations, the system proved resilient: it presented minimal damage only at the steel jackets that were protecting the ends of the columns. It reached more than 20% drift without any concrete damage. The residual deformations were negligible and controlled by the sliding restrainers. Eventually, the system collapsed because of the unexpected failure of a tendon. This shows that the stability of the whole system depends on the tendons, which should be designed with large safety factors and they should be able to hold the structure, even if one of them fails.

The sliding restrainers that were used proved sufficient to restrain the structure from excessive sliding, even under strong vertical acceleration, while they allowed it to rock freely. The compressive force–deformation curve of the spring device (Figure 6.14f) was well-predicted by the Almen and Laszlo analytical model (Almen & Laszlo, 1936).

The test results served as a model validation dataset for a simple model that is based on rigid body dynamics. It was proven that despite the general belief that 3D rocking motion is unpredictable, a simple model was able to predict the statistics of the displacement of the center of mass of the slab to sets of ground motions that characterize the seismic hazard, namely the CDFs of the time maxima to individual excitations.

More work is needed to characterize such systems: their behavior under larger column axial load should be explored, stiffer springs that could lead to positive post-uplift stiffness should be studied, solutions employing prestressing should be tested, a method to design the protective steel jackets should be developed, torsion should be better understood by testing

specimens with eccentric masses, and more realistic geometries should be studied.

Acknowledgements

References

Almen, J. O., & Laszlo, A. (1936). The uniform-section disk spring. *Trans. Am. Soc. Mech. Eng.*, *58*(4).

Bachmann, J. A., Jost, C., Studemann, Q., Vassiliou, M. F., & Stojadinovic, B. (2016). An analytical model for the dynamic response of an elastic SDOF system fixed on top of a rocking single-story frame structure: Experimental validation. *ECCOMAS Congress 2016: Proceedings of the 7th European Congress on Computational Methods in Applied Sciences and Engineering*, *3*, 5023–5062.

Bachmann, J. A., Strand, M., Vassiliou, M. F., Broccardo, M., & Stojadinović, B. (2018). Is rocking motion predictable? *Earthquake Engineering & Structural Dynamics*, *47*(2), 535–552.

Bachmann, J. A., Vassiliou, M. F., & Stojadinović, B. (2017). Dynamics of rocking podium structures. *Earthquake Engineering & Structural Dynamics*, *46*(14), 2499–2517.

Bantilas, K. E., Kavvadias, I. E., & Vasiliadis, L. K. (2021a). Seismic response of elastic multidegree of freedom oscillators placed on the top of rocking storey. *Earthquake Engineering & Structural Dynamics*, *50*(5), 1315–1333.

Bantilas, K. E., Kavvadias, I. E., & Vasiliadis, L. K. (2021b). Analytical investigation of the seismic response of elastic oscillators placed on the top of rocking storey. *Bulletin of Earthquake Engineering*, *19*(2), 1249–1270.

Billington, S. L., & Yoon, J. K. (2004). Cyclic Response of Unbonded Posttensioned Precast

Columns with Ductile Fiber-Reinforced Concrete. *Journal of Bridge Engineering*, *9*(4), 353–363.

Bu, Z.-Y., Ou, Y.-C., Song, J.-W., & Lee, G. C. (2016). Hysteretic Modeling of Unbonded Posttensioned Precast Segmental Bridge Columns with Circular Section Based on Cyclic Loading Test. *Journal of Bridge Engineering*, *21*(6), 04016016.

Buckle, I. G., Constantinou, M. C., Diceli, M., & Ghasemi, H. (2006). *Seismic Isolation of Highway Bridges* (No. MCEER-06-SP07).

Calvi, G., Palermo, A. G., & Pampanin, S. (2004). *Use of 'controlled rocking' in the seismic design of bridges*. 13th World Conference on Earthquake Engineering (13 WCEE), Vancouver, Canada.

CEN. (2004a). *Eurocode 2: Design of concrete structures—Part 1-1: General rules and rules for buildings*. Comité Européen de Normalisation.

CEN. (2004b). *Eurocode 8: Design of Structures for Earthquake Resistance, Part 1: General Rules, Seismic Actions and Rules for Buildings*. Comité Européen de Normalisation.

Cheng, C.-T. (2008). Shaking table tests of a self-centering designed bridge substructure. *Engineering Structures*, *30*(12), 3426–3433.

Cherepinskiy, Y. (2004). *Seismic isolation of buildings with application of the kinematics bases*. 13th World Conference on Earthquake Engineering, Vancouver, Canada.

Christopoulos, C. (2004). Frequency Response of Flag-Shaped Single Degree-of-Freedom Hysteretic Systems. *Journal of Engineering Mechanics*, *130*(8), 894–903.

Christopoulos, C., Tremblay, R., Kim, H.-J., & Lacerte, M. (2008). Self-Centering Energy Dissipative Bracing System for the Seismic Resistance of Structures: Development and Validation. *Journal of Structural Engineering*, *134*(1), 96–107.

Cohagen, L. S., Pang, J. B. K., Stanton, J. F., & Eberhard, M. O. (2008). *A Precast Concrete Bridge Bent Designed to Re-Center after an Earthquake* (Rep No. WA-RD 684.3/TNW 2008-09). Washington State Department of Transportation.

Del Giudice, L., Wrobel, R., Leinenbach, C., & Vassiliou, M. F. (2020). *Static testing of additively manufactured microreinforced concrete specimens for statistical structural model validation at a small scale*. 8th International Conference on Advances in Experimental Structural Engineering (8AESE).

ElGawady, M. A., & Sha'lan, A. (2011). Seismic Behavior of Self-Centering Precast Segmental Bridge Bents. *Journal of Bridge Engineering*, *16*(3), 328–339.

FEMA. (2009). *Quantification of building seismic performance factors* (FEMA-P695). Federal Emergency Management Agency.

Giouvanidis, A. I., & Dimitrakopoulos, E. G. (2017). Seismic Performance of Rocking Frames with Flag-Shaped Hysteretic Behavior. *Journal of Engineering Mechanics*, *143*(5), 04017008.

Guerrini, G., Restrepo, J. I., Massari, M., & Vervelidis, A. (2015). Seismic Behavior of Posttensioned Self-Centering Precast Concrete Dual-Shell Steel Columns. *Journal of Structural Engineering*, *141*(4), 04014115.

Housner, G. W. (1963). The behavior of inverted pendulum structures during earthquakes. *Bulletin of the Seismological Society of America*, *53*(2), 403–417.

Kashani, M. M., Gonzalez-Buelga, A., Thayalan, R. P., Thomas, A. R., & Alexander, N. A. (2018). Experimental investigation of a novel class of self-centring spinal rocking column. *Journal of Sound and Vibration*, *437*, 308–324.

Konstantinidis, D., Kelly, J. M., & Makris, N. (2008). *Experimental Investigation on the Seismic Response of Bridge Bearings*. Earthquake Engineering Research Center, University of California.

Konstantinidis, D., & Makris, N. (2005). Seismic response analysis of multidrum classical columns. *Earthquake Engineering & Structural Dynamics*, *34*(10), 1243–1270.

Li, C., Bi, K., & Hao, H. (2019). Seismic performances of precast segmental column under bidirectional earthquake motions: Shake table test and numerical evaluation. *Engineering Structures*, *187*, 314–328.

Liu, R., & Palermo, A. (2017). Quasi-Static Testing of a 1/3 Scale Precast Concrete Bridge Utilising a Post-Tensioned Dissipative Controlled Rocking Pier. *Proceedings of 16th World Conference on Earthquake Engineering*. 16th World Conference on Earthquake Engineering, Santiago, Chile.

Liu, R., & Palermo, A. (2020). Multi-"Hinge" Hierarchical Activation to Improve Structural Robustness of Post-tensioned Rocking Piers. *Special Publication*, *341*, 202–225.

Makris, N., & Konstantinidis, D. (2003). The rocking spectrum and the limitations of practical design methodologies. *Earthquake Engineering & Structural Dynamics*, *32*(2), 265–289.

Makris, N., & Vassiliou, M. F. (2013). Planar rocking response and stability analysis of an array of free-standing columns capped with a freely supported rigid beam. *Earthquake Engineering & Structural Dynamics*, *42*(3), 431–449.

Makris, N., & Vassiliou, M. F. (2014). Are Some Top-Heavy Structures More Stable? *Journal of Structural Engineering*, *140*(5), 06014001.

Makris, N., & Vassiliou, M. F. (2015). Dynamics of the Rocking Frame with Vertical Restrainers. *Journal of Structural Engineering*, *141*(10), 04014245.

Malomo, D., Mehrotra, A., & DeJong, M. J. (2021). Distinct element modeling of the dynamic response of a rocking podium tested on a shake table. *Earthquake Engineering & Structural Dynamics*, *50*(5), 1469–1475.

Mander, J. B., & Cheng, C. T. (1997). *Seismic Resistance of Bridge Piers Based on Damage Avoidance Design* (Techncial Report NCEER-97-0014; pp. 1–144). National Center for Earthquake Engineering Research.

Marriott, D., Pampanin, S., & Palermo, A. (2009). Quasi-static and pseudo-dynamic testing of unbonded post-tensioned rocking bridge piers with external replaceable dissipaters. *Earthquake Engineering & Structural Dynamics*, *38*(3), 331–354.

Mashal, M. (2015). *Post-Tensioned Earthquake Damage Resistant Technologies for Accelerated Bridge Construction*.

Mashal, M., & Palermo, A. (2019). Low-Damage Seismic Design for Accelerated Bridge Construction. *Journal of Bridge Engineering*, *24*(7), 04019066.

MATLAB (Version R2019a). (2019). [Computer software]. The Mathworks Inc.

Motaref, S., Saiidi, M. S., & Sanders, D. (2014). Shake Table Studies of Energy-Dissipating Segmental Bridge Columns. *Journal of Bridge Engineering*, *19*(2), 186–199.

Mouzakis, H. P., Psycharis, I. N., Papastamatiou, D. Y., Carydis, P. G., Papantonopoulos, C., & Zambas, C. (2002). Experimental investigation of the earthquake response of a model of a marble classical column. *Earthquake Engineering & Structural Dynamics*, *31*(9), 1681–1698.

Nakaki, S. D., Stanton, J. F., & Sritharan, S. (1999). An Overview of the PRESSS Five-Story Precats Test Building. *PCI Journal*, *44*(2), 26–39.

Ou, Y.-C., Tsai, M.-S., Chang, K.-C., & Lee, G. C. (2010). Cyclic behavior of precast segmental concrete bridge columns with high performance or conventional steel reinforcing bars as energy dissipation bars. *Earthquake Engineering & Structural Dynamics*, *39*(11), 1181–1198.

Palermo, A., Pampanin, S., & Carr, A. J. (2005). *Efficiency of simplified alternative modelling approaches to predict the seismic response of precast concrete hybrid systems*. fibSymposium "Keep Concrete Attractive".

Palermo, A., Pampanin, S., & Marriott, D. (2007). Design, Modeling, and Experimental Response of Seismic Resistant Bridge Piers with Posttensioned Dissipating Connections. *Journal of Structural Engineering*, *133*(11), 1648–1661.

Panagiotou, M., Trono, W., Jen, G., Kumar, P., & Ostertag, C. P. (2015). Experimental Seismic Response of Hybrid Fiber-Reinforced Concrete Bridge Columns with Novel Longitudinal Reinforcement Detailing. *Journal of Bridge Engineering*, *20*(7), 04014090.

Papaloizou, L., & Komodromos, P. (2009). Planar investigation of the seismic response of ancient columns and colonnades with epistyles using a custom-made software. *Soil Dynamics and Earthquake Engineering*, *29*(11), 1437–1454.

Papantonopoulos, C., Psycharis, I. N., Papastamatiou, D. Y., Lemos, J. V., & Mouzakis, H. P. (2002). Numerical prediction of the earthquake response of classical columns using the distinct element method. *Earthquake Engineering & Structural Dynamics*, *31*(9), 1699–1717.

Priestley, M. J. N., Sritharan, S., Conley, J. R., & Pampanin, S. (1999). Preliminary Results and Conclusions from the PRESSS Five-Story Precast Concrete Test Building. *PCI Journal*, *44*(6), 42–67.

Priestley, M. J. N., & Tao, J. R. (1993). Seismic Response of Precast Prestressed Concrete Frames With Partially Debonded Tendons. *PCI Journal*, *38*(1), 58–69.

Qu, H., Li, T., Wang, Z., Wei, H., Shen, J., & Wang, H. (2018). Investigation and verification on seismic behavior of precast concrete frame piers used in real bridge structures: Experimental and numerical study. *Engineering Structures*, *154*, 1–9.

Reggiani Manzo, N., & Vassiliou, M. F. (2019). Displacement-based analysis and design of rocking structures. *Earthquake Engineering & Structural Dynamics*, *48*(14), 1613–1629.

Reggiani Manzo, N., & Vassiliou, M. F. (2021a). *A negative stiffness reinforced concrete system for resilient seismic design*. fib Symposium 2021: Concrete Structures: New trends for Eco-Efficiency and Performance.

Reggiani Manzo, N., & Vassiliou, M. F. (2021b). Simplified analysis of bilinear elastic systems exhibiting negative stiffness behavior. *Earthquake Engineering & Structural Dynamics*, *50*(2), 580–600.

Restrepo, J. I., & Rahman, A. (2007). Seismic Performance of Self-Centering Structural Walls Incorporating Energy Dissipators. *Journal of Structural Engineering*, *133*(11), 1560–1570.

Routledge, P. J., Cowan, M. J., & Palermo, A. (2016). Low-damage detailing for bridges—A case study of Wigram-Magdala Bridge. *Proceedings of the New Zealand Society for Earthquake Engineering Annual Conference*. 2016 NZSEE Conference.

Sakai, J., Jeong, H., & Mahin, S. (2006). *Reinforced concrete bridge columns that re-center following earthquakes*. 8th U.S. National Conference on Earthquake Engineering, San Francisco, USA.

Salehi, M., Valigura, J., Sideris, P., & Liel, A. B. (2021). Experimental Assessment of Second-Generation Hybrid Sliding-Rocking Bridge Columns under Reversed Lateral Loading for Free and Fixed End Rotation Conditions. *Journal of Bridge Engineering*, *26*(10), 04021071.

Sideris, P., Aref, A. J., & Filiatrault, A. (2014a). Large-Scale Seismic Testing of a Hybrid Sliding-Rocking Posttensioned Segmental Bridge System. *Journal of Structural Engineering*, *140*(6), 04014025. https://doi.org/10.1061/(ASCE)ST.1943-541X.0000961

Sideris, P., Aref, A. J., & Filiatrault, A. (2014b). Quasi-Static Cyclic Testing of a Large-Scale Hybrid Sliding-Rocking Segmental Column with Slip-Dominant Joints. *Journal of Bridge Engineering*, *19*(10), 04014036.

Sideris, P., Aref, A. J., & Filiatrault, A. (2015). Experimental Seismic Performance of a Hybrid Sliding–Rocking Bridge for Various Specimen Configurations and Seismic Loading Conditions. *Journal of Bridge Engineering*, *20*(11), 04015009.

Stanton, J. F., Stone, W. C., & Cheok, G. S. (1997). A hybrid reinforced precast frame for seismic regions. *PCI Journal*, *42*(2), 20–23.

Thonstad, T., Kennedy, B. J., Schaefer, J. A., Eberhard, M. O., & Stanton, J. F. (2017). Cyclic Tests of Precast Pretensioned Rocking Bridge-Column Subassemblies. *Journal of Structural Engineering*, *143*(9), 04017094.

Thonstad, T., Mantawy, I. M., Stanton, J. F., Eberhard, M. O., & Sanders, D. H. (2016). Shaking Table Performance of a New Bridge System with Pretensioned Rocking Columns. *Journal of Bridge Engineering*, *21*(4), 04015079.

Trono, W., Jen, G., Panagiotou, M., Schoettler, M., & Ostertag, C. P. (2015). Seismic Response of a Damage-Resistant Recentering Posttensioned-HYFRC Bridge Column. *Journal of Bridge Engineering*, *20*(7), 04014096.

Tsopelas, P., Constantinou, M. C., Kim, Y. S., & Okamoto, S. (1996). Experimental Study of Fps System in Bridge Seismic Isolation. *Earthquake Engineering & Structural Dynamics*, *25*(1), 65–78.

Uzdin, A. M., Doronin, F. A., Davydova, G. V., Avidon, G. È., & Karlina, E. A. (2009). Performance analysis of seismic-insulating kinematic foundations on support elements with negative stiffness. *Soil Mechanics and Foundation Engineering*, *46*(3), 99–107.

Vassiliou, M. F. (2018). Seismic response of a wobbling 3D frame. *Earthquake Engineering & Structural Dynamics*, *47*(5), 1212–1228.

Vassiliou, M. F., Broccardo, M., Cengiz, C., Dietz, M., Dihoru, L., Gunay, S., Mosalam, K. M., Mylonakis, G., Sextos, A., & Stojadinovic, B. (2021a). Shake table testing of a rocking podium: Results of a blind prediction contest. *Earthquake Engineering & Structural Dynamics*, *50*(4), 1043–1062.

Vassiliou, M. F., Burger, S., Egger, M., Bachmann, J. A., Broccardo, M., & Stojadinovic, B. (2017). The three-dimensional behavior of inverted pendulum cylindrical structures during earthquakes. *Earthquake Engineering & Structural Dynamics*, *46*(14), 2261–2280.

Vassiliou, M. F., Cengiz, C., Dietz, M., Dihoru, L., Broccardo, M., Mylonakis, G., Sextos, A., & Stojadinovic, B. (2021b). Dataset from the shake table tests of a rocking podium structure. *Earthquake Spectra*, *37*(3), 2107–2125.

Vassiliou, M. F., Cengiz, C., Dietz, M., Dihoru, L., Broccardo, M., Mylonakis, G., Sextos, A., & Stojadinovic, B. (2021c). Data set from shake table tests of free-standing rocking bodies. *Earthquake Spectra*, *37*(4), 2971–2987.

Vassiliou, M. F., & Makris, N. (2015). Dynamics of the Vertically Restrained Rocking Column. *Journal of Engineering Mechanics*, *141*(12), 04015049.

Wang, J., Wang, Z., Tang, Y., Liu, T., & Zhang, J. (2018). Cyclic loading test of self-centering precast segmental unbonded posttensioned UHPFRC bridge columns. *Bulletin of Earthquake Engineering*, *16*(11), 5227–5255. https://doi.org/10.1007/s10518-018-0331-y

Wasserman, L. (2013). *All of Statistics: A Concise Course in Statistical Inference*. Springer Science & Business Media.

White, S., & Palermo, A. (2016). Quasi-Static Testing of Posttensioned Nonemulative Column-Footing Connections for Bridge Piers. *Journal of Bridge Engineering*, *21*(6), 04016025.

Yamashita, R., & Sanders, D. H. (2009). Seismic Performance of Precast Unbonded Prestressed Concrete Columns. *ACI Structural Journal*, *106*(6), 821–830.

Zhong, C., & Christopoulos, C. (2021). Finite element analysis of the seismic shake-table response of a rocking podium structure. *Earthquake Engineering & Structural Dynamics*, *50*(4), 1223–1230.

Appendix 1

Table A1.1. Excitations.

Exc. ID	\multicolumn{3}{c}{Earthquake}			Recording Station	PEER RSN	$\overline{PGA}$ when $\overline{PGV}$ = 33.5 cm/s (in the model scale)
	M	Year	Name				
Pulse Like Records							
1	6.5	1979	Imperial Valley-06		El Centro Array #6	181	0.38g
2	6.5	1979	Imperial Valley-06		El Centro Array #7	182	0.36g
3	6.9	1980	Irpinia, Italy-01		Sturno	292	0.36g
4[b]	6.5	1987	Superstition Hills-02		Parachute Test Site	723	0.31g
5	6.9	1989	Loma Prieta		Saratoga – Aloha	802	0.56g
6	6.7	1992	Erzincan, Turkey		Erzincan	821	0.36g
7	7.0	1992	Cape Mendocino		Petrolia	828	0.63g
8	7.3	1992	Landers		Lucerne	879	0.53g
9	6.7	1994	Northridge-01		Rinaldi Receiving Sta	1063	0.44g
10	6.7	1994	Northridge-01		Sylmar – Olive View	1086	0.53g
11	7.5	1999	Kocaeli, Turkey		Izmit	1165	0.47g
12	7.6	1999	Chi-Chi, Taiwan		TCU065	1503	0.42g
13[b]	7.6	1999	Chi-Chi, Taiwan		TCU102	1529	0.22g
14	7.1	1999	Duzce, Turkey		Duzce	1605	0.45g
15	6.61	1971	San Fernando		Pacoima Dam (upper left abut)	77	1.03g
16	7.35	1978	Tabas_ Iran		Tabas	143	0.56g
17	6.93	1989	Loma Prieta		Saratoga - W Valley Coll.	803	0.38g
18	6.9	1995	Kobe_ Japan		Takarazuka	1119	0.63g
19	6.9	1995	Kobe_ Japan		Takatori	1120	0.38g
20	6.93	1989	Loma Prieta		Los Gatos - Lexington Dam	3548	0.32g
21	7.01	1992	Cape Mendocino		Bunker Hill FAA	3744	0.26g
22	6.6	2003	Bam_ Iran		Bam	4040	0.64g
23	6.63	2004	Niigata_ Japan		NIGH11	4228	0.81g
24	7.1	1979	Montenegro_ Yugoslavia		Bar-Skupstina Opstine	4451	0.53g
25	7	2010	Darfield_ New Zealand		GDLC	6906	0.44g
26	7.2	2010	El Mayor-Cucapah_ Mexico		El Centro Array #12	8161	0.37g
No Pulse Like Records							
27	6.8		Gazli, USSR		Karakyr	126	0.86g
28	6.5	1979	Imperial Valley-06		Bonds Corner	160	1.17g
29	6.5	1979	Imperial Valley-06		Chihuahua	165	0.73g
30	6.8	1985	Nahanni, Canada		Site 1	495	1.88g
31	6.8	1985	Nahanni, Canada		Site 2	496	1.09g
32	6.9	1989	Loma Prieta		BRAN	741	0.87g
33	6.9	1989	Loma Prieta		Corralitos	753	0.88g
34	7.0	1992	Cape Mendocino		Cape Mendocino	825	1.20g
35	6.7	1994	Northridge-01		LA – Sepulveda VA	1004	0.83g
36	6.7	1994	Northridge-01		Northridge – Saticoy	1048	0.61g
37	7.5	1999	Kocaeli, Turkey		Yarimca	1176	0.27g
38	7.6	1999	Chi-Chi, Taiwan		TCU067	1504	0.42g
39	7.6	1999	Chi-Chi, Taiwan		TCU084	1517	0.50g
40[b]	7.9	2002	Denali, Alaska		TAPS Pump Sta. #10	2114	0.24g
41[b]	6.95	1940	Imperial Valley-02		El Centro Array #9	6	0.54g
42	7.35	1978	Tabas_ Iran		Dayhook	139	0.83g
43	6.54	1987	Superstition Hills-02		Superstition Mtn Camera	727	1.59g
44	6.9	1995	Kobe_ Japan		Kobe University	1108	0.52g
45	7.14	1999	Duzce_ Turkey		Lamont 375	1617	1.84g
46	6.61	2000	Tottori_ Japan		SMNH01	3947	1.43g

47	6.52	2003	San Simeon_ CA	Cambria - Hwy 1 Caltrans Bridge	3979	0.79g
48	6.52	2003	San Simeon_ CA	Templeton - 1-story Hospital	4031	1.07g
49[b]	6.63	2004	Niigata_ Japan	NIG017	4207	0.85g
50[a]	6.63	2004	Niigata_ Japan	NIG019	4209	0.88g
51	7.1	1979	Montenegro_ Yugoslavia	Ulcinj - Hotel Albatros	4457	0.65g
52	6.8	2007	Chuetsu-oki_ Japan	Kashiwazaki NPP_ Unit 1: ground surface	4894	0.53g
Far Field Records						
53	6.7	1994	Northridge	Beverly Hills – Mulhol	953	0.55g
54	6.7	1994	Northridge	Canyon Country-WLC	960	0.76g
55	7.1	1999	Duzce, Turkey	Bolu	1602	0.95g
56	7.1	1999	Hector Mine	Hector	1787	0.59g
57	6.5	1979	Imperial Valley	Delta	169	0.71g
58	6.5	1979	Imperial Valley	El Centro Array #11	174	0.68g
59	6.9	1995	Kobe, Japan	Nishi-Akashi	1111	0.92g
60	6.9	1995	Kobe, Japan	Shin-Osaka	1116	0.61g
61	7.5	1999	Kocaeli, Turkey	Duzce	1158	0.43g
62	7.5	1999	Kocaeli, Turkey	Arcelik	1148	0.41g
63	7.3	1992	Landers	Yermo Fire Station	900	0.40g
64	7.3	1992	Landers	Collwater	848	0.74g
65	6.9	1989	Loma Prieta	Capitola	752	0.83g
66	6.9	1989	Loma Prieta	Gilroy Array #3	767	0.84g
67	7.4	1990	Manjil, Iran	Abbar	1633	0.83g
68	6.5	1987	Superstition Hills	El Centro Imp. Co.	721	0.51g
69	6.5	1987	Superstition Hills	Poe Road (temp)	725	0.79g
70	7.6	1999	Chi-Chi, Taiwan	CHY101	1244	0.33g
71	7.6	1999	Chi-Chi, Taiwan	TCU045	1485	0.78g
72	6.6	1971	San Fernando	LA – Hollywood Stor	68	0.80g
73	6.5	1976	Friuli, Italy	Tolmezzo	125	1.07g
74	6.19	1966	Parkfield	Temblor pre-1969	33	1.27g
75	6.61	1971	San Fernando	Lake Hughes #12	71	1.48g
76	6.53	1979	Imperial Valley-06	Calexico Fire Station	162	0.83g
77	6.06	1980	Mammoth Lakes-01	Long Valley Dam (Upr L Abut)	231	1.51g
78	6.6	1981	Corinth_ Greece	Corinth	313	0.74g
79	6.36	1983	Coalinga-01	Cantua Creek School	322	0.78g
80	6.36	1983	Coalinga-01	Parkfield - Fault Zone 14	338	0.62g
81	6.19	1984	Morgan Hill	Gilroy Array #4	458	1.22g
82[b]	6.6	1987	New Zealand-02	Matahina Dam	587	0.66g
83	5.99	1987	Whittier Narrows-01	Downey - Birchdale	614	0.82g
84	5.99	1987	Whittier Narrows-01	Inglewood - Union Oil	625	1.24g
85	5.99	1987	Whittier Narrows-01	LA - 116th St School	626	1.24g
86	5.99	1987	Whittier Narrows-01	LB - Orange Ave	645	0.69g
87	5.99	1987	Whittier Narrows-01	Santa Fe Springs - E.Joslin	692	1.06g
88[b]	6.54	1987	Superstition Hills-02	Westmorland Fire Sta	728	0.51g
89	6.93	1989	Loma Prieta	UCSC Lick Observatory	810	1.62g
90	7.28	1992	Landers	Joshua Tree	864	0.61g
91	6.69	1994	Northridge-01	Santa Monica City Hall	1077	1.45g
92	6.9	1995	Kobe_ Japan	Amagasaki	1101	0.58g
93	7.62	1999	Chi-Chi_ Taiwan	TCU095	1524	0.94g
94	7.37	1990	Manjil_ Iran	Qazvin	1636	0.87g

[a] The test was not performed at the low intensity.
[b] The test was not performed at the high intensity.

Test order ("L" for low intensity, "H" for high intensity):

L01, L04, L06, L13, L20, L21, L37, L40, L70, L02, L25, L26, L12, L62, L17, L22, L34, H62, L03, L87, L78, L71, L46, L83, L93, L31, L67, L61, H87, L82, L43, H34, L85, L89, L07, L86, L75, L58, L30, L19, L23, L73, L84, L32, L11, L14, H83, L74, L47, L66, L05, L18, L24, H77, L09, L53, H2, H84, L45, L15, L59, L16, L41, L52, H43, L42, H75, H85, H8, L65, L33, L81, H45, H86, L68, H64, L54, H73, L80, L35, L64, L69, L56, H74, L49, L10, H65, L76, H7, L92, L77, H18, L44, H32, H9, H33, H36, H92, L63, L51, H47, H31, H48, L91, L28, L48, H28, H21, H21, L79, H71, L36, L29, L60, H53, L55, H20, H15, H17, L39, H55, H23, H50, H22, H35, H56, H19, H5, L38, H54, H60, L90, L72, H11, H24, H44, H6, H10, H67, H59, H80, H12, L94, H78, H90, H69, H39, H51, H66, H25, H37, H94, H3, H76, L88, H93, H52, H91, H29, H42, H70, H63, H16, L27, H30, H89, H46, H1, H81, H27, L57, H14, H26, H57, H58, H61, H38, H68, H72, H79, H88

Appendix 2 - Derivation of the planar lateral load-deformation response of the system with shifted tendon

The equations presented in Section 6.2 present two simplifications: (a) the restraining system is assumed to be linear and (b) the tendon always stays in the centerline of the column. The actual system tested (a) uses a slightly nonlinear restraining system and (b) includes a duct in the column for constructional reasons, which allows the tendon to slightly deviate from the centerline. To this end, the pushover curve of Figure 6.9 was computed based on a model that can take into account both the nonlinearity of the restraining system, and the existence of the gap between the tendon and the duct.

The planar lateral load–deformation response of the system composed of N rigid columns of total mass $N \times m_c$, a rigid beam of mass m_b and restrained by a perfectly elastic restraining system with stiffness k_{res}, when subjected to a lateral force F applied at the beam can be derived via the principle of virtual work:

$$F \cdot \delta u - \left(\frac{m_b g}{N} + \frac{N m_c}{2} \right) \cdot \delta v = \delta V_S \tag{A2.1}$$

where V_s is the potential energy of the restraining system. Assuming that the columns are able to uplift, but not to slide, the virtual horizontal (δu) and vertical (δv) displacements are:

$$\delta u = \frac{du}{d\theta} \cdot \delta \theta = 2R \cdot \cos(\alpha - \theta) \cdot \delta \theta \tag{A2.2}$$

$$\delta v = \frac{dv}{d\theta} \cdot \delta \theta = 2R \cdot \sin(\alpha - \theta) \cdot \delta \theta \tag{A2.3}$$

In which, R is the semi-diagonal length of the column; α is the slenderness of the column, given by the angle between the semi-diagonal of the column and the vertical direction; and θ is

the tilt angle of the column.

Substituting Equations (A2.2) and (A2.3) into Equation (A2.1) yields:

$$F \cdot 2R\cos(\alpha - \theta) = \left(\frac{m_b}{Nm_c} + \frac{1}{2}\right) \cdot Nm_c g \cdot 2R\sin(\alpha - \theta) + N \cdot \frac{dV_S}{d\Delta\ell} \cdot \frac{d\Delta\ell}{d\theta} \qquad \text{(A2.4)}$$

where $\Delta\ell$ is the elongation of the restraining system. The force of the restraining system is $F_{res} = \frac{dV_S}{d\Delta\ell}$, and Equation (A2.4) becomes:

$$F = \left(\frac{m_b}{Nm_c} + \frac{1}{2}\right) \cdot Nm_c g \tan(\alpha - \theta) + \frac{N \cdot F_{res}}{2R\cos(\alpha - \theta)} \cdot \frac{d\Delta\ell}{d\theta} \qquad \text{(A2.5)}$$

When the gap between the tendon and tendon duct is taken into account, assuming that the tendon passes from (a) the center of the duct at the bottom end of the column and (b) the center of the duct at the top of the beam, the deformation of the restraining system is (Figure A2.1, left):

$$\Delta\ell = \sqrt{\left[2R \cdot \cos(\alpha - \theta) + (\ell_{ten} - 2h) - b \cdot \sin\theta\right]^2 + \left[2R \cdot \sin(\alpha - \theta) - b \cdot (1 + \cos\theta)\right]^2} - \ell_{ten} \qquad \text{(A2.6)}$$

in which, b and h are the half-width and half-height of the column, respectively; and ℓ_{ten} is the initial length of the tendon. When the tendon has touched the duct, the deformation of the restraining system is given by:

$$\Delta\ell = \sqrt{((b - c)\sin\theta)^2 + ((b - c)(1 - \cos\theta) + c)^2} + \sqrt{(2h)^2 + c^2} - 2h \qquad \text{(A2.7)}$$

where $c = \frac{(\phi_{duct} - \phi_{ten})}{2}$.

To produce Figure 6.9, the above equations were numerically solved in Matlab.
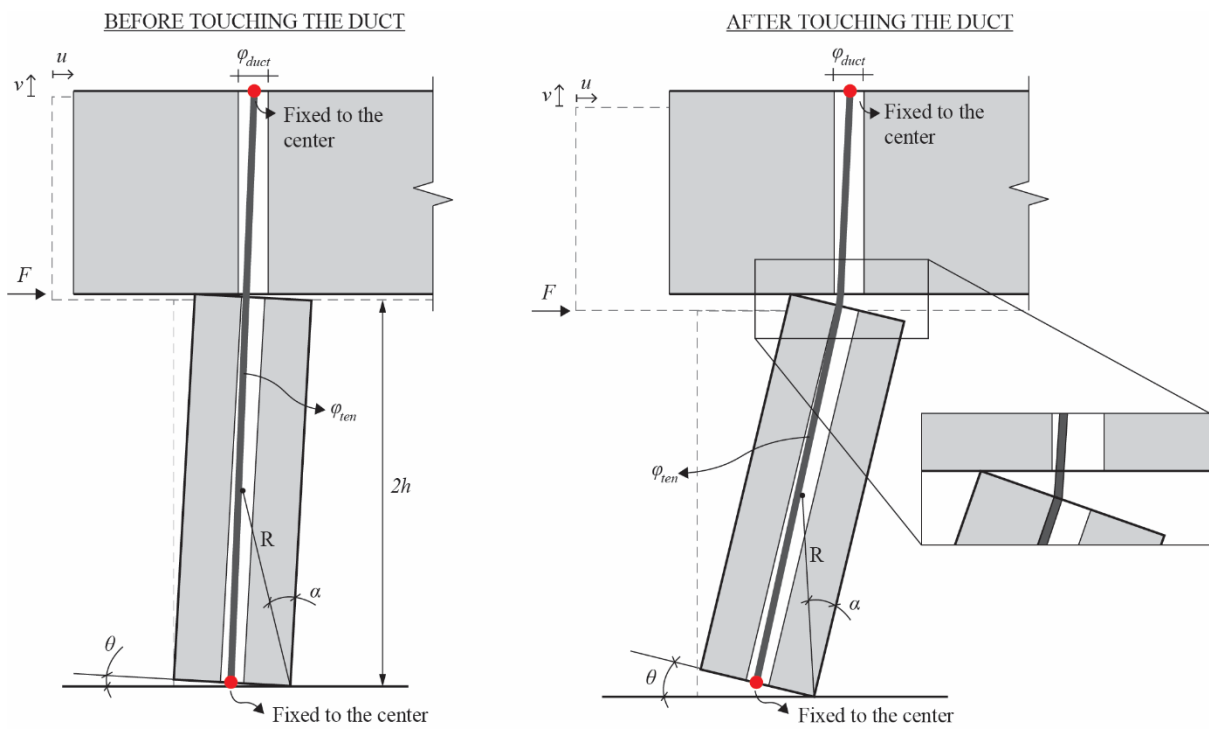
Figure A2.1. Geometry of a rocking system where the tendon shifts from the centerline.

7. Conclusions and Future Research

Abstract

This chapter summarizes the key findings and contributions of this dissertation. It also presents the individual conclusions of each chapter. Moreover, the main limitations of this study are clearly stated and suggestions for future research are offered.

7.1. Synopsis and key conclusions

This dissertation consists of seven chapters that summarize the work conducted on the seismic behavior of rocking bridge piers that present negative lateral stiffness. Although there is a vast number of analytical and numerical studies on the topic, rocking bridge piers with negative lateral stiffness have not been widely applied. With an overall goal of bringing such systems to practice, this dissertation proposed a simplified design method for systems with negative lateral stiffness and provided further experimental evidence on their seismic resilience. The individual conclusions of each chapter are presented below.

Displacement-based analysis and design of rocking structures

Chapter 2 studied the dynamic response of rigid rocking blocks by expressing the equations of motion in terms of the top horizontal displacement of the block. The problem was first assessed using analytical pulses and dimensionless terms. Later, the problem was assessed using recorded ground motions. The main conclusions are:

- Expressing the dimensionless displacement demand ($u_{max} \cdot \omega_p^2 / a_p$) as a function of the dimensionless strength parameter ($a_p / gtan\alpha$) and the dimensionless size-frequency parameter (ω_p / p or $b \cdot \omega_p^2 / a_p$) showed that, far from the overturning region, the displacement demand mainly depends on the strength parameter, and the size-frequency parameter can be neglected.

- Returning to dimensional terms, but still adopting analytical pulses as excitations, it was shown, once again, that the displacement demand of the block mainly depends on its slenderness, not on its size – as long as it is away from the overturning region.

- Using recorded ground motions, median spectra (i.e. displacement demand versus slenderness) for blocks of different sizes were constructed using the FEMA P695 set of ground motions. A median spectrum for a large block ($2H = 1000$ m), which would not overturn in practice, was also constructed. As long as overturning is avoided, the spectra of blocks of different sizes, including the large block ($2H = 1000$ m), match well.

- A preliminary design methodology was presented, in which the spectrum of the block that does not overturn (i.e. $2H = 1000$ m) was used. Applying this design methodology to a case study, it was shown that the simplified method can predict the median displacement demand of the block reasonably well. In most cases, it predicted the

median displacement demand with an error smaller than 20%, and in all cases the error was smaller than 40%.

Simplified analysis of bilinear elastic systems exhibiting negative stiffness

Chapter 3 generalized the work presented in Chapter 2 for other systems with negative lateral stiffness. It first presented a general equation of motion that can describe the dynamics of different systems that present an initial pre-uplift deformability, a negative post-uplift stiffness, and do not dissipate energy while unloading. Then, a simplified system (ZSBE system) with zero post-uplift stiffness was proposed for predicting the displacement demand of the different systems. Two approaches were suggested for predicting the displacement demand of the systems: the equal displacement rule (also shown in Chapter 2), and the equal energy rule. The validity of both approaches was assessed using the set of recorded ground motions proposed by FEMA P695. The main conclusions are:

- In order to assess the validity of the equal displacement rule, median and 90th percentile spectra (i.e. displacement demand versus normalized uplift force) were constructed for quasi-rigid systems with different displacement capacity (u_{cap}), and for the ZSBE system. Once the systems with finite displacement capacity were far from overturning, their median spectra compared reasonably well with the median spectra of the ZSBE system.

- The ZSBE spectra underpredicted the displacement demand of the systems with finite displacement capacity, suggesting that the equal displacement rule is unconservative.

- Similarly, the equal energy rule was assessed by constructing median and 90th percentile spectra. Once more, the median spectra for systems with finite displacement capacity agreed well with the spectra of the ZSBE system, showing that the equal energy rule also offers a good prediction of the displacement demand.

- Differently from the equal displacement rule, the equal energy rule overpredicted the displacement demand of the systems with finite displacement capacity. Therefore, it is a conservative approach.

- However, there were not enough ground motions to accurately predict 90th percentile spectra. Therefore, the curves should only be perceived as an indication of the motion-to-motion variability of the set of ground motions.

- The equal displacement rule and equal energy rule were also evaluated for a case study of a bridge-like structure of specific geometry. The case study confirmed the previous observations. The equal displacement rule underestimated the displacement demand of the structure, while the equal energy rule overpredicted it in most cases. In any case, none of the rules led the system to collapse, probably because of the adopted safety factor (FS=2.5).

- The pre-uplift deformability has an important influence on the displacement demand predicted by the ZSBE system. However, for all cases and ground motions considered in this study, two possible criteria could be proposed for considering the pre-uplift deformability negligible: (1) if the predicted displacement demand is larger than 50 cm; or (2) if the system has a normalized uplift force smaller than 0.2.

Uniform risk spectra for rocking structures

Chapter 4 presented a methodology for constructing Uniform Risk Spectra (URS) for systems with negative lateral stiffness, using ZSBE spectra (Chapter 3) within the framework of performance-based engineering. Spectra with 2%, 10%, and 50% probability of exceedance in 50 years, constructed with the geomean of the PGA or PGV as intensity measure, were presented for six locations in Europe. Then, the efficiency of the intensity measures was indirectly assessed through bootstrapping. At the end of the chapter, an analytical approximation of the spectra is proposed. The main conclusions are:

- The PGA-based URS predicted larger displacement demands than the PGV-based URS with the same probability of exceedance and for the same location. This could possibly be attributed to the higher variance of the Ground Motion Prediction Equations (GMPE) for PGA. However, it is also important to note that the fragility curves used for constructing each one of the spectra were obtained from different incremental dynamic analyses. Thus, one should be careful when comparing the spectra constructed with different intensity measures.

- The bootstrapping analysis revealed that, for predicting the peak rocking response, the geomean of the PGV is a more efficient intensity measure than the geomean of PGA. This could be observed by the narrower 90% confidence interval of the PGV-based spectra. Therefore, PGV-based URS better represent the overturning risk.

- The geomean of the PGA proved to be more efficient than the geomean of the PGV for predicting the rocking initiation. This agrees with previous studies and follows from the uplifting condition for rocking systems (PGA $> f_{up}/m$).

- An exponential function was fitted to the PGV-based spectra. The function overpredicts the displacement demand of structures with $f_{up}/(mg) < 0.05$. A three-fold function could have been used to better predict this region of the spectra. However, as this corresponds to very slender systems not used in practice, simplicity was preferred.

Cyclic tests of a precast restrained rocking system for sustainable and resilient seismic design of bridges

Chapter 5 presented the results of the quasi-static cyclic tests performed on two specimens at 1:5 scale. The specimens comprised a restrained rocking column connected to a reinforced concrete cap-beam through an unbonded tendon in series with disc springs. The disc springs increased the flexibility of the restraining system, leading to a structural system with negative lateral stiffness. In both specimens, the columns were not connected to the floor. The specimens differed in terms of the column ends protection. In one of the specimens the column ends were protected by a steel jacket, while the ends of the other column were only protected by steel discs. During the cyclic tests, the specimens were subjected to a maximum drift ratio of 16%. The specimen with the column protected by steel jackets was also subjected to a pushover test, reaching a maximum drift ratio of approximately 32%. The main observations and conclusions of the quasi-static tests are:

- The lateral force-drift ratio curves showed that both specimens presented no strength reduction during the cyclic tests.

- The loops, however, enclosed an area, indicating that there was some energy dissipation. As no damage could be observed in the specimens, it was concluded that the energy dissipation probably comes from the friction in the setup, and/or the friction between the tendon and tendon duct.

- It can also be depicted from the lateral force-drift ratio curves that the columns slid. However, for none of the amplitudes, the columns touched the sliding restrainer.

- The columns and restraining systems were designed based on a 2D rigid body analytical model. Comparing the experimental and analytical lateral force-drift ratio curves, one could conclude that the analytical model predicts reasonably well the uplift force and

post-uplift lateral stiffness of the system. Furthermore, the specimen presented an initial positive stiffness that inherently cannot be captured by a rigid body model.

- The force and deformation measured for the stack of springs agreed well with the analytical equations proposed by Almen and Laszlo (1936). The recorded forces in the restraining system revealed, however, that the complete restraining system (i.e. tendon + stack of springs) was slightly more flexible than it was predicted by the analytical equations.

- Visual observations and the deflection shapes presented in Chapter 5 suggested that the compression zone at the interfaces between the column and the cap-beam, as well as between the column and the floor essentially collapses to a compression point.

- No concrete spalling or cracks could be identified. The only observed damage was a dent in the top steel jacket, caused by local buckling. The minor damage was probably a consequence of improper casting, which resulted in air pockets inside the steel jacket.

- The lateral force-drift ratio curve of the pushover test showed that the specimen protected by the steel jackets presented almost no strength reduction, even after being subjected to a drift ratio of 31.8%.

- No further damages, other than the existing dent in the steel jacket, were observed after the pushover test.

Shaking table tests of a resilient bridge system with precast reinforced concrete columns equipped with springs

Chapter 6 reported the results of the shaking table tests and presented a statistical validation of a 3D rigid body model. The tested specimen was composed of a reinforced concrete slab supported by four rocking columns. Similarly to the columns tested in the first part of this experimental campaign (Chapter 5), the columns were not connected to the ground and they were only connected to the slab through an unbonded tendon in series with disc springs. Differently from the quasi-static tests, the rocking bridge system was equipped with stoppers, which were designed to engage only after large displacements. The specimen was designed with negative lateral stiffness, and the same specimen was subjected to 181 excitations, scaled to two different levels of PGV. The main conclusions of this chapter are:

- The measured lateral force-drift ratio curves revealed that the analytical model (also adopted for the design of the specimen of Chapter 5) overpredicts the uplift force of the system, and, once again, cannot predict the pre-uplift positive stiffness.

- The slab experienced significant torsion.

- During the tests, it was observed that the columns slid and, in some cases, climbed the sliding restrainer. However, in none of the tests (except for the one that the system failed), the columns overpassed the sliding restrainer.

- The columns were visually inspected after each excitation. No concrete spalling or cracks were observed. During the first 180 excitations, the only observed damage was some abrasion of the edges of the steel protection. Due to the large forces in the top end of the column, the abrasion in the top steel jacket was more pronounced.

- The stoppers engaged in few tests (5 out of 181). With the exception of the excitation that caused collapse of the specimen, the redundant mechanism was effective in preventing the overturning of the specimen.

- The collapse of the specimen was caused by the premature failure of the tendons of two of the columns. The failure occurred in the threaded sockets at a load smaller than the yielding load provided by the manufacturer. Such a failure highlights the importance of the design of the restraining system.

- Lastly, the chapter presented a statistical validation of a simple 3D rigid body model. Despite the simplicity of the model, the empirical cumulative distribution function (CDF) of the numerical model agreed reasonably well with the empirical CDF obtained from the experiments. In most cases, the numerical CDF was contained inside the 95% confidence interval of the experimental CDF.

- Using the two-sample Kolmogorov-Smirnov test, for almost all cases, none or small evidence was found for rejecting the hypothesis that the empirical CDFs belong to the same distribution.

- The median responses obtained from the experiments and the numerical model were also compared. In 7 out of 8 cases, the numerical model predicted the median response with a deviation of less than 30% to the median experimental response.

- However, the model disregards several physical mechanisms observed in the tests and more tests under different conditions and geometries should be conducted for its validation.

7.2. Limitations and Future Research

The main limitations of the work summarized in this dissertation and suggestions for future research are:

- The simplified design method developed in Chapter 2 to 4 was mainly assessed for quasi-rigid systems, while the influence of the pre-uplift deformability was only briefly discussed. In future work, it is recommended that the spectra are further explored for systems with different pre-uplift deformability.

- Furthermore, the spectra were developed for planar motion. Their validity for three-dimensional motion should be further explored in future research.

- The set of ground motions proposed by FEMA P695 was widely used in this dissertation, both for the development of the simplified design method and for the shaking table tests. As the response of systems with negative lateral stiffness is highly nonlinear, the conclusions of this dissertation should be validated for other sets of ground motions.

- Due to the limitations of both setups, the experimental campaign presented in this dissertation consisted of tests on 1:5 scale specimens subjected to a normalized axial load of 3.3% or 5%. Even though the adopted normalized axial load can be encountered in practice, it is rather on the low side of the range of typical bridges. Since a larger axial load could lead to a shift of the neutral axis of the cross-section of the column ends, as well as more significant damages, the influence of the axial load on the seismic behavior of the rocking bridge pier should be further investigated.

- The source of energy dissipation in the quasi-static cyclic tests could not be asserted. However, two possible sources were pointed out: (1) friction in the setup, or (2) friction between the tendon and the tendon's duct. In future work, it is recommended the use of a 3D load cell underneath the column, which can measure only the horizontal force applied to the specimen. If one is interested in quantifying the friction between the tendon and the tendon's duct, load cells at the top and bottom end of the tendon should be used (Salehi, 2020).

- Due to the scale of the specimens and the reduced space within the cross-section of the columns, the tendons were anchored through threaded sockets screwed to the bottom end of the columns and top of the slab. However, during the shaking table tests, two drawbacks of this anchorage system were observed: (1) the series of excitations loosens the nut that anchors the tendon at the top of the slab, creating a slack in the tendons,

and (2) the tendon's failure occurred at the threaded sockets. Therefore, in future work, the anchorage system should be improved.

- During the shaking table tests, it was observed that the specimen experiences torsion. Although the specimen was symmetric, the torsion originated from small and unavoidable imperfections of the specimen. Therefore, the influence of the torsion on the seismic behavior of the system should be further investigated through more shaking table tests of a rocking system with eccentric mass. Moreover, the influence of torsion on systems with negative torsional stiffness should be analytically explored.

- The statistical validation of the numerical model presented in Chapter 6 cannot be considered definitive. As mentioned in Chapter 6, the model does not capture a number of mechanisms observed in the tests, such as torsion of the slab and columns, or the sliding of the columns. Therefore, it is important that the numerical model is statistically validated against data from other experimental campaigns, in which a different set of ground motions and a different specimen geometry is adopted.

- The steel jackets and steel discs that were protecting the column ends were designed empirically and conservatively. A more precise design method should be developed.

- In this study, a combination of disc springs that resulted in negative post-uplift stiffness was used. Alternatively, disc springs that would result in positive post-uplift stiffness can be used. This would lead to a behavior closer to conventional seismic isolation.

References

Almen, J. O., & Laszlo, A. (1936). The uniform-section disk spring. *Trans. Am. Soc. Mech. Eng.*, *58*(4).

Salehi, M. (2020). *Nonlinear modeling, dynamic analysis, and experimental testing of hybrid sliding-rocking bridges*. [Ph.D. Thesis]. Texas A&M University.

Appendix 1 – Equivalence between the unrestrained rocking system (Ch. 2) and the Negative Stiffness Bilinear Elastic Oscillator (Ch.3, 4)

The mathematical equivalence between the response of the unrestrained rectangular rocking block (Figure A1.1, left) and the Negative Stiffness Bilinear Elastic (NSBE) oscillator (Figure A1.1, right) is obtained by matching the terms of their equations of motion. From Chapter 2, Equation (2.1), the equation of motion of the unrestrained rectangular rocking block is:

$$\frac{4}{3}mR^2\ddot{\theta} + mgR\sin(\alpha - \theta) = -m\ddot{u}_g R\cos(\alpha - \theta) \tag{A1.8}$$
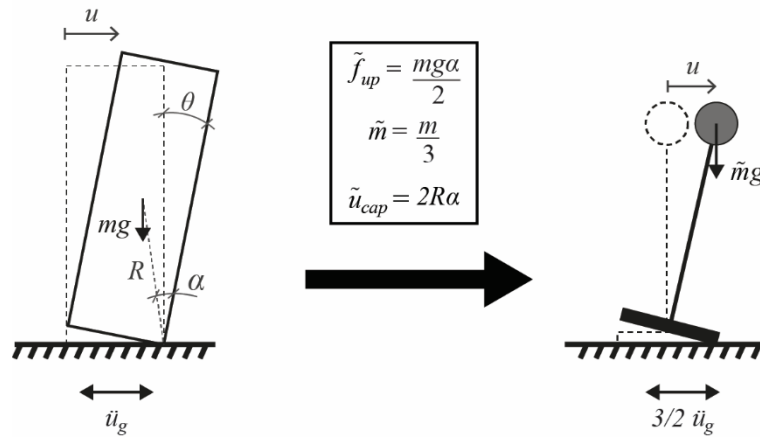
Figure A1.1. Equivalence between the rectangular rocking block (left) and the NSBE oscillator (right).

And, from Chapter 3, Equation (3.2), the equation of motion of the NSBE oscillator, when $u_{up} = 0$, is:

$$\tilde{m} \cdot \ddot{u}(t) + \tilde{f}_{up} \cdot \left(1 - \frac{u(t)}{\tilde{u}_{cap}}\right) = -\Gamma\tilde{m} \cdot \ddot{u}_g(t) \tag{A1.9}$$

Note that for the two systems to be equivalent, the excitation applied to the NSBE oscillator must be scaled by a factor Γ.

In order to match the terms, Equation (A1.8) is first linearized (Equation (A1.3)) and expressed in terms of the top horizontal displacement (Equation (A1.4)):

$$\begin{cases} \sin(\alpha - \theta) \approx (\alpha - \theta) \\ \cos(\alpha - \theta) \approx 1 \end{cases} \rightarrow \frac{4}{3}mR^2\ddot{\theta} + mgR(\alpha - \theta) = -m\ddot{u}_g R \tag{A1.10}$$

$$\frac{4}{3}mR^2\left(\frac{\ddot{u}}{2R}\right)+mgR\left(\alpha-\frac{u}{2R}\right)=-m\ddot{u}_g R \quad \rightarrow \quad \frac{1}{3}m\ddot{u}+\frac{mg\alpha}{2}\left(1-\frac{u}{2R\cdot\alpha}\right)=-\frac{3}{2}\left(\frac{m}{3}\right)\ddot{u}_g \qquad (A1.11)$$

Then, matching the terms of Equation (A1.9) and (A1.11), we obtain the equivalence between the systems.

$$\tilde{m}=\frac{m}{3} \qquad \tilde{f}_{up}=\frac{mg\alpha}{2} \qquad \tilde{u}_{cap}=2R\alpha=2R\sin\alpha \qquad \Gamma=\frac{3}{2} \qquad (A1.12)$$

Figure 2.10, Figure 2.11, and Figure 2.12 cannot be directly deduced from Figure 3.10, Figure 3.11, and Figure 3.12 because, in Chapter 2, the coefficient of restitution r depends on the slenderness α of the block (Equation (2.3)), while, in Chapter 3, the coefficient of restitution is constant and equal to $r = 0.95$. Moreover, as derived above, the spectra for the NSBE oscillator (Chapter 3) would also have to be constructed using ground motions scaled to an intensity 3/2 times larger (i.e., $\Gamma = 3/2$) than the intensity of the ground motions used to construct the spectra for the rocking block (Chapter 2).

$$\frac{4}{3}mR^2\left(\frac{\ddot{u}}{2R}\right)+mgR\left(\alpha-\frac{u}{2R}\right)=-m\ddot{u}_g R \quad \rightarrow \quad \frac{1}{3}m\ddot{u}+\frac{mg\alpha}{2}\left(1-\frac{u}{2R\cdot\alpha}\right)=-\frac{3}{2}\left(\frac{m}{3}\right)\ddot{u}_g$$

Appendix 2 – Complementary data

This appendix presents complementary data to Chapters 3 and 4, which could not be presented in the original papers due to the space limitation specified by the publishing journal.

A2.1. Complementary data to Chapter 3

A2.1.1. Median and 90th percentile spectra for systems with u_{up} = 0.005 m

- Equal Displacement Rule
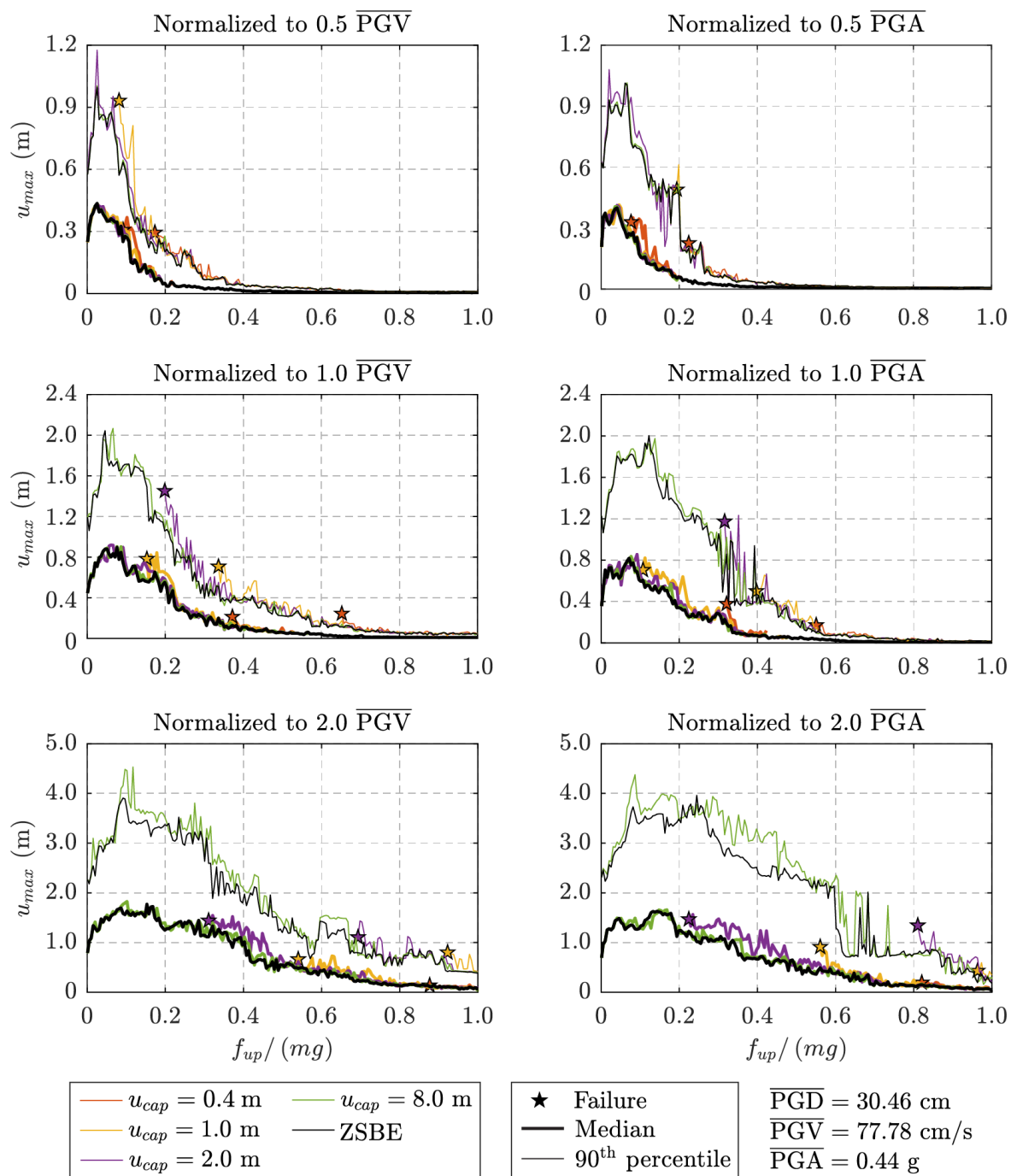
Figure A2.1. Median displacement spectra for near-field pulse-like record set, u_{up} = 0.005 m.
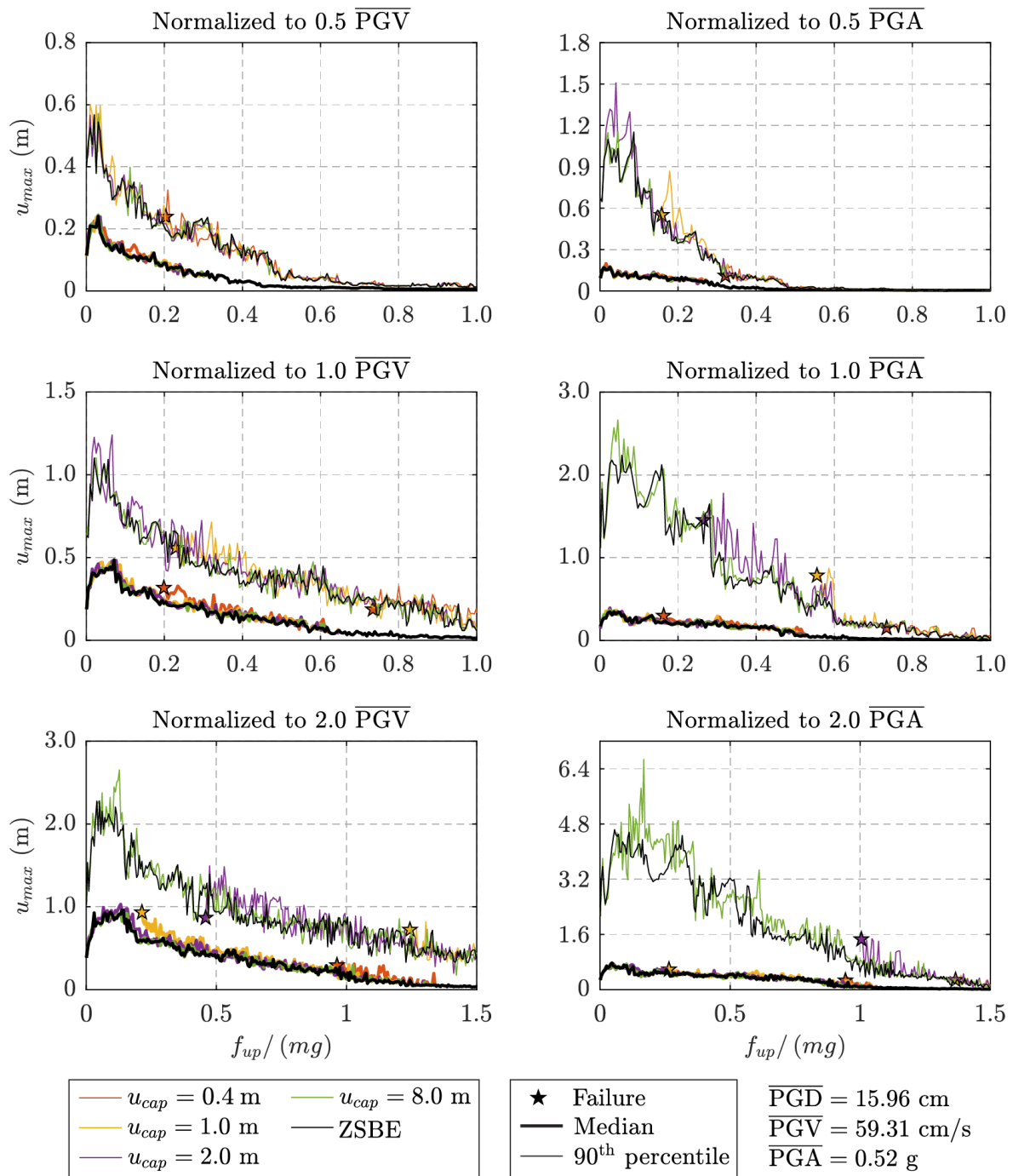
Figure A2.2. Median displacement spectra for near-field no pulse-like record set, $u_{up} = 0.005$ m.
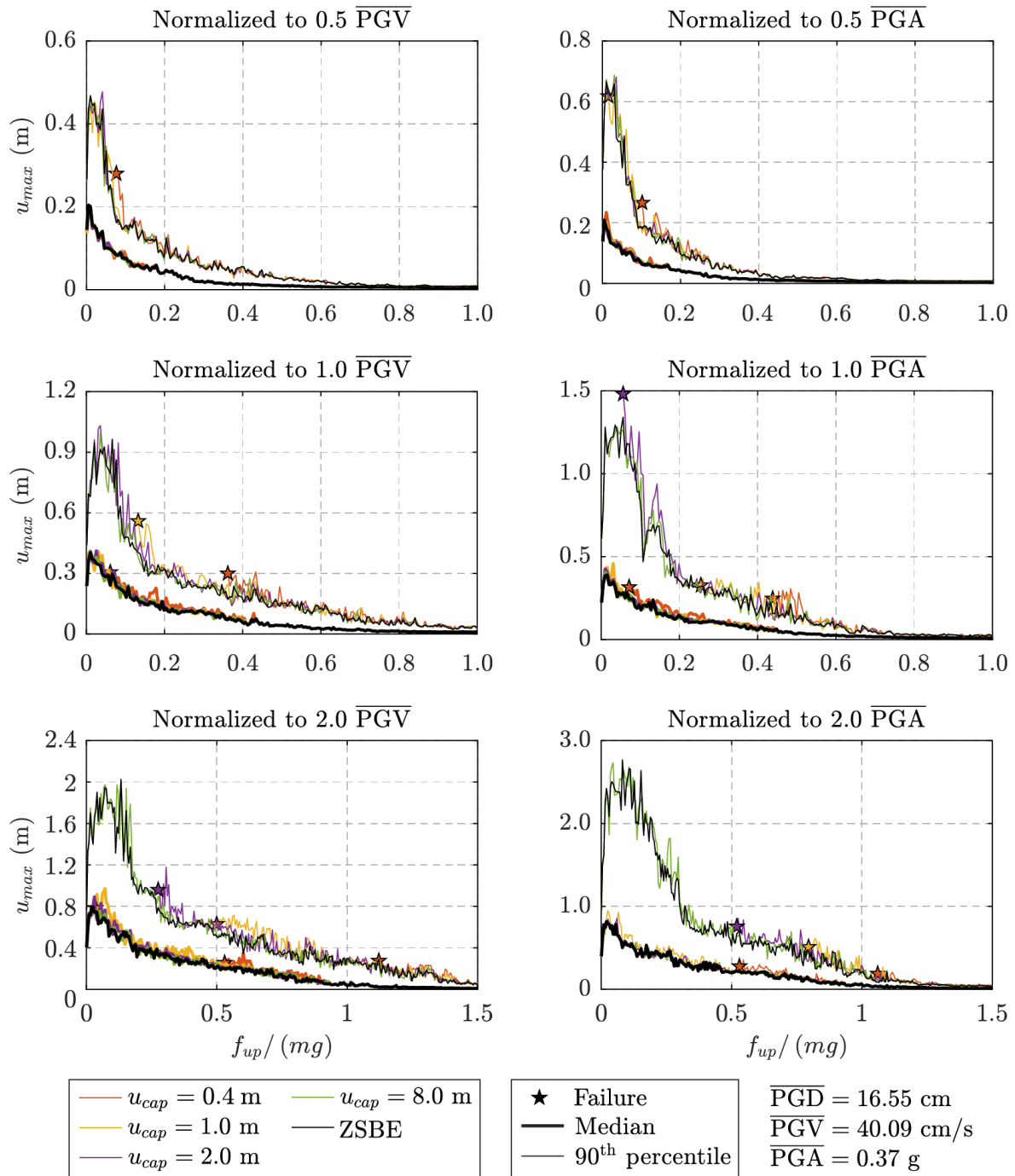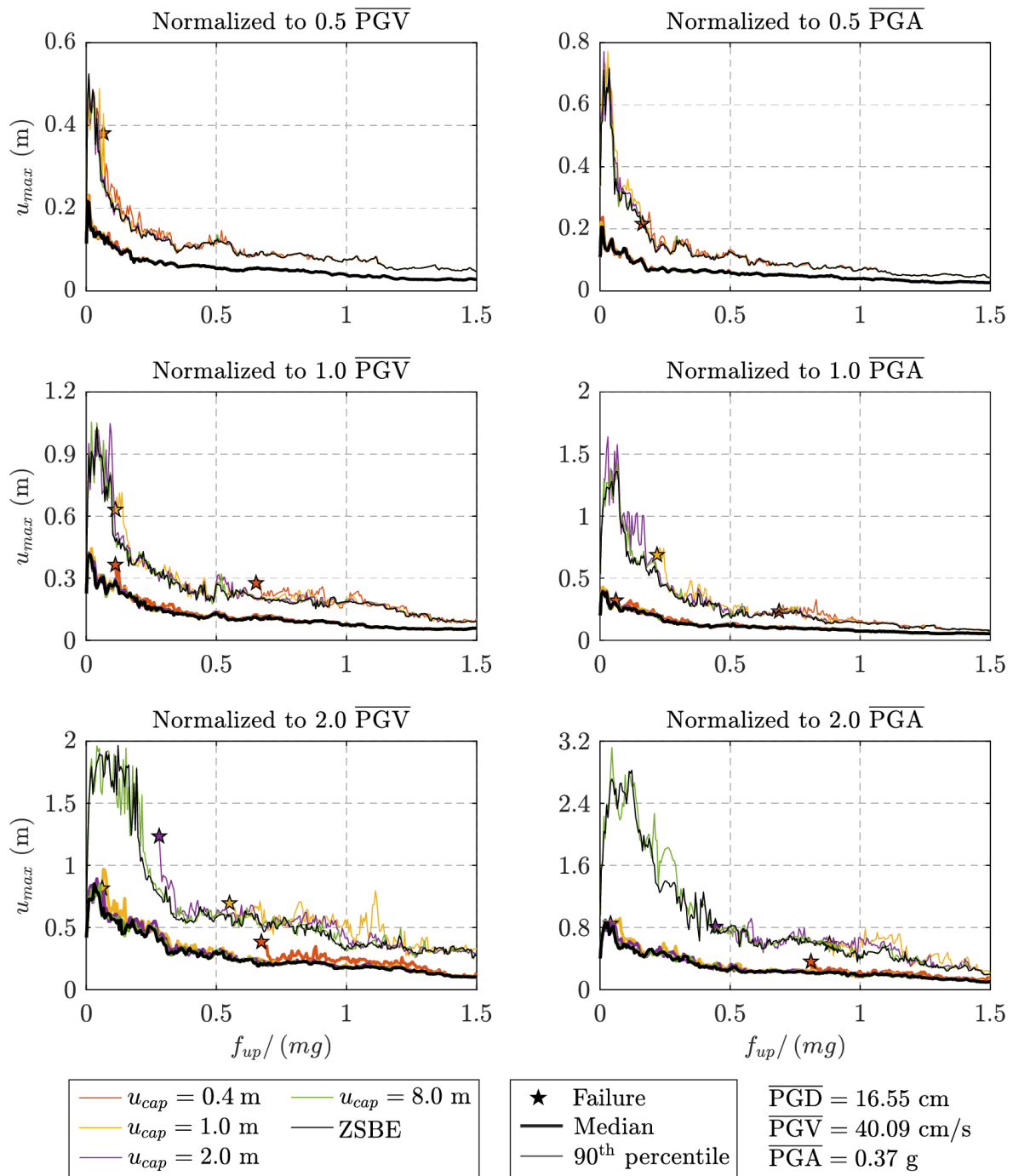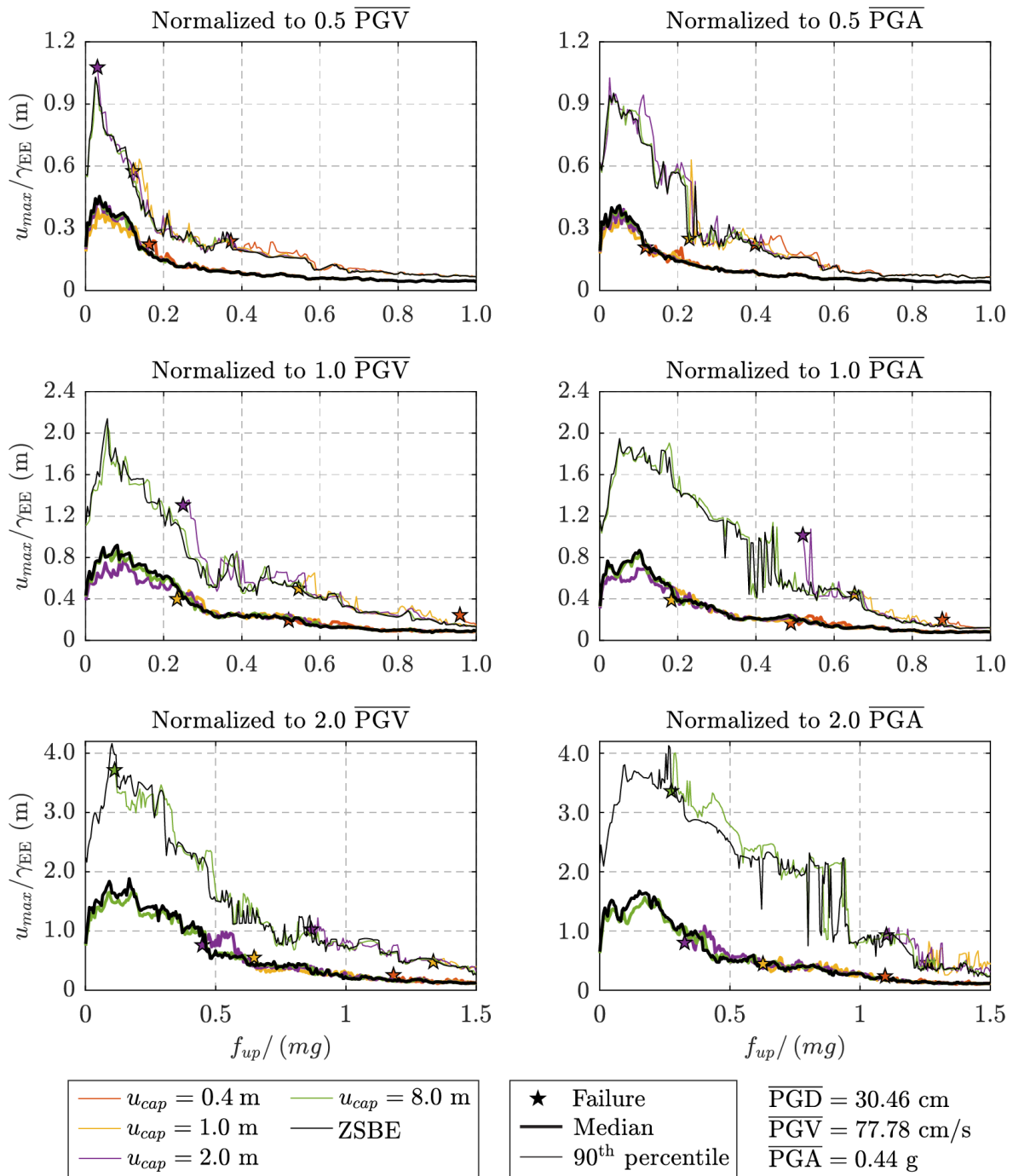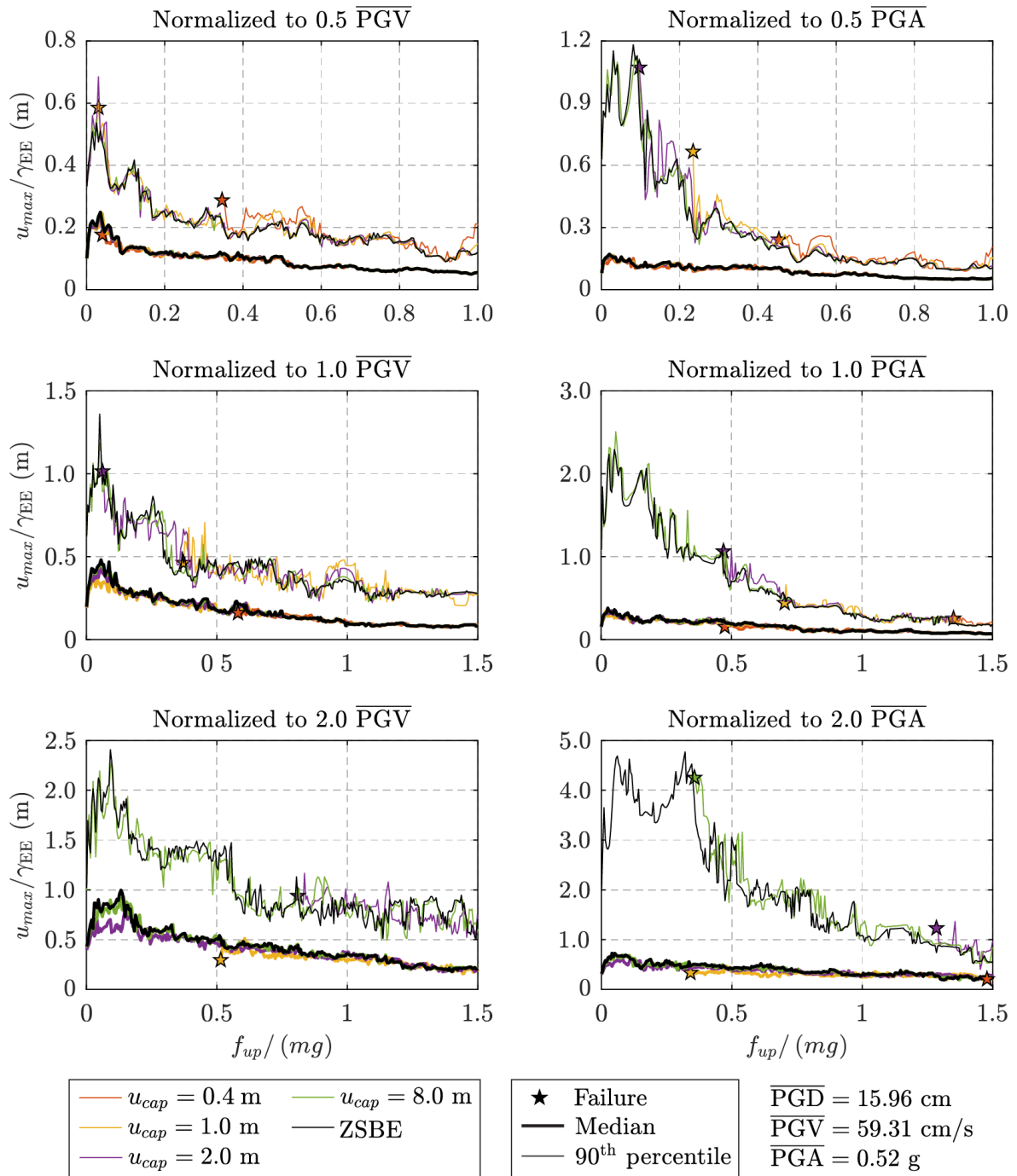
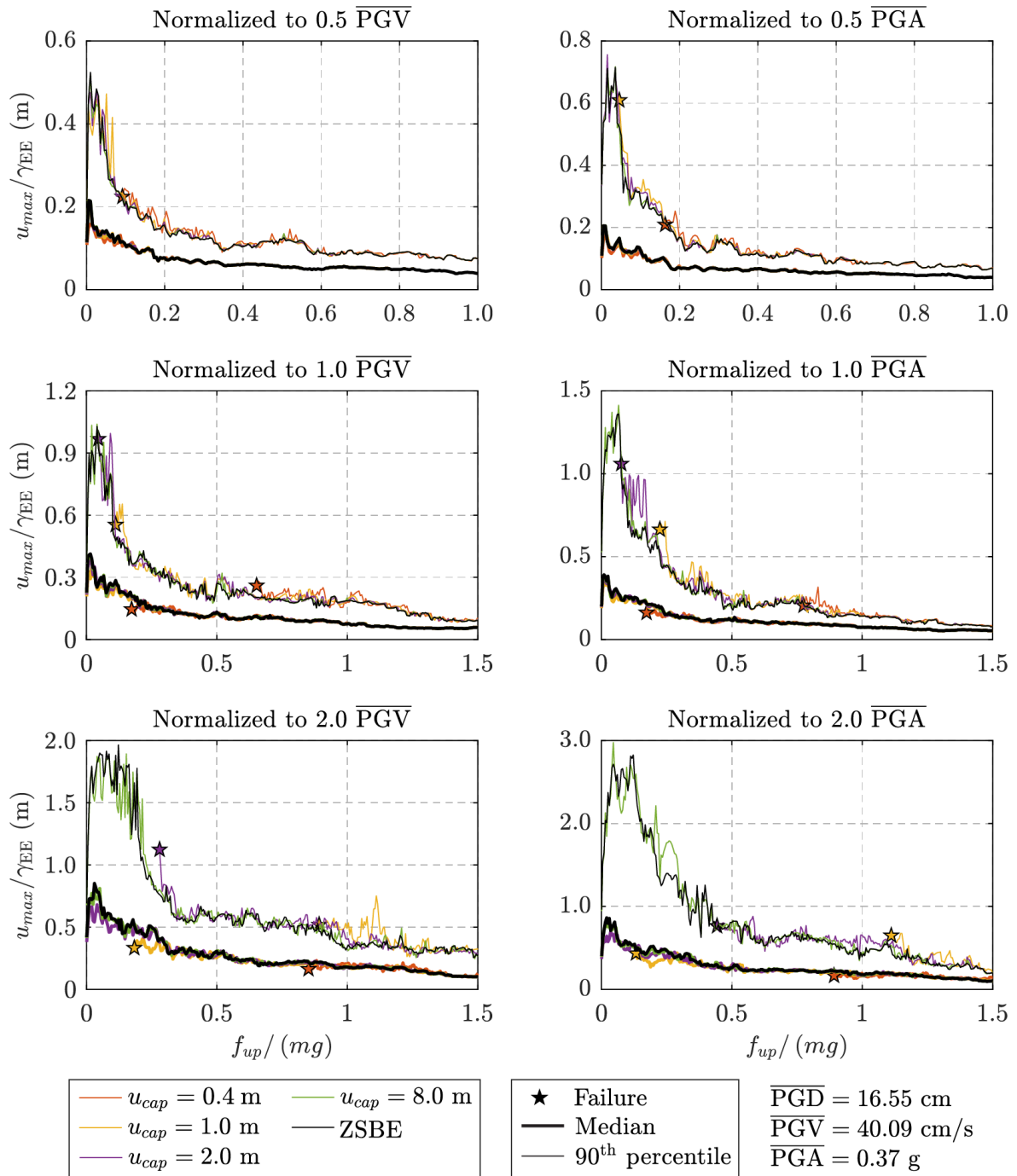**Figure A2.3.** Median displacement spectra for far-field record set, $u_{up} = 0.005$ m.

- Equal Energy Rule
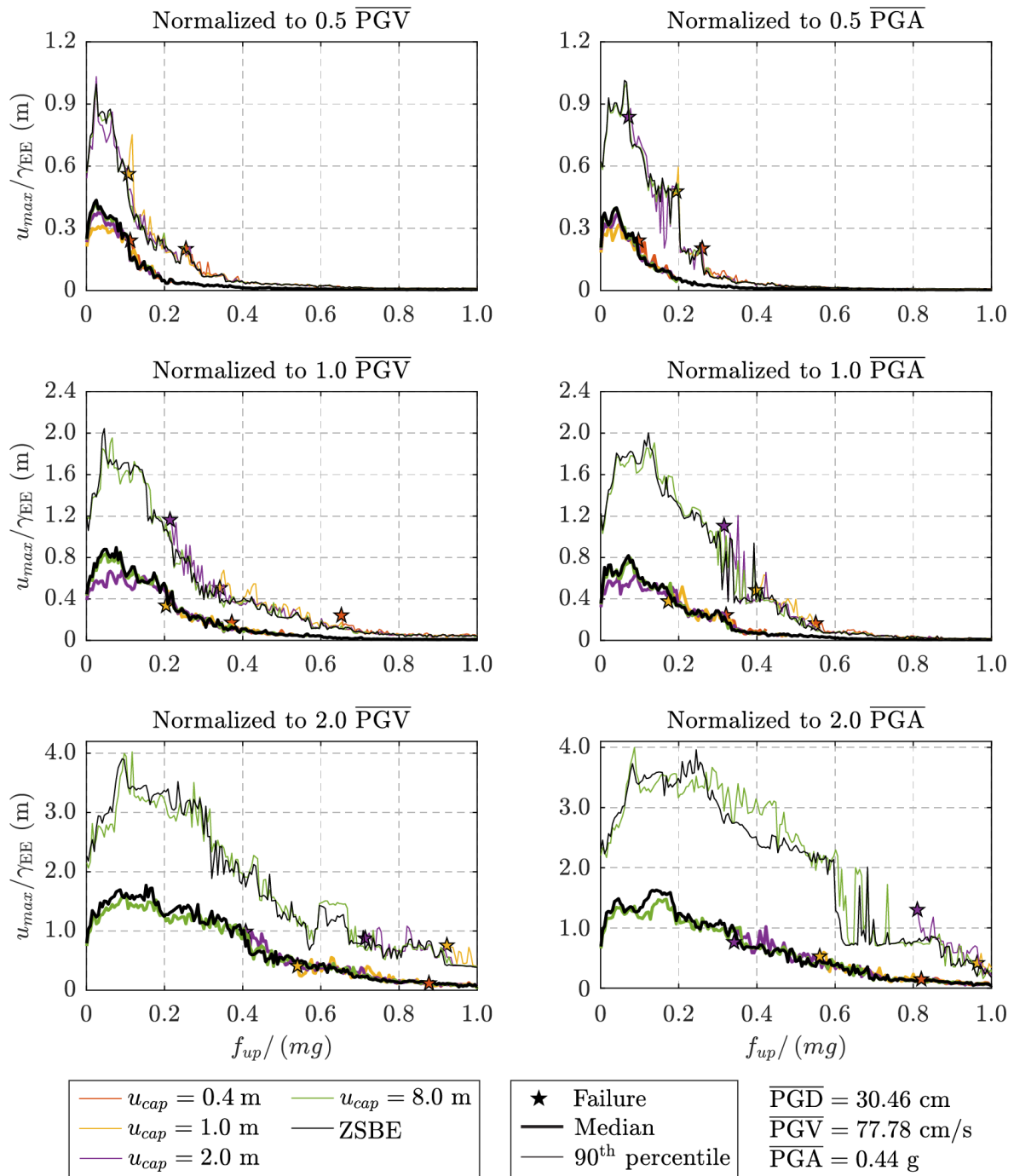
Figure A2.4. Median displacement spectra normalized by γ_{EE} for near-field pulse-like record set, $u_{up} = 0.005$ m.
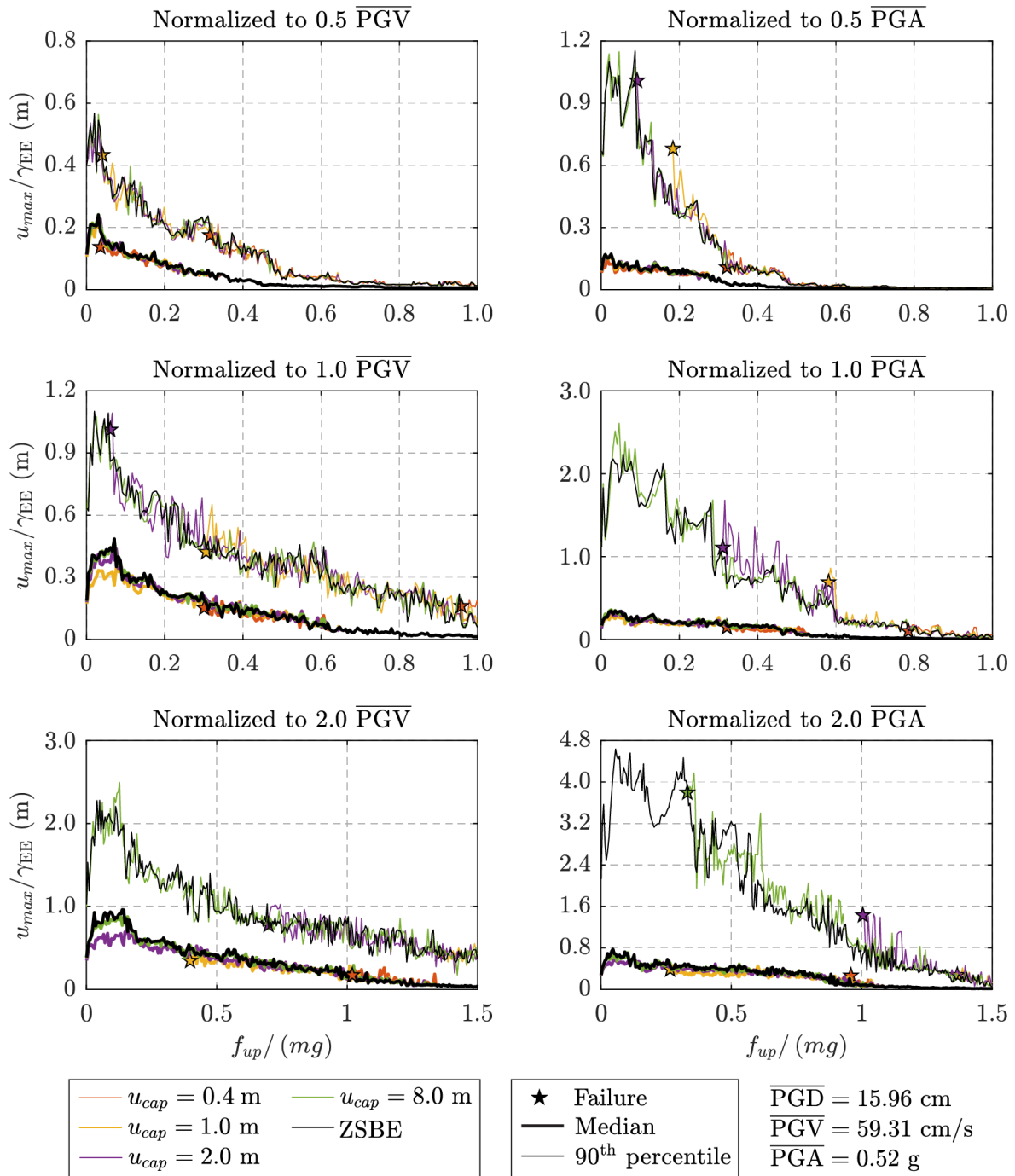
Figure A2.5. Median displacement spectra normalized by γ_{EE} for near-field no pulse-like record set, u_{up} = 0.005 m.
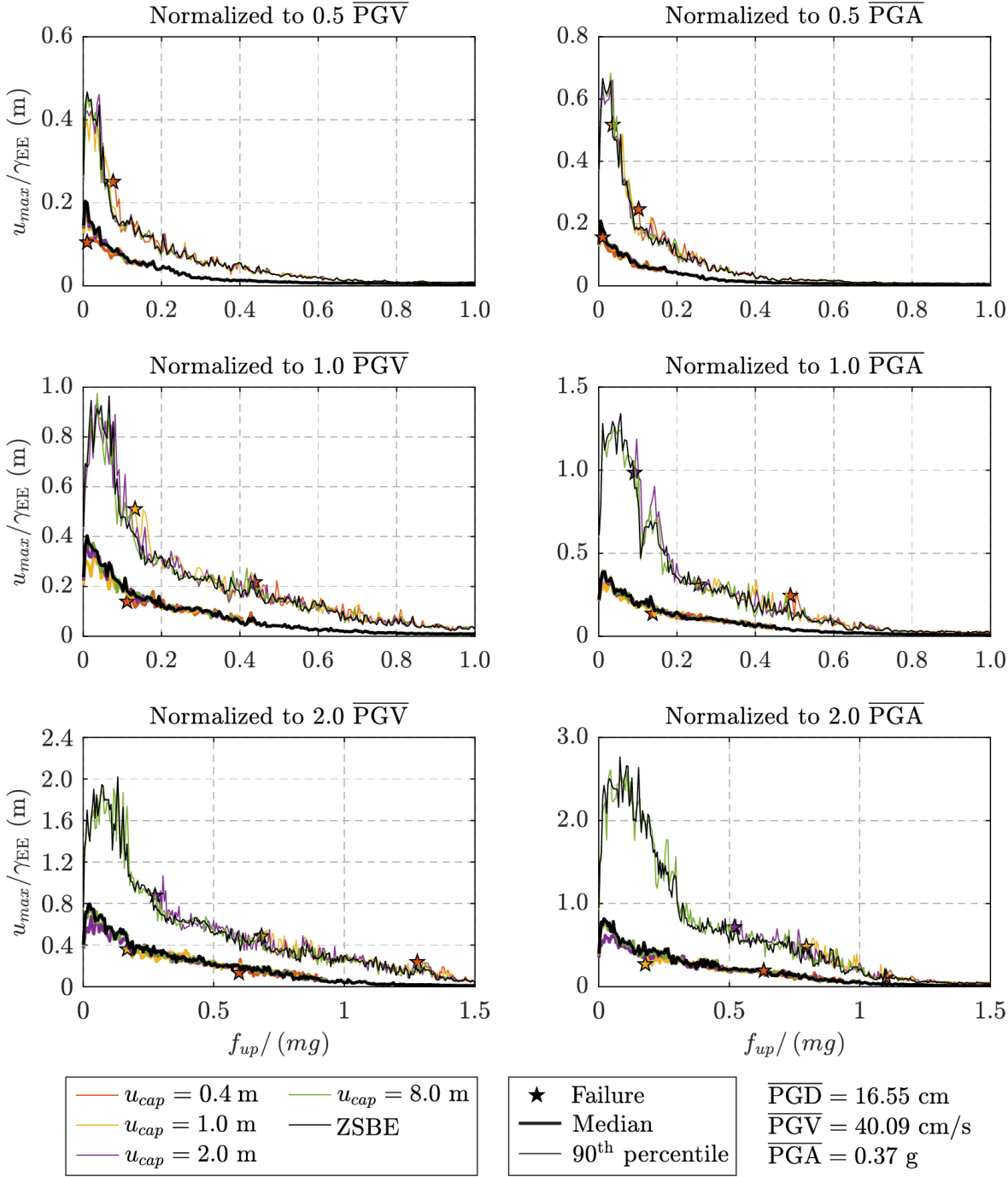
Figure A2.6. Median displacement spectra normalized by γ_{EE} for far-field record set, $u_{up} = 0.005$ m.

A2.1.2. Median and 90th percentile spectra for systems with u_{up} = 0.05 m

- Equal Displacement Rule
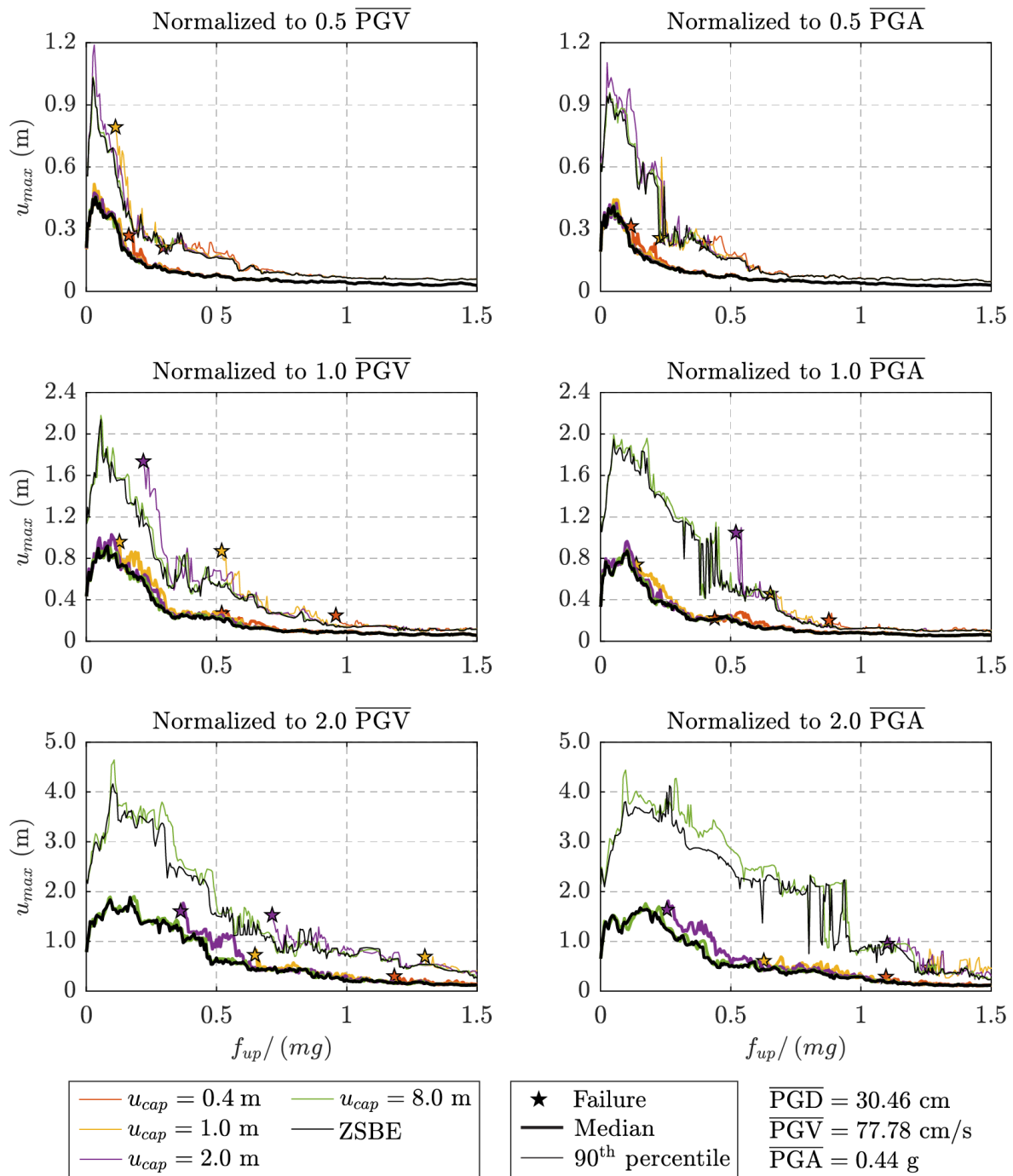
Figure A2.7. Median displacement spectra for near-field pulse-like record set, u_{up} = 0.05 m.
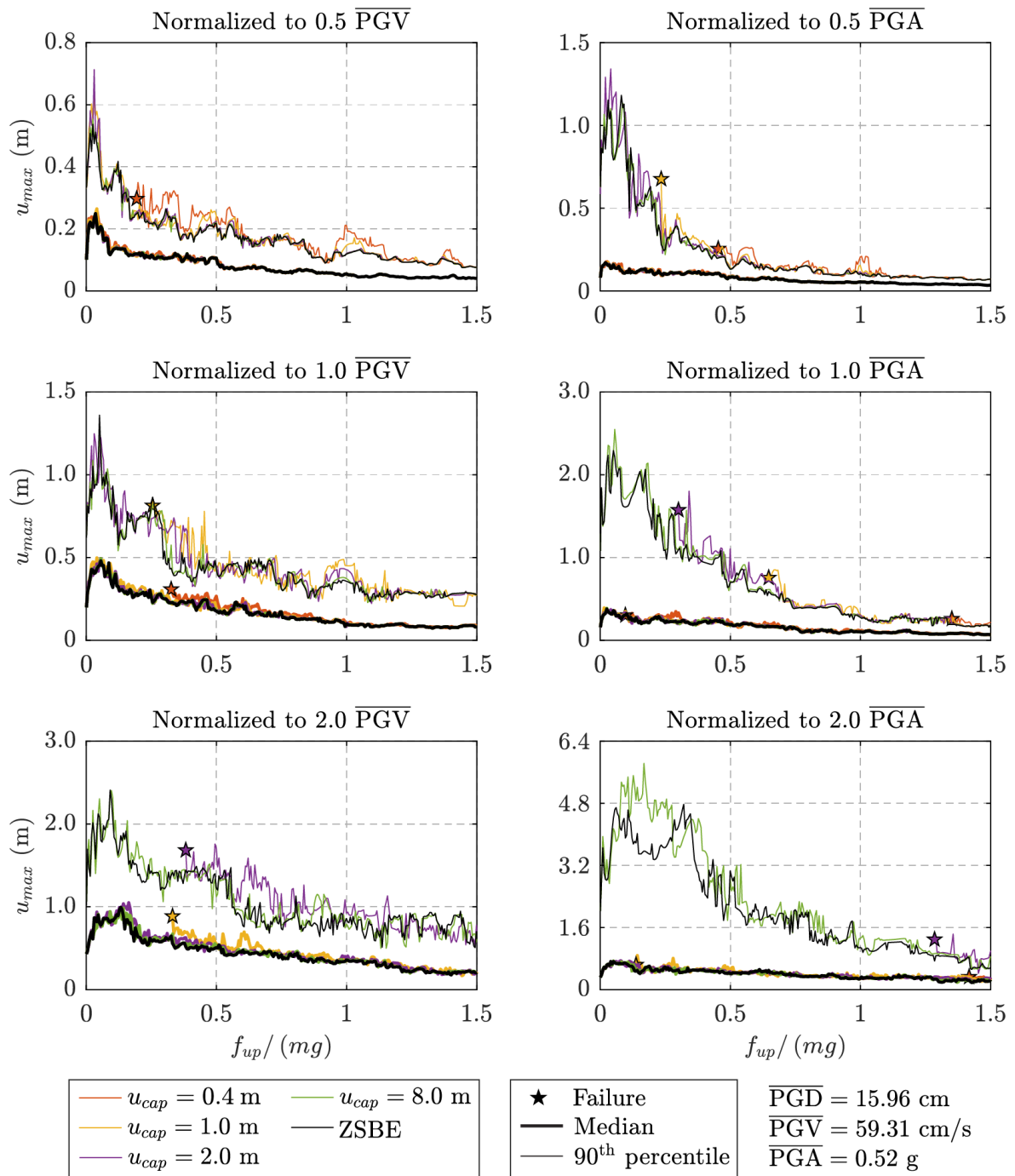
Figure A2.8. Median displacement spectra for near-field no pulse-like record set, $u_{up} = 0.05$ m.

Figure A2.9. Median displacement spectra for far-field record set, $u_{up} = 0.05$ m.

- Equal Energy Rule

Figure A2.10. Median displacement spectra normalized by γ_{EE} for near-field pulse-like record set, $u_{up} = 0.05$ m.

Figure A2.11. Median displacement spectra normalized by γ_{EE} for near-field no pulse-like record set, $u_{up} = 0.05$ m.
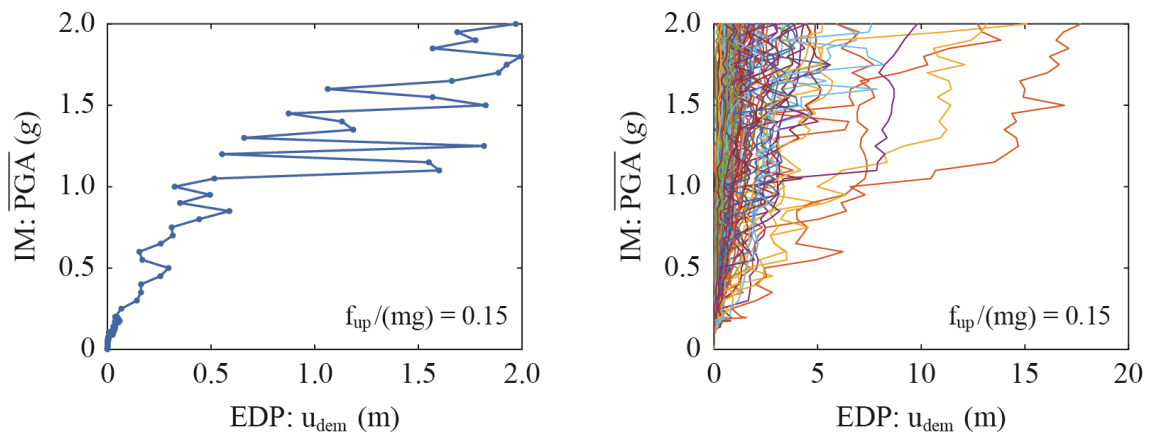
Figure A2.12. Median displacement spectra normalized by γ_{EE} for far-field record set, $u_{up} = 0.05$ m.

A2.2. Complementary data to Chapter 4
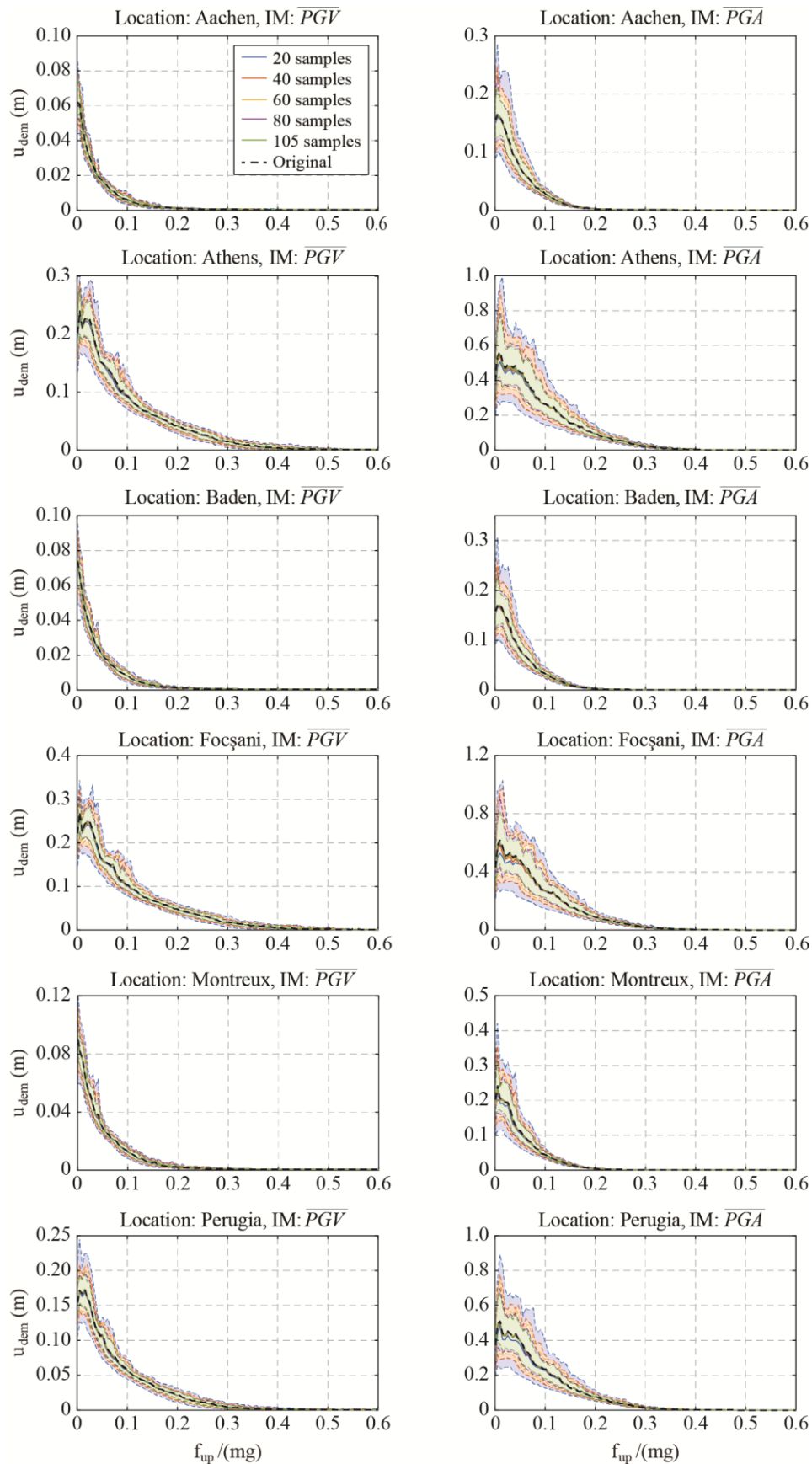
A2.2.1. IDA Curves
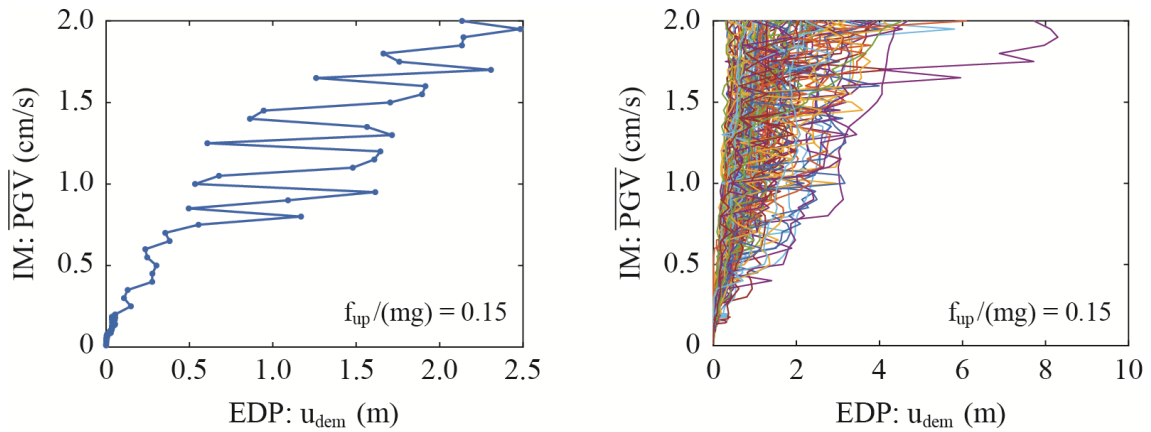
Figure A2.13. Typical IDA curve for a single ground motion (left) and the complete set of ground motions (right) for systems with $f_{up}/(mg) = 0.15$ and using $\overline{PGV}$ as IM.
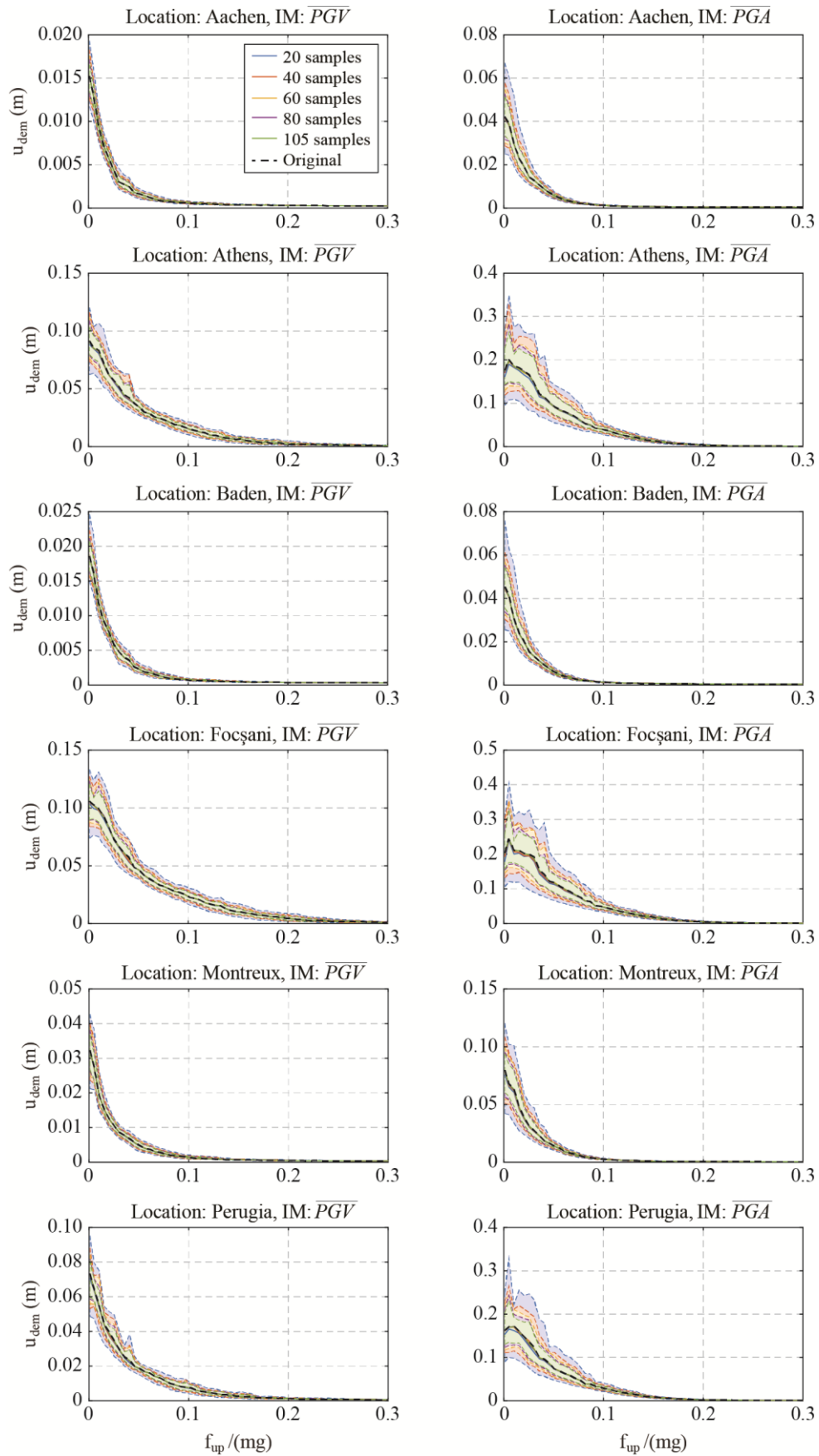

Figure A2.14. Typical IDA curve for a single ground motion (left) and the complete set of ground motions (right) for systems with $f_{up}/(mg) = 0.15$ and using $\overline{PGA}$ as IM.

A2.2.2. Bootstrapping analysis

Figure A2.15. Median and 90% confidence interval for the spectra with 10% in 50 years probability of exceedance.

Figure A2.16. Median and 90% confidence interval for the spectra with 50% in 50 years probability of exceedance.